Circulation Agreement

In presenting this dissertation as a partial fulfillment of the requirements for an advanced degree from Emory University, I agree that the Library of the University shall make it available for inspection and circulation in accordance with its regulations, governing materials of this type. I agree that permission to copy from, or to publish, this dissertation may be granted by the professor under whose direction it was written, or, in his absence, by the Dean of the Graduate School when such copying or publication is solely for scholarly purposes and does not involve potential financial gain. It is understood that any copying from, or publication of, this dissertation which involves potential financial gain will not be allowed without written permission.

_____

Zhen Xie

Ab initio Molecular Potential Energy Surface Construction and Molecular Dynamics Simulation for Small Molecules

By

Zhen Xie
Doctor of Philosophy

Department of Chemistry

Joel M. Bowman, Ph.D.
Adviser

Michael C. Heaven, Ph.D.
Committee Member

James T. Kindt, Ph.D.
Committee Member

Accepted:

Lisa A. Tedesco, Ph.D.
Dean of the Graduate School

Date

Ab initio Molecular Potential Energy Surface Construction and Molecular Dynamics Simulation for Small Molecules

By

Zhen Xie
B.S., University of Science and Technology of China, 2003
M.S., Emory University, 2007

Adviser: Joel M. Bowman, Ph.D.

An Abstract of
A dissertation submitted to the Faculty of the Graduate School of Emory University in partial fulfillment of the requirements for the degree of Doctor of Philosophy

Department of Chemistry

2008

Abstract

For the theoretical study of the chemical reactions, potential energy surface (PES) plays a crucial role. High quality PESs are always desired; however, there are many challenges in constructing these surfaces, and one of them is caused by the molecular permutation symmetry. In this dissertation, several methods targeting at the invariant property of the PES are addressed, especially the most advanced approach using the invariant polynomials. Based on the high quality PESs constructed with intrinsic permutation symmetry, extensive quasiclassical trajectory simulations of the small molecule reactions H_2 + $H_3{}^+$, H + CH_4, CH_5^+/CH_5 and H_3O^+/H_3O including their isotopomers are performed to understand the underlying microscopic reaction mechanism. In addition to the study of the dynamics of chemical reactions, some static properties of H_5^+ and CH_5^+ are also investigated based upon diffusion Monte Carlo methods. By the good agreement between the theoretical simulation results and the available experimental data, it indicates that quasiclassical trajectory simulation based on accurate potential energy surface is a powerful method to investigate and further understand the microscopic chemical reaction mechanism.

Ab initio Molecular Potential Energy Surface Construction and Molecular Dynamics Simulation for Small Molecules

By

Zhen Xie
B.S., University of Science and Technology of China, 2003
M.S., Emory University, 2007

Adviser: Joel M. Bowman, Ph.D.

A dissertation submitted to the Faculty of the Graduate School of Emory University in partial fulfillment of the requirements for the degree of Doctor of Philosophy

Department of Chemistry

2008

I dedicate this dissertation to my father Genxing Xie*, who inspired my enthusiasm in science & technology. I also dedicate this dissertation to my mother* Baodi Tang*, who gave me the strength to move forward on the way to pursuing knowledge. I dedicate this work and give special thanks to my beloved wife* **Chang Liu** *for being there with me throughout the entire doctorate program.*

Acknowledgements

First of all, I would like to give the most sincere thank to my adviser, Professor Joel M. Bowman, for his inspirational instructions and patient guidance during the passed five years. His efforts lead me step by step to advance in my study and research, and finally make this dissertation possible.

Here I also thank Dr. Michael C. Heaven and Dr. James T. Kindt for serving as my committee members, giving very nice comments and suggestions.

I would express my great appreciation to Dr. Bastiaan J. Braams for his valuable help and instructions on the invariant polynomial fitting methods.

I also want to express my appreciation to Dr. Tianquan Lian, Dr. Keiji Morokuma, Dr. M.C. Lin, Dr. Michael C. Heaven, Dr. James T. Kindt and Dr. Joel M. Bowman for the wonderful courses they taught in chemistry.

I acknowledge the previous and current members of Dr. Bowman's group, especially Dr. Xiubin Zhang, Dr. Xinchuan Huang, Dr. Tiao Xie, Dr. Zhong Jin, Dr. Alex Kaledin, Dr. Martina Kaledin, Dr. Jaime Rheinecker Clayton, Dr. Benjamin Shepler, Chao Chen and Yimin Wang for their friendship and valuable discussions.

I also acknowledge Dr. Djamaladdin (Jamal) G. Musaev, Dr. Stephen Irle and Dr. Guishan Zheng for their help on the Emerson Center computer facilities.

I am especially grateful to Ann Dasher for the graduate study advice, Susan Browne and Jianli Zhao for their coordination work.

I thank our collaborators Ms. Jennifer Mann and Dr. Robert Continetti at University of California, San Diego, who performed the wonderful experiments on $e+CH_5^+$ and $e+H_3O^+$.

Last but not least, I thank my parents, my sisters and my wife for their unlimited love and support all these years.

Table of Contents

List of Figures

List of Tables

1 Introduction

1.1 Chemical Reactions, Quasiclassical Trajectory Simulation and Potential Energy Surface

There are numerous chemical reactions occurring every second in the universe, and to understand these chemical reactions is the goal of many scientific researchers. Many instruments and theoretical methods have been developed to facilitate the researchers to understand the chemical reactions. Quasiclassical trajectory (QCT) simulation is one of the methods developed to investigate those chemical reactions. In the 1930s, classical trajectory calculations were carried out to theoretically investigate the dynamics of the reactive collisions [1–3]. The approach known as QCT method had developed very rapidly since the 1960s. The prefix "quasi" means the assignment of quantum states to the rotational and vibrational states of the reactants, and it is mainly developed by Karplus et al [4]. It was gradually substituted by a series of quantum mechanical approximation methods in 1970s and 1980s [5–7]. However, detailed analysis of many quantum effects for chemical reactions reported in the literature demonstrated that they were, to a considerable extent, describable with classical mechanics. This situation has led in recent times to a reconsideration of the QCT method for the investigation of reactive collisions. During the 1990s, the quality of available potential energy surface (PES) was improved greatly, which shed new light on the QCT methods. The PES, describing the interactions of the molecular species, is crucial for the theoretical simulation. Without an *accurate* PES, no matter how accurate the model is, the simulation is doomed to fail; while with an *accurate* PES, even though the model has some limitations or shortcomings, the simulation

can still provides some valuable information about the chemical reactions. In most cases, quasiclassical trajectory simulation based on high quality *ab initio* potential energy surface is such a combination that can describe a lot of chemical reactions reasonably as shown in the second part of this thesis.

1.2 Outline

This thesis is organized as following: part I is most involved in the theory and methods for the invariant potential energy function fitting, some basic calculations on the surface, and the methods to set up the initial conditions for quasiclassical trajectory simulation. The analysis of the final states of the trajectory simulation is addressed too. The whole section 3.2 is devoted to the notorious ZPE issue in QCT. Part II is mainly about various molecule systems we've studied mostly based on QCT simulations. Section 4, 5, 6 are devoted to the H_5^+ system. Section 7 and Section 8 are mostly for the H + CH_4 reaction and its isotopomer reaction. Section 9 is the study of the charge exchange reaction of CH_5^+ and the dissociation of CH_5. Section 10 is for the currently ongoing project on the charge exchange reaction of H_3O^+ and the dissociation of H_3O. Finally, a brief summary is given in Section 11.

Part I

Theory and Methods

2 *Ab initio* Molecular Potential Energy Construction

2.1 Molecule Symmetry and Representation

A molecule is a collection of atoms in three-dimensional space, and every atom has its coordinates. Consequently, in order to represent a molecule uniquely, every atom should be represented. One of the most straightforward representations is to specify the Cartesian coordinates for all the atoms, i.e., the x, y and z values for each atom. This results in a $3n$ tuple to represent a molecule that has n atoms in space and is usually called XYZ representation of a molecule. As is known, there are $3n - 6$ degrees of freedom for a non-linear n-atom molecule, and $3n - 5$ for a linear molecule. Obviously, there is some redundancy in the XYZ representation, and this redundancy is caused by the molecule symmetry. This symmetry includes molecular translational symmetry and rotational symmetry, since a molecule keeps the same if it is translated or rotated in space, especially its potential energy. To construct a potential energy function of a molecule, it is a requirement that the function should be invariant with the translation and rotation motions. There are basically two approaches to satisfy the symmetry requirement. One is to build the symmetry into the functional form of the potential energy function, and the other is to represent the molecule in a way such that the representation is invariant under the translation and rotation motions. The first approach may be involved, and here we just consider the second approach since it is relatively easy to represent a molecule and also consider the translational and rotational symmetry. There are many other representations that have been developed for molecules. Here we just focus on the bond length representation.

The bond length representation of a molecule is nothing but specifying all the $\frac{n(n-1)}{2}$ bond lengths for a general n-atom molecule. It is obvious that the bond lengths are invariant with respect to the translation and rotation of a molecule, which is the main property we desired for potential energy surface fitting. Before we celebrate that we have found the right representation of a molecule, a few other issues need to be considered. The first issue we need to consider is existence and uniqueness. Existence and forward uniqueness are obvious, but backward uniqueness does not exist. It is a mapping from a molecule to a vector for a representation. For forward uniqueness, it is the uniqueness of the bond length vector for a given molecule configuration; and backward uniqueness is the uniqueness to construct a molecule given the bond length vector. Fig. 2.1 shows a counterexample for backward uniqueness. In chemistry, especially organic chemistry, the molecules in Fig. 2.1(a) and (b) are two different molecules, and their chemical properties may differ significantly. Fortunately, the

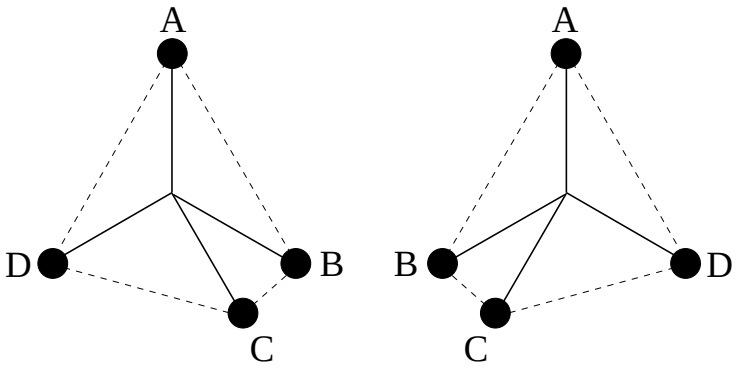

Figure 2.1: A counterexample for bond length representation backward uniqueness

potential energies for the two molecules in Fig. 2.1 are the same, and as a result, we do not need to distinguish this kind of molecules. Consequently, we still have the desired "uniqueness" for the bond length representation. The second issue we need

to consider is the degree of freedom (DOF) of the bond length representation and the actual DOF of a molecule. As shown previously, for an n-atom non-linear molecule, there are $3n-6$ DOF ($3n-5$ for linear molecule), and there are $\frac{n(n-1)}{2}$ DOF for the bond length representation. Table 2.1 list the first few DOF of a molecule and that using the bond length representation. Since the degree of freedom of a molecule

Table 2.1: Degree of freedom of molecules and the bond length representation

n (# of Atoms)	2	3	4	5	6	7	8	9	10	$\cdots$
Molecule Degree of Freedom	1	3	6	9	12	15	18	21	24	$\cdots$
Bond Length Representation	1	3	6	10	15	21	28	36	45	$\cdots$

is linear on the number of atoms n, but the number of bond lengths is quadratic on n, it is expected that these two degree of freedoms will diverge eventually. As can be seen in Table 2.1, for $n = 2, 3, 4$, these two DOFs are exactly the same, and the difference between them for $n = 5, 6$ or even $n = 7$ are small, but when $n \geq 8$, the difference increases very quickly. For an "good" representation, the degree of freedom should equal to the actual degree of freedom for efficiency, and as a result, the bond length representation is considered as "good" for $n \leq 7$. In most of the small molecule studies, 7 is a big number and it can cover a lot of small molecules. For larger molecules that have more than 7 atoms, a new representation may be needed for efficiency.

Up to this point, the bond length representation is a "good" representation for small molecules, and it is capable to represent the translational and rotational symmetries of molecules. However, there is still another symmetry called permutation symmetry that needs consideration. To explain the permutation symmetry, we take the H_3O molecule as an example. As can be seen, there are three identical H atoms

in H_3O. If we label the four atoms in H_3O as 1, 2, 3, 4 and restrict 4 to O atom, then the corresponding bond length vector can be represented as $(r_{12}, r_{13}, r_{14}, r_{23}, r_{24}, r_{34}$. If we permute H atom 1 with 2, the H_3O molecule keeps the same but the the bond length vector changes to $(r_{12}, r_{23}, r_{24}, r_{13}, r_{14}, r_{34}$. Now the problem becomes clear, in the bond length representation, different order of likely atoms generate different bond length vectors, while the potential of the energy should be the same no mater the order of the likely atoms is. This is the most difficult part for the molecule bond length representation in potential energy fitting and it is further discussed in Subsection 2.4.

2.2 Molecular PES Least Squares Fitting

Before the discussion of implementing of permutation symmetry into the PES fitting, we first discuss some of the general strategies in PES fitting.

In the bond length representation of a molecule, any molecule of n atoms is represented as a vector $(r_{1,2}, r_{1,3}, \cdots, r_{1,n}, r_{2,3}, \cdots, r_{2,n}, \cdots, r_{n-1,n})^T$. In a short notation, it is $\mathbf{x} = (x_1, x_2, \cdots, x_m)^T$ where $m = \frac{n(n-1)}{2}$. The potential energy V of the molecule is a function of $\mathbf{x}$ or $V \equiv V(\mathbf{x})$. Physically, there might be some complicated functional form for the function $V(\mathbf{x})$, considering the simplicity and accuracy, one approach is just to expand $V(\mathbf{x})$ in polynomial basis function. As a result, the actual potential energy $V(\mathbf{x})$ can be approximated by

$$f(\mathbf{x}) = \sum_{\alpha_1, \cdots, \alpha_m} a_{\alpha_1, \cdots, \alpha_m} x_1^{\alpha_1} \cdots x_m^{\alpha_m}.$$

or in a short notation as

$$f(\mathbf{x}) = \sum_i a_i B_i(\mathbf{x}), \tag{2.1}$$

where $B_i(\mathbf{x})$ is a polynomial basis function. In the PES fitting problem, suppose we collected a large amount of molecules $M_1, \cdots, M_n$, and they are represented as $\mathbf{x}_1, \cdots, \mathbf{x}_n$. For every molecule M_i, there is an potential energy value E_i associated with it, hence every data entry is a tuple $(\mathbf{x}_i, E_i)$. All the $\mathbf{x_i}$ variables are called independent variables and E_i are dependent variables. The least squares method is to find a model function $f(\mathbf{x}, \beta)$ where the vector β holds the coefficients for each basis function as $B_i(\mathbf{x})$ in Eq. 2.1. We wish to find the coefficients for which the model "best" fit the data. The least squares methods defines the "best" as when the sum, S, of squared residuals

$$S = \sum_{i=1}^{i=n} r_i^2 \tag{2.2}$$

is minimum.

A residual is defined as the difference between the values of the dependent variable and the model as

$$r_i = E_i - f(\mathbf{x}_i, \beta).$$

The least squares system can be constructed easily providing the data set in PES constructing.

The object function in the linear least squares system is Eq. 2.2 or more explicitly,

$$S = \sum_{i=1}^{n} \left(E_i - f(\mathbf{x}_i, \beta)\right)^2. \tag{2.3}$$

The minimum of the sum of squares is found by setting the gradient to zero. Since the model contains n parameters there are n gradient equations.

$$\frac{\partial S}{\partial \beta_j} = -2 \sum_i \frac{\partial f(\mathbf{x}_i, \beta)}{\partial \beta_j} (E_i - f(\mathbf{x}_i, \beta)) = 0,\ j = 1, \cdots, n.$$

The least squares system is linear since the model function is just a linear combinations of all the basis function $B_i(\mathbf{x})$, or

$$f(\mathbf{x}_i, \beta) = \sum_{j=1} \beta_j B_j(\mathbf{x}_i),$$

Therefore,

$$\frac{\partial f(\mathbf{x}_i, \beta)}{\partial \beta_j} = B_j(\mathbf{x}_i)$$

and the gradient equations become

$$\sum_i B_j(\mathbf{x}_i)(E_i - f(\mathbf{x}_i, \beta)) = 0.$$

Denote $A_{ij} = B_j(\mathbf{x}_i)$, then

$$f(\mathbf{x}_i, \beta) = \sum_j \beta_j A_{ij}$$

$$\sum_i A_{ij} \left(E_i - \sum_k \beta_k A_{ik} \right) = 0.$$

Rearrange the above equation, we get

$$\sum_i A_{ij} E_i = \sum_{ik} A_{ij} \beta_k A_{ik}$$

or

$$A^T E = A^T A \beta \tag{2.4}$$

which is called the **normal equations** of linear system.

Solution of the normal equations yield the least squares estimator $\hat{\beta}$, of the pa-

rameter values, or the coefficients.

The expressions given above are based on the implicit assumption that all the measurements are uncorrelated and have equal uncertainty. The Gauss-Markov theorem shows that, when this is so, $\hat{\beta}$ is a *best linear unbiased estimator*. If, however, the energies are uncorrelated but have different uncertainties, a modified approach must be adopted. Aitken showed that when a weighted sum of squared residues is minimized, $\hat{\beta}$ is the best linear unbiased estimator if each weight is equal to the reciprocal of the variance of the measurement.

$$S = \sum_{i=1}^{n} W_{ii} r_i^2, W_{ii} = \frac{1}{\sigma_i^2}. \tag{2.5}$$

The matrix form Eq. 2.5 is

$$(A^T W A)\beta = A^T W E, \tag{2.6}$$

where matrix A is defined as $A_{ij} = B_j(\mathbf{x}_i)$.

When the energy errors are uncorrelated, the weight matrix W is diagonal. If the errors are correlated, the weight matrix should be equal to the inverse of the variance-covariance matrix of the observations, but this does not affect the matrix expression of the normal equations and the parameters are still *best linear unbiased estimator*.

The general solution to the least squares system (Eq. 2.4) can be written as

$$\hat{\beta} = \left(A^T A\right)^{-1} A^T E. \tag{2.7}$$

In practice, the normal equations are not used due to the numerical unsteadiness. Instead, orthogonal decomposition of the A matrix is adopted for the purpose of the

numerical stability.

The linear system in the matrix form can be written as

$$A\beta = E$$

where $A \in \mathbb{R}^{n\times m}, \beta \in \mathbb{R}^m,$ and $E \in \mathbb{R}^n, (n > m)$, after the QR decomposition of A, the linear system can be written as

$$QR\beta = E$$

where $Q \in \mathbb{R}^{n\times n}$ is an orthogonal matrix and $R \in \mathbb{R}^{n\times m}$ is partitioned into $m \times m$ blocks R_m, and a $(n-m) \times m$ zero block. R_m is upper triangular, and R can be written as

$$R = \begin{bmatrix} R_m \\ 0 \end{bmatrix}$$

After the QR decomposition of A matrix, the parameter vector β can be solved easily by a backward substitution due to the triangular nature of R_m.

An alternative decomposition of the A matrix is the singular value decomposition (SVD) [8]

$$A = U\Sigma V^T, \tag{2.8}$$

where $A \in \mathbb{R}^{n\times m}, U \in \mathbb{R}^{n\times n}, V \in mathbbR^{m\times m}$ and $\Sigma \in \mathbb{R}^{n\times m}$ is a matrix with non-negative numbers on the diagonal and zeros off the diagonal. Both U and V are orthogonal matrices. After the SVD decomposition of A matrix, the linear system $A\beta = E$ can be solved easily as $\hat{\beta} = V\Sigma^{-1}U^T E$. Incorporating the truncated SVD approach, this decomposition gives a more stable and exact answer for the estimation

of β.

Similarly, the matrix form the weighted least squares problems can be written as

$$\sqrt{W}A\beta = \sqrt{W}E,$$

both QR and SVD decomposition of $\sqrt{W}A$ matrix can be adopted to solve the problem.

The least squares method may theoretically solve the PES fitting problem, but in reality, there are still some issues, especially when approximating the potential energy function using polynomials.

Fig. 2.2 just shows the weakness of the least squares fitting using the usual polynomial basis functions.

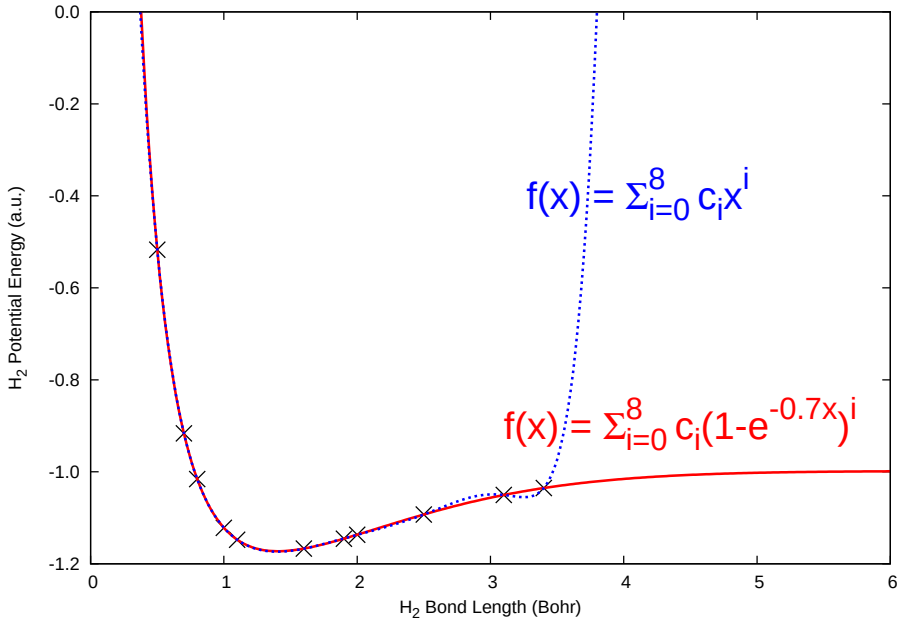

Figure 2.2: The failure of the usual polynomial based least squares fitting and an alternative solution by changing the variables.

In one dimensional case, theoretically, it is possible for a function expanded in the polynomial basis to go through all the data point when the degree of basis function getting higher and higher. This is not desired since the prediction for the fitted model function becomes very poor.

In the example of H_2 PES shows in Fig. 2.2, the known data points are scattered, and the dotted blue lines shows the usual polynomial based function. As we can see, the model function may fit the data available region reasonably well, but blowed up right outside the data point region. There is method by selecting the data points as the Chebyshev nodes, which will reduce the oscillation of the model function, but in the PES fitting process, it is difficult to sample the data point by following the Chebyshev nodes, especially in the high dimensional space. An easy alternative method to overcome the weakness of the usual polynomial basis function is by changing the variables. As shown in Fig. 2.2, by change the usual bond length variable x to $1 - \exp(-0.7x)$, the model function behaves much better than the unchanged one in both the data available region and extended region. There are many choices for the variable change, and particularly in the PES fitting process, due to the nature of the PES, a new variable which decays to a constant in the large values, and increases sharply in the short value region will be suitable. The choice of variables also depends on the molecule system, and in the later applications, we can notice different choice of the variable changes.

2.3 Invariant Fitting Strategies

To implement the permutation symmetry into the potential energy surface fitting is not a trivial task and several approaches have been developed. One of the most

straightforward approach, which will be discussed on the following section. Another approach is a restricted coefficients approach, and it will be discussed in Section 2.3.2. The most advanced approach is to use the invariant polynomial, it is complicated and will be addressed in Section 2.4.

2.3.1 Straightforward Approach

The basic idea of the "straightforward approach" approach is to duplicate the data set. For example, suppose we want to fit a PES for H_2O molecule, and we have some configurations of H_2 $M_1, \cdots, M_n$ with energy $E_1, \cdots, E_n$. Based on $M_1, \cdots, M_n$ and $E_1, \cdots, E_n$, we can set up a least square system as in Section 2.2, and get a potential energy function f, for any given configuration M_i, we can predict the potential energy symbolically as $f(M_i)$. Due to the permutation symmetry of the H_2O molecule, the representation of the water molecule changes from M_i to M_i' if we switch the two H atoms. The molecule does no change, but the representation changes since the representation does not reflect the permutation symmetry. Since both M_i and M_i' are corresponding to the same water molecule, their potential energy should be the same. As a result, we would require $f(M_i) = f(M_i')$, which is not usually true during the fitting process provided $M_1, \cdots, M_n$ and $E_1, \cdots, E_n$. In the straightforward approach, the molecule configurations are just duplicated. For H_2O, there are only one non-trivial permutation, and for every configuration M_i, the only possible other configuration is M_i'. If both M_i and M_i' are included in the data set, then hopefully, the final fitted function has the permutation symmetry. In summary, the original data set is $\{M_1, \cdots, M_n\}$ and $\{E_1, \cdots, E_n\}$, and the new data set is $\{M_1, \cdots, M_n\} \oplus \{M'_1, \cdots, M'_n\}$ and $\{E_1, \cdots, E_n\} \oplus \{E'_1, \cdots, E'_n\}$.

The straightforward approach may work for some simple molecules which do not have many likely atoms. This approach is easy to implement. However, one of major drawback of this approach is when the molecule becomes a litter more complicated, for example, H_3O, only one more H atom is added to the H_2O molecule, but there are 5 non-trivial permutation. This extra 5 permutation need to make the data set 5 times larger than the original one, which will make the potential energy fitting process much longer. Generally, for a molecule $x_a y_b$, the new data set will be $a!b! - 1$ times larger the original data set, this is extremely undesired. In addition, by the duplication of data set, there is no guarantee for the fitted potential energy to be invariant under the permutation. In other word, $f(M_i) = f(M_i')$ may not satisfied even if in the date set both M_i and M_i have the same energy.

2.3.2 Restricted Coefficients Approach

In the straightforward approach, the data set gets duplicated, and the fitted PES function may have *loose* invariant property. In order to make the invariant property be exact, a restricted coefficients approach is developed.

In order to show the idea behind restricted coefficients approach, we may examine a simple example. Suppose we want to fit a function f of two variables x, y. The date set we have is $x_1, \cdots, x_n$, $y_1, \cdots, y_n$ and $E_1, \cdots, E_n$. Based on the least squares fitting strategy as in Section 2.2, the basis functions are $x^\alpha y^\beta$ where α and β are non-negative integers. Generally, the function f is expressed as

$$f(x, y) = \sum_{\alpha,\beta} a_{\alpha,\beta} x^\alpha y^\beta. \tag{2.9}$$

To introduce some permutation symmetry into this example, we require the function

f to be invariant to the permutation of x and y. That is, f needs to satisfy

$$f(x, y) = f(y, x).$$

From Eq. 2.9, we get

$$f(y, x) = \sum_{\alpha,\beta} b_{\alpha,\beta} y^{\alpha} x^{\beta}.$$

or

$$f(y, x) = \sum_{\alpha,\beta} a_{\beta,\alpha} x^{\beta} y^{\alpha}. \tag{2.10}$$

Comparing Eq. 2.9 and Eq. 2.10, we need to restrict $a_{\alpha,\beta} = a_{\beta,\alpha}$. In other word, the coefficients for the $x^{\beta}y^{\alpha}$ and $x^{\alpha}y^{\beta}$ should be the same in order to satisfy the permutation symmetry of $f(x, y)$. As a result of restricting the coefficients, the function $f(x, y)$ may be expanded as

$$f(x, y) = \sum_{\alpha,\beta} a_{\alpha+\beta}(x^{\alpha}y^{\beta} + x^{\beta}y^{\alpha}). \tag{2.11}$$

In Eq. 2.11, the permutation invariant property $f(x, y) = f(y, x)$ is satisfied rigorously. In addition, by restrict the coefficients, the final least square system may reduce the size dramatically. For the above example, the original adjacent matrix in least squares system may be $n \times m$, where n is the number of data points and m is the number of coefficients. The new adjacent matrix's size after the coefficients restriction reduces to $n \times \frac{m}{2}$. For large molecules, this factor is significant.

In the real molecule example such as H_3O, we can see that this approach is basically the same. For H_3O, we can use $x_1, \cdots, x_n$ to denote $(r_{12}, r_{13}, r_{14}, r_{23}, r_{24}, r_{34})$ which is the bond length vector of H_3O. Table 2.2 shows an example on a basis func-

tion $x_1^1x_2^0x_3^2x_4^3x_5^1x_6^2$. After the restriction of coefficient, we can see that $x_1^1x_2^0x_3^2x_4^3x_5^1x_6^2$, $x_1^1x_2^3x_3^1x_4^0x_5^2x_6^2$, $x_1^3x_2^0x_3^2x_4^1x_5^1x_6^2$, $x_1^0x_2^1x_3^2x_4^3x_5^2x_6^1$, $x_1^0x_2^3x_3^2x_4^1x_5^2x_6^1$ and $x_1^3x_2^1x_3^1x_4^0x_5^2x_6^2$ share a common coefficient.

Table 2.2: Illustration of the coefficients restriction on a basis function $x_1^1x_2^0x_3^2x_4^3x_5^1x_6^2$ for H_3O molecule in potential energy function fitting.

permutation	representation	Power Index	Basis Term
(1)	$(x_1, x_2, x_3, x_4, x_5, x_6)$	(1,0,2,3,1,2)	$x_1^1x_2^0x_3^2x_4^3x_5^1x_6^2$
(12)	$(x_1, x_4, x_5, x_2, x_3, x_6)$	(1,3,1,0,2,2)	$x_1^1x_2^3x_3^1x_4^0x_5^2x_6^2$
(13)	$(x_4, x_2, x_6, x_1, x_5, x_3)$	(3,0,2,1,1,2)	$x_1^3x_2^0x_3^2x_4^1x_5^1x_6^2$
(23)	$(x_1, x_1, x_3, x_4, x_6, x_5)$	(0,1,2,3,2,1)	$x_1^0x_2^1x_3^2x_4^3x_5^2x_6^1$
(123)	$(x_4, x_1, x_5, x_2, x_6, x_3)$	(0,3,2,1,2,1)	$x_1^0x_2^3x_3^2x_4^1x_5^2x_6^1$
(132)	$(x_2, x_4, x_6, x_1, x_3, x_5)$	(3,1,1,0,2,2)	$x_1^3x_2^1x_3^1x_4^0x_5^2x_6^2$

By the restriction of the coefficients, the number of coefficients for the potential energy function be reduced by a large factor related to the molecule of interest. Table 2.3 show the comparison between the coefficient restrict approach and the non-restricted one.

Table 2.3: Comparison of the basis size for the potential energy function of H_3O at certain degree using restricted coefficients and non-restricted ones

Maximum Degree	1	2	3	4	5	6	7	8	9
Basis Size (restricted)	3	9	23	51	103	196	348	590	960
Basis Size (non-restricted)	7	28	84	210	462	924	1716	3003	5005

By the implementation of restricted coefficient approach, the fitting efficiency enhanced greatly along with the *exact* permutation invariant property. For H_3O molecule, suppose we originally have 10000 data points, and we want to fit the potential energy function up to degree 8. In the straightforward approach, we need to solve a least system of 60000×3003, while using the restrict coefficients approach, we

only need to solve a least squares system of size 10000×590 which is much smaller.

The restricted coefficients approach is better than the straightforward approach in most of the aspect except for the implementation (coding) process.

The restricted coefficients approach can be applied for small molecules, one of its drawback is the evaluation time for the fitted function. As can be seen in Eq. 2.11, both $x^\alpha y^\beta$ and $x^\beta y^\alpha$ needed to be evaluated if we want the function value at some point (x, y), though the coefficients may reduced a lot. This limitation is due to the lack of recursive relation between all the basis functions. As a result, this approach is superseded by an advance approach with the adoption of invariant polynomials, especially *primary invariants* and *secondary invariants*. Based on primary and secondary invariants, all the invariant polynomials cane be generated recursively, and this can further reduce the function evaluation time which is extremely important for the various application using PES. This new approach is discussed in Section 2.4.

2.4 Invariant Polynomials

Invariant polynomials of finite group are the fundamentals in the PES fitting with permutation invariant property. It is a whole research field in Algebra and here I can just briefly outline some of the important results which are closely related to our invariant PES fitting approach. The proofs of the theorems, propositions, corollaries are not provided here for the purpose of compactness. See the book [9] by Harm Derksen and Gregor Kemper for details.

Before the introduction of polynomials, we define the monomial,

Definition 2.1 *A* **monomial** *in* $x_1, x_2, \cdots, x_n$ *is a product of the form*

$$x_1^{\alpha_1} \cdot x_2^{\alpha_2} \cdots x_n^{\alpha_n},$$

where all of the exponents $\alpha_1, \alpha_2, \cdots, \alpha_n$ *are non-negative integers. The* **total degree** *of this monomial is the sum* $\alpha_1 + \alpha_2 + \cdots + \alpha_n$.

We can simplify the notation for monomial as follows: let $\alpha = (\alpha_1, \cdots, \alpha_n)$ be an n-tuple of non-negative integers. Then we set

$$x^\alpha = x_1^{\alpha_1} \cdot x_2^{\alpha_2} \cdots x_n^{\alpha_n}.$$

Let $|\alpha| = \alpha_1 + \alpha_2 + \cdots + \alpha_n$ and denote it as the total degree of the monomial x^α.

Definition 2.2 *A* **polynomial** f *in* $x_1, \cdots, x_n$ *with coefficients in field* k *is a finite linear combination (with coefficients in* k*) of monomial. We will write a polynomial* f *in the form*

$$f = \sum_\alpha a_\alpha x^\alpha, \quad a_\alpha \in k,$$

where the sum is over a finite number of n*-tuples* $\alpha = (\alpha_1, \cdots, \alpha_n)$. *The set of all polynomials in* $x_1, \cdots, x_n$ *with coefficients in* k *is denoted* $k[x_1, \cdots, x_n]$.

For example,

$$f = x^3yz + \frac{5}{2}x^2y^3 - 7xyz + z^2$$

is a polynomial in $\mathbb{Q}[x, y, z]$.

Definition 2.3 *Let* $f = \sum_\alpha a_\alpha x^\alpha$ *be a polynomial in* $k[x_1, \cdots, x_n]$.

1. *We call* a_α *the* **coefficients** *of the monomial* x^α.

2. *If* $a_\alpha \neq 0$, *then we call* $a_\alpha x^\alpha$ *a* **term** *of* f.

3. *The* **total degree** *of* f, *denoted deg(*f*), is the maximum* $|\alpha|$ *such that the coefficient* a_α *is nonzero.*

The sum and product of two polynomials is again a polynomial. We say that a polynomial f divides a polynomial g provided that $g = fh$ for some $h \in k[x_1, \cdots, x_n]$.

As can be shown that under addition and multiplication, $k[x_1, \cdots, x_n]$ satisfies all of the field axioms except of the existence of multiplicative inverse. Such a mathematical structure is called a commutative ring, therefore, $k[x_1, \cdots, x_n]$ is usually called as a *polynomial ring*.

With the definition of monomials and polynomials, we come to the invariants of finite groups.

Symmetric polynomials arises naturally when studying the invariant, and here is the definition,

Definition 2.4 *A polynomial* $f \in k[x_1, \cdots, x_n]$ *is* **symmetric** *if*

$$f(x_{i_1}, \cdots, x_{i_n}) = f(x_1, \cdots, x_n)$$

for every possible permutation $x_{i_1}, \cdots, x_{i_n}$ *of the variables* $x_1, \cdots, x_n$.

For example, if the variables are x, y and z, then $x^2+y^2+z^2$ and xyz are obviously symmetric. The following symmetric polynomials are very important in the later discussion.

Definition 2.5 *Given variables $x_1, \cdots, x_n$, we define $\sigma_1, \cdots, \sigma_n \in k[x_1, \cdots, x_n]$ by the formulas*

$$\begin{aligned}
\sigma_1 &= x_1 + \cdots + x_n, \\
&\vdots \\
\sigma_r &= \sum_{i_1 < i_2 < \cdots < i_r} x_{i_1} x_{i_2} \cdots x_{i_r}, \\
&\vdots \\
\sigma_n &= x_1 x_2 \cdots x_n.
\end{aligned}$$

Thus, σ_r is the sum of all monomials that are products of r distinct variables. In particular, every term of σ_r has total degree of r. These symmetric polynomials $\sigma_1, \cdots, \sigma_n$ are called the **elementary symmetric functions**.

Theorem 2.6 (The fundamental Theorem of Symmetric Polynomials) *Every symmetric polynomial in $k[x_1, \cdots, x_n]$ can be written uniquely as a polynomial in the elementary symmetric functions $\sigma_1, \cdots, \sigma_n$.*

In dealing with symmetric polynomials, it is often convenient to work with ones that are *homogeneous*. Here is the definition,

Definition 2.7 *A polynomial $f \in k[x_1, \cdots, x_n]$ is* **homogeneous** *of total degree d provided that every term appearing in f has total degree d.*

For example, the ith elementary symmetric function σ_i is homogeneous of total degree i. An important fact is that every polynomial can be written uniquely as a sum of homogeneous polynomials. Namely, given $f \in k[x_1, \cdots, x_n$, let f_d be the sum of all

terms of f of total degree d. Then each f_d is homogeneous and $f = \sum_d f_d$. We can f_d the dth *homogeneous component* of f.

We can understand symmetric polynomials in terms of their homogeneous components as follows.

Proposition 2.8 *A polynomial $f \in k[x_1, \cdots, x_n]$ is symmetric if and only if all if its homogeneous components are symmetric.*

Now we will give some basic definition for invariants of finite matrix groups, and here we assume that for the field k we discussed, its *characteristic* is zero.

Definition 2.9 *Let $GL(n, k)$ be the set of all invertible $n \times n$ matrices with entries in the field k.*

From the knowledge in matrix and the above definition, it is obvious $GL(n, k)$ is a group, and it is customarily called the *general linear group.*

The permutation groups we are interested in for PES fitting are subsets of $GL(n, k)$.

Definition 2.10 *A finite subset $G \subset GL(n, k)$ is called a* **finite matrix group** *provided it is nonempty and closed under matrix multiplication. The number of elements of G is called the* **order** *of g and is denoted as $|G|$.*

An example of the finite matrix group is given by

$$A = \begin{pmatrix} 0 & -1 \\ 1 & 0 \end{pmatrix} \in GL(2, k).$$

The permutation group is no doubt the finite matrix group we are interested in for PES fitting.

Let τ denote a permutation $x_{i_1}, \cdots, x_{i_n}$ of $x_1, \cdots, x_n$. Since τ is determined by what it does to the subscripts, we will set $i_1 = \tau(1), i_1 = \tau(2), \cdots, i_n = \tau(n)$. Then the corresponding permutation of variables is $x_{\tau(1)}, \cdots, x_{\tau(n)}$.

We can create a matrix form τ as follows. Consider the linear map that takes $(x_1, \cdots, x_n)$ to $(x_{\tau(1)}, \cdots, x_{\tau(n)})$. The matrix representing this linear map is denoted M_τ and is called a *permutation matrix*. Thus, M_τ has the property that under matrix multiplication, it permutes the variables according to τ:

$$M_\tau \cdot \begin{pmatrix} x_1 \\ \vdots \\ x_n \end{pmatrix} = \begin{pmatrix} x_{\tau(1)} \\ \vdots \\ x_{\tau(n)} \end{pmatrix}.$$

It is easy to show that M_τ is obtained from the identity matrix by permuting its columns according to τ. As an example, consider the permutation τ that takes (x, y, z) to (y, z, x). Here $\tau(1) = 2, \tau(2) = 3$ and $\tau(3) = 1$, and

$$M_\tau \cdot \begin{pmatrix} x \\ y \\ z \end{pmatrix} = \begin{pmatrix} 0 & 1 & 0 \\ 0 & 0 & 1 \\ 1 & 0 & 0 \end{pmatrix} \begin{pmatrix} x \\ y \\ z \end{pmatrix} = \begin{pmatrix} y \\ z \\ x \end{pmatrix}.$$

Since there are $n!$ way to permute the variables, we get $n!$ permutation matrices. Furthermore, this set is closed under matrix multiplication, and it is easy to show that

$$M_\tau \cdot M_\nu = M_{\nu\tau},$$

where $\nu\tau$ is the permutation takes i to $\nu(\tau(i))$. Thus the permutation matrices form

a finite matrix group in $GL(n,k)$. In group theory, this kind of permutation matrices is denoted as S_n.

In PES fitting, due to the representation of the molecules, we can not direct study the permutation matrices S_n, instead, it is just a group G.

Definition 2.11 *Let $G \subset GL(n,k)$ be a finite matrix group, then a polynomial $f(x) \in k[x_1, \cdots, x_n]$ is* **invariant under** *G if*

$$f(\mathbf{x}) = f(A \cdot \mathbf{x})$$

for all $A \in G$. The set of all invariant polynomials is denoted $k[x_1, \cdots, x_n]^G$.

Example If we consider the group $S_n \subset GL(n,k)$ of permutation matrices, then it is obvious that

$$k[x_1, \cdots, x_n]^{S_n} = \{\text{all symmetric polynomials in } k[x_1, \cdots, x_n]\}$$

or

$$k[x_1, \cdots, x_n]^{S_n} = k[\sigma_1, \cdots, \sigma_n]. \quad \blacksquare$$

Thus, every invariants can be written as a polynomial in finitely many invariants. In addition, we know that the representation in terms of the elementary symmetric functions is unique. Hence, we have a very explicit knowledge of the invariants of S_n.

In the case of a general finite matrix group G, we have

Proposition 2.12 *Let $G \subset GL(n,k)$ be a finite matrix group. Then the set $k[x_1, \cdots, x_n]^G$ is closed under addition and multiplication and contains the constant polynomials.*

Multiplication and addition in $k[x_1, \cdots, x_n]^G$ automatically satisfies the distribution, association etc properties since these properties are true in $k[x_1, \cdots, x_n]$, and it is a *ring*. Furthermore, we say that $k[x_1, \cdots, x_n]^G$ is a *subring* of $k[x_1, \cdots, x_n]$.

Same as symmetric polynomials whose homogeneous components are also symmetric, we have

Proposition 2.13 *Let $G \subset GL(n, k)$ be a finite matrix group. Then a polynomial $f \in k[x_1, \cdots, x_n]$ is invariant under G if and only if all of its homogeneous components are.*

Proposition 2.13 allows us to reduce the case of homogeneous invariants.

The following lemma provides an explicit criteria to tell whether a polynomial is invariant under the action of group G.

Lemma 2.14 *Let $G \subset GL(n, k)$ be a finite matrix group and suppose that we have $A_1, \cdots, A_m \in G$ such that every $A \in G$ can be written in the for*

$$A = B_1 B_2 \cdots B_t,$$

*where $B_i \in \{A_1, \cdots, A_m\}$ for every i (we say that $A_1, \cdots, A_m$ **generate** G). Then $f \in k[x_1, \cdots, x_n]$ is in $k[x_1, \cdots, x_n]^G$ if and only if*

$$f(\mathbf{x}) = f(A_1 \cdot \mathbf{x}) = \cdots = f(A_m \cdot \mathbf{x}).$$

Lemma 2.14 provides a method to check whether $f \in k[x_1, \cdots, x_n]$ is in $k[x_1, \cdots, x_n]^G$, and we need further method to determine, in an algorithm fashion, the ring of invariants $k[x_1, \cdots, x_n]^G$ of a finite group $G \subset GL(n, k)$. Here we assume that the field k

has characteristic zero. We begin by some definitions,

Definition 2.15 *Given $f_1, \cdots, f_m \in k[x_1, \cdots, x_n]$, we let $k[f_1, \cdots, f_m]$ denote the subset of $k[x_1, \cdots, x_n]$ consisting of all polynomial expressions in $f_1, \cdots, f_m$ with coefficients in k.*

This means that the elements $f \in k[f_1, \cdots, f_m]$ are those polynomials which can be written in the form

$$f = g(f_1, \cdots, f_m),$$

where g is a polynomial in m variables with coefficients in k.

Since $k[f_1, \cdots, f_m]$ is closed under multiplication and addition and contains the constants, it is a subring of $k[x_1, \cdots, x_n]$. We say that $k[f_1, \cdots, f_m]$ is *generated by* $f_1, \cdots, f_m$ *over* k.

An important tool in the study of $k[x_1, \cdots, x_n]^G$ is the *Reynolds operator*, which is defined as follows.

Definition 2.16 *Given a finite matrix $G \subset GL(n, k)$, the* **Reynolds operator** *of G is the map $R_G : k[x_1, \cdots, x_n] \to k[x_1, \cdots, x_n]$ defined by the formula*

$$R_G(f)(\mathbf{x}) = \frac{1}{|G|} \sum_{A \in G} f(A \cdot \mathbf{x})$$

for $f(\mathbf{x}) \in k[x_1, \cdots, x_n]$.

Note that the division by $|G|$ is allowed since k has characteristic zero. The Reynolds operator has the following crucial properties.

Proposition 2.17 *let R_G be the Reynolds operator of the finite matrix group G.*

1. *R_G is k-linear in f.*

2. *If $f \in k[x_1, \cdots, x_n]$, then $R_G(f) \in k[x_1, \cdots, x_n]^G$.*

3. *If $f \in k[x_1, \cdots, x_n]^G$, then $R_G(f) = f$.*

It is easy to prove that, for any monomial x^α, the Reynolds operator gives us a homogeneous invariant $R_G(x^\alpha)$ of total degree $|\alpha|$ whenever it is nonzero. The following theorem of Emmy Noether shows that we can always find finitely many of these invariants that generate $k[x_1, \cdots, x_n]^G$.

Theorem 2.18 *Given a finite matrix group $G \subset GL(n, k)$, we have*

$$k[x_1, \cdots, x_n]^G = k[R_G(x^\beta) : |\beta| \leq |G|].$$

In particular, $k[x_1, \cdots, x_n]^G$ is generated by finitely many homogeneous invariants.

Theorem 2.18 guarantees that for finite matrix group $G \subset GL(n, k)$, there exist finite number of generators for the invariant polynomial ring $k[x_1, \cdots, x_n]^G$. In addition, Theorem 2.18 provides a method to list all the generators. The main drawback of Theorem 2.18 is that when $|G|$ is large, we need to compute the Reynolds operator for *lots* of monomials. For example, consider the cyclic group $C_8 \subset GL(2, \mathbb{R})$ of order 8 generated by the 45° rotation

$$A = \frac{1}{\sqrt{2}} \begin{pmatrix} 1 & -1 \\ 1 & 1 \end{pmatrix} \in GL(2, \mathbb{R}).$$

In this case, Theorem 2.18 says that $k[x, y]^{C_8}$ is generated by 44 invariants $R_{C_8}(x^i y^j)$, $i + j \leq 8$. In reality, only 3 are needed. For large groups, thing are even worse, es-

pecially if more variables are involved. Fortunately, there are more efficient methods for finding a generating set of invariants. The main tool is *Molien's Theorem*, which enables one to predict in advance the number of linearly independent homogeneous invariants of given total degree d.

Now the question becomes how to generate all the $f \in k[x_1, \cdots, x_n]^G$, and this is achieved by the so called *primary invariants* and *secondary invariants*.

Definition 2.19 *A set $f_1, \cdots, f_r \in k[x_1, \cdots, x_n]$ of homogeneous elements is called a* **homogeneous system of parameters** *if*

1. *$f_1, \cdots, f_r$ are algebraically independent and*

2. *$k[x_1, \cdots, x_n]$ is a finitely generated module over $k[f_1, \cdots, f_r]$.*

If $f_1, \cdots, f_r \in k[x_1, \cdots, x_n]^G$ is a homogeneous system of parameters, then we call the f_i **primary invariants**. The invariant ring $k[x_1, \cdots, x_n]^G$ is a finite $k[f_1, \cdots, f_r]$-module, say

$$k[x_1, \cdots, x_n]^G = Fg_1 + Fg_2 + \cdots + Fg_s,$$

where F is the polynomial ring $k[f_1, \cdots, f_r]$ and $g_1, \cdots, g_s \in k[x_1, \cdots, x_n]^G$ homogeneous. The invariants $g_1, \cdots, g_s$ are called **secondary invariants**.

More importantly, Hochster and Roberts proved that

Theorem 2.20 (Hochster and Roberts) *If G is linearly reductive group, then $k[x_1, \cdots, x_n]^G$ is Cohen-Macaulay.*

Since every finite group is linear reductive group, we know that $k[x_1, \cdots, x_n]^G$ is Cohen-Macaulay, and there is a decomposition

$$k[x_1, \cdots, x_n]^G = Fg_1 \oplus Fg_2 \oplus \cdots \oplus Fg_s \tag{2.12}$$

with $g_1, \cdots, g_s \in k[x_1, \cdots, x_n]^G$ homogeneous, and actually $g_1, \cdots, g_s$ are secondary invariants. The decomposition 2.12 is often called **Hironaka decomposition**.

As a result, given the primary and secondary invariants, the invariant polynomial ring $k[x_1, \cdots, x_n]^G$ can be generated explicitly. Here we will not dig into the algorithm for the computing of the primary and secondary invariants, and they can be generated using some well known algebra system such as MAGMA [10].

Now we will study some real example H_3O by the usage of primary and second invariants along with the Molien series.

Example There are 4 atoms in H_3O, and we can label them as 1, 2, 3 and 4. We also explicit label the O atom as 4, and then 1, 2, 3 are equivalent due to the equivalence of the three H atoms. There are $\binom{4}{2}$ bond lengths for a 4 atom molecule, they are

$$r^T = (r_{12}, r_{13}, r_{14}, r_{23}, r_{24}, r_{34})$$

Denote $x^T = (x_1, \cdots, x_6)$ as a short notation of $r^T = (r_{12}, r_{13}, r_{14}, r_{23}, r_{24}, r_{34})$, and we use $x^T = (x_1, \cdots, x_6)$ to represent the molecule H_3O.

Since all the three H atoms are equivalent in H_3O, the permutation group of H_3O is S_3. The elements of group S_3 are

$$(1), (12), (13), (23), (123), (132).$$

All these elements can act directly on the H_3O molecule, hence on the r vector. For

instance,

$$(12)\cdot\begin{pmatrix} r_{12} \\ r_{13} \\ r_{14} \\ r_{23} \\ r_{24} \\ r_{34} \end{pmatrix} = \begin{pmatrix} r_{12} \\ r_{23} \\ r_{24} \\ r_{13} \\ r_{14} \\ r_{34} \end{pmatrix}$$

In the x notation,

$$(12)\cdot\begin{pmatrix} x_1 \\ x_2 \\ x_3 \\ x_4 \\ x_5 \\ x_6 \end{pmatrix} = \begin{pmatrix} x_1 \\ x_4 \\ x_5 \\ x_2 \\ x_3 \\ x_6 \end{pmatrix}$$

As a result, the permutation matrix corresponding to the action (12) is

$$\begin{pmatrix} 1 & 0 & 0 & 0 & 0 & 0 \\ 0 & 0 & 0 & 1 & 0 & 0 \\ 0 & 0 & 0 & 0 & 1 & 0 \\ 0 & 1 & 0 & 0 & 0 & 0 \\ 0 & 0 & 1 & 0 & 0 & 0 \\ 0 & 0 & 0 & 0 & 0 & 1 \end{pmatrix}$$

and

$$\begin{pmatrix} 1 & 0 & 0 & 0 & 0 & 0 \\ 0 & 0 & 0 & 1 & 0 & 0 \\ 0 & 0 & 0 & 0 & 1 & 0 \\ 0 & 1 & 0 & 0 & 0 & 0 \\ 0 & 0 & 1 & 0 & 0 & 0 \\ 0 & 0 & 0 & 0 & 0 & 1 \end{pmatrix} \cdot \begin{pmatrix} x_1 \\ x_2 \\ x_3 \\ x_4 \\ x_5 \\ x_6 \end{pmatrix} = \begin{pmatrix} x_1 \\ x_4 \\ x_5 \\ x_2 \\ x_3 \\ x_6 \end{pmatrix}.$$

There are 6 this kind of permutation matrix and they compose a group $G \subset GL(6, \mathbb{Q})$.

For this particular permutation group G, the Molien series is

Order	0	1	2	3	4	5	6	7	8	9	10	$\cdots$
Molien Series	1	2	6	14	28	52	93	152	242	370	546	$\cdots$

and the primary invariants are

$$f_1 = x_1 + x_2 + x_4,$$

$$f_2 = x_3 + x_5 + x_6,$$

$$f_3 = x_1^2 + x_2^2 + x_4^2,$$

$$f_4 = x_3^2 + x_5^2 + x_6^2,$$

$$f_5 = x_1^3 + x_2^3 + x_4^3,$$

$$f_6 = x_3^3 + x_5^3 + x_6^3.$$

and the secondary invariants are

$$
\begin{aligned}
g_1 &= 1 \\
g_2 &= x_1x_3 + x_1x_5 + x_2x_3 + x_2x_6 + x_4x_5 + x_4x_6, \\
g_3 &= x_1^2x_3 + x_1^2x_5 + x_2^2x_3 + x_2^2x_6 + x_4^2x_5 + x_4^2x_6, \\
g_4 &= x_1x_3^2 + x_1x_5^2 + x_2x_3^2 + x_2x_6^2 + x_4x_5^2 + x_4x_6^2, \\
g_5 &= g_2^2, \\
g_6 &= g_2^3
\end{aligned}
$$

According to Eq: 2.12, the invariant polynomial ring

$$k[x_1, \cdots, x_6]^G = Fg_1 \oplus Fg_2 \oplus Fg_3 \oplus Fg_4 \oplus Fg_4 \oplus Fg_5 \oplus Fg_6$$

where $F = k[f_1, \cdots, f_6]$.

As a result, we can compute all the f in $k[x_1, \cdots, x_6]^G$. In application, we usually cut the f to some maximum degree. ∎

2.5 Normal Mode Analysis

A classical model for molecular vibration is a set of N points masses(the nuclei), each of which vibrates about an equilibrium position. One of the main goal of Normal mode analysis is to describe these vibrational motions. In order to describe these motions, we should have a coordinates system. The most natural one is the Cartesian Coordinates. Let $x_1, y_1, z_1, \cdots, x_N, y_N, z_N$ be the Cartesian coordinates of an N atom molecule. $x_{1,e}, y_{1,e}, z_{1,e}, \cdots, x_{N,e}, y_{N,e}, z_{N,e}$ be the coordinates in the equilibrium values. $m_1, m_2, \cdots, m_N$ be the mass of these N nuclei.

The $3N$ Cartesian displacement coordinates, which measure the displacement of each nucleus from equilibrium, are defined as:

$$g_1 = x_1 - x_{1,e}, g_2 = y_1 - y_{1,e}, g_3 = z_1 - z_{1,e}, \cdots \tag{2.13}$$

The classical kinetic energy of vibration about the equilibrium position is

$$T = \frac{1}{2} \sum_{i=1}^{3N} m_{C(i/3)} \left(\frac{dg_i}{dt} \right)^2 \tag{2.14}$$

where $C(x)$ is the smallest integer that greater or equal to real number x.

To simplify this equation, we define *mass-weighted Cartesian displacement coordinates* $q_1, q_2, \cdots, q_{3N}$:

$$q_i = \sqrt{m_{C(i/3)}} g_i \tag{2.15}$$

The kinetic energy becomes

$$T = \frac{1}{2} \sum_{i=1}^{3N} \left(\frac{dq_i}{dt} \right)^2 = \frac{1}{2} \sum_{i=1}^{3N} \dot{q}_i^2 \tag{2.16}$$

In matrix notation

$$T = \frac{1}{2} \dot{\mathbf{q}}' \dot{\mathbf{q}} \tag{2.17}$$

For a molecule, the vibrational potential energy V is given by the function U:

$$V = U(q_1, q_2, \cdots, q_{3N}) \tag{2.18}$$

We expand the potential energy in a Taylor series about the equilibrium positions, which correspond to $q_1 = q_2 = \cdots = q_{3N} = 0$. The potential energy is a function of several variables, and the Taylor-series expansion is

$$U = U_e + \sum_{i=1}^{3N} \left(\frac{\partial U}{\partial q_i}\right)_e q_i + \frac{1}{2}\sum_{i=1}^{3N}\sum_{j=1}^{3N} \left(\frac{\partial^2 U}{\partial q_i \partial q_j}\right)_e q_i q_j + \frac{1}{6}\sum_{i=1}^{3N}\sum_{j=1}^{3N}\sum_{k=1}^{3N} \left(\frac{\partial^3 U}{\partial q_i \partial q_j \partial q_k}\right)_e q_i q_j q_k + \cdots \quad (2.19)$$

For equilibrium, the partial potential energy difference along each q should be 0. Hence:

$$\left(\frac{\partial U}{\partial q_i}\right)_e = 0, i = 1, 2, \cdots, 3N \quad (2.20)$$

We should neglect terms higher than quadratic in (2.19); this is a good approximation if the vibrations are small. Equation 2.19 becomes

$$U = U_e + \frac{1}{2}\sum_{i=1}^{3N}\sum_{j=1}^{3N} u_{i,j} q_i q_j \quad (2.21)$$

$$u_{i,j} \equiv \left(\frac{\partial^2 U}{\partial q_i \partial q_j}\right)_e \quad (2.22)$$

In matrix notation,

$$U = U_e + \frac{1}{2}\mathbf{q}'\mathbf{U}\mathbf{q} \quad (2.23)$$

where the matrix $\mathbf{U}$ has the elements u_{ij} and the column vector $\mathbf{q}$ has elements $q_1, q_2, \cdots, q_{3N}$.

We now solve for the classical-mechanical vibration motion for the potential energy

(Eq: 2.21). Newton's second law $F_i = ma_i$ and the definition of potential energy give

$$F_i = -\frac{\partial V}{\partial g_i} = m_{C(i/3)} \frac{d^2 g_i}{dt^2} \tag{2.24}$$

where F_i is the ith component of force acting on the mass $m_{C(i/3)}$. The mass-weighted coordinate q_i is defined by Eq 2.15,hence

$$\frac{\partial V}{\partial g_i} = \frac{\partial V}{\partial q_i}\frac{\partial q_i}{\partial g_i} = \sqrt{m_{C(i/3)}}\frac{\partial V}{\partial q_i} \tag{2.25}$$

$$\frac{d^2 g_i}{dt^2} = \frac{d^2}{dt^2}\left(\frac{q_i}{\sqrt{m_{C(i/3)}}}\right) = \frac{1}{\sqrt{m_{C(i/3)}}}\frac{d^2 q_i}{dt^2} \tag{2.26}$$

Substitution of Eq 2.25 and Eq 2.26 into Eq 2.24 gives

$$\frac{d^2 q_i}{dt^2} + \frac{\partial V}{\partial q_i} = 0, i = 1, 2, \cdots, 3N \tag{2.27}$$

V is given by Eq 2.21 and contains a double sum over the q's. Hence $\partial V/\partial q_i$ will contain a single sum over the q's. Thus *each* differential equation in Eq 2.27 involves *all* the q_i's which complicates the solution process. To get a simpler set of differential equations, we will carry out a change of variables. The change of variables we want is one that reduces the double sum in Eq 2.21 to a single sum of squares. The **U** matrix is real symmetry matrix and hence can be diagonalized to a diagonal matrix using a unitary matrix **L**:

$$\mathbf{L}'\mathbf{U}\mathbf{L} = \mathbf{\Lambda} \tag{2.28}$$

The column vectors of **L** defines an orthonormal coordinate system. Let **Q** be the

coordinates in that space. Here

$$\mathbf{Q} = \mathbf{L}'\mathbf{q} \text{ and } \mathbf{q} = \mathbf{L}\mathbf{Q} \tag{2.29}$$

$$q_i = \sum_{k=1}^{3N} l_{ik} Q_k, i = 1, 2, \cdots, 3N \tag{2.30}$$

Substitute Eq 2.29 into Eq 2.17 and Eq 2.23 gives

$$T = \frac{1}{2}\dot{\mathbf{q}}'\dot{\mathbf{q}} = \frac{1}{2}(\mathbf{L}\dot{\mathbf{Q}})'\mathbf{L}\dot{\mathbf{Q}} = \frac{1}{2}\dot{\mathbf{Q}}'\mathbf{L}'\mathbf{L}\dot{\mathbf{Q}} = \frac{1}{2}\dot{\mathbf{Q}}'\dot{\mathbf{Q}} \tag{2.31}$$

$$T = \frac{1}{2}\sum_{k=1}^{3N=6} \dot{Q}_k^2 \tag{2.32}$$

and

$$U - U_e = \frac{1}{2}\mathbf{q}'\mathbf{U}\mathbf{q} = \frac{1}{2}(\mathbf{L}\mathbf{Q})'\mathbf{U}(\mathbf{L}\mathbf{Q}) = \frac{1}{2}\mathbf{Q}'\mathbf{L}'\mathbf{U}\mathbf{L}\mathbf{Q} = \frac{1}{2}\mathbf{Q}'\mathbf{\Lambda}\mathbf{Q} \tag{2.33}$$

$$U = U_e + \frac{1}{2}\sum_{k=1}^{3N-6} \lambda_k Q_k^2 \tag{2.34}$$

Therefor

$$\frac{d^2 Q_k}{dt^2} = \sum_{i=1}^{3N} l_{ik}\frac{d^2 q_i}{dt^2} = -\sum_{i=1}^{3N} l_{ik}\frac{\partial V}{\partial q_i} \tag{2.35}$$

and

$$\frac{\partial V}{\partial Q_k} = \sum_{i=1}^{3N} \frac{\partial V}{\partial q_i}\frac{\partial q_i}{\partial Q_k} = \sum_{i=1}^{3N} \frac{\partial V}{\partial q_i} l_{ik} \tag{2.36}$$

Hence

$$\frac{d^2 Q_k}{dt^2} + \frac{\partial V}{\partial Q_k} = 0, k = 1, 2, \cdots, 3N \tag{2.37}$$

$$\frac{d^2Q_k}{dt^2} + \lambda_k Q_k = 0, k = 1, 2, \cdots, 3N \tag{2.38}$$

These equations of motion can be solved at once to give

$$Q_k = B_k \sin(\lambda_k^{1/2} t + b_k), k = 1, 2, \cdots, 3N \tag{2.39}$$

where B_k and b_k are constants. Use Eq 2.30 and Eq 2.39, we find for the mass-weighted Cartesian coordinates

$$q_i = \sum_{k=1}^{3N} A_{ik} \sin(\lambda_k^{1/2} + b_k), i = 1, 2, \cdots, 3N \tag{2.40}$$

where

$$A_{ik} \equiv l_{ik} B_k \tag{2.41}$$

Let us look at the physical nature of the solutions Eq 2.40. We first consider the special case with all arbitrary constant $B_k = 0$, except $B_m \neq 0$. For this case, Eq 2.40 becomes

$$q_i = A_{im} \sin(\lambda_m^{1/2} t + b_m), i = 1, 2, \cdots, 3N \tag{2.42}$$

In this case, the coordinates of each atom vibrate in phase with one another with the same frequency $\nu_m = \lambda_m^{1/2}/2\pi$. Each such vibration is called *Normal mode* of vibration.

Let us summarize the result. In order to study the vibrational motions of the mass nuclei, we used the *mass-weighted* Cartesian coordinates $\mathbf{q}$, and then we get mass-weighted Hessian matrix $\mathbf{U}$. Diagonalize Hessian matrix gives matrix $\mathbf{L}$ and $\mathbf{\Lambda}$ which satisfy $\mathbf{L'UL} = \mathbf{\Lambda}$. The diagonal element of $\mathbf{\Lambda}$ λ can gives the frequencies of these

normal mode by $\nu_m = \lambda_m^{1/2}/2\pi$. $\mathbf{Q} = \mathbf{L}'\mathbf{q}$ defines the *Normal Coordinates*. The motion of the normal coordinates can be described by $Q_k = B_k \sin(\lambda_k^{1/2} t + b_k)$. Since $\mathbf{q} = \mathbf{LQ}$, we can describe the vibrational motion in mass-weighted coordinates system after we know $\mathbf{L}$ and $\mathbf{Q}$. When $\mathbf{q}$ is known, then the usual Cartesian coordinates motion can be known.

2.6 Molecular Geometry Optimization

The geometry of a molecule determines many of its physical and chemical properties. This is why it is very important that we understand the geometry of a molecule when running computations. Given a potential energy surface (PES), a geometry is just a point on it, and there are many other points on the PES. Among all the points on a surface, there are some points distinct from others. They are

Local Maxima: that point on the potential energy surface that is the highest value in a particular section or region of the PES

Global Maxima: that point on the potential energy surface that is the highest value in the entire PES

Local Minima: that point on the potential energy surface that is the lowest value in a particular section or region of the PES

Global Minima: that point on the PES that is the lowest value in the entire PES

Saddle Point: a point on the PES that is a maximum in one direction and a minimum in the other. Saddle points represent a transition structure connecting two equilibrium structures.

As for minima and maxima, they can be illustrated using the following Fig. 2.3.

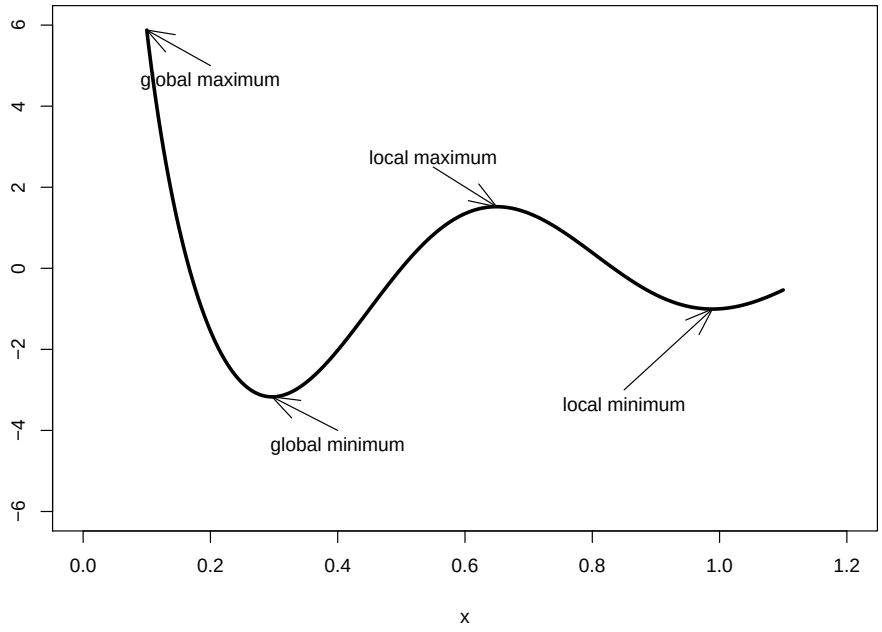

Figure 2.3: Illustration of maxima and minima on a 1D curve

In reality, local and global minima are more important than maxima, since minima are corresponding to geometries that are relative stable than others. In addition, a global minimum is also a local minimum, and usually it is very difficult to determine that if a local minimum is actually the global minimum.

From Fig. 2.3, it is easy to see that all the minima and maxima (except for those boundary points) are extreme points on PES, i.e., the first derivative of the PES or the gradient at those points are zero. For minima, the second derivative of the PES at that point is positive, and negative for those maxima. This is the case in 1-dimension space, for n-dimensional space, there are n first order derivatives, and n non-zero second order derivative (suppose it is in the orthogonal coordinate space). If all of

the first derivative are zero and all the second order derivative are positive at some point, then that point is a minimum. If all the first derivatives are zero and second derivatives are negative at some point, then it is a maxima.

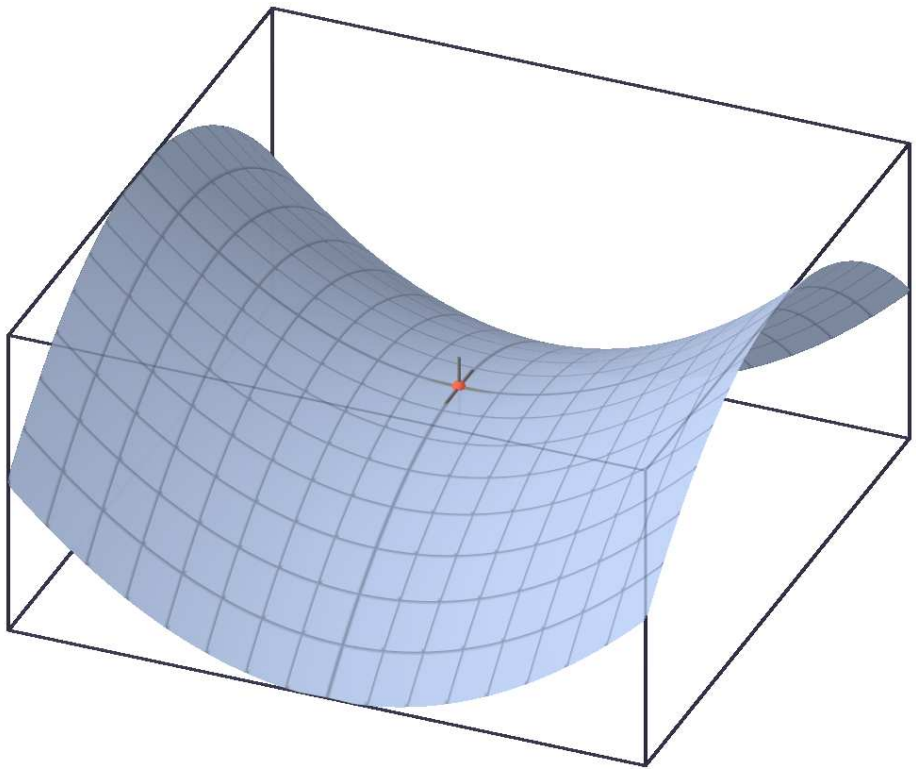

Figure 2.4: Saddle point with the coordinates of $z = x^2 - y^2$.

There may be many local maxima and minima, but only one global minima and maxima. In addition, a PES can have saddle points as illustrated in Fig. 2.4. Saddle point is a point that is maximum in some directions and minimum in the others. It takes its name in that graphically it looks like a saddle when plotted. A saddle point represents a transition structure connecting two equilibrium structures. For a saddle point in n-dimension space, if there are only one negative second order derivative, and all the others are positive, then it is called first order saddle point. If there

are k negative second order derivative, then it is called k^{th} order saddle point. In the study of chemical reaction, only first order saddle point may of interest. The characterization of saddle points, local minima will be addressed more in Section 2.5.

There are possibly many saddle points and local minima and one global minimum, and they are all called stationary points since their first order derivatives are all zero. The stationary points are very important to chemical reactions and also important in characterization potential energy surfaces. The purpose of geometry optimization is to locate the stationary points based on some geometry for the molecule.

There are a number of different algorithms for performing optimizations, such as Berny, Fletcher-Powell, quasi-Newton, and others. Most of these optimization algorithms also calculate the second derivative of the energy with respect to the coordinates, known as a Hessian. The Hessian serves to specify the curvature of the surface for that particular geometry, and thus "optimizes" the determination of how to vary the geometry for the next step. There are also things that the computational chemist can do to make optimizations behave better such as:

- use of symmetry or dummy atoms
- counting the number of internal coordinates
- forcing strong coupling between internal coordinates
- better initial guess for the geometry
- providing an initial guess for the Hessian
- testing stationary points

Here we just focus on quasi-Newton methods in optimization.

The potential energy surface or function is nothing but a multivariate function and can be represented as $f(\mathbf{x}$, where $\mathbf{x}$ represents a point in multi-dimensional space, or a molecule configuration. If a function f has only one variable x, it is well known that $f(x+h)$ can be expanded as Taylor series

$$f(x+h) = f(x) + hf'(x)|_x + \frac{h^2}{2} f''(x)|_x + \mathcal{O}(h^3) \tag{2.43}$$

providing $\|h\|$ is small.

Similarly, if f is a scalar function over vector space $\mathcal{R}^n$, $f(\mathbf{x}+\mathbf{h})$ can also be expanded as a Taylor series:

$$f(\mathbf{x}+\mathbf{h}) = f(\mathbf{x}) + \sum_i h_i \left.\frac{\partial f}{\partial x_i}\right|_{\mathbf{x}} + \frac{1}{2}\sum_{ij} h_i h_j \left.\frac{\partial^2 f}{\partial x_i \partial x_j}\right|_{\mathbf{x}} + \mathcal{O}(|\mathbf{h}|^3) \tag{2.44}$$

if $\|\mathbf{h}\|^2$ is small.

The optimization criteria is $f'(x) = 0$ for 1D case and $\nabla f = 0$ in multi-dimensional space.

In 1D case, suppose we have x which is very close to the stationary point we can looking for, and only a small step h is need to reach the target, then we have

$$f'(x+h) = f'(x) + hf''(x)|_x + \mathcal{O}(h^2) = 0.$$

Neglect the small term $\mathcal{O}(h^2)$ since h is small, we get

$$f'(x) + hf''(x)|_x \approx 0.$$

Consequently,

$$h \approx -\frac{f'(x)}{f''(x)}.$$

There for the final position

$$x' = x + h = x - \frac{f'(x)}{f''(x)}.$$

Similarly, in the n dimensional space, we get

$$\frac{\partial f(\mathbf{x}+\mathbf{h})}{\partial \mathbf{x}} = \begin{pmatrix} \frac{\partial f}{\partial x_1} \\ \frac{\partial f}{\partial x_2} \\ \vdots \\ \frac{\partial f}{\partial x_n} \end{pmatrix} + \begin{pmatrix} \sum_i h_i \frac{\partial^2 f}{\partial x_i \partial x_1} \\ \sum_i h_i \frac{\partial^2 f}{\partial x_i \partial x_2} \\ \vdots \\ \sum_i h_i \frac{\partial^2 f}{\partial x_i \partial x_n} \end{pmatrix} + \cdots = 0$$

and

$$\nabla f|_{\mathbf{x}} + H|_{\mathbf{x}} \cdot \mathbf{h} \approx 0. \tag{2.45}$$

As a result,

$$\mathbf{h} = -H|_{\mathbf{x}}^{-1} \cdot \nabla f|_{\mathbf{x}} \tag{2.46}$$

Finally,

$$\mathbf{x}' = \mathbf{x} + \mathbf{h} = \mathbf{x} - H|_{\mathbf{x}}^{-1} \cdot \nabla f|_{\mathbf{x}}. \tag{2.47}$$

In summary, given any function $f(\mathbf{x})$ and the initial point $\mathbf{x}$ which is close to the saddle point of function $f(\mathbf{x})$, we can update the point $\mathbf{x}$ to $\mathbf{x}+\mathbf{h}$ where $\mathbf{h} = -H|_{\mathbf{x}}^{-1} \cdot \nabla f|_{\mathbf{x}}$. This is the algorithm for quasi-newton method in optimization.

In real application, usually we can not have a point which is close enough (only one step away) to the real target we are looking for, therefore, the above algorithm need to be exercised multi-times until the gradient is small enough or the step size **h** is small enough. In addition, Eq. 2.47 usually is not good enough, and some modification need to be adopted to achieve better result. One approach to add a parameter λ in the front of **h**, and using the updating equation as

$$\mathbf{x}' = \mathbf{x} + \lambda\mathbf{h} = \mathbf{x} - \lambda H|_{\mathbf{x}}^{-1} \cdot \nabla f|_{\mathbf{x}}. \tag{2.48}$$

The main part of the FORTRAN 90 code for geometry optimization is listed below to show the iterative process and the implementation of the coefficient λ (`coef` in code).

```
do while(imxg>cmxg .and. n <= maxc) !not converged yet
   hess = hessian(p,pes)

   if(present(mask)) then
      disp = matmul(inverse(hess,mask),grad)
   else
      disp = matmul(inverse(hess),grad)
   end if

   coef = 1.0
   do while(coef>1.0E-5)
      tdisp = disp * coef
      tp    = p - tdisp
      grad  = gradient(tp,pes)
      maxg  = maxval(abs(grad))
      if(maxg>imxg*1.1) then
         coef = coef * 0.5
         cycle
      else
         p = tp
         imxg = maxg
         exit
      end if
   end do

   if(coef <= 1.0E-5) then
      if(flag) write(*,*) 'Optimization Terminated!'
      return
   end if

   enrg = pes(p)                !energy at the new position
   maxd = maxval(abs(tdisp))    !maximum displacement
   n = n + 1                    !move to the next cycle
   if(flag) write(*,'(A,I3,A,F10.7,A,F10.7,A,F15.9)') &
     "STEP:",n," MAX_GRAD:",imxg," MAX_DISP:", maxd," ENERGY:", enrg
end do
```

Note that in the optimization, there is a subroutine called `inverse` which is supposed to get the inverse of the Hessian matrix. In the code, it is just mainly a diagonalization step. Let H denote the Hessian matrix. For the Hessian matrix, we know it must be symmetric, i.e., $H^T = H$, and it can be diagonalized as

$$H = UDU^{-1}$$

where U is a unitary matrix and D is diagonal matrix. To get the inverse of H, we can just compute the inverse of UDU^{-1} as $(UDU^{-1})^{-1} = UD^{-1}U^{-1}$. Since D is diagonal, its inverse is easy to compute and finally we get the inverse of Hessian H.

In real situation, due to the choose of different representation of a molecule, there may be some redundancy in the molecule representation, consequently, there may be some very small number in the diagonal of D matrix. If we compute the inverse of D, this will cause some problem. In coding, this difficulty is overcome by force the inverse of several small values in D matrix to be 0.

For the above derivation, we notice that $\mathbf{x}$ is a general representation of a molecule configuration, and it can be a representation in any coordinate system. One of the most common coordinate system is the Cartesian coordinates, where $\mathbf{x}$ is just the $3n$ xyz coordinates. We can also represent a molecule using the internal coordinates system such as "Z-Matrix" representation. Once we can express the potential energy function in Z-Matrix coordinates, we can take the advantage of Z-Matrix representation, and perform contained optimization. Here I just briefly outline the steps in optimization in different coordinates system.

Suppose we initially have the potential energy function f which is expressed in coordinate system A, and $\mathbf{x}$ is a configuration in A. The goal here is we want to

optimize the same configuration in another coordinates system B. We also assume that a configuration in B is represented by $\mathbf{y}$, and there is a unique transform function F which can convert $\mathbf{x}$ in A to $\mathbf{y}$ in B, i.e., $\mathbf{y} = F(\mathbf{x})$, $\mathbf{x} = F^{-1}(\mathbf{y})$. Now the target function $f(\mathbf{x})$ in coordinates system A becomes $g(\mathbf{y})$ in coordinates system B, and the relation between $f(\mathbf{x})$ and $g(\mathbf{y})$ is $g(\mathbf{y}) = f(\mathbf{x}) = f(F^{-1}(\mathbf{y}))$. Now the optimization reduced to the original optimization. From another point of view, in quasi-newton's algorithm, gradient and Hessian are needed at the current coordinates system, but since we can convert the coordinates from one to another, we can calculate the gradient and Hessian easily from a potential energy function in another coordinates system.

3 Molecular Dynamics Simulation

3.1 Initial Conditions

The initial conditions is crucial in the quasi-classical trajectory simulations. The initial conditions are supposed to mimic the quantum effects in the classical system during the simulation, and there are quite a few methods developed for setting up the initial conditions, and here we just focus on normal mode sampling method.

3.1.1 Normal Mode Sampling

In this subsection, I just talk about to set the molecule in it lowest vibrational state($v = 0$).

In order to sampling in the phase space, normal mode analysis was done first. Suppose there are n normal modes of a molecule, and the harmonic frequencies for these modes are ω. The harmonic zero point energy for these modes are $\mathbf{E} = \frac{1}{2}\omega$. The energy E_i is the total energy for mode i, it includes the potential energy and the kinetic energy of mode i. The total energy E_i is distributed to the phase space as following:

1. generate a random number $0 \leq \theta \leq 1$
2. $P_i = \sqrt{2E_i}\sin(2\pi\theta)$
3. $Q_i = \frac{\sqrt{2E_i}}{\omega_i}\cos(2\pi\theta)$

Here we note,

$$E_i = \frac{P_i^2 + \omega_i^2 Q_i^2}{2}. \tag{3.1}$$

Here we also note that both P_i and Q_i can be plus or minus. So, two random numbers(R_1andR_2) are generated separately. If $R_1 > 0.5$, then Q_i is set to minus, otherwise, Q_i is set to plus. It is similar for the sign of P_i.

Here we can see that the sampling is in the normal coordinates. After the phase space sampling is done, the coordinates should be transformed to the usual Cartesian coordinates.

3.1.2 Rotational Sampling

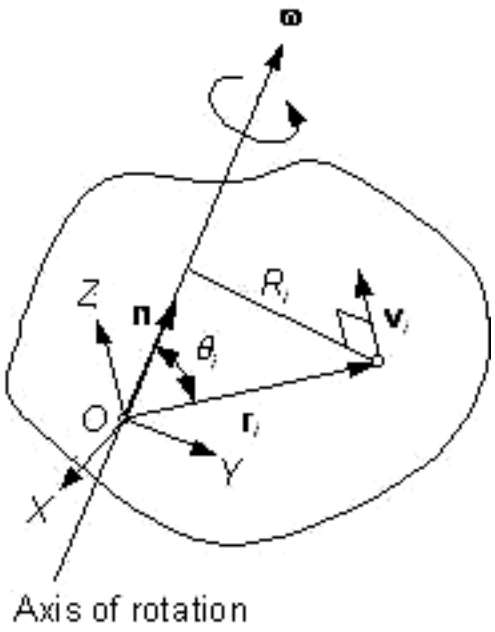

Figure 3.1: Rigid body

Classical Mechanics of A Rigid Rotor Angular momentum of a rigid body(Fig 3.1) can be obtained from the sum of the angular momentums of the particles forming the

body:

$$\mathbf{J} = \sum_{i=1}^{n} L_i = \sum_{i=1}^{n} \mathbf{r}_i \times (m_i \mathbf{v}_i) = \sum_{i=1}^{n} m_i [\mathbf{r}_i \times (\omega \times \mathbf{r}_i)] \tag{3.2}$$

where $\mathbf{r}_i$ is the position vector of particle i, and ω the angular velocity vector of the rigid body. Now, let

$$\mathbf{r}_i \equiv \begin{bmatrix} x_i \\ y_i \\ z_i \end{bmatrix} \tag{3.3}$$

and

$$\omega = \begin{bmatrix} \omega_x \\ \omega_y \\ \omega_z \end{bmatrix} \tag{3.4}$$

Thus,

$$\mathbf{J} = \begin{bmatrix} \sum_{i=1}^{n} m_i(y_i^2 + z_i^2) & -\sum_{i=1}^{n} m_i x_i y_i & -\sum_{i=1}^{n} m_i x_i z_i \\ -\sum_{i=1}^{n} m_i y_i x_i & \sum_{i=1}^{n} m_i(z_i^2 + x_i^2) & -\sum_{i=1}^{n} m_i y_i z_i \\ -\sum_{i=1}^{n} m_i z_i x_i & -\sum_{i=1}^{n} m_i z_i y_i & \sum_{i=1}^{n} m_i(x_i^2 + y_i^2) \end{bmatrix} \begin{bmatrix} \omega_x \\ \omega_y \\ \omega_z \end{bmatrix} \tag{3.5}$$

Let

$$I_{xx} \equiv \sum_{i=1}^{n}(y_i^2 + z_i^2),\ I_{yy} \equiv \sum_{i=1}^{n}(z_i^2 + x_i^2),\ I_{zz} \equiv \sum_{i=1}^{n}(x_i^2 + y_i^2)$$

$$I_{xy} = I_{yx} \equiv -\sum_{i=1}^{n} m_i x_i y_i$$

$$I_{xz} = I_{zx} \equiv -\sum_{i=1}^{n} m_i x_i z_i$$

$$I_{yz} = I_{zy} \equiv -\sum_{i=1}^{n} m_i y_i z_i$$

Then,

$$\mathbf{J} = \begin{bmatrix} I_{xx} & I_{xy} & I_{xz} \\ I_{yx} & I_{yy} & I_{yz} \\ I_{zx} & I_{zy} & I_{zz} \end{bmatrix} \begin{bmatrix} \omega_x \\ \omega_y \\ \omega_z \end{bmatrix} = I\omega \tag{3.6}$$

The angular moment of a molecule with n atoms can also be expanded as:

$$\begin{aligned} J_x &= \sum_{i=1}^{n} m_i(y_i v_{zi} - z_i v_{yi}) \\ J_y &= \sum_{i=1}^{n} m_i(z_i v_{xi} - x_i v_{zi}) \\ J_z &= \sum_{i=1}^{n} m_i(x_i v_{yi} - y_i v_{xi}) \end{aligned} \tag{3.7}$$

Here we note that the above expression is in the center of mass frame and these is no movement for the center of mass.

In the principle axis frame, Eq (3.7) also holds and Eq (3.6) can be simplifies as

$$\begin{aligned} J_x &= I_{xx}\omega_x \\ J_y &= I_{yy}\omega_y \\ J_z &= I_{zz}\omega_z \end{aligned} \tag{3.8}$$

When the **J** of a molecule is calculated in the principle axis frame following Eq (3.7), ω can also be calculated as:

$$\begin{aligned} \omega_x &= J_x/I_{xx} \\ \omega_y &= J_y/I_{yy} \\ \omega_z &= J_z/I_{zz} \end{aligned} \tag{3.9}$$

spherical top	$I_a = I_b = I_c$
prolate symmetric top	$I_a \neq I_b \neq I_c$
oblate symmetric top	$I_a = I_b \neq I_c$
asymmetric top	$I_a \neq I_b \neq I_c$

Add in the Desired Rotational Energy The rotational energy is added to the molecule by changing the velocity of each atom in the molecule.

$$\mathbf{v} = \mathbf{v_0} - \omega_\mathbf{0} \times \mathbf{r} + \omega \times \mathbf{r} \tag{3.10}$$

When the ω is known, then it is easy to add in the desired rotational velocity as following:

$$v_x = v_{x0} - (z\omega_{y0} - y\omega_{z0}) + (z\omega_y - y\omega_z)$$
$$v_y = v_{y0} - (x\omega_{z0} - z\omega_{x0}) + (x\omega_z - z\omega_x)$$
$$v_z = v_{z0} - (y\omega_{x0} - x\omega_{y0}) + (y\omega_x - x\omega_y)$$

Rotational Energy Once the quantum number J is determined, the rotational energy can be calculated for symmetric tops using the following equations:

$$E = \frac{J(J+1)\hbar^2}{2I} \text{ (spherical)} \tag{3.11}$$

$$E/h = BJ(J+1) + (C-B)K^2 \text{ (oblate)} \tag{3.12}$$

$$E/h = BJ(J+1) + (A-B)K^2 \text{ (prolate)} \tag{3.13}$$

where

$$J = 0, 1, 2, \cdots \; K = 0, \pm 1, \pm 2, \cdots, \pm J \tag{3.14}$$

and

$$A \equiv \frac{h}{8\pi^2 I_a} \;\geq\; B \equiv \frac{h}{8\pi^2 I_b} \;\geq\; C \equiv \frac{h}{8\pi^2 I_c} \tag{3.15}$$

As for linear molecule,

$$E/h = BJ(J+1) \text{ (linear)} \tag{3.16}$$

In the principle axis system, the rotational energy(E_{rot}) can be expressed as:

$$E_{rot} = \frac{1}{2}(I_x\omega_x^2 + I_y\omega_y^2 + I_z\omega_z^2). \tag{3.17}$$

Consequently, we can generate three random number ω_x, ω_y and ω_z and scale them to satisfy Eq. 3.17.

Boltzmann Distribution and Sampling According to Boltzmann distribution, the ratio of the state when a molecule has a rotation quantum number J to the $J = 0$ state is:

$$r = (2J + 1)\exp\left(\frac{-E_{rot}(J)}{kT}\right) \tag{3.18}$$

It is a little complicate to generate a random number satisfying distribution as Eq (3.18). However, is it easy to relative ratio of each rotation state J to the zero rotational state. The truncating to some large J(usually 2 is large enough at low temperature). After obtaining all the ratio at different rotational state, we can scale these probability to make the sum to 1. Thus, we can divide the range $[0, 1]$ to some small segments and finally generate the quantum number J which satisfies Boltzmann distribution.

Before adding the new angular velocity, we should remove the possible angular movement in the molecule.

3.1.3 Relative Position and Energy

After sampling the vibrational and rotational energy for each fragments, the relative position of these fragments should also be set up. Here we use H_3^+ + HD as an example to show how to set up the relative position of H_3^+ and HD.

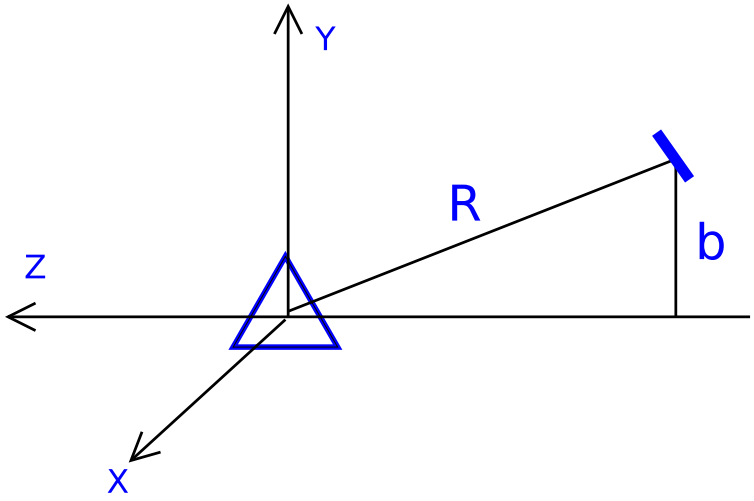

Figure 3.2: Relative position for collision

First, the H_3^+ is moved to the origin. At the origin, two random angle θ and φ are generated and the H_3^+ fragment is rotated in the 3D space according to these angles. similarly, the HD fragment is rotated and move to the point $(0, b, -\sqrt{R^2 - b^2})$. Then the whole molecule is move to the center of mass frame.

In order to make the fragments to collide with each other, there should be some relative energy(E_{rel}) in these two fragments.

There are also some conditions should be satisfied when adding in this relative energy E_{rel},

$$\begin{cases} m_1 v_1 = m_2 v_2 \\ \frac{1}{2} m_1 v_1^2 + \frac{1}{2} m_2 v_2^2 = E_{rel} \end{cases} \tag{3.19}$$

where m_1 is the mass of fragment 1 and m_2 is the mass of fragment 2. v_1 and v_2 are the center of mass velocities for the fragments.

Let

$$\frac{1}{\mu} = \frac{1}{m_1} + \frac{1}{m_2} \tag{3.20}$$

Then

$$v_1 = \frac{1}{m_1}\sqrt{2\mu E_{rel}} \text{ and } v_2 = \frac{1}{m_2}\sqrt{2\mu E_{rel}} \tag{3.21}$$

3.2 Zero Point Energy Constraint in Quasiclassical Trajectory

Abstract

A method to constrain the zero-point energy in quasi-classical trajectory calculations is proposed and applied to Henon-Heiles system. The main idea of this method is to smoothly eliminate the coupling terms in the Hamiltonian as the energy of any mode falls below a specified value.

3.2.1 Introduction

A well-known shortcoming of the quasi-classical trajectory method is the failure to enforce zero-point energy(ZPE) [11–24]. This is of course an error inherent in classical mechanics, because ZPE is a manifestation of the quantum uncertainty principle. Consequently, no matter how accurately one can assign the ZPE to each normal mode of a molecule initially, after a number of steps the energies in these modes may fluctuate. One consequence of this energy fluctuation may be the formation of reaction products with energy less than ZPE. This can also become a critical issue if the ZPE is comparable to the barrier height of a reaction.

The energy fluctuation between modes for a multi-mode Hamiltonian is caused by the mode-mode coupling. If there was only one mode in the Hamiltonian, the mode energy would be conserved. In the case of separable modes, the energies for these modes would be conserved too. Any coupling terms between the modes in the Hamiltonian cause energy transfer between them. Without any control of the coupling term, it is possible for one mode to transfer its energy to other modes and to lose energy less than the zero-point energy.

Independently, Bowman and co-workers [25] and Miller and co-workers [19] proposed a method to constrain the ZPE by changing the sign of momentum when the energy of any mode reaches the ZPE. This method did prevent energy from going below the ZPE, however, since the momentum change occurs instantaneously it is equivalent to an infinite impulse that is perhaps too abrupt and can cause noise in say a classical correlation function. Here we propose another method to constrain the ZPE by smoothly switching off mode coupling when the energy in a mode drops below the ZPE. An application is made to the degenerate Henon-Heiles system.

3.2.2 Method and Application

Method Consider a general n-mode Hamiltonian written as

$$H = H_0 + V_c(1, \ldots, N), \tag{3.22}$$

where H_0 is a separable, zero-order Hamiltonian given by $\sum_i h_i$ and V_c is an intrinsic coupling term. The objective is to eliminate coupling when the energy in a mode or modes (defined according to H_0) drops below a specified value. How this is done for the mode(s) in question depends to some extent on how the coupling potential is represented. One possibility is to write V_c in an n-mode representation as follows [26]

$$V_c(1, \ldots, N) = \sum_{i>j} V^{(2)}(i,j) + \sum_{i>j>k} V^{(3)}(i,j,k) + \cdots \tag{3.23}$$

Then the proposal is to modify this representation of V_c by the following expression

$$V_c(1, \ldots, N) = \sum_{i>j} V^{(2)}(i,j)S(i)S(j) + \sum_{i>j>k} V^{(3)}(i,j,k)S(i)S(j)S(k) + \cdots \tag{3.24}$$

where $S(i)$ is a switching function that depends on the energy in mode i. One possible expression for $S(i)$ that contains the flavor of the approach is the unit step function $\theta[\epsilon_i(t) - \epsilon_{i,zpe}]$, where $\epsilon_i(t)$ is the energy of mode i at time t. Clearly this "instantly" turns off the coupling between mode i and all other modes if the mode i energy drops below the zero-point energy of that mode. This is too abrupt in two important ways. First, as written this is an explicitly time-dependent term which can "spoil" energy conservation and second once the mode coupling is totally eliminated it cannot "return". This means that mode i is basically eliminated from further coupling in

the dynamics. To deal with both of these defects we propose a smoother switching and one that is not explicitly a function of time. Thus we propose $S(i)$ to be given by $S[h_i - \epsilon_{i,zpe}]$, where $S(x)$ is a simple polynomial function [27]

$$S(x) = \begin{cases} 0, & x < 0 \\ 10x^3 - 15x^4 + 6x^5, & 0 \le x \le 1 \\ 1, & x > 1 \end{cases} \tag{3.25}$$

Note that in most instances h_i is given by the sum of a kinetic energy and potential. For energies near the ZPE h_i would be well represented by a harmonic oscillator Hamiltonian although this is not essential. In any case $S[h_i - \epsilon_{i,zpe}]$is polynomial in the momentum and coordinate of mode i and thus modifies the equations of motion in a straightforward fashion. This is illustrated in an application to the Henon-Heiles system in the next section. Before considering that application we make some remarks on other possible forms for the coupling potential and how the switching off of mode coupling could be implemented. One form that is very widely used is a simple multinomial representation of V_c, i.e., an expansion about a minimum,

$$V_c(q_1, \cdots, q_N) = \sum C_{n_1 \cdots n_N} q_1^{n_1} \cdots q_N^{n_N}. \tag{3.26}$$

In this case one could simply multiply each term by the appropriate product of switching functions.

Another more general strategy is to replace each mode coordinate q_i by $S(i)q_i$. The advantage of this strategy is that it can be implemented even in the absence of an analytical expression for V_c, *e.g.*, in direct-dynamics calculations. In this case V_c

is given by the full potential(calculated "on-the-fly") minus the separable(harmonic or possible anharmonic potential). Then each coordinate is replaced by $S(i)q_i$ and $V_c(q_1, \cdots, q_N)$ is replaced by $V_c(S(1)q_1, \cdots, S(N)q_N)$. Thus, if $S(i)$ approaches zero the variable $S(i)q_i$ approaches zero, its reference value, and is decoupled from the coupling potential. This would probably render analytical differentiation quite complex and one would have to resort to numerical differentiation in order to propagate the classical equations of motion.

Application We consider the degenerate Henon-Heiles Hamiltonian of reference 25:

$$H = \frac{1}{2}(p_1^2 + p_2^2 + q_1^2 + q_2^2) + q_1^2 q_2 - \frac{1}{3}q_2^3. \tag{3.27}$$

$h_1 = \frac{1}{2}(p_1^2 + q_1^2)$ is clearly the Hamiltonian for the first mode and $h_2 = \frac{1}{2}(p_2^2 + q_2^2) - \frac{1}{3}q_2^3$ is the Hamiltonian for the second mode, and the coupling term is $V_{12} = q_1^2 q_2$.

According to Eq. (3.24) the modified Hamiltonian is:

$$H = h_1(p_1, q_1) + h_2(p_2, q_2) + S(x_1)S(x_2)V_{12}(q_1, q_2) \tag{3.28}$$

where $x_1 = \frac{h_1(p_1,q_1)-a_1}{b_1-a_1}$ and $x_2 = \frac{h_2(p_2,q_2)-a_2}{b_2-a_2}$. Here a_1, a_2, b_1 and b_2 are constants that determine the range over which the switching occurs.

We used the Velocity-Verlet algorithm to integrate the equations of motion. In this algorithm, p and q are updated according to the following equations:

$$q(t + \Delta t) = q(t) + \dot{q}(t)\Delta t + \frac{1}{2}\ddot{q}(t)\Delta t^2 \tag{3.29}$$

$$p(t + \Delta t) = p(t) + \frac{1}{2}\left(\dot{p}(t) + \dot{p}(t + \Delta t)\right)\Delta t \tag{3.30}$$

According to Hamilton's equations,

$$\dot{p}_1 = -\frac{\partial H}{\partial q_1} \equiv H_{q_1} \text{ and } \dot{p}_2 = -\frac{\partial H}{\partial q_2} \equiv H_{q_2} \tag{3.31}$$

$$\dot{q}_1 = \frac{\partial H}{\partial p_1} \equiv H_{p_1} \text{ and } \dot{q}_2 = \frac{\partial H}{\partial p_2} \equiv H_{p_2}. \tag{3.32}$$

Thus,

$$\ddot{q}_1 = \frac{\partial H_{p_1}}{\partial p_1}\dot{p}_1 + \frac{\partial H_{p_1}}{\partial p_2}\dot{p}_2 + \frac{\partial H_{p_1}}{\partial q_1}\dot{q}_1 + \frac{\partial H_{p_1}}{\partial q_2}\dot{q}_2 \tag{3.33}$$

$$\ddot{q}_2 = \frac{\partial H_{p_2}}{\partial p_1}\dot{p}_1 + \frac{\partial H_{p_2}}{\partial p_2}\dot{p}_2 + \frac{\partial H_{p_2}}{\partial q_1}\dot{q}_1 + \frac{\partial H_{p_2}}{\partial q_2}\dot{q}_2. \tag{3.34}$$

Since the Hamiltonian of the Henon-Heiles system (Eq. 3.27) and the form of the switch function(Eq. 3.25) are known analytical functions, all the derivatives can be calculated analytically. However, for this exercise all of the time derivatives $\dot{q}_1, \dot{q}_2, \dot{p}_1, \dot{p}_2, \ddot{q}_1, \ddot{q}_2$ were calculated using Mathematica 5.1 [28].

3.2.3 Results and Discussion

We considered the same total energy of 0.16 as in reference 25 and this energy was equally divided between the two modes at $t = 0$. The phase space trajectories of these two modes for the unconstrained dynamics and the mode energies are shown in Fig. 3.3. As seen each mode loses all of its energy at some times during the trajectory and there is complete energy transfer back and forth between the two modes. Also note that the energy in a given mode can exceed the total energy, as seen in this figure. This occurs when the energy in the other mode drops to near zero.

We now apply mode switching with switch ranges $0.00 - 0.08$ and $0.02 - 0.10$. The

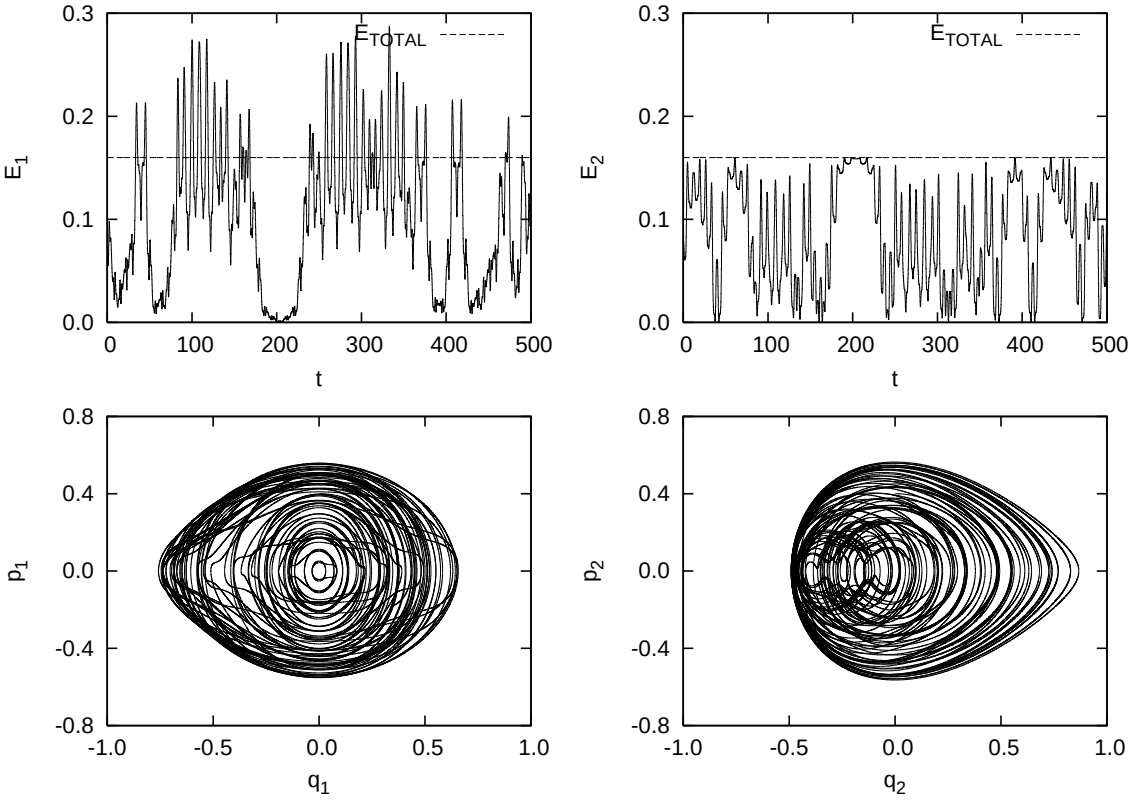

Figure 3.3: Mode energy profile and p, q relation of the fully coupled Henon-Heiles system

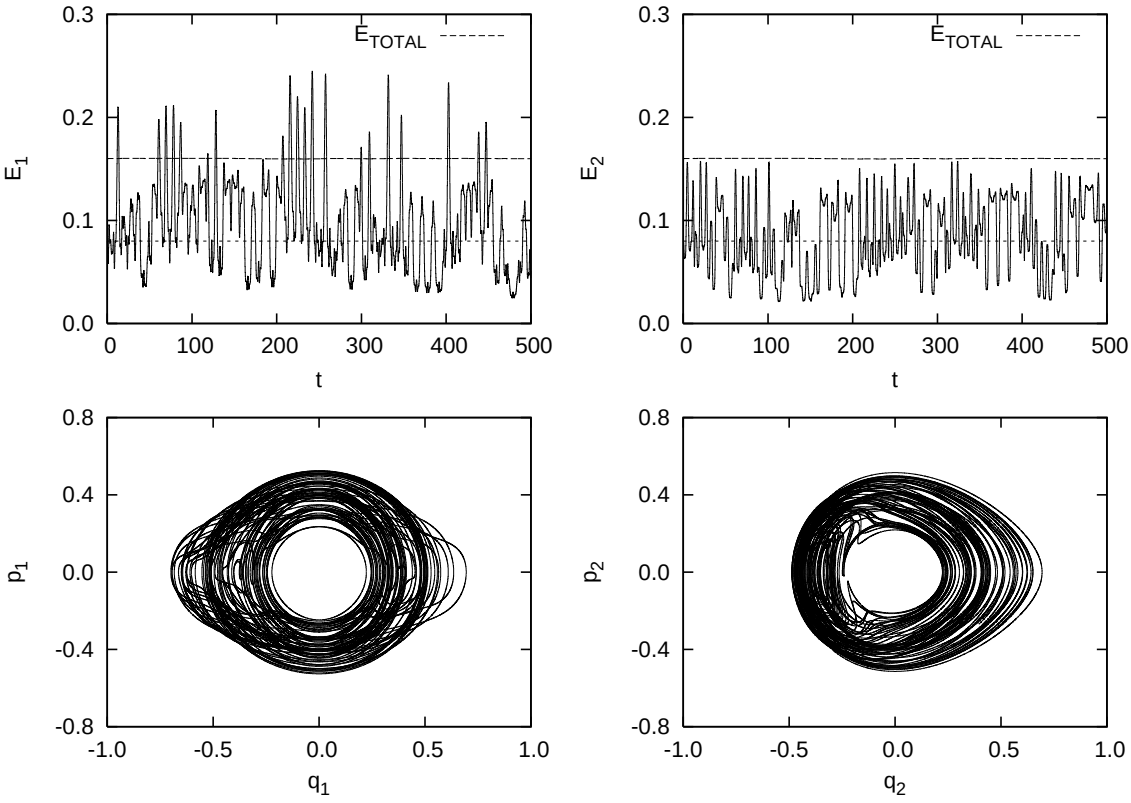

Figure 3.4: Mode energy profile and p, q relation of the Henon-Heiles system when setting the switch range to $[0.00, 0.08]$

results for the first range are shown in Fig. 3.4 and for the second range in Fig. 3.5. As seen both switch ranges work effectively and in neither case does the switching actually reach the limit of zero and so energy exchange between the modes continues throughout this time course of this trajectory. (Note that the energy range is not meant to literally enforce the zero-point energy in this system, because that energy is actually above the dissociation energy of this model.)

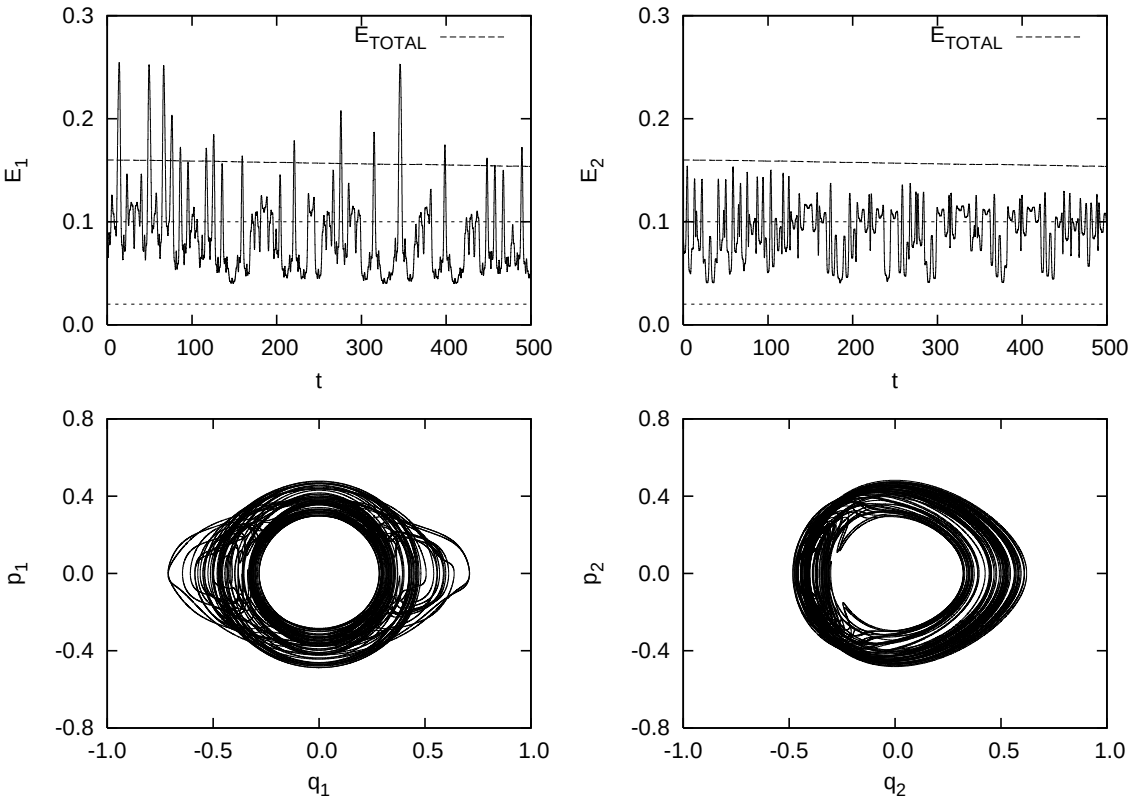

Figure 3.5: Mode energy profile and p, q relation of the Henon-Heiles system when setting the switch range to $[0.02, 0.10]$

In summary a new method to smoothly switch off mode coupling has been proposed with the aim of mitigating zero-point energy leak has been presented and demonstrated for a two-mode Henon-Heiles model.

3.3 Final Conditions

The final conditions of the classical trajectories include the relative energy of the two fragments, the scattering angle θ, the vibrational and rotational energies of the fragments. Of course, it will be better to determine the quantum vibrational and rotational states of those fragments.

Suppose we have a reaction:

$$A + B \longrightarrow C + D, \tag{3.35}$$

and the vector $\mathbf{R}$ defines the separation of C and D. μ is the reduced mass of C and D.

3.3.1 Relative Velocity and Translation Energy

Then, the relative energy of C and D,

$$E_{rel} = \frac{\mu}{2}\dot{\mathbf{R}} \cdot \dot{\mathbf{R}} \tag{3.36}$$

where $\dot{\mathbf{R}}$ is the relative velocity of the center of mass of C and D.

3.3.2 Velocity Scattering Angle

The velocity scattering angle θ is defined as the angle between the relative velocity vector for the reactions $\dot{\mathbf{R}}_\mathbf{0}$ and the product's relative velocity vector $\dot{\mathbf{R}}$:

$$\theta = \cos^{-1}\left(\frac{\dot{\mathbf{R}} \cdot \dot{\mathbf{R}}_\mathbf{0}}{\dot{R}\dot{R}_0}\right) \tag{3.37}$$

If the relative position and velocity are set up as described in Section 3.1.3, then the scattering angle can be easily calculates as:

$$\theta = \cos^{-1}\left(\frac{\dot{\mathbf{R}}(3)}{\|\dot{\mathbf{R}}\|_2^{1/2}}\right) \tag{3.38}$$

3.3.3 Internal Vibrational Energy

As stated in section 3.1.1, the internal vibration energy of a molecule includes the potential energy(E_p) and the kinetic energy(E_T).

The potential energy E_p is calculates as the energy difference of the equilibrium geometry and the current geometry. E_T is simply the sum of kinetic energies of every atom.

3.3.4 Rotational Energy

The rotational energy is calculated simply as Eq (3.17). Firstly, the fragment is transfered to the principle axis frame. Secondly, the angular momentum is calculated as Eq (3.7). Thirdly, the rotational velocities are calculates as Eq (3.9).

3.4 Propagation Algorithm

The engine of a molecular dynamics program is its time integration algorithm, required to integrate the equation of motion of the interacting particles and follow their trajectory.

Time integration algorithms are based on finite difference methods, where time is discretized on a finite grid, the time step Δt being the distance between consecutive points on the grid. Knowing the positions and some of their time derivatives at time t

(the exact details depend on the type of algorithm), the integration scheme gives the same quantities at a later time $t + \Delta t$. By iterating the procedure, the time evolution of the system can be followed for long times.

Of course, these schemes are approximate and there are errors associated with them. In particular, one can distinguish between

Truncation errors related to the accuracy of the finite difference method with respect to the true solution. Finite difference methods are usually based on a Taylor expansion truncated at some term, hence the name. These errors do not depend on the implementation: they are intrinsic to the algorithm.

Round-off errors related to errors associated to a particular implementation of the algorithm. For instance, to the finite number of digits used in computer arithmetics.

Both errors can be reduced by decreasing Δt.For large Δt, truncation errors dominate, but they decrease quickly as Δt is decreased. For instance, the Verlet algorithm discussed in Section 3.4.1 has a truncation error proportional to Δt^4 for each integration time step. Round-off errors decrease more slowly with decreasing Δt,and dominate in the small Δt limit. Using 64-bit precision (corresponding to "double precision" when using Fortran on the majority of today's workstations) helps to keep round-off errors at a minimum.

Two popular integration methods for MD calculations are the Verlet algorithm and predictor-corrector algorithms. They are quickly presented in the sections below. For more detailed informations on time integration algorithms, the reader is referred to refs. [29, 30] for a general survey.

3.4.1 Verlet Algorithm

In molecular dynamics, the most commonly used time integration algorithm is the so-called Verlet algorithm [31, 32]. The basic idea is to write two third-order Taylor expansions for the positions $\mathbf{r}(t)$, one forward and one backward in time. Calling $\mathbf{v}$ the velocities, $\mathbf{a}$ the accelerations, and $\mathbf{b}$ the third derivatives of $\mathbf{r}$ with respect to t, one has:

$$\mathbf{r}(t+\Delta t) = \mathbf{r}(t) + \mathbf{v}(t)\Delta t + \frac{1}{2}\mathbf{a}(t)\Delta t^2 + \frac{1}{6}\mathbf{b}(t)\Delta t^3 + \mathcal{O}(\Delta t^4) \tag{3.39}$$

$$\mathbf{r}(t-\Delta t) = \mathbf{r}(t) - \mathbf{v}(t)\Delta t + \frac{1}{2}\mathbf{a}(t)\Delta t^2 - \frac{1}{6}\mathbf{b}(t)\Delta t^3 + \mathcal{O}(\Delta t^4) \tag{3.40}$$

Adding Eq. 3.39 and Eq. 3.40 gives

$$\mathbf{r}(t+\Delta t) = 2\mathbf{r}(t) - \mathbf{r}(t-\Delta t) + \mathbf{a}(t)\Delta t^2 + \mathcal{O}(\Delta t^4) \tag{3.41}$$

This is the basic form of the Verlet algorithm. Since we are integrating Newton's equations, $\mathbf{a}(t)$ is just the force divided by the mass, and the force is in turn a function of the positions $\mathbf{r}(t)$:

$$\mathbf{a}(t) = -\frac{1}{m}\nabla V\left(\mathbf{r}(t)\right) \tag{3.42}$$

As one can see, the truncation error of the algorithm when propagating the system by Δt is of order Δt^4, even without the explicitly third derivatives. This algorithm is also simple to implement, accurate and stable.

A problem with this version of the Verlet algorithm is that velocities are not

directly generated. However, they are required to compute the kinetic energy K, whose evaluation is necessary to test the conservation of the total energy $E = K + V$. This is one of the most important tests to verify that a MD simulation is proceeding correctly. One could compute the velocities from the positions by using

$$\mathbf{v}(t) = \frac{\mathbf{r}(t + \Delta t) - \mathbf{r}(t - \Delta t)}{2\Delta t}. \tag{3.43}$$

However, the error associated to this expression is of order Δt^2 instead of Δt^4.

To overcome this difficulty, some variants of the Verlet algorithm have been developed. They give rise to exactly the same trajectory, and differ in what variables are stored in memory and at what times. The *leap-frog* algorithm [33], is one of such variants where velocities are handled somewhat better.

An even better implementation of the same basic algorithm is the so-called *velocity Verlet* scheme, where positions, velocities and accelerations at time $t+\Delta t$ are obtained from the same quantities at time t in the following way:

$$\mathbf{r}(t + \Delta t) = \mathbf{r}(t) + \mathbf{v}(t)\Delta t + \frac{1}{2}\mathbf{a}(t)\Delta t^2 \tag{3.44}$$

$$\mathbf{v}(t + \Delta t) = \mathbf{v}(t) + \frac{\mathbf{a}(t) + \mathbf{a}(t + \Delta t)}{2}\Delta t \tag{3.45}$$

The propagation for position $\mathbf{r}$ and $\mathbf{v}$ shown as in Eq. 3.44 and Eq. 3.45 are the main time integration algorithm implemented in the following MD simulations.

Part II

Applications

4 *Ab initio* Global Potential Energy Surface for $H_5^+ \rightarrow H_3^+ + H_2$

Abstract

An accurate global potential energy surface (PES) is reported for H_5^+ based on more than 100,000 CCSD(T)/aug-cc-pVTZ *ab initio* energies. This PES has full permutational symmetry with respect to interchange of H atoms and dissociates to H_3^+ and H_2. Ten known stationary points of H_5^+ are characterized and compared to previous *ab initio* calculations. Quantum Diffusion Monte Carlo calculations are performed on the PES to obtain the zero-point energy of H_5^+ and the anharmonic dissociation energy (D_0) of $H_5^+ \rightarrow H_3^+ + H_2$. The rigorous zero-point state of H_4D^+ is also calculated and discussed within the context of a strictly classical approach to obtain the branching ratio of the reaction $H_4D^+ \rightarrow H_3^+ + HD$ and $H_2D^+ + H_2$. Such an approach is taken using the PES and critiqued based on the properties of the quantum zero-point state. Finally, a simple procedure for adding the long range interaction energy is described.

4.1 Introduction

The H_5^+ cation plays a very important role in ion-molecule chemistry in interstellar space [34]. A key point is the H/D ratio in space and the reaction $H_3^+ + HD \rightleftharpoons H_2D^+ + H_2$ is of particular interest. This is a challenging system to study theoretically [35–38], and the potential energy surface is a pre-requisite to a rigorous dynamics calculation. Two potential surfaces have been reported in the literature [36, 37]. The first, based on the diatomics-in-molecules approach, used limited *ab initio* electronic energies and so is not very accurate. A second potential surface is based on a Shepard-type interpolation of numerous local force fields, fit to MP2/6-311G(d,p) *ab initio* calculations of the energy, gradient and second derivatives. The MP2 energies were replaced by coupled cluster ones [CCSD(T)/6-311G(d,p)] and the final interpolated surface was denoted CCSD(T)-MP2. This surface has the important property of permutational invariance with respect to interchange of the H atoms. This was achieved by replicating the force-fields upon permutation of the H atoms. We will examine the accuracy of this surface in this paper.

The H_5^+ potential is known to contain ten stationary points, corresponding to minima and saddle points. Perhaps the most accurate *ab initio* calculations of these stationary points are those of Prosmiti *et al.* [36] who performed QCISD calculations with a large basis(cc-pVQZ). Kutzelnigg *et al.* [39] studied the four lowest energy conformers with CC-R12 calculations using a 16s8p6d/10s6p4d basis. It is reasonable to assume that these various stationary points are important in the chemical reaction and thus it is important that they be accurately represented in a global potential energy surface. We present such a potential energy surface here.

This surface is a highly precise fit to of order 10^5 *ab initio* energies, obtained

using the CCSD(T) method with an aug-cc-pVTZ basis which is expect to give more accurate energies than the basis used in reference 37. In the next subsection we describe the generation of these *ab initio* energies and their fitting, using an approach that builds in the permutational symmetry directly into the fit. This approach has been used recently to obtain potential energy surface for CH_5^+ [40,41], $H_3O_2^-$ [42] and $H_5O_2^+$ [43]. The accuracy of the fit is also presented in that subsection.

In Subsection 4.3 properties of the ten stationary points on the potential surface are presented and compared to previous calculations. Quantum Diffusion Monte Carlo calculations of the zero-point energies of H_5^+ and the separated fragments $H_2 + H_3^+$ are presented and the zero-point energy of H_4D^+ is also reported. A limited classical calculation of the branching ratio of the unimolecular dissociation of H_4D^+ is also presented in that subsection. Finally, in Subsection 4.4 we describe a simple procedure to add the standard long range ion-induced dipole and ion-quadrupole interaction to the potential energy surface. A summary and conclusions are given in Subsection 4.5.

4.2 Fitting Procedures

4.2.1 Sampling Strategy and *ab initio* Calculation

H_5^+ has nine degrees of freedom, so it would be very expensive if a grid method was used to generate the points for a fit. For example, if only 10 points were sampled along each degree of freedom this would result in a total of 10^9 points. Obviously, it would be unfeasible to do this many *ab initio* calculations. An approach that is feasible, and which we have used previously, is to base a fit on "scattered data". In our previous work on CH_5^+ [40, 41], these data were obtained from classical, direct-dynamics calculations. In the present case we performed roughly 100 trajectories

ranging from 3 kcal/mol to 50 kcal/mol above the global minimum. These were all started from the global minimum and each trajectory was run for 1000 steps. All the direct-dynamics trajectories were run at the MP2/aug-cc-pVTZ level using MOLPRO [44].

A total of roughly 100,000 geometries were obtained from these trajectories, and a small selection of high energy points were added to make the data set cover more regions. Finally, 105,888 geometries were fit to an analytical function form which has "built-in" full permutational symmetry, as described below.

This functional form uses all ten internuclear distances and Table 4.1 shows the internuclear distance distribution of this data set. This statistical information indicates that the data points obtained using the direct-dynamics method span the internuclear distance space fairly completely. Note, the permutational symmetry built into the fit effectively permutes these data among the five H atoms.

After obtaining these data points, the more accurate method CCSD(T) was used to calculate the energy with an aug-cc-pVTZ basis set at all of the configurations.

4.2.2 Fitting *ab initio* Data

In our previous fits using permutational symmetry a single global expression was used to represent the fitting function [40–43]. Here we take a different approach, which is a generalization of the many-body expansion technique [45]. Thus, the expression for the potential energy function is given as follows:

$$V_{H_5^+} = \sum V_H^{(1)} + \sum V_{H_2}^{(2)} + \sum V_{H_3}^{(3)} + \sum V_{H_5}^{(5)}. \tag{4.1}$$

Table 4.1: Internuclear distance distribution (number of configurations) for each H pair

	Internuclear Distance (Angström)							
atom pair	0-1	1-2	2-3	3-4	4-5	5-6	6-7	7-8
H_1-H_2	1002	1747	67063	14054	8646	6454	4857	2065
H_1-H_3	1854	2851	66425	13331	7850	6328	5507	1742
H_1-H_4	99868	5387	88	272	138	72	63	0
H_1-H_5	27649	48846	7839	6713	5519	4841	3127	1354
H_2-H_3	95774	6938	857	1036	788	195	178	122
H_2-H_4	1255	1952	66473	14081	9187	6160	4505	2275
H_2-H_5	47899	38533	7061	4682	3014	2876	1098	725
H_3-H_4	2214	2469	66789	12943	8837	5434	5111	2091
H_3-H_5	47006	38530	7265	4273	4128	2973	1046	667
H_4-H_5	27019	49524	7525	6811	5642	4583	3258	1526

$V_H^{(1)}$ is the (constant) energy of a single H atom, $V_{H_2}^{(2)}$ is a two-body term which is a function of the separation of the two H atoms and which tends asymptotically to zero as the internuclear distance approaches infinity. The three-body term $V_{H_3}^{(3)}$ goes to zero as any fragments H and H_2 separate to infinity and $V_{H_5}^{(5)}$ goes to zero as any fragments separate. In particular this term goes to zero as the fragments H_3^+ and H_2 separate. The four-body term $V_{H_4}^{(4)}$ is absent in the above expression due to the lack of data for the H_4 and H_4^+ fragments which are not relevant in reaction $H_5^+ \rightarrow H_3^+ + H_2$.

The functional form used here for the various n-body terms is the product of a polynomial $P_N(\mathbf{R})$ and a damping function $d(\mathbf{R})$,

$$V^{(n)} = P_N(\mathbf{R}) d(\mathbf{R}) \tag{4.2}$$

where $\mathbf{R}$ denotes the internuclear distance vector and the damping function has the

following form:

$$d(\mathbf{R}) = \max\left(0, 1 - \frac{\|\mathbf{R}\|_2^{1/2}}{n \cdot a}\right)^5 \tag{4.3}$$

where n is the length of $\mathbf{R}$, i.e., the number of internuclear distances, and a is a constant. This constant is adjusted to give smooth asymptotic behavior. In the present case a equals 7.0 Bohr. The polynomials $P_N(\mathbf{R})$ are simple functions of $\mathbf{R}$ and are made manifestly permutationally invariant using the techniques described elsewhere [43]. The maximum power for the two-body terms is 8, 7 for the three-body terms, and 5 for the five-body terms.

The above expression for the PES was least-squares fit to the 105,888 energies. The RMS fitting error for the whole data set is 45.7 cm^{-1}. It is much smaller for the low energy part of those points and increases slightly for high energy points. The relation between the RMS error and energy is shown in Fig. 4.1 along with the number of configurations up to the energy indicated.

4.3 Results and Discussion

4.3.1 Properties of Stationary Points on the PES

As reported previously by Yamaguchi *et al.* [35] there are ten stationary points on the H_5^+ PES. (These authors did not obtain a full PES, but did locate and characterize these stationary points.) We located these stationary points on the present PES. Note that these points were not explicitly included in the data set used to obtain the fit. Fig. 4.2 shows the geometry and symmetry of all these stationary points. The corresponding bond lengths for these stationary points are listed in Table 4.2. These geometries agree well with previous reported ones [35, 36, 38, 39].

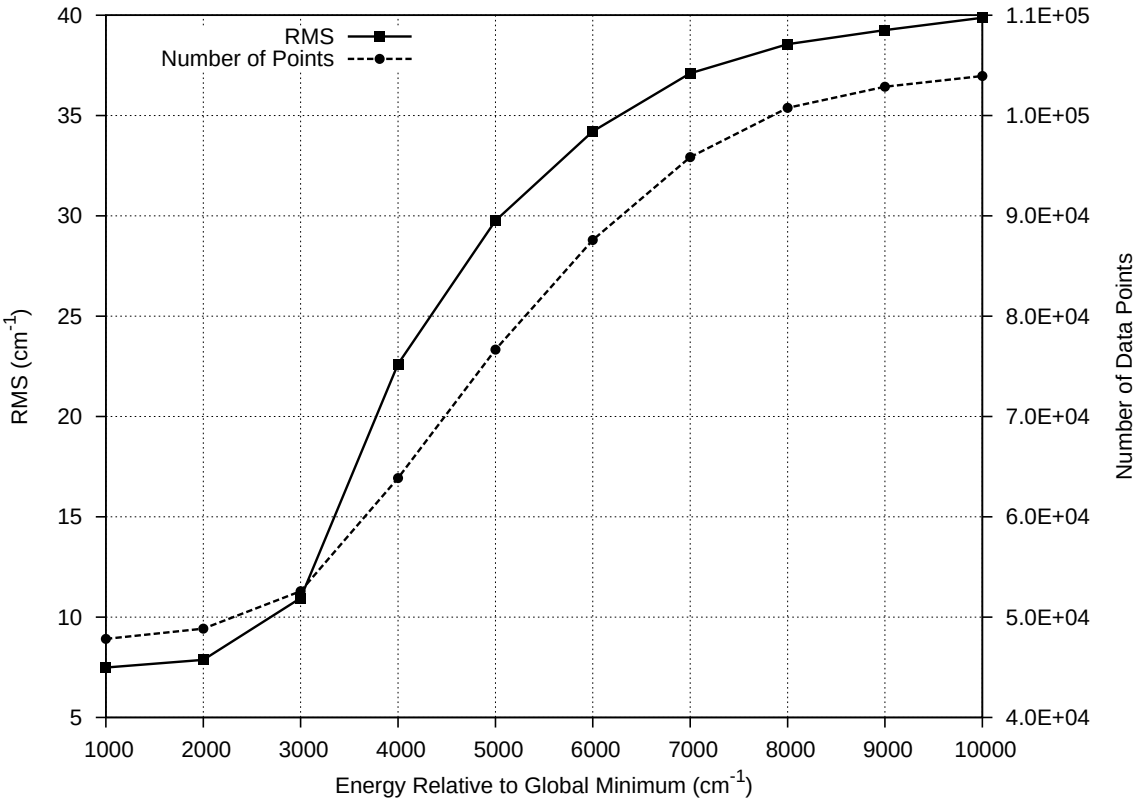

Figure 4.1: The relation between RMS and Energy(relative to global minimum) level of the data set and the number of data points below each energy level

A comparison of the energies of these points obtained from the PES and the *ab initio* calculations is given in Table 4.3. The maximum deviation of the PES is 165.3 cm^{-1} and the minimum deviation is less than 1 cm^{-1}. This is quite good agreement, especially when it is recalled that these stationary points, except the global minimum, were not explicitly included in data used in the fit. Including them would probably not result in much smaller differences with *ab initio* values unless they were assigned large weights, and for the purpose of generating a global PES, we see no reason to do this.

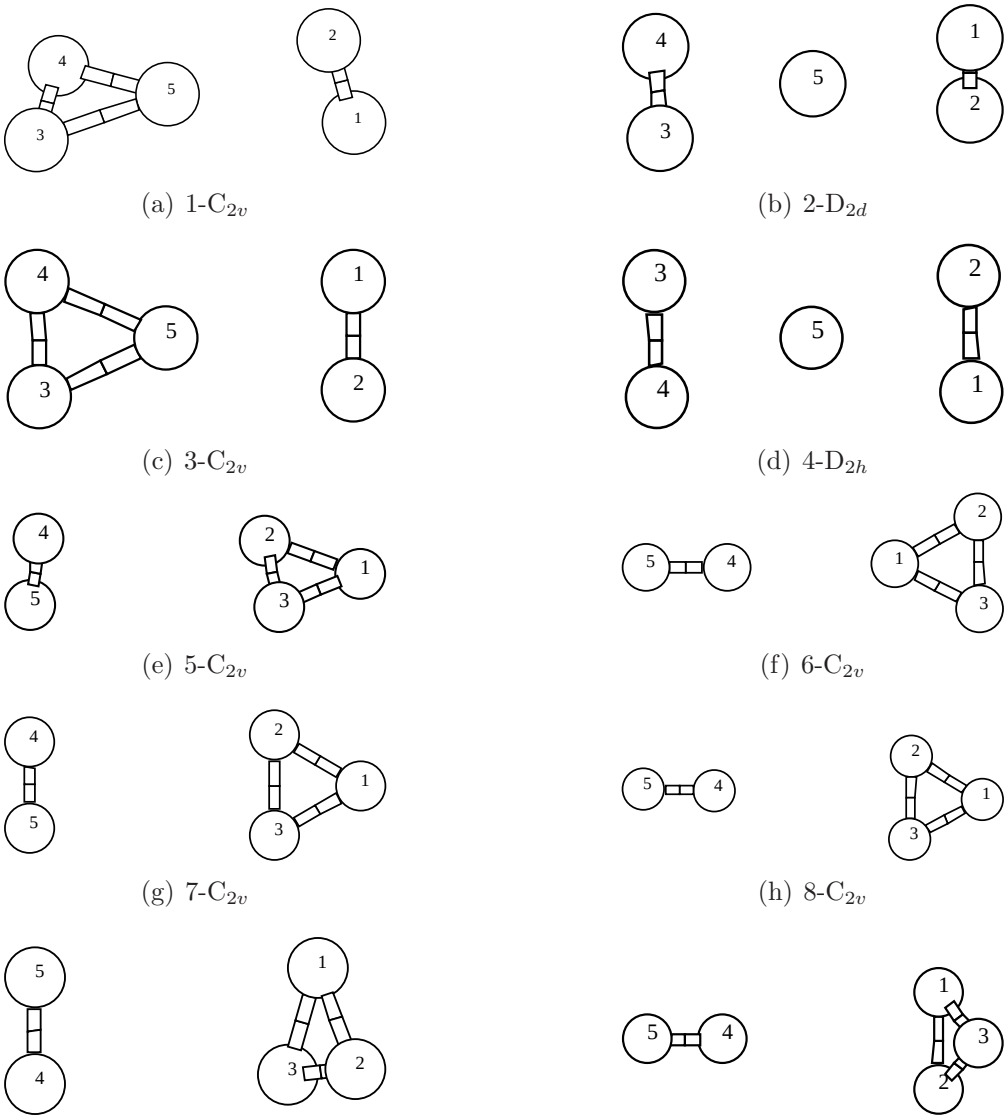

Figure 4.2: Geometry of ten stationary points

Table 4.2: Bond distances (Å) of the ten stationary points on the PES

Bond	1-C_{2v}	2-D_{2d}	3-C_{2v}	4-D_{2h}	5-C_{2v}	6-C_{2v}	7-C_{2v}	8-C_{2v}	9-C_s	10-C_{3v}
1 2	0.7677	0.7853	0.7674	0.7853	0.8749	0.8902	0.8745	0.8717	0.8734	0.8693
1 3	2.2459	2.1831	2.3214	2.2533	0.8749	0.8902	0.8745	0.8717	0.8734	0.8693
1 4	2.2459	2.1831	2.1831	2.1120	2.8453	1.5582	2.9065	2.8280	2.5937	2.3653
1 5	1.3359	1.1263	1.3474	1.1267	2.8453	2.3051	2.9065	3.5708	2.4505	3.0912
2 3	2.2459	2.1831	2.1831	2.1120	0.8706	0.8562	0.8698	0.8734	0.8738	0.8693
2 4	2.2459	2.1831	2.3214	2.2533	2.1401	2.3776	2.1243	2.1191	2.4988	2.3653
2 5	1.3359	1.1263	1.3474	1.1267	2.1401	3.1152	2.2727	2.8500	2.5748	3.0912
3 4	0.8107	0.7853	0.8116	0.7853	2.1401	2.3776	2.2727	2.1190	2.4936	2.3653
3 5	0.9832	1.1263	0.9794	1.1267	2.1401	3.1152	2.1243	2.8500	2.5774	3.0912
4 5	0.9832	1.1263	0.9794	1.1267	0.7498	0.7469	0.7501	0.7428	0.7457	0.7388

Table 4.3: Energy comparison between present *ab initio* CCSD(T)/aug-cc-pVTZ and PES (Hartree) and their difference (cm^{-1}) for the ten stationary points

Conformer	*ab initio*	PES	Difference
1-C_{2v}	-2.52799394	-2.5280145	4.5
2-D_{2d}	-2.52777327	-2.5277767	0.8
3-C_{2v}	-2.52755496	-2.5275454	-2.1
4-D_{2h}	-2.52725219	-2.5272847	7.1
5-C_{2v}	-2.52103732	-2.5208799	-34.5
6-C_{2v}	-2.51759316	-2.5170415	121.1
7-C_{2v}	-2.52045808	-2.5203725	-18.8
8-C_{2v}	-2.51593652	-2.5166298	152.2
9-C_s	-2.51828572	-2.5184193	29.3
10-C_{3v}	-2.51490248	-2.5156554	165.3

A comparison of energies at stationary points of the present *ab initio* calculations and the PES based on them with previous high-level *ab initio* calculations (assumed to be benchmark results) is given in Table 4.4. We also show results from the previous PES of reference 37. As seen the present *ab initio* and PES absolute energies are closer to the benchmark CC-R12 energy at the global minimum (difference of 830 cm^{-1}) than the energy of the PES of reference 37 (difference of 2980 cm^{-1}). This also holds at the other stationary points. This table shows that the current PES agrees very well with these benchmark calculations, with an average absolute deviation of 58 cm^{-1}. (The CC-R12 energies are used as the benchmark results for three stationary points indicated and for the other stationary points the QCISD ones are used as the benchmark results.) For the previous PES [37] the average absolute deviation is 175 cm^{-1}.

Table 4.4: Energy Comparison for the ten known stationary points between indicated *ab initio* calculations, current PES and a previously reported PES. The value for 1-C_{2v} is the absolute global minimum energy in Hartree. Other values are the energies in wavenumber relative to the global minimum.

Conformer	1-C_{2v}	2-D_{2d}	3-C_{2v}	4-D_{2h}	5-C_{2v}	6-C_{2v}	7-C_{2v}	8-C_{2v}	9-C_s	10-C_{3v}
CC-R12[1]	-2.531794	61.5	96.6	182.2						
QCISD[2]	-2.530509	64.1	95.5	181.9	1543.6	2299.0	1672.2	2663.3	2171.3	2834.5
CCSD(T)[3]	-2.527994	48.4	96.4	162.8	1526.8	2282.7	1653.9	2646.3	2130.7	2873.2
PES[3]	-2.528015	52.2	103.0	160.2	1565.9	2408.3	1677.2	2498.7	2105.9	2712.5
previous PES[4]	-2.518215	27.9	89.5	146.5	1970.9	2125.2	1988.9	2496.8	2540.5	2801.9

[1] Reference 39
[2] Reference 38
[3] this work
[4] Reference 37

A normal mode analysis was performed on the PES at the ten stationary points and the results are given in Table 4.5. Benchmark quantum calculations have only been done at the minimum and one saddle point. A comparison with those results is given in Table 4.6. As seen the harmonic frequencies from the PES agree very well with those from the benchmark calculations.

Table 4.5: Harmonic frequencies (cm^{-1}) at the stationary points on the PES

mode	1-C_{2v}	2-D_{2d}	3-C_{2v}	4-D_{2h}	5-C_{2v}	6-C_{2v}	7-C_{2v}	8-C_{2v}	9-C_s	10-C_{3v}
1	211	503i	211i	508i	431i	658i	429i	443i	343i	402i
2	487	217	474	217i	227	654i	202i	438i	320i	402i
3	829	971	795	906	321	253	279	90	17	183i
4	882	971	1011	1147	449	350	418	186	406	183i
5	1190	1430	1041	1346	570	370	493	350	413	339
6	1799	1616	1824	1418	2659	2636	2677	2748	2782	2823
7	2128	1616	2151	1761	2824	2666	2830	2820	2786	2823
8	3666	3861	3658	3858	3478	3408	3481	3422	3455	3460
9	4091	3924	4086	3912	4299	4362	4287	4428	4353	4494

Table 4.6: Comparison of the PES normal mode frequencies with previous benchmark results

	1-C_{2v}			2-D_{2d}	
Mode No.	CCSD(T)/AVQZ[1]	QCISD(T)/AVQZ[1]	PES[2]	CCSD(T)/AVQZ[1]	PES[2]
1	206	206	211	531i	503i
2	495	502	487	224	217
3	812	815	829	962	971
4	866	868	882	962	971
5	1170	1174	1190	1411	1430
6	1838	1840	1799	1593	1616
7	2131	2134	2128	1593	1616
8	3668	3670	3666	3892	3861
9	4115	4118	4091	3965	3924

[1] Reference 38
[2] this work

4.3.2 Dissociation Properties

The PES describes the dissociation of H_5^+ to H_2 and H_3^+. The potential for H_2 is shown in Fig. 4.3 along with an independent calculation based on a full CI/aug-cc-pVTZ calculation. As seen the potential from the PES agrees very well with the full CI/aug-cc-pVTZ one.

Consider next the H_3^+ potential from the PES. A contour plot of the potential in the two internuclear distances for the collinear arrangement is shown in Fig. 4.4. A corresponding plot is shown in Fig. 4.5 with $\angle H-H-H$ fixed at 60^o. These contour plots show the symmetry and smoothness of the potential.

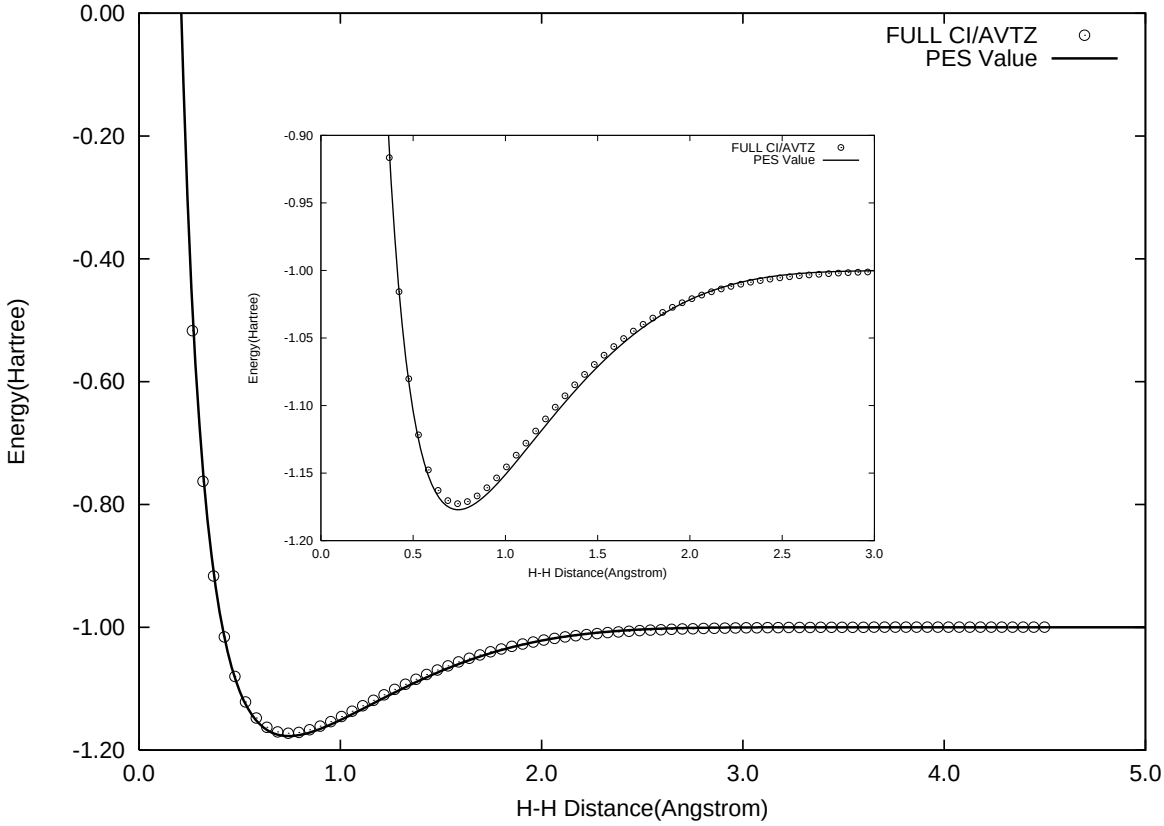

Figure 4.3: H_2 potential from the H_5^+ PES, the energy for H_2 is shifted up 1.0 Hartree

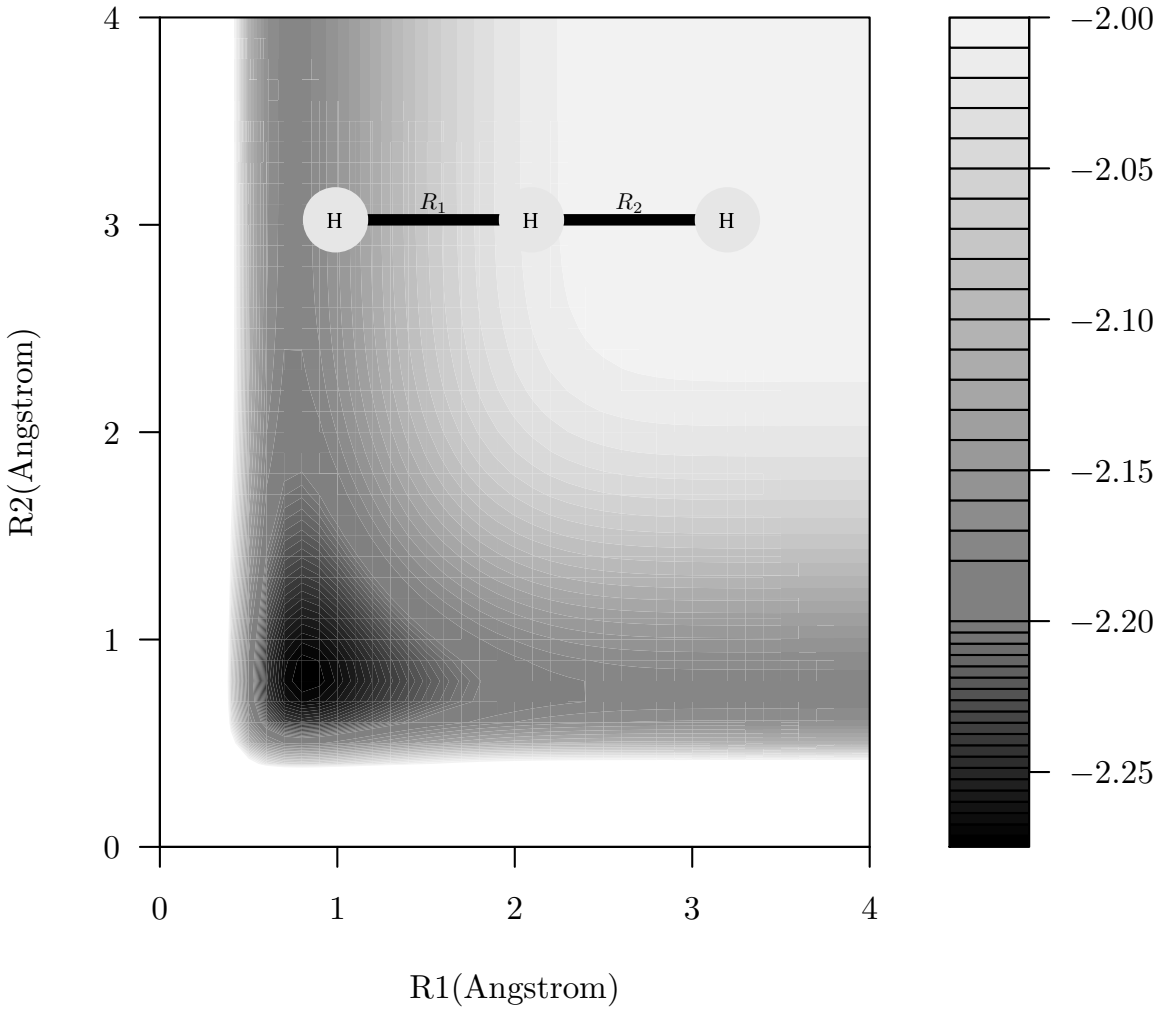

Figure 4.4: Contour plot of scheme A

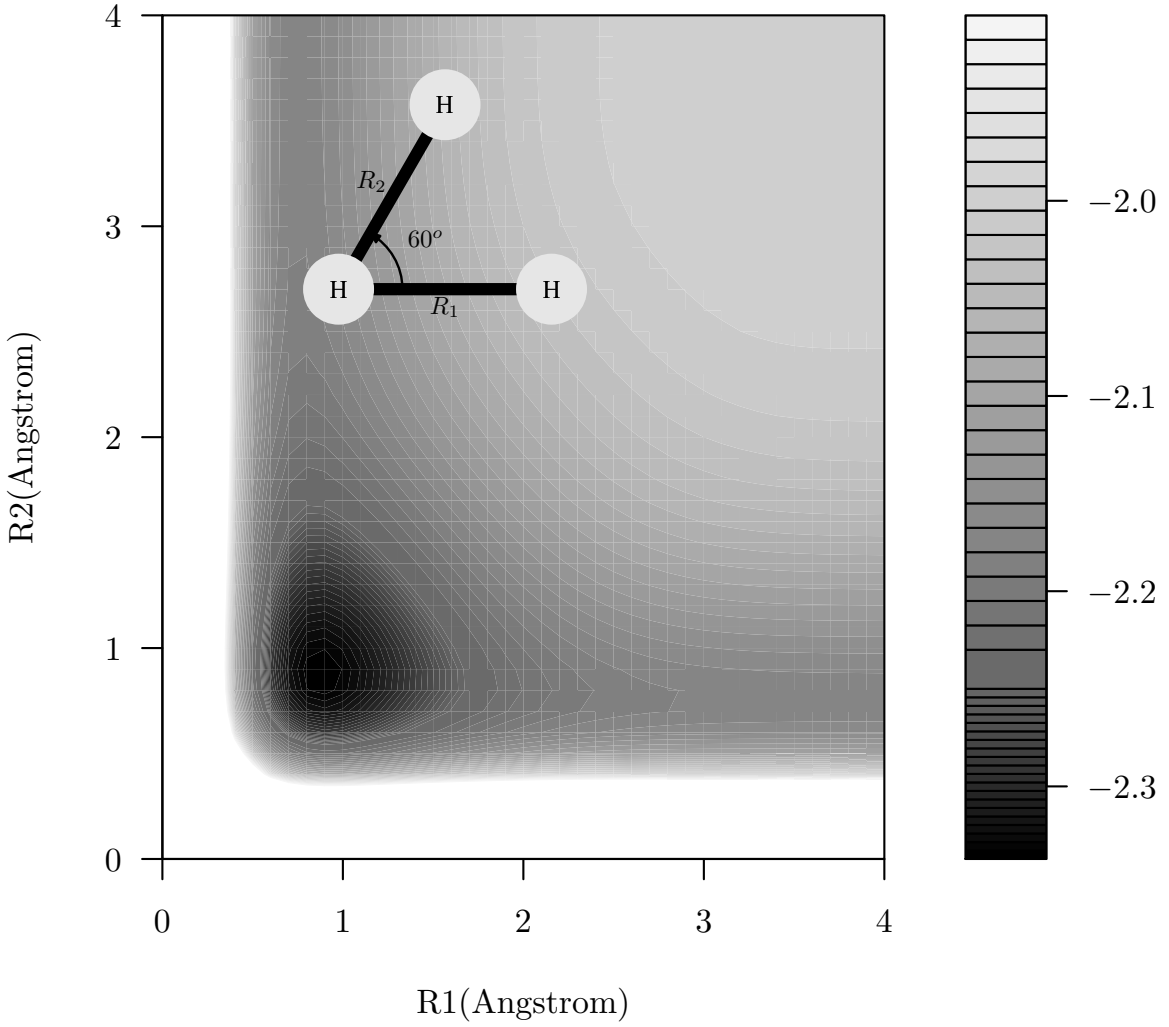

Figure 4.5: Contour plot of scheme B

The equilibrium geometry of H_3^+ is equilateral triangular, and the HH bond length is 0.8747 Angström which is very close to the experimental value [46]. The harmonic normal mode frequencies of H_3^+ from the PES are 3399 and 2786(E) cm^{-1} which are close to benchmark values [47], 3428 and 2775(E) cm^{-1}.

For H_2 on the PES, the equilibrium bond length is 0.7433 Angström which is only 0.0016 Angström longer than the benchmark value [48] 0.7415 Angström. In addition, the H_2 harmonic frequency on the PES is 4388 cm^{-1}, which agrees well with the benchmark value of 4401 cm^{-1} [49]. Thus, the fragments are accurately described by the present PES.

Numerous efforts have been devoted to obtain the dissociation energy(D_e and D_0) of H_5^+ [35, 36, 39, 50–58]. The most recent experimental values of D_0 are 6.6±0.3 kcal/mol [55] and 7.0±0.1 kcal/mol [57], and the most accurate theoretical value for D_e is 8.58 kcal/mol [39]. On the present PES, D_e equals 8.30 kcal/mol. Based on the harmonic normal frequencies for H_5^+, H_3^+, and H_2 we obtain an estimate of D_0 of 5.57 kcal/mol, which is not in good agreement with experiment. H_5^+ is highly fluxional and so the harmonic approximation for its zero-point energy (ZPE) is highly suspect. For this reason we performed quantum Diffusion Monte Carlo calculations of the ZPE of H_5^+ and the combined separated fragments H_3^+ and H_2. Details and results of these calculations are described next.

Twenty thousand walkers were propagated for 5000 steps for each of ten DMC "trajectories". Fig. 4.6 shows the imaginary time evolution of the ZPE of H_5^+ for one trajectory, which was initiated at the global minimum. Fig. 4.7 shows the evolution of the ZPE of the initially separated H_3^+ and H_2 fragments. As seen, after a time interval of stability where the ZPE of the separated fragments can be determined, the ZPE

decreases at around $\tau = 5000$(a.u.) and then becomes steady again at the H_5^+ ZPE. Thus, the ZPE of both H_5^+ and the fragments can be obtained in one simulation.

In the global minimum region, the interval in imaginary time 3000 to 7000(a.u.) was chosen as the stable region in which to collect ZPE data. A standard analysis of the distribution of values leads to an average ZPE of 7210 cm^{-1} (20.61 kcal/mol) with a standard deviation of 11 cm^{-1}.

The ZPE values in the imaginary time interval 2500 to 4000 were chosen as the stable region for the separated fragments. The analysis of these values leads to an average ZPE of 9424 cm^{-1} (26.94 kcal/mol) with a standard deviation of 9 cm^{-1}.

Based on these DMC results, we obtain a value for D_0 of 6.33±0.03 kcal/mol which agrees well with Beuhler's experimental result [55]. However, it is slightly outside the error bar range of the estimate reported by Hiraoka and Mori [57]. This result is quite gratifying and also indicates the importance of doing a rigorous calculation of the ZPE and not relying on the harmonic approximation, which leads to a poor estimate of D_0.

We used the PES in a preliminary dynamics study of the unimolecular dissociation of the complexes that can be formed in the astrophysically important reaction $H_3^+ + HD \rightleftharpoons [H_4D^+] \rightleftharpoons H_2D^+ + H_2$. This study is strictly classical and is done in part to test the PES in a more global way than simply examining the properties of isolated configurations. The second motivation is to raise suspicions about a classical approach, when at least one quantum aspect of the unimolecular dissociation is shown to be at variance with the corresponding classical picture.

In considering a purely classical description of the unimolecular dissociation of the complex H_4D^+ trajectories have to be initiated at some initial configuration. One

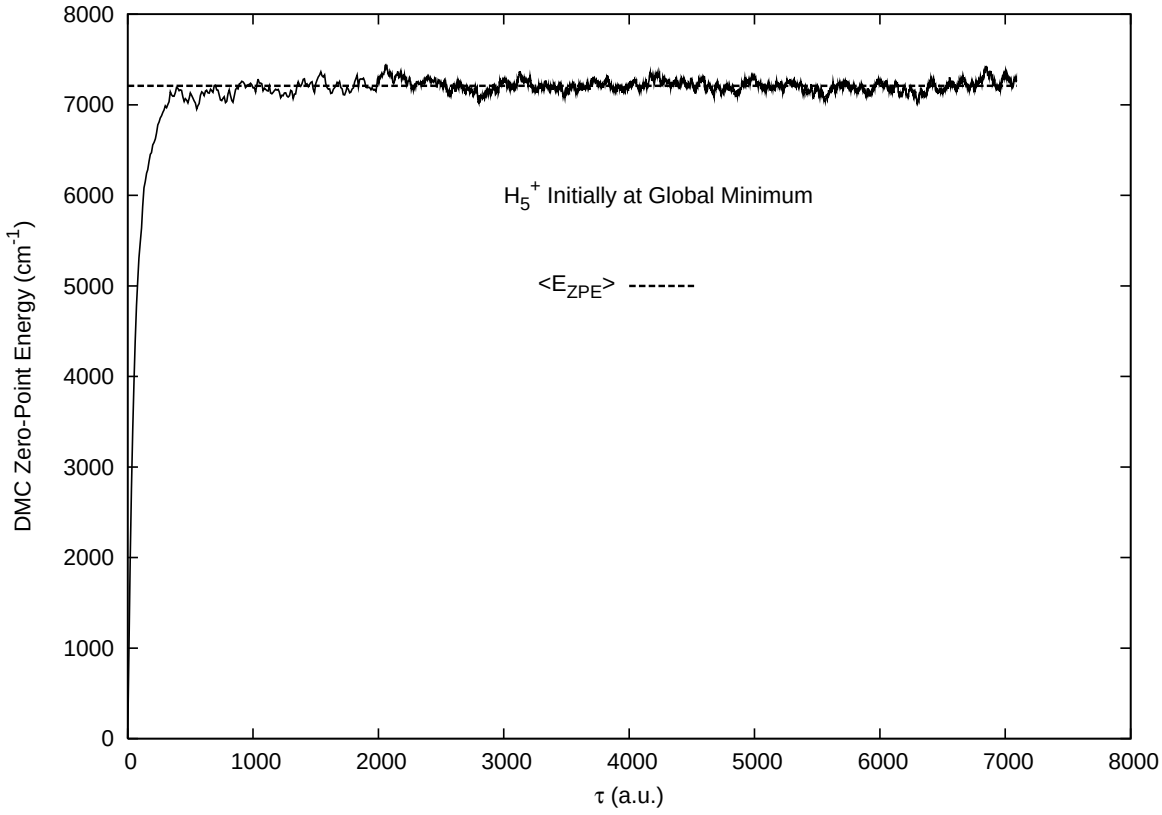

Figure 4.6: DMC simulation at the global minimum

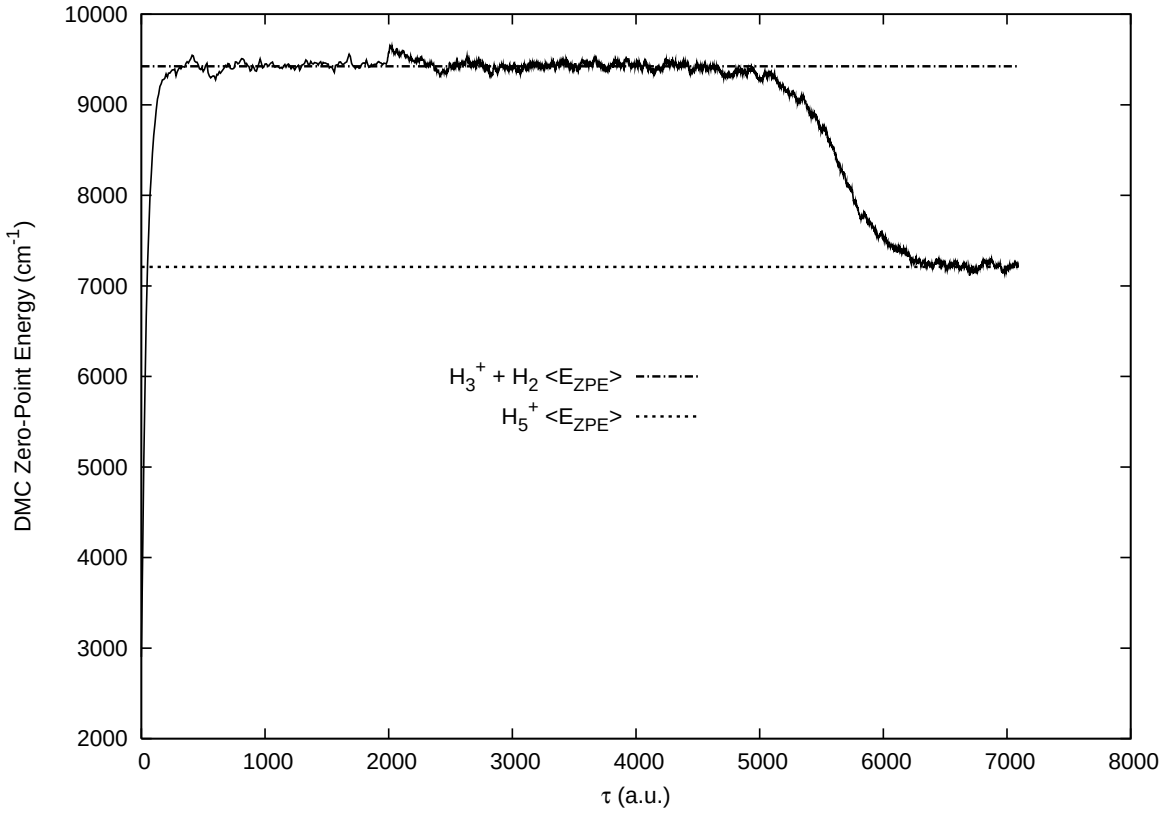

Figure 4.7: DMC simulation at the dissociation limit

reasonable way to pick initial configurations is to note that the global minimum of H_5^+ is of C_{2v} symmetry (see Fig. 2(a)) and thus, the H atoms are not all equivalent. According to that figure there are three classes of hydrogens and referring to Fig. 2(a), we see that H(1) and H(2) are in the same class, H(3) and H(4) belong to second class, and H(5) alone is the third class. As a result of this inequality, the singly deuterated molecule can have three different configurations, as indicated below (see Equation 4.4 - 4.6). Note the atom with the charge indicated is atom no. 5 in Fig. 2(a).

$$H_3^+ \cdots HD \rightarrow \begin{cases} H_3^+ + HD \\ H_2D^+ + H_2 \end{cases} \tag{4.4}$$

$$DH_2^+ \cdots H_2 \rightarrow \begin{cases} H_2D^+ + H_2 \\ H_3^+ + HD \end{cases} \tag{4.5}$$

$$H_2D^+ \cdots H_2 \rightarrow \begin{cases} H_2D^+ + H_2 \\ H_3^+ + HD \end{cases} \tag{4.6}$$

This inequality of initial configurations could lead to different outcomes of the unimolecular dynamics, depending on the relative time scale of dissociation and intermolecular energy redistribution. Both time scales are expected to depend on the total energy and here we consider a total energy of 28.6 kcal/mol. This is roughly 2 kcal/mol above the ZPE of the most endoergic product. Of course classical dynamics does not obey ZPE constraints; however, consideration of the ZPE of the products is often included in classical simulations, so that correct energetic thresholds are enforced. Note we have not considered the ZPE of the reactant complex; however, we return to this point below.

We performed 1000 classical trajectories for each at five initial configurations, for a total of 5000 trajectories. The initial momenta were selected randomly with the constraints of the fixed total energy and zero total angular momentum. As noted above there are three distinct classes of configurations and we could have restricted the initial configurations to these. However, as a test of the symmetry of the PES we did not do this. We did verify subsequently that equivalent configuration did give the same branching ratio (within the usual statistical uncertainty of running a finite number of trajectories). The branching ratio for the three distinct initial configurations is given in Table 4.7. As seen, there are substantial differences depending on the initial configuration. This indicates that the complex has "memory" of its initial configuration, i.e., the dynamics is not statistical. With this in mind it is also easy to rationalize the large difference in branching for the $H_2D^+ \cdots H_2$ initial configuration. Clearly the "least motion path" is to form the products $H_2D^+ + H_2$ products. Further, the path to form the other products $HD + H_3^+$ would require a significant re-arrangement of the initial configuration, e.g., an internal rotation of the H_2D^+ fragment. It should be clear from consideration of other initial configurations that the path to make H_3^+ from the $H_2D^+ \cdots H_2$ initial configuration is the most indirect one and so it is not surprising that the branching ratio to make these products from this configuration is the smallest among all initial configurations.

We now consider a critique of these classical calculations, based on consideration of the quantum ZPE. First, to contrast the results for a standard harmonic treatment of the ZPE with a rigorous DMC one, we calculated the harmonic ZPE at each of the three distinct configurations of H_4D^+. The results are $H_3^+ \cdots HD$: 7248.4 cm^{-1}, $DH_2^+ \cdots HH$: 7185.1 cm^{-1}; $HHD^+ \cdots HH$: 7243.5 cm^{-1}, indicating that

the $DH_2^+ \cdots HH$ configuration is the most stable one. This result could be incorporated into the classical calculation to weight the initial configurations accordingly (albeit to a 0 K distribution). However, a rigorous DMC calculation of the ZPE suggests a different picture. The DMC ZPE was calculated starting the "trajectories" from these initial configurations as well as from the 2-D_{2d} saddle point (see Fig. 2(b)). The result is an average ZPE equal to 6826±15 cm^{-1}, i.e., a single value. This is not a surprising result given that this molecular cation is highly fluxional. However, it does not necessarily imply that the three classes of initial configurations are all equally probably, as was assumed in the classical simulation.

Obviously a more thorough classical simulation is required, including of course a study of the bimolecular reaction as well as the unimolecular one. We plan to carry this out in the near future, using the present PES.

Table 4.7: Classical branching ratio of products H_4D^+ indicated to initial configuration

Reaction Channel			Ratio
$H_3^+ \cdots HD$	$\rightarrow$	$HD + H_3^+$	0.549
	$\rightsquigarrow$[1]	$H_2 + H_2D^+$	0.451
$DHH^+ \cdots H_2$	$\rightsquigarrow$	$HD + H_3^+$	0.379
	$\rightarrow$	$H_2 + H_2D^+$	0.621
$HHD^+ \cdots H_2$	$\rightsquigarrow$	$HD + H_3^+$	0.067
	$\rightarrow$	$H_2 + H_2D^+$	0.933

[1] the squiggle arrow indicates a non-least motion path.

4.4 Long Range Interaction

In order to carry out scattering calculations of, for example, the H_2 and H_2D^+ reaction at low temperatures of relevance in interstellar space, the long range interaction is

very important. This interaction is not adequately contained in the present PES, owing to the use of damping functions in eq. 4.2. As discussed by Prosmiti *et al.* [36] the relevant long range interaction is the sum of the charge-induced dipole(U_4 term) and the charge-quadrupole(U_3 term). These are given by

$$U_4 = -\left[\frac{1}{2}\alpha + \frac{1}{3}(\alpha_{\parallel} - \alpha_{\perp})P_2(\cos\theta)\right]/R^4 \tag{4.7}$$

$$U_3 = Q_{H_2}P_2(\cos\theta)/R^3, \tag{4.8}$$

where R is the distance from center of mass of H_3^+ to center of mass of H_2, θ is the angle between $\overrightarrow{R}$ and the H_2 bond. $\alpha, \alpha_{\parallel}$ and $\alpha_{\perp}$ are the average, parallel and perpendicular polarizabilities of the H_2 molecule, and Q_{H_2} is the quadrupole moment of H_2. We adopt this form for the long range potential and take for the H_3^+ and H_2 intermolecular potentials the ones from the PES. The H_2 polarizability and quadrupole moment were taken from Wolniewicz *et al.* [59,60]. The dependence of Q_{H_2} in particular on the H_2 internuclear distance, r_{HH} is quite strong [59, 60] and so a spline interpolation was incorporated to obtain Q_{H_2} and the polarizability as a function of r_{HH}.

This long range potential is "blended" into the PES by using a simple switching technique that is commonly used for such purposes. Thus, the complete potential, V, is given by

$$V(\mathbf{x}) = (1 - S(R))PES(\mathbf{x}) + S(R)(U_4 + U_3 + V_{H_3^+} + V_{H_2}) \tag{4.9}$$

where the switching function S varies between 0 and 1, has the following form [27]:

$$S(x) = 10x^3 - 15x^4 + 6x^5, (0 \leq x \leq 1) \tag{4.10}$$

where

$$x = \frac{R - R_a}{R - R_b} \tag{4.11}$$

where R_a and R_b are ending points of the switch region of fitted PES and the long range interaction and R is the center of mass distance of H_3^+ and H_2. Outside of this switching region S is either 0 or 1.

We plan to use the full potential in various scattering calculations of the reaction. The hope will be to improve agreement between classical calculations done previously [37] and experiment at very low temperatures.

4.5 Summary

A potential energy surface for H_5^+ based on more than 100,000 CCSD(T)/aug-cc-pVTZ *ab initio* energies was reported. The fit was obtained by a standard least-squares approach; however, using a novel many-body, permutationally invariant form. This PES is accurate up to 15000 cm^{-1} or 43 kcal/mol relative to the global minimum, and dissociates correctly to the fragments H_3^+ and H_2. Ten known stationary points were located and characterized on the PES. A comparison with previous benchmark energies at these stationary points showed an average absolute difference of only 58 cm^{-1}. A normal mode analysis was also done at these points and again agreement with the limited benchmark results is excellent. Quantum Diffusion Monte Carlo calculations of the H_5^+ and $H_3^+ + H_2$ zero-point energies were reported. These rigorous ZPEs together with the value of D_e of 8.30 kcal/mol result in a dissociation energy, D_0, of 6.33 kcal/mol which is in very good agreement with one experiment and slightly outside the error bars of another. By contrast the value of D_0 obtained using harmonic estimates of the ZPEs equals 5.57 kcal/mol, which is in poor agreement

with experiment.

A preliminary classical dynamics calculation of the unimolecular dissociation of H_4D^+ was reported. The dependence of the branching ratio to form the two products, H_2D^++H_2 and H_3^++HD on the initial classical configuration (the location of the D atom in H_4D^+) was studied at one total energy. A marked dependence was found; however, the determination of the rigorous ZPE casts some doubt on localization assumption of the classical calculation.

Finally, the long range ion-induced dipole and charge-quadrupole interactions were added to the fitted PES to make it extend to long range. The extended potential will be needed in scattering calculations, especially at very low temperatures, of interest in astrophysical applications. Such calculations are planned in the future.

Acknowledgements We thank the National Science Foundation(CHE-0431998, CHE-0443375) for financial support. Support for computational resources from ONR/DURIP is acknowledged. We thank Anne McCoy for her assistance in running the quantum Diffusion Monte Carlo calculations.

5 Theoretical Study of the Formation and Destruction of H_2D^+ via Reactions $HD+H_3^+ \leftrightarrow H_2+H_2D^+$

Abstract

Detailed quasiclassical trajectory calculations of the title reaction on the recent *ab initio*-based H_5^+ potential energy surface [Z. Xie, B.J. Braams and J.M. Bowman, J. Chem. Phys. **122**, 224307 (2005)] are reported. Both forward and reverse reaction were studied in detail. k_1 and k_{-1} from 10 to 300 K were calculated. The different channels cross section and products state distributions are also reported. The competing of hopping and complex forming mechanism for the formation and destruction of $H_2D^+$is also addressed in detail.

5 THEORETICAL STUDY OF THE FORMATION AND DESTRUCTION OF H_2D^+ VIA REACTIONS $HD + H_3^+ \leftrightarrow H_2 + H_2D^+$

5.1 Introduction

H_3^+, the simplest polyatomic molecule, has been identified as the main driver of gas phase, ion-molecular chemistry in the interstellar medium for a long time. A remarkable demonstration of the fundamental role that H_3^+ plays in interstellar chemistry has been revealed in the observed untrahigh deuterium fractionation in protostars [61]. Some pioneering experimentalists and theorists were engaged in this molecule [34, 61, 62], and an accurate global *ab initio* potential energy for H_5^+ was developed which enables more rigorous theoretical studies [63].

Though many theoretical works were involved in the characterization of H_3^+ and H_5^+, there is no detailed treatments of the collision dynamics of H_2D^+ describing its formation and destruction. Most of the understanding to the reaction $HD + H_3^+ \leftrightarrow H_2 + H_2D^+$ is based on simple thermodynamics arguments, or crude reaction models such as H atom exchange and proton jump, or statistical considerations by the assumption of long-lived collision complex H_4D^+.

Deuterated isotopomers play an very important role in the low-temperature interstellar clouds and attract many interests in recent years [34]. One of the most interest issues about these deuterated isotopomers is the abundance ratios of the singly deuterated species to the normal ones tends to be factors of up to 10^4 greater than the D/H elemental ratio of typical 2×10^{-5}.

H_2D^+ ion is a singly deuterated molecule of special importance. Its role in interstellar ion chemistry, especially for deuterating other molecules, has been discussed throughly [64, 65]. H_2D^+ is supposed to be formed via the classical proton-deuteron exchange reaction [34]. A few high quality quantum mechanical calculations have been done for the H_5^+ ion and a few potential energy surface(PES) are available [36, 37].

5 THEORETICAL STUDY OF THE FORMATION AND DESTRUCTION OF H_2D^+ VIA REACTIONS $HD + H_3^+ \leftrightarrow H_2 + H_2D^+$

The most recent PES with permutational invariant symmetry and capable describing the reaction $HD + H_3^+ \leftrightarrow H_2 + H_2D^+$ was developed in our group [63]. Nonetheless, there exists no detailed calculation of the reaction rate constant and reaction dynamics describing the formation of H_2D^+. Therefore, in order to get some clue of the mechanics of the formation of the H_2D^+ and shine some light on the reaction $HD + H_3^+ \leftrightarrow H_2 + H_2D^+$, we carried out the detailed quasiclassical trajectory calculation of the reaction on our newly developed potential energy surface.

Because H_5^+ is relatively weakly bound, *i.e.*, $D_e = 8.30$ kcal/mol [63], it cannot be safely assumed that the reaction $H_3^+ + H_2$ proceeds statistically via a long-lived H_5^+ complex. Indeed in the literature describing experimental measurements of the rate constant or cross section of this reaction (as well as a number of astrophysically important reactions involving istopologs) a proton hop and a hydrogen exchange mechanism for the reaction have been invoked.The former mechanism is presumed to occur in a direct reaction, that is without the need to form a complex and the latter mechanism is believed to occur via a complex.Gerlichand Oka and co-workershave used this terminology and have interpreted their data in terms of these mechanisms.As an illustration of these two mechanisms consider Gerlich's argument for the $D_3^+ + H_2$ reaction

$$D_3^+ + H_2 \longrightarrow \begin{cases} HD_2^+ + HD & (R1) \\ H_2D^+ + D_2 & (R2) \end{cases}$$

If these products are exclusively formed via a long-lived $H_2D_3^+$ complex the ratio of the cross sections of (R2) to (R1) should be 0.5 based on very simple statistical argument which just counts up the number of ways the products can be formed from

$H_2D_3^+$. In several experimentsthis ratio varies considerably from roughly 0.5 at the lowest energies/temperatures to much larger than 1 at higher energies. For example at a temperature of 300 K Giles *et al.* reported a ratio of 2 which is 4 times larger than the simple statistical result. Since (R2) can also occur via a simple proton hop mechanism it was argued that this mechanism becomes increasingly dominant as the collision energy increases which is accompanied by a decrease in the cross section for complex formation. This argument reasonably assumes that (R1) can only occur via a complex-forming mechanism.

The argument of Oka and co-workers applies to the reactions

$$p\text{-}H_3^+ + p\text{-}H_2 \longrightarrow \begin{cases} p\text{-}H_3^+ + H_2 & (R3) \\ o\text{-}H_3^+ + H_2 & (R4) \end{cases} .$$

Cordonnier *et al.* argued reasonably that reaction (R4) cannot occur via a simple proton hop. They estimated the proton hopping rate constant to be roughly 2.4 times larger than the exchange rate constant at 400 K.

The proton hop mechanism is envisioned, again quite reasonably, as being a direct and perhaps even a somewhat long range mechanism whereas the exchange mechanism is envisioned as requiring complex formation. As appealing as these simple characterizations are the actual dynamics may be subtle. Indeed in a limited study of the classical dynamics on a global potential energy surface we showed that the dissociation dynamics of the $HD + H_3^+$ complex did not produce a statistical distribution of products and this has been also noted in recent review paper Gerlich et al.In earlier work Moyano and Collins performed quasiclassical trajectory calculations of the $HD + H_3^+$ and $D_2^+ + H_3^+$ reactions using an interpolated potential energy surface (based

on MP2/6-311G(d,p) calculations and thus an approximate description of the correct long range electrostatic behavior). These authors concurred with earlier experimental evidence that the reaction dynamics cannot be characterized as scrambling via a long-lived collision complex.

Given the intriguing dynamics of the H_5^+ system and its relevance in astrophysics we present a detailed quasiclassical trajectory study of the reaction of HD with H_3^+ here. We use the global CCSD(T)/avtz potential energy surface we reported recently which does contain an accurate description of the long range ion-induced dipole and ion-quadrupole interaction. A major goals of this work is to characterize the reaction dynamics in detail and to hopefully better understand the proton hopping and exchange mechanisms.

The paper is organized as follows. In the next subsection we discuss the long range behavior of the PES. Following that we give some details of the quasiclassical trajectory calculations. In subsection 5.3 we present our results and comparison with experiment. We give a summary and conclusions in the final subsection.

5.2 Calculation

5.2.1 Reaction Channels

The main reactions we considered here are the following two:

$$
\begin{array}{l}
\mathrm{HD} + \mathrm{H_3^+} \longrightarrow \left\{ \begin{array}{lll} \mathrm{HD} + \mathrm{H_3^+} & \text{non-reactive} & \\ \mathrm{H_2} + \mathrm{H_2D^+} & \text{HH Forming (HHF)} & \left\{ \begin{array}{lll} \text{H-Hopping} & \text{(HHP)} \\ \text{H-D Exchange} & \text{(HDE)} \end{array} \right. \\ \mathrm{H'D} + \mathrm{H_3^+} & \text{H-H Exchange (HHE)} & \end{array} \right. \quad (5.1) \\
\\
\mathrm{H_2} + \mathrm{H_2D^+} \longrightarrow \left\{ \begin{array}{lll} \mathrm{H_2} + \mathrm{H_2D^+} & \text{non-reactive} & \\ \mathrm{HD} + \mathrm{H_3^+} & \text{HD Forming (HDF)} & \left\{ \begin{array}{lll} \text{H-Hopping A} & \text{(HHPA)} \\ \text{H-Hopping B} & \text{(HHPB)} \\ \text{H-D Exchange A} & \text{(HDEA)} \\ \text{H-D Exchange B} & \text{(HDEB)} \end{array} \right. \\ \mathrm{H'H''} + \mathrm{H_2D^+} & \text{HH Forming (HHF)} & \left\{ \begin{array}{lll} \text{D-Hopping} & \text{(DHP)} \\ \text{H-H Exchange A} & \text{(HHEA)} \\ \text{H-H Exchange B} & \text{(HHEB)} \\ \text{H-H Exchange C} & \text{(HHEC)} \\ \text{H-H Exchange D} & \text{(HHED)} \end{array} \right. \end{array} \right. \quad (5.2)
\end{array}
$$

Eq. 5.1 shows the all the possible forward reaction channels. Since the first channel is just the non-reactive channel, only the reactive and exchange channels were considered. (The same rule is applied to the reverse reaction in the following.) Theoretically there are 6 types of combinations to make H_2, while in the trajectory calculations, we just distinguish them by "H-Hopping", "H-D Exchange" and "H-H Exchange" mechanism as shown in Fig. 5.1.

As for the reverse reaction shown by Eq. 5.2, we note that are there 4 H atoms reactants, as a result, there are 4 types of HD in the "HD Forming" channel and they are distinguished with each other as "HHPA", "HHPB", "HDEA" and "HDEB" as in Eq. 5.2. The "Hopping" and "Exchange" mechanisms are similar to those in Fig. 5.1 for the forward reaction.

Similarly, there are 5 possible combinations for the "HH Forming" channel. They are labeled as "DHP", "HHEA", "HHEB", "HHEC" and"HHED" as in Eq. 5.2. Four of these sub-channels are similar expect for the "DHP" one differs significantly from others.

5.2.2 Potential Energy Surface with Long Range Interaction

The long range interaction for the H_2 and H_2D^+ is crucial for the scattering calculations of H_2 and H_2D^+ reaction at low temperatures of relevance in interstellar space. This interaction is not adequately contained in our reported PES [63] owing to the use of damping functions in fitting. As discussed by Prosmiti *et al.* [36] the relevant long range interaction is the sum of the charge-induced dipole (U_4 term) and the charge-quadrupole (U_3 term). These are given by

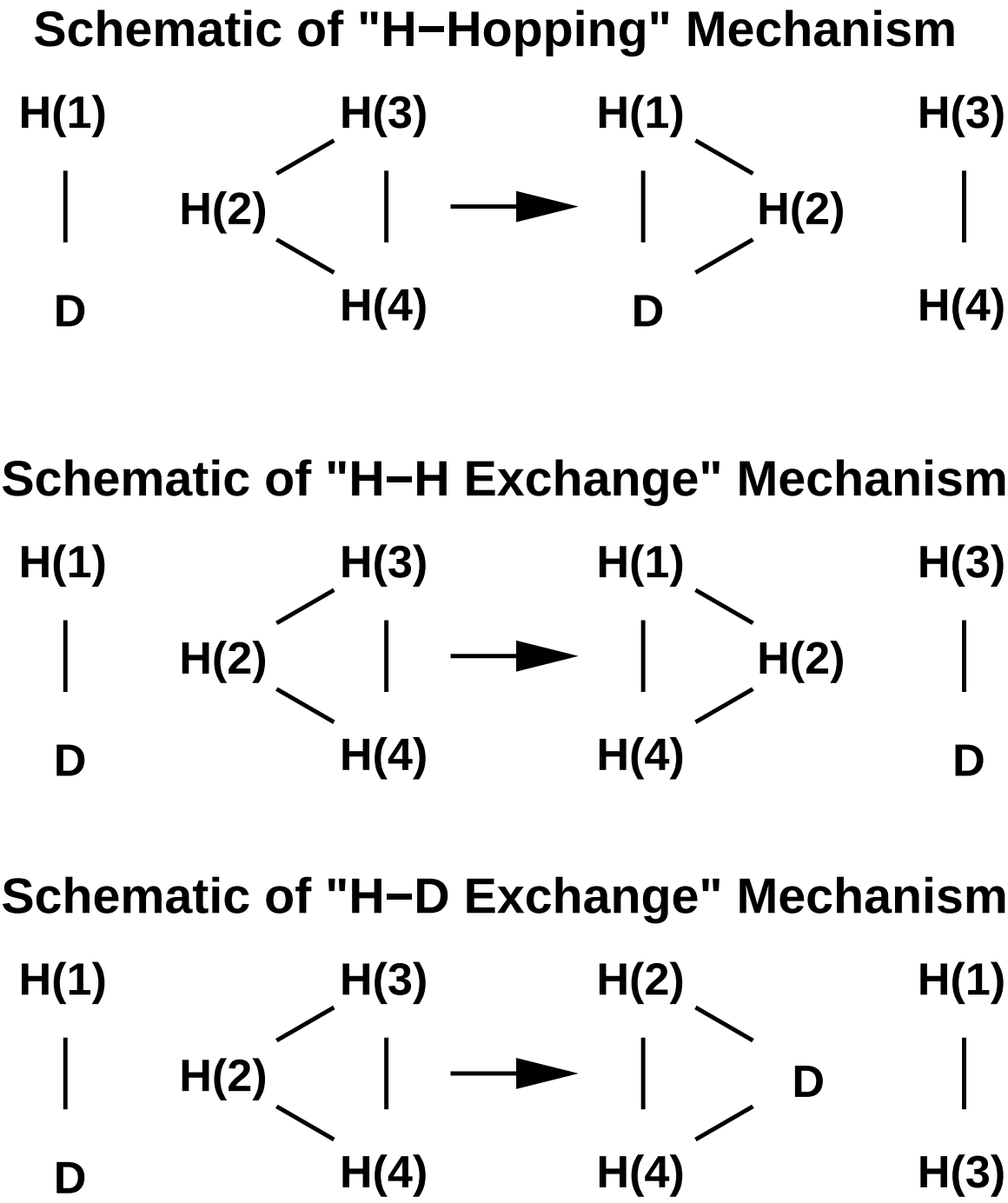

Figure 5.1: Schematic of "H-Hopping", "H-H Exchange" and "H-D Exchange" mechanism for the forward reaction $HD + H_3^+ \longrightarrow H_2 + H_2D^+,\ H'D + H_3^+$

$$U_4 = -\left[\frac{1}{2}\alpha + \frac{1}{3}(\alpha_\parallel - \alpha_\perp)P_2(\cos\theta)\right]/R^4, \tag{5.3}$$

$$U_3 = Q_{H_2}P_2(\cos\theta)/R^3. \tag{5.4}$$

where R is the distance from center of mass of H_3^+ to the center of mass of H_2, θ is the angle between $\mathbf{R}$ and the H_2 bond. $\alpha, \alpha_\parallel$ and $\alpha_\perp$ are the average, parallel and perpendicular polarizabilities of the H_2 molecule, and Q_{H_2} is the quadrupole moment of H_2. We adopt this form for the long range potential and take for the H_3^+ and H_2 intermolecular potentials the ones from the PES. The H_2 polarizability and quadrupole moment were taken from Wolniewicz *et al.* [59, 60]. The dependence of Q_{H_2} in particular on the H_2 inter-nuclear distance, r_{HH} is quite strong [59, 60] and so a spline interpolation was incorporated to obtain Q_{H_2} and the polarizability as a function of r_{HH}.

This long range potential is "blended" into the PES by using a simple switching technique that is commonly used for such purposes. Thus, the complete potential, V, is given by

$$V(\mathbf{x}) = (1 - S(R))PES(\mathbf{x}) + S(R)(U_4 + U_3 + V_{H_3^+} + V_{H_2}) \tag{5.5}$$

where the switching function S varies between 0 and 1, has the following form [27]:

$$S(x) = 10x^3 - 15x^4 + 6x^5, (0 \leq x \leq 1) \tag{5.6}$$

where

$$x = \frac{R - R_a}{R - R_b} \tag{5.7}$$

where R_a and R_b are ending points of the switch region of fitted PES and the long range interaction and R is the center of mass distance of H_3^+ and H_2. Outside of this switching region S is either 0 or 1.

A contour plot of the PES (R, θ dependence) is shown in Fig. 5.2, which describes the long range behavior of the PES. Especially the region where the incoming H_2 approaching the vicinity of H_3^+ (H_2D^+).

The figure clearly shows the incoming H_2 angular dependence of the PES. When the angle is small or the two H atoms in the incoming H_2 is shooting the target in a line, there is a barrier which is about 200 cm^{-1}. Noticing that this barrier is very high Com pairing the collision energy, it supposed to effect the reaction significantly. When the two H atoms in H_2, are approaching the target side by side (is this case the angle we defined in Fig. 5.2 is large or close to 90 degree), this is no barrier. This long range PES behavior has a dramatic effect for the different rotational states of incoming H_2 or HD as addressed later.

5.2.3 Initial Conditions for Quasiclassical Trajectory

The initial conditions for the quasiclassical trajectories are essentially the usual ones [66]. For the title reaction, both monomers were at the ground ro-vibrational state. Harmonic zero-point energy was added to both reactants initially and random sampling of initial normal-mode coordinates and momenta was done. Standard adjustments were made to enforce zero angular momentum.

The initial conditions are critical in quasiclassical trajectory simulation. In this

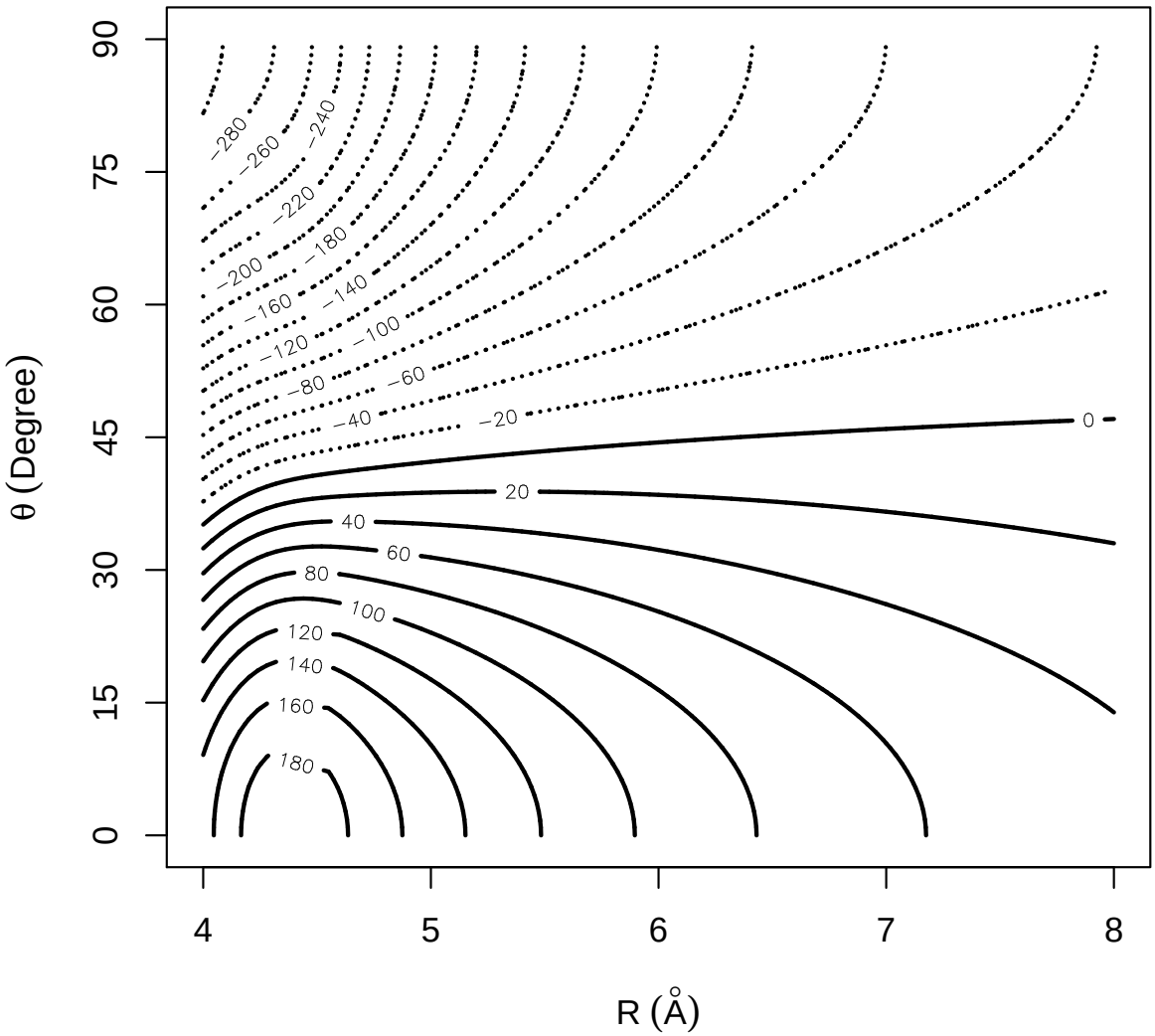

Figure 5.2: Contour plot of the long range behavior of the H_5^+ potential energy surface. The energies (relative to the H_5^+ dissociation limit energy) are in cm^{-1}, and R is the center of mass distance of H_3^+, and H_2 is in its equilibrium structure. θ is the angle of H_2 orientation and the center of mass position vector of H_3^+ and H_2

calculation, the harmonic zero-point energies were carefully sampled into each normal mode in phase space. For the forward reaction (Eq. 5.1), due to the spin statistics limitation, the rotational quantum number J for H_3^+ was set only to 1. As for HD, $J = 0$ and $J = 1$ were both sampled. Before collision, the monomers HD and H_3^+ were separated in 100 Bohr and the orientation of these monomers were randomly selected. The collision energies(E_{col}) for the collisions were 5, 10, 25, 40, 50, 60 and 90 cm^{-1}. The impact parameter was scan from 0 to a larger number until zero reaction probability was reached. At each given set of parameters (E_{col}, b, J_{HD}, $J_{H_3^+}$), 2000 initial relative configurations of HD and H_3^+ were sampled and then run until finally the products dissociated. The same procedure was applied for the reverse reaction except that the rotational quantum number of H_2D^+ was set to 0 and the collision energies were 100, 150, 200, 250, 300, 350 and 400 cm^{-1} considering the reaction barrier of 89.87 cm^{-1}.

The ZPE leaking problem is notorious in QCT studies and it was discussed in a series of paper [63, 67, 68] on trajectory calculations. In this study, we kept all the trajectories, and we want to show how big the problem could be when comparing to experimental results in this case. This issue will be discussed in later subsections.

5.3 Results and Discussion

5.3.1 Forward Reaction: Forming of H_2D^+

Cross Sections The reaction cross section is a key step to understand the reactions $HD + H_3^+ \leftrightarrow H_2 + H_2D^+$. For the forward reactions at various collision energies, it was found that the cross sections were decreasing exponentially as collision energy increasing as shown in Table 5.1 and Fig. 5.3. Since the forward reaction is exothermic,

there is no barrier for the formation of H_2D^+, the cross section increasing exponentially in the low temperature limit. This partially supports the arguments that in the lower temperature limit, the fraction of deuterated H_3^+ (H_2D^+) is untrahight [62]. From a pure statistic point view with the assumption that the reaction undergoes a long-lived complex, the ratio to give H_2 over H'D should be about 2. However, the classical trajectory calculations showed that is ratio is 10, which is significantly great that 2. This large ratio supported the experimental evidence for the "incomplete scrambling" of H and D [62].

Table 5.1: Cross sections (Bohr^2) for forward reaction $HD+H_3^+ \longrightarrow H_2+H_2D^+$, $H'D+H_3^+$

E_{coll} (cm^{-1})	$H_2 + H_2D^+$ (HHF)		H'D + H_3^+ (HDF)	
	$j_{HD} = 0$	$j_{HD} = 1$	$j_{HD} = 0$	$j_{HD} = 1$
05	3137.45	1138.22	303.42	122.44
10	2141.00	828.97	207.86	87.18
25	1236.51	564.33	116.35	54.35
40	920.60	463.85	74.67	43.31
50	815.33	431.19	71.16	36.33
60	753.72	399.53	61.04	34.77
90	549.27	328.13	42.07	25.40

Fig. 5.3 shows clearly that the cross sections change with the initial rotational state of the incoming HD. The reaction is much easier to occur for the rotational cold HD ($j = 0$) than the rotational hot species ($j = 1$). The reaction probability was further examined to shine some light on it. As shown in Fig. 5.4, the main difference lies in the fact that the reaction probability drops very quickly as increasing the impact parameter for rotational hot HD, while it is almost constant for the rotational cold HD until the impact parameter approaching b_{max}. Considering the nature of the long range behavior of the PES as shown in Fig. 5.2, there is a strong dependence on

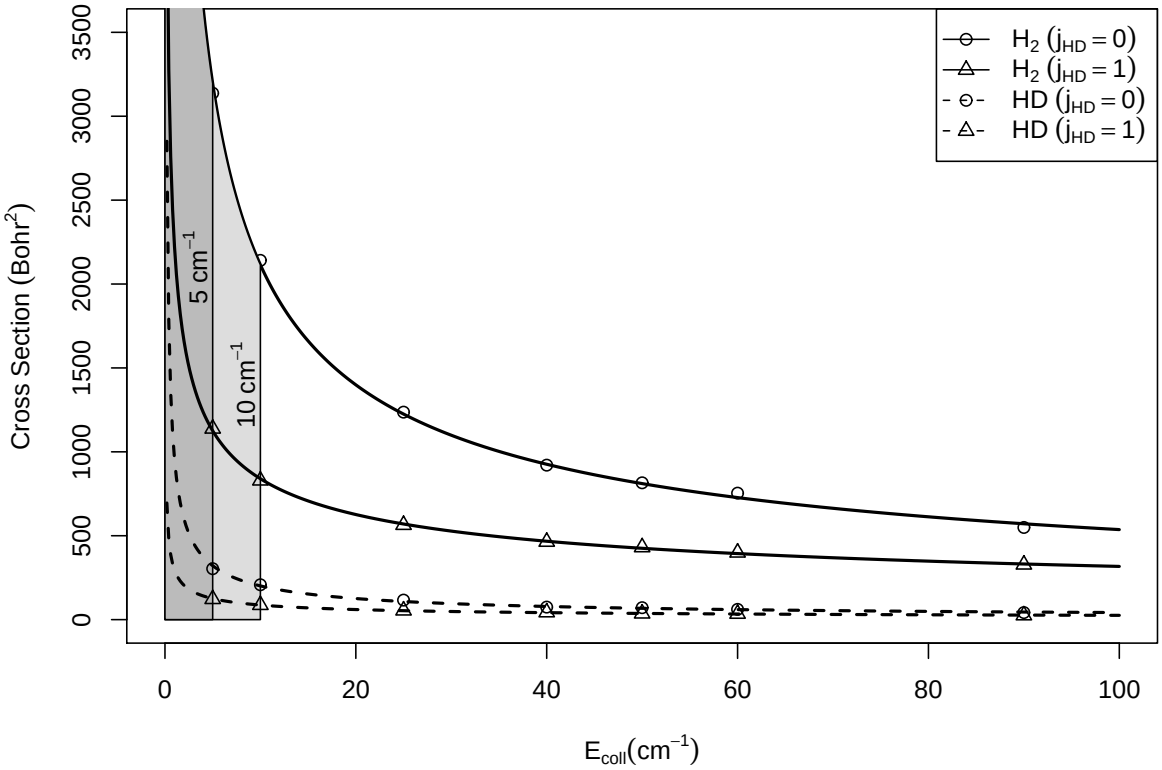

Figure 5.3: $HD + H_3^+ \longrightarrow H_2 + H_2D^+$, $H'D + H_3^+$ cross sections changing with collision energies and their dependence on the initial rotational states of HD

the orientation of the HD. For the side-by-side (H and D atoms are side by side and θ is close to 90°) shooting HD, these is no barrier and this is more likely to be the roadway for the rotational code HD, since this kind of HD is much easier to adapt its orientation and follows the downhill pathway. For the rotational hot HD molecules, they are rotating very fast comparing their translation. As a consequence, they have the capability to approaching the PES barrier for small θ, and bounced back.

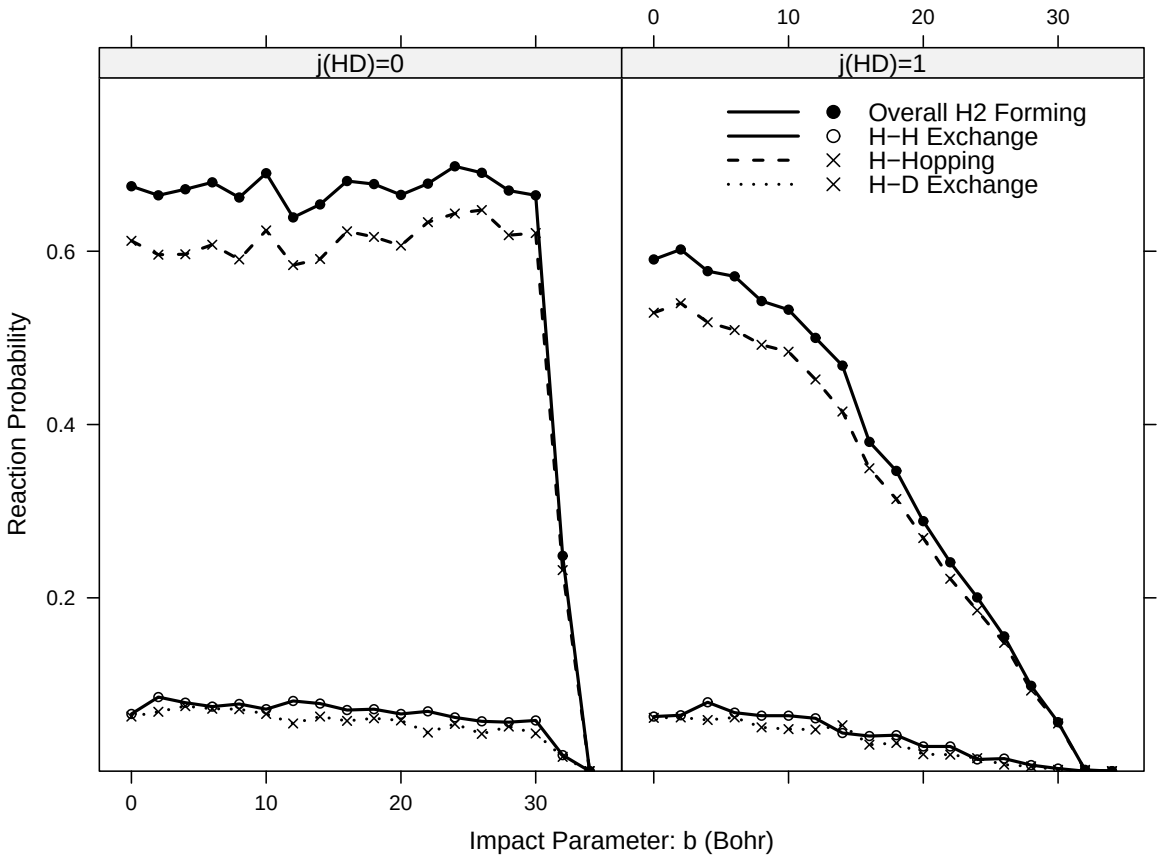

Figure 5.4: $HD + H_3^+ \longrightarrow H_2 + H_2D^+$, $H'D + H_3^+$ reaction probabilities changing with impact parameters at collision energy 10 cm^{-1} and their dependence on the initial rotational states of HD. The solid lines are for the two main channels of H_2 forming and HD forming. The H_2 forming channels can be divided into "H-Hopping" and "H-D Exchange" two sub-channels as shown in dashed and dotted lines.

"Hopping" and "Complex Forming" are two different reaction mechanism for the

title reactions, but there is no detailed theoretical simulation has been performed as we known. The "Hopping" mechanism is supposed to be faster than the "Complex Forming" one [69].There should be some evidences in the QCT simulations and they are shown in Fig. 5.5. The time steps profile keeps similar at different impact parameters b. A dramatic effect is observed for different rotational state of HD.

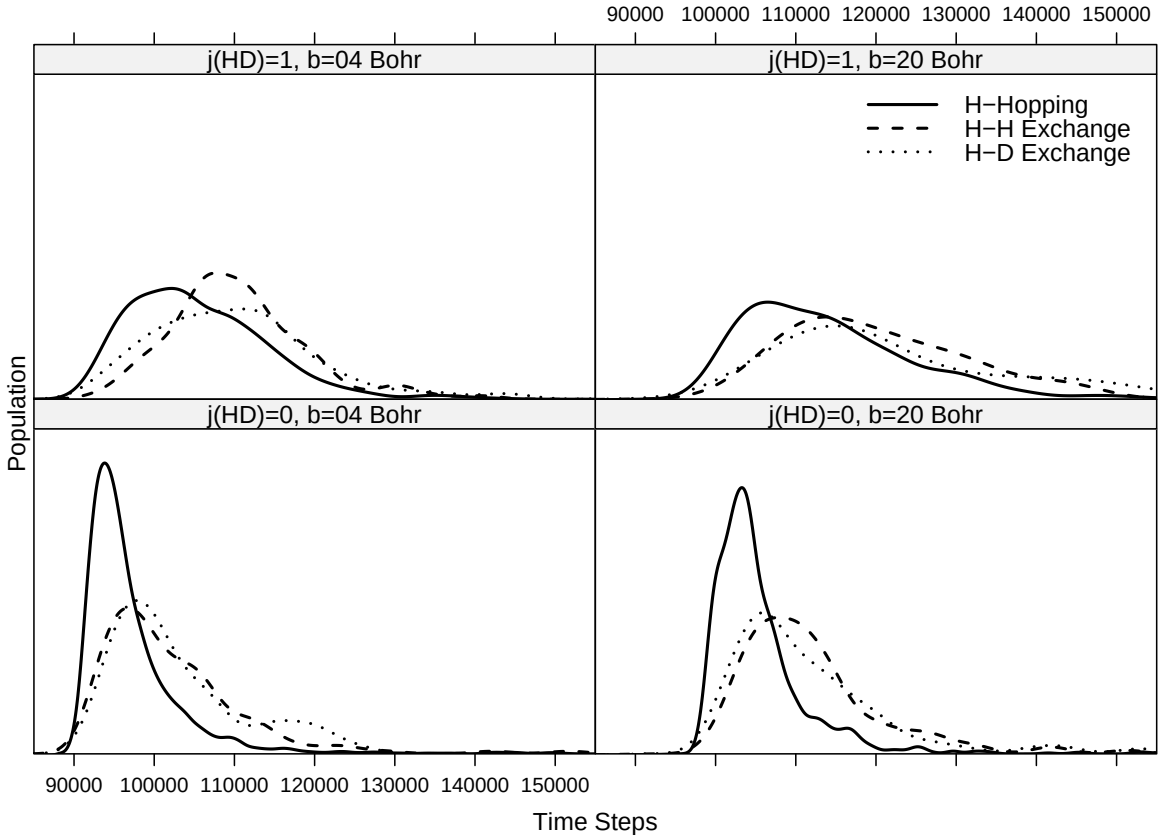

Figure 5.5: Total time steps for the reaction $HD + H_3^+ \longrightarrow H_2 + H_2D^+$, $H'D + H_3^+$ at collision energy 10 cm^{-1} and initial states as indicated.

Reaction Rate Constant The reaction rate constant can be further calculated based on the reaction cross section as in Table 5.1. Being aware of the zero-point energy issue and the limitation of classical picture, it is not surprised to see that

the calculated rate constant from cross subsection should be large than the actual values. As expected, the calculated rate constant shown in Fig. 5.6 is higher than the available experimental result [34, 70]. The low temperature limit (10 K) is extremely hard for both experiments and theoretical simulations. Comparing to the latest result reported by Gerlich *et al.* in 2002, the trajectory result is $2.3 \times 10^{-09}\text{cm}^{-1}/s$ great than the experimental values by a factor of 7. At high temperature, the deviation from experiments are quite small. To further show the significance or sensitivity of the rate constant at low temperature limit, some artificial numerical experiments were performed. As shown in Fig. 5.3, a mandatory cut line at 5 cm^{-1} was added to zero out the cross section blow 5 cm^{-1}. A modified temperature depend rate constant was calculated based on the cross section data above the threshold. As can be seen in Fig. 5.6, the rate constant drops dramatically in the low temperature limit. If the threshold was moved to 10 cm^{-1}, the behavior of the rate constant totally changed in the low temperature region. However, there is almost no effect in the high temperature region. In the classical picture, there are no too many options to deal with this difficulty. It's left open to more rigorous quantum mechanics calculation.

The reaction rate constants calculated at 10 K with $j_{\text{HD}} = 1$ is $9.18 \times 10^{-10}, 6.63 \times 10^{-10}\text{and}4.02 \times 10^{-10}\,\text{cm}^3/\text{s}$.

H_2 and H'D Angular Distributions From the cross section ratio to give H_2D^+ and H'D in previous subsection, the trajectory calculation already showed that formation of H_2D^+ can not be fully regards as the dissociation product of the long-lived complex H_4D^+. The product angular distribution will further strengthen this argument. From the statistical point of view, if the reactions undergoes a long-lived complex, then the product would be almost uniformly scattered from 0 to 180 de-

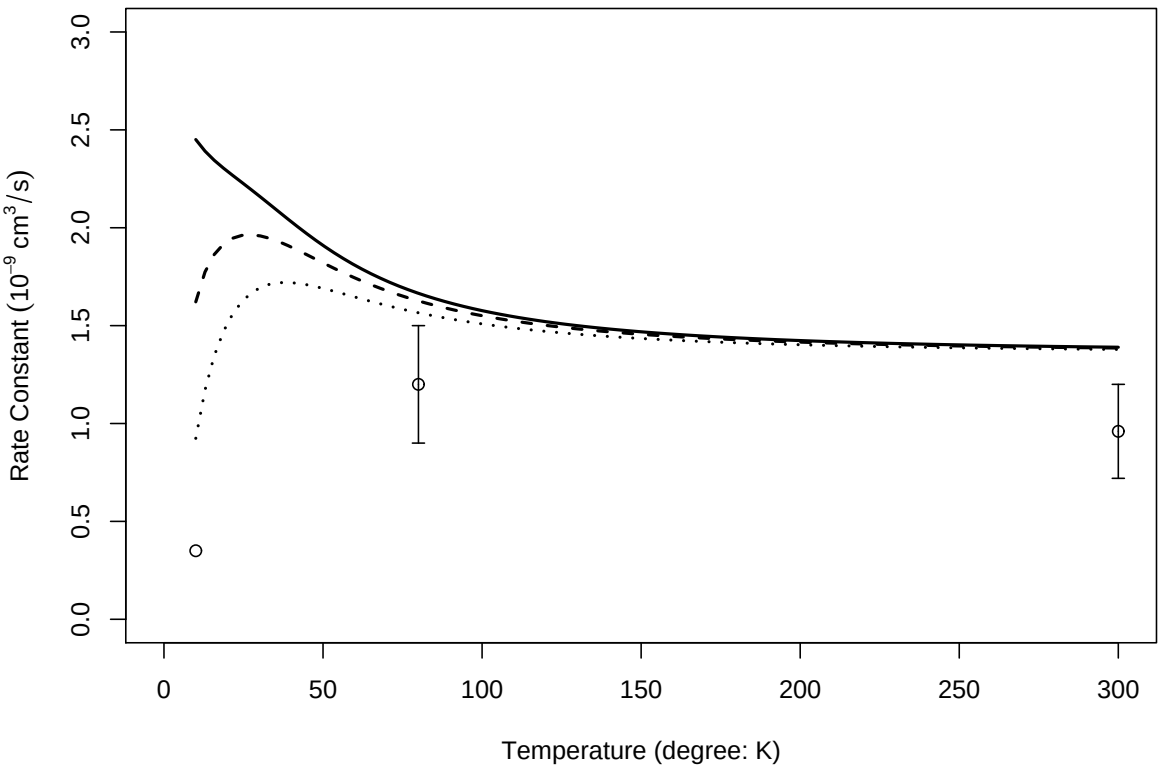

Figure 5.6: $HD + H_3^+ \longrightarrow H_2 + H_2D^+$, $H'D + H_3^+$ rate constant calculated based on the cross sections. The experimental data at 10 K is from reference 34 and other data are from reference 70

gree. Otherwise, there must be some fingerprints in the product angular distribution pattern. It's easy to image that the reactive channel in reaction 5.1 can undergo a mixture of striping, rebound and complex mechanism. For the exchange channel in reaction 5.1, it is impossible for an incoming molecular to pick up an atom in another molecule and then leaves away. There must be some long-lived complex formed and finally dissociated to H'D. All these features can be seen in Fig. 5.7. First of all, both the scattering angle of the H_2 and H'D have a very broad distribution. This suggests that long-lived complex was formed in some extent. Agreed with the intuition, the angular distribution of H'D was almost flat over the whole range, and there was a wide peak in the H_2 angular distribution which indicated some non-longlived complex mechanism. This supported the argument about the incomplete scrambling of H and D atom [62].

5.3.2 Reverse Reaction: Destructing of H_2D^+

Nature is a balance and so reactions. It's shown that the forward reaction populates the H_2D^+ molecule especially in low temperature limit, and it is also need to show the possible destructing of H_2D^+ especially in low temperature limit, then the argument that the fraction of deuterated $H_3^+$is extremely high in proto-star can be fully understand in the classical frame.

Cross Sections Similar to the forward reaction or the forming of H_2D^+, the reaction cross section is the key step in understanding the reaction mechanism. It's a little more complicated for the reverse reaction comparing to the forward reaction since there are more channels opened as addressed in subsection 5.2.1.

The channels are labels as HHPA, HHPB, HDEA, HDEB, DHP, HHEA, HHEB,

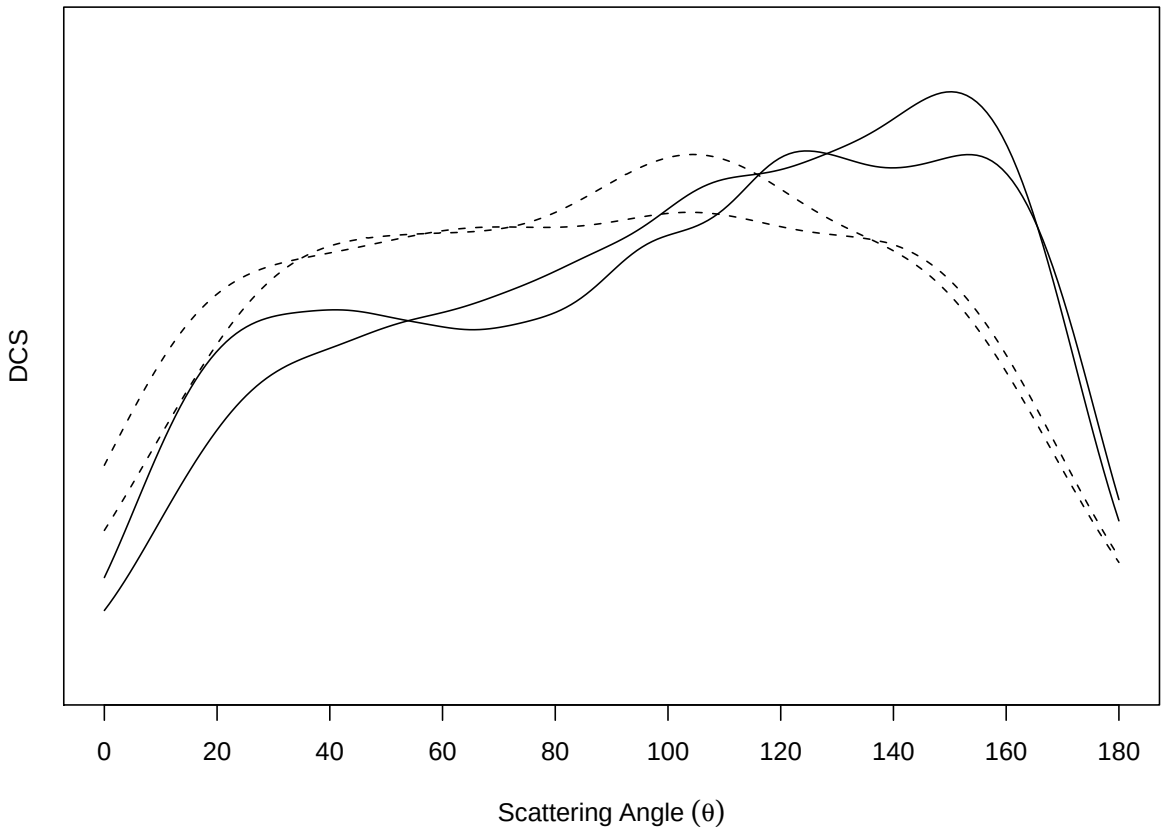

Figure 5.7: H_2 and H'D angular distributions

HHEC, HHED. These 9 channels fall into two main categories as the "HDF" and "HHF" channels. The reason that the channels were filtered into so many channels is for more insight into the destructing of H_2D^+. In channel HHPA and HHPB, the hydrogen in the final HD is from the reactant H_2D^+, or one proton in H_2D^+hopped to the H_2 part. Channel HDEA and HDEB are different from HHPA and HHPB in that the H atom in HD is from the reactant H_2. There is obviously no simple "Hopping" mechanism to for these channels are some complex must be formed and then followed by "H-D Exchange". To simplify the notation, a symbol such as CS(X) is used to denote the cross section of channel "X". As expected, CS(HHPA) should be roughly equally to CS(HHPB) since the equivalence of the two H atoms in H_2D^+, and there should be no significant difference between CS(HDEA) and CS(HDEB). This is exactly the result came out from the trajectory calculations as show in Table 5.2. A noticeable feature of these cross sections is that CS(HDEA) or CS(HDEB) is very small comparing to CS(HHPA) and CS(HHPB). This is not surprise with the assumption that "Hopping" is much faster and easier than the "Exchange" mechanism.

Channels DHP, HHEA, HHEB, HHEC and HHED are also expect to give small cross section except for channel DHP, in which case the Deuterium is supposed to hop from H_2D^+ to H_2 part. CS(DHP) is much greater that CS(HHEA) and so on, but it is still significantly smaller than CS(HHPA) and CS(HHPB).

From a pure statistical point of view, the probability for the "H-Hopping" is twice of that of "D-Hopping". Further considering the mass difference of H and D atoms, it is not too surprise to see that the CS(DHP) is only a small fraction of CS(HHPA) or CS(HHPB). Similar situation was also observed in reaction H + CHD_3 we studied [68].

Table 5.2: Cross sections ($Bohr^2$) for reverse reaction $H_2 + H_2D^+ \longrightarrow HD + H_3^+$, H'H" + H_2D^+

E_{coll} (cm^{-1})	$j_{HH} = 0$								
	HD + H_3^+ (HDF)				H'H" + H_2D^+ (HHF)				
	HHPA	HHPB	HDEA	HDEB	DHP	HHEA	HHEB	HHEC	HHED
100	194.28	192.27	6.09	7.49	90.00	10.89	11.20	10.92	10.99
150	135.49	132.22	4.88	6.15	77.58	7.11	6.64	5.77	6.74
200	111.26	108.49	4.50	4.95	69.84	5.98	5.43	6.05	5.01
250	94.35	98.42	4.34	4.06	66.04	4.88	4.12	3.86	4.15
300	86.94	86.56	4.06	3.27	61.67	3.66	2.55	3.67	4.43
350	84.92	81.69	2.99	2.31	58.54	2.57	2.37	3.15	3.55
400	70.23	71.34	2.84	2.07	59.20	2.42	1.87	2.67	3.08
	$j_{HH} = 1$								
	HD + H_3^+ (HDF)				H'H" + H_2D^+ (HHF)				
	HHPA	HHPB	HDEA	HDEB	DHP	HHEA	HHEB	HHEC	HHED
100	104.75	107.24	5.79	6.37	59.11	7.92	7.86	7.85	7.51
150	78.80	83.20	5.07	5.01	51.46	5.44	4.92	6.10	5.64
200	71.37	67.02	3.95	5.15	45.67	3.69	5.02	4.28	3.54
250	58.37	63.93	3.23	3.33	46.12	3.74	4.46	3.93	3.39
300	57.88	54.69	4.06	3.00	42.51	3.06	3.21	3.30	3.35
350	51.28	52.88	2.90	2.80	41.23	2.79	1.60	2.69	3.11
400	48.27	48.35	2.68	2.26	39.86	2.49	2.15	2.67	2.43

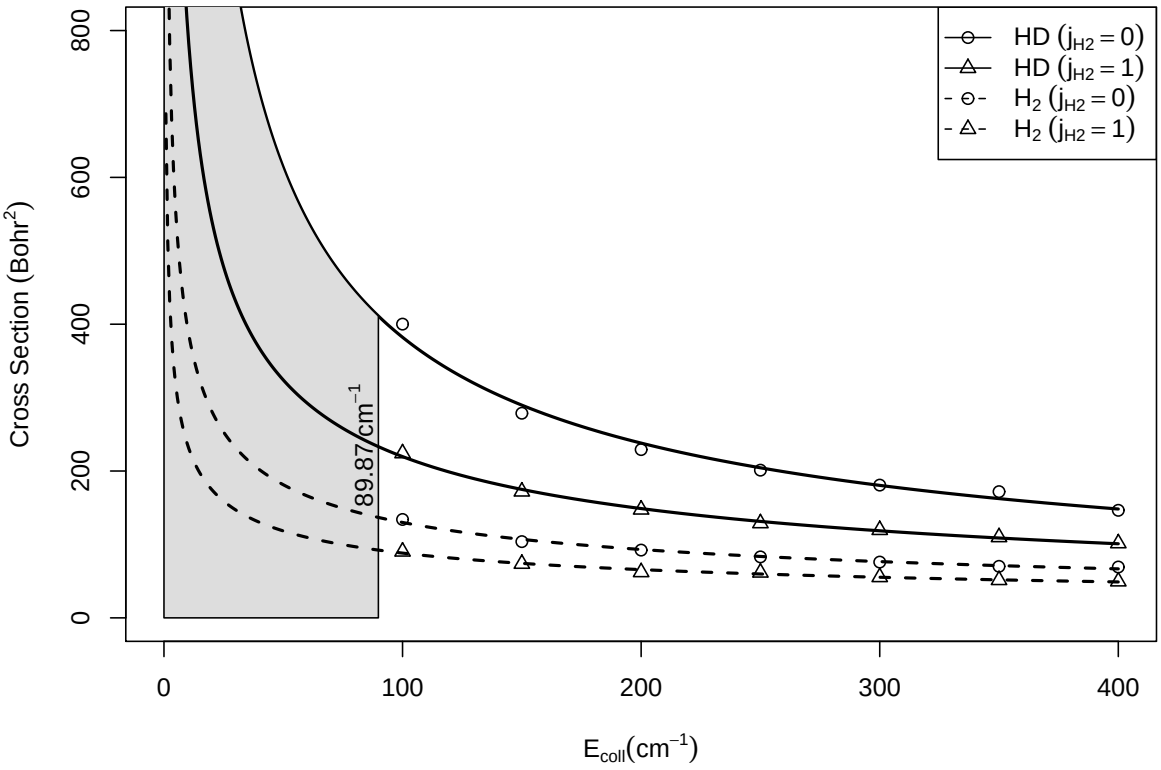

Figure 5.8: $H_2 + H_2D^+ \longrightarrow HD + H_3^+$, H'H" + H_2D^+ cross sections changing with collision energies and its dependence on the initial rotational state of H_2

Reaction Rate Constant Similar to the forward reaction, the reverse reaction rate constant was also calculated in a similar way except that there is a threshold for the reverse reaction. From Diffusion Monte Carlo calculation, we get the energy difference of the products and reactants to be 89.87 cm^{-1} (this energy difference is caused by the ZPE difference of the reactants and products). Due to the spin statistics limitation, as stated elsewhere [62], the H_3^+ rotational motion can not be 0. In addition, with the consideration of the initial rotational state of H_2, the actual threshold should be larger than 89.87 cm^{-1}. Since the classical picture is not very accurate about the state to state scattering, here we just adopt the number 161.1

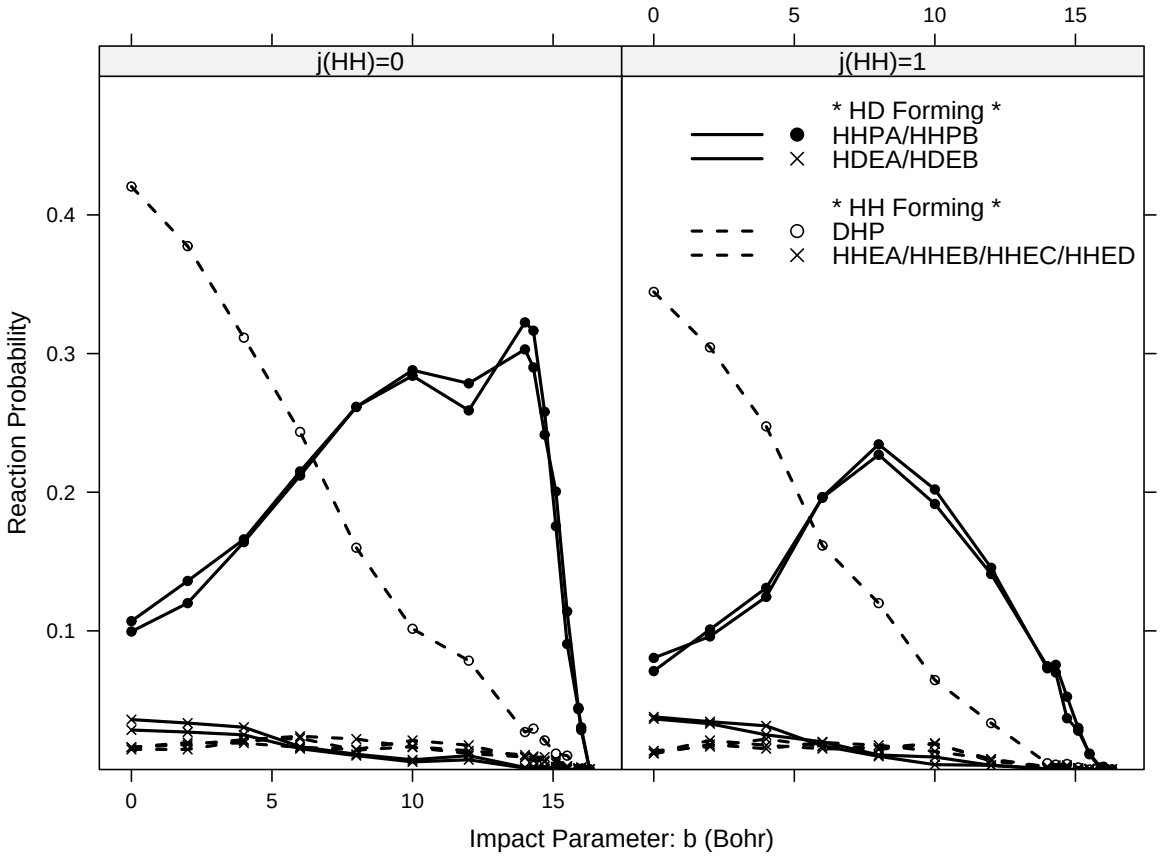

Figure 5.9: $H_2 + H_2D^+ \longrightarrow HD + H_3^+$, H'H" $+ H_2D^+$ reaction probabilities changing with impact parameter at collision energy 100 cm^{-1} and its dependence on the initial rotational state of H_2. The solid and dashed lines separate the two main channels: HD forming and H_2 forming. Circle ($\bullet$ or $\circ$) and cross ($\times$) are further used to distinguish "Hopping" and "Exchange" sub-channels.

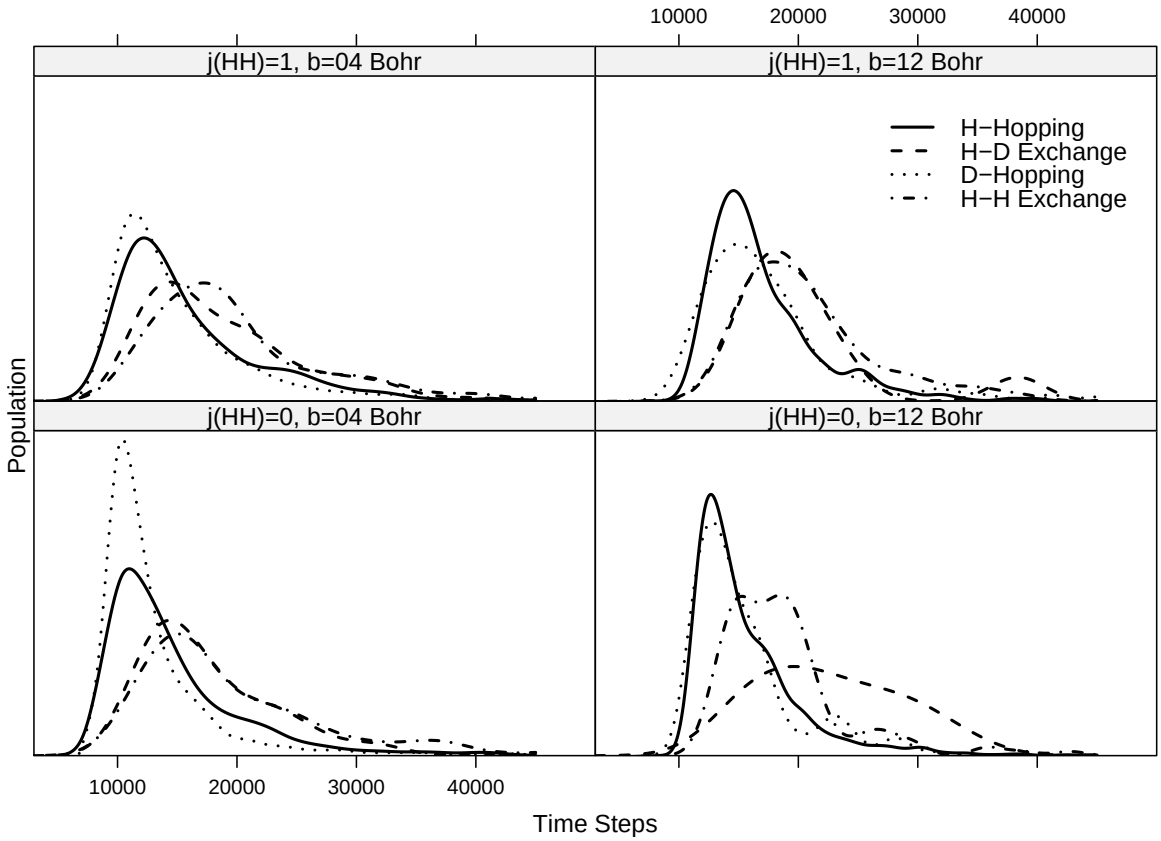

Figure 5.10: Total time steps for the reaction $H_2 + H_2D^+ \longrightarrow HD + H_3^+$, H'H" $+ H_2D^+$ at collision energy 100 cm^{-1} and initial states as indicated.

cm^{-1} as the threshold for both *p*-H and *o*-H. The reaction rate constant calculated based on this threshold is shown in Fig. 5.11. Another two lines were also shown in this figure to show how sensitive the rate constant when varying the threshold.

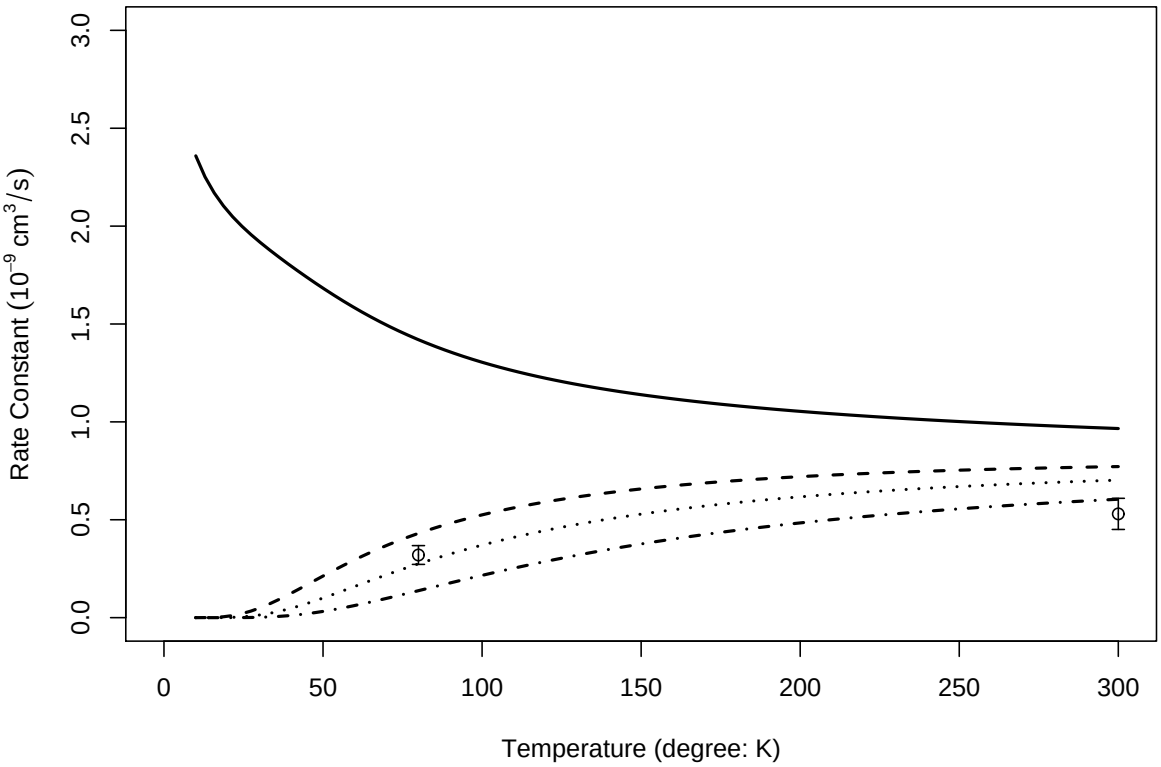

Figure 5.11: $H_2 + H_2D^+ \longrightarrow HD + H_3^+$, H'H" + H_2D^+rate constant

As can be seen in the Fig. 5.11, if we assume there is no threshold, which is the assumption hold by classical trajectories, the cross sections are extrapolated to infinity when the collision energy tends to zero. The rate constant based on this assumption obviously gave a wrong behavior. If the threshold was enforced at 89.87 cm^{-1}, which is lower that the actual threshold, the calculation gave a much better result, although it is quite above the known experimental results. If the threshold was enforced at 161.61 cm^{-1}, the calculated results went through the experimental data. As discussed

by Gerlich [62], the enthalpy of the H_2D^+destruction would be 161.1-118.4 cm^{-1}, a modified rate constant calculation was also performed and shown in Fig. 5.11. From these artificial enforcement of the reaction threshold, though not accurate enough, we can still notice that in the reverse reaction rate constant is quite in range and the classical trajectory result agreed with the experimental. If we suppose the rate constant using the cross sections cut from 118.4 cm^{-1}, finally we reach to a expression $K_e = 0.91 * \exp(152.35K/T)$ which gives $K_e \approx 1.5$ at 300 K.

Angular Distributions The angular distributions of the reaction products can help to give an illusive picture of the reaction mechanism. From Fig. 5.12, there are mainly two series of distribution, one is flat and the other is a little peaked at low scattering angle. The flat distribution is corresponding to H'H" distribution which was from complex mechanism, and the peaked distribution was for HD which was from the combination of striping and complex forming mechanism.

5.4 Summary

In summary, we studied that quasiclassical trajectories on the potential energy surface of H_5^+ implemented with long range interaction. After examining numerous trajectories, we calculated the rate constant for reaction $HD + H_3^+ \rightarrow H_2 + H_2D^+$ in temperature range 0-300 K. The comparison with the experimental data was not bad in the hight temperature region, while in the lower temperature region, the deviation was large. This may partially because the ZPE "leaking" problem in quasiclassical trajectory simulation. Furthermore, we also studied the angular distribution of the collision products of HD with H_3^+, the result was against the long lived "complex"

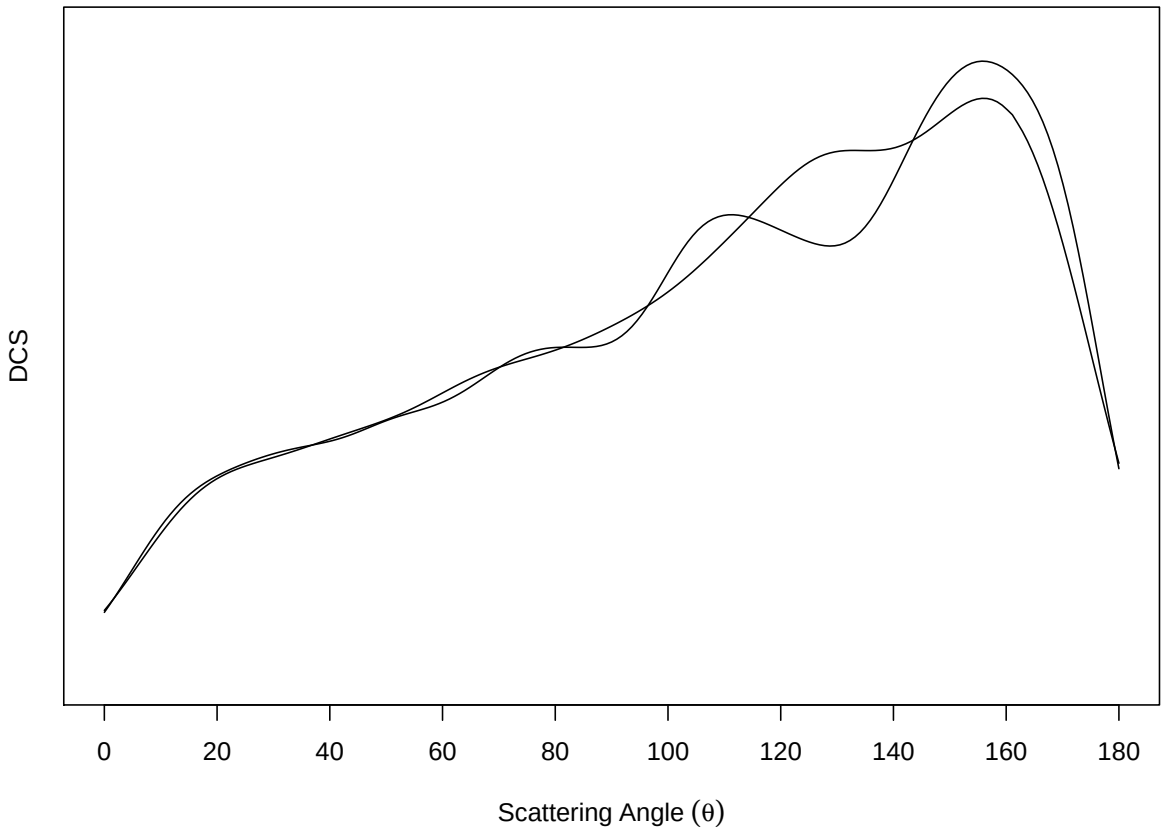

Figure 5.12: HD and H'H" angular distribution

mechanism and the reaction probability was against the classical proton-deuteron exchange mechanism. Finally, we propose that the reaction may undergo a "strip" process in which HD striped a proton from H_3^+ ion and then left away. When the impact parameter was small, the fragment containing D tended to bounce back, and in the large impact parameter region, the fragment containing D tended to move forward. Due to the ZPE "leaking" problem, some uncertainty may induced in our calculation. How to overcome the ZPE "leaking" problem in quasiclassical trajectory simulation remains a challenge for us and that is out next in QCT study. A tentative approach was proposed and more through work will be done in future.

Acknowledgments We thank the National Science Foundation(CHE-0431998, CHE-0443375) for financial support. Support for computational resources from ONR/DURIP is acknowledged. We thank Anne McCoy for her assistance in running the quantum Diffusion Monte Carlo calculations.

6 Vibrational Ground State Properties of H_5^+ and its Isotopomers from Diffusion Monte Carlo Calculations

Abstract

Diffusion Monte Carlo computations, with and without importance sampling, of the zero-point properties of H_5^+ and its isotopomers using a recent high accuracy global potential energy surface are presented. The global minimum of the potential possesses C_{2v} symmetry, but the calculations predict a D_{2d} geometry for zero-point averaged structure of H_5^+ with one H atom "in the middle" between two HH diatoms. The predicted zero-point geometries of the deuterated forms have H in the middle preferred over D in the middle and for a nonsymmetric arrangement of D atoms the preferred arrangement is one which maximizes the number of D as the triatomic ion. We speculate on the consequences of these preferences in scattering of H_2 + H_3^+ and isotopomers at low energies, such as those in the interstellar medium.

6 VIBRATIONAL GROUND STATE PROPERTIES OF H_5^+ AND ITS ISOTOPOMERS FROM DIFFUSION MONTE CARLO CALCULATIONS

6.1 DMC Study of the Ground State Structure of H_5^+ and its Isotopomers

6.1.1 Introduction

The cations H_n^+ and its isotopomers play important roles in the deuterium fractionation in interstellar space [34]. The first molecule of the series larger than a diatomic is H_3^+ whose identification in interstellar space was reported relatively recently [71] and since then it has been the subject of much experimental and theoretical work [61, 72–74]. H_5^+ is an even more challenging system. It has been observed experimentally since 1962 [75], but the experimental evidence is scarce and only low resolution spectra of a few vibrational states are available [76, 77]. Just as challenging is its theoretical description. Until recently, two potential energy surfaces were reported in the literature, relatively low accuracy diatomics in molecules [36] and a Shepard-type interpolation of several local force fields fitted to MP2 and CCSD(T) energies [37] In this work, we will use the recently reported potential energy surface of Xie et al., which is a generalized many-body expansion that has full permutational symmetry and was fitted to roughly 100000 different geometries using the CCSD(T) method and an aug-cc-pVTZ basis set [63]. These and other *ab initio* studies find that the global minimum is a C_{2v} structure; with, however, numerous low-lying saddle points. Using a diffusion Monte Carlo (DMC) strategy with no importance sampling the quantum zero-point energy (ZPE) was determined to be $7210 \pm 11 \mathrm{cm}^{-1}$ and the dissociation energy of H_5^+ into H_3^+ and H_2 as 6.33 kcal/mol. This dissociation energy is in very good agreement with one experiment [55] and just outside the error bars of another [57].

These encouraging results motivated us to undertake a complete characterization of the vibrational ground state of H_5^+ and its deuterated counterparts. We would like to answer the following questions: What is the symmetry of the H_5^+ ground state? Will D prefer the central position or one of the H_2 sites of DH_4^+? What is the preferred configuration of $D_2H_3^+$? These questions will be answered in the framework of DMC. The DMC without importance sampling has the advantage of making no assumptions about the nature of wave function. However, the extraction of distribution functions, which help us to characterize the ground state of the system, is not totally straightforward. That is not the case when using importance sampling, where the knowledge of the system, in the form of a reasonably derived trial wave function, is used to speed up the calculation and lower the variance of the estimated quantities. The extraction of the distribution functions in this case is indeed straightforward and is only limited by the quality of the trial wave function.

In this work, we perform a comparison between the quantities computed using diffusion Monte Carlo, with and without importance sampling, to determine the ground state properties of H_5^+ and some of its isotopomers. In the next section, we will have a brief description of the details of our calculations. In Sec. 6.1.3 , we present and discuss the results of our simulations, including some speculations on their implications for the reactive scattering mechanism. Concluding remarks are given in Sec. 6.1.4.

6.1.2 Methodology

In this work, we use two different diffusion Monte Carlo techniques to simulate the ground state properties of H_5^+ and its isotopomers. The first one is the more direct diffusion Monte Carlo approach [78] that directly simulates the Schröger equation in

imaginary time. In this method there is no trial wave function and the walkers are distributed according to $\Phi(R)$, the ground state wave function of the system. This is a powerful method to determine the ground state energy of the system. However, the extraction of structural properties, such as distribution functions, is not straightforward. To address this and also to present an independent approach we also employ importance sampling diffusion Monte Carlo [79]. This method also starts from the diffusion equation in imaginary time, but the walkers are distributed according to a "mixed" distribution [79, 80] $f(R) = \Phi(R)\Psi(R)$ where $\Phi(R)$ is the ground state of the system and $\Psi(R)$ is a trial wave function that represents a reasonable guess of the true ground state. This method has the advantage that the extraction of the structural properties is straightforward and we use linear and geometric extrapolated estimates as described in Ref. 80. The error in these estimates is proportional to the square of the difference between the ground state and the trial wave function. So, an accurate determination of the computed quantities and their variances will depend strongly on the accuracy of the wave function. In our calculation of the ground state of H_5^+, DH_4^+, $D_2H_3^+$, $D_3H_2^+$, and D_4H^+ we employed the following trial wave function that has been frequently used as a first approximation to the vibrational ground state of molecules as follows [81, 82]:

$$\Psi(R) = \exp\left(\sum_{\mu,\nu} \Delta S_\mu A_{\mu\nu} \Delta S_\nu\right), \tag{6.1}$$

where $A_{\mu\nu}$ are variational parameters and $\Delta S_\mu = q_\mu - q_\mu^0$, and q_μ and q_μ^0 are generalized coordinates and their equilibrium values, respectively. The parameters are optimized to minimize a linear combination of the energy and its variance.

To compute the expectation values of local operators that do not commute with

the Hamiltonian one could also use variational path integral [83] or reptation Monte Carlo methods [84]. However, our trial function is very accurate, as exemplified by the ZPE and their standard deviations, so we could accurately extract such quantities using the importance sampling DMC.

For each of the systems studied in this work 20000 walkers were propagated for 5000 steps of 1.0 a.u. for each of the ten DMC "trajectories" in the simulations without importance sampling. The importance sampling simulations propagated the same number of walkers for 20000 steps, each of 0.5 a.u, for five different trajectories.

6.1.3 Results and Discussion

H_5^+ The minimum of the potential energy surface [63] used in this work is of C_{2v} symmetry and represents a H_2 bonded to H_3^+ [see Fig. 6.1(a)]. However, the D_{2d} saddle point [Fig. 6.1(b)] is only 57 cm^{-1} above the global minimum [63]. Therefore, it is possible that the maximum amplitude of the ground state wave function may be either at the C_{2v} minima or the D_{2d} saddle point. To investigate this we will use DMC calculations, with and without importance sampling, to determine pair distribution functions and other diagnostics.

The trial wave function used in this work is symmetric with respect to the exchange of the central atom between the two equivalent C_{2v} minima. The DMC zero-point energy of H_5^+ using such a trial wave function as the starting point of the simulation was calculated as $7208 \pm 4 cm^{-1}$. This result is excellent with the previous result of $7210 \pm 11 cm^{-1}$ [63]. We have also computed the "exact" anharmonic dissociation energy of H_5^+ to be 6.37 ± 0.01 kcal/mol, in agreement with the result of Xie et al [63]. These first results show that both DMC implementations, one using a trial

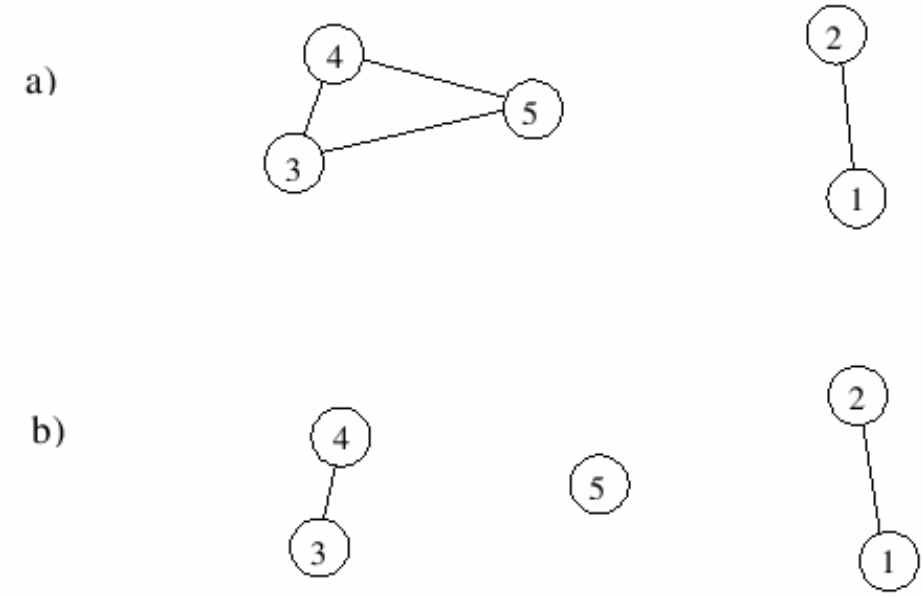

Figure 6.1: (a) C_{2v} global minimum of the PES of H_5^+. (b) D_{2d} saddle point of the PES of H_5^+.

wave function and importance sampling and the other using only walkers starting at a given configuration, yield the same ground state energies for this system. The issue now is whether we can answer questions about the ground state geometry of H_5^+ using the different approaches. To answer this we compute several distribution functions. First consider the overall HH pair distribution function, obtained with the importance sampling DMC, shown in Fig. 6.2. Also displayed are the different HH distances at the C_{2v} global minimum and at the lowest D_{2d} saddle point. One can clearly identify two peaks in the distribution function with the major one containing a shoulder. Moreover, as seen, these peaks/shoulders are in good agreement with the HH bond distances corresponding to the D_{2d} saddle point configuration and do not correspond to those at the C_{2v} minimum. This is our first indication of a symmetric D_{2d} ground state configuration.

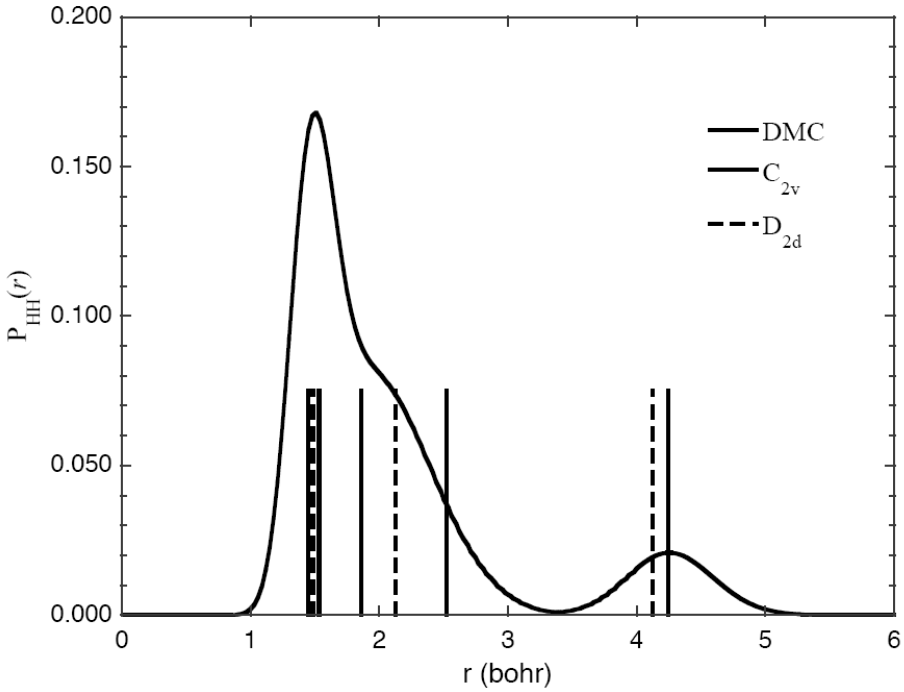

Figure 6.2: HH pair distribution function of H_5^+ from importance sampling simulations. The full continuous line is the extrapolated estimate of the pair distribution function. The vertical sticks represent the bond lengths at the C_{2v} global minimum (solid) and at the lowest D_{2d} (dashed) saddle point of the PES

A more definitive confirmation is obtained from the distribution function describing the position of the "central" atom along the principal axis with lower moment of inertia shown on Fig. 6.3. As one can see the distribution is symmetric about zero,

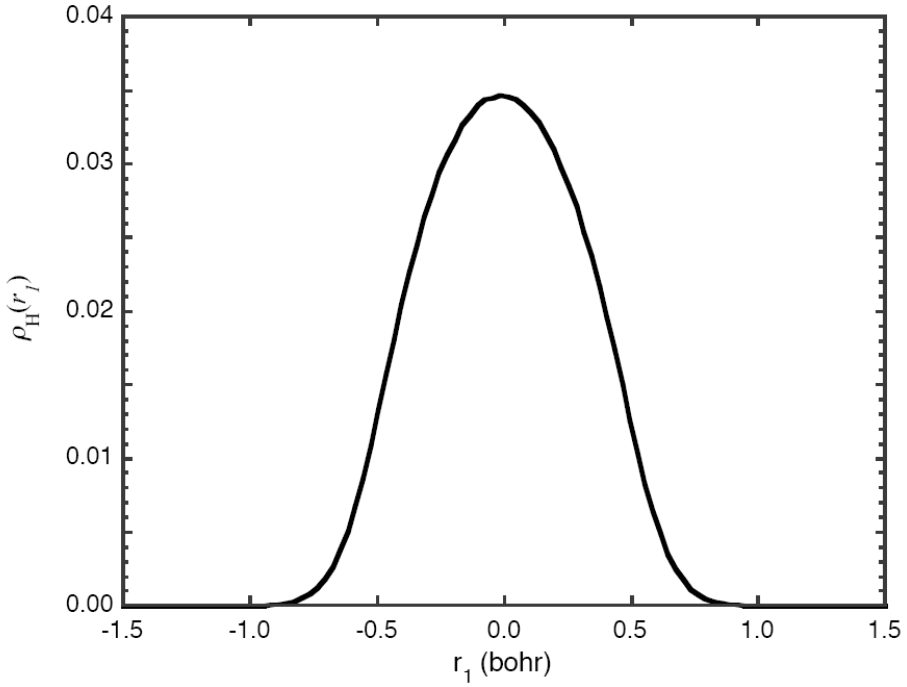

Figure 6.3: Distribution of the central H in H_5^+ along the principal axis of the lowest moment of inertia as obtained in the importance sampling simulations.

consistent with a ground state of D_{2d} symmetry. Next, consider the results from the DMC approach without importance sampling, namely, the distribution (over walkers) of the quantity $(r_{15}+r_{25}-r_{35}-r_{45})/2$ (refer to Fig. 6.1 for definition of indices). This is shown in Fig. 6.4. The distribution is centered at the origin consistent with a state of D_{2d} symmetry but not C_{2v} symmetry, confirming that indeed both approaches predict a D_{2d} ground state in which the largest probability is to find the proton in the center and not on one of the equivalent C_{2v} wells. One further piece of evidence supporting this conclusion is the average bond distances shown in Fig. 6.5. In the

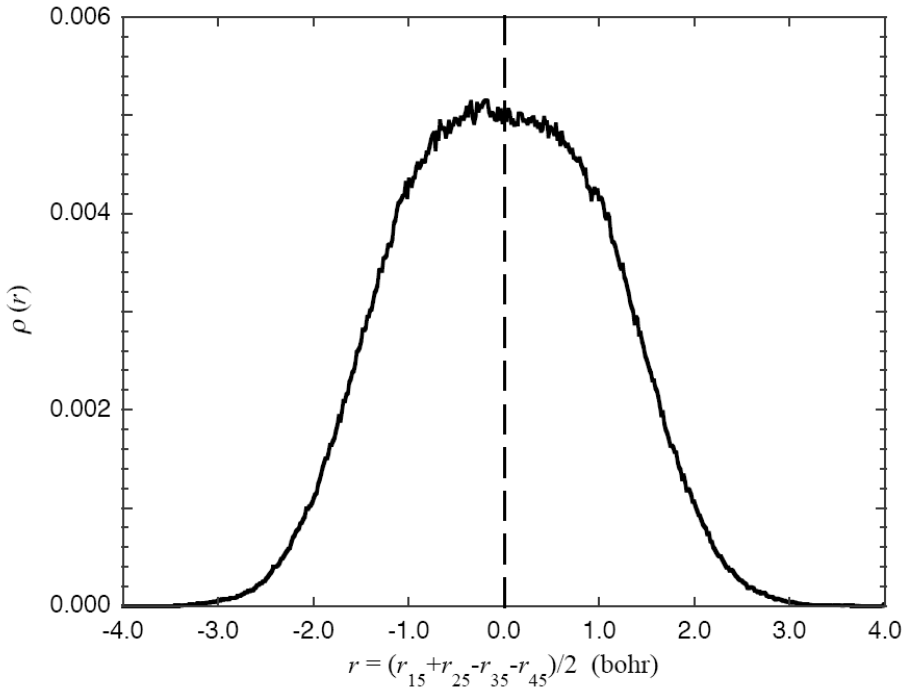

Figure 6.4: Distribution of the difference $(r_{15} + r_{25} - r_{35} - r_{45})/2$ as obtained in the DMC simulations, without importance sampling, of the ground state of H_5^+.

case of H_5^+ there are only three distinct values, namely, 1.55, 2.27, and 4.34 bohrs ($r_{13} = r_{23} = r_{14} = r_{24}$, not shown in the figure), which again is an indication of a D_{2d} ground state.

H_4D^+ We turn our attention to the single deuterated species to investigate how deuteration affects the geometry of the ground vibrational state. This is by itself an interesting issue; however, we are further motivated to investigate this because of the role of this complex in deuterium fractionation in interstellar space through the reaction $H_3^+ + HD \leftrightarrow H_2D^+ + H_2$. At the very low temperatures of the interstellar medium it is reasonable to assume that the (relatively weakly bound) H_4D^+ complex is formed as a transient intermediate. A further reasonable speculation is that the ground vibrational state is the dominant quantum state of this complex and thus our investigation of the properties of this state is further motivated by this possibility.

In our previous paper [63], a classical trajectory study of the unimolecular dissociation of the complex H_4D^+ into its fragments was carried out starting at the C_{2v} minimum and considering the three different initial complexes $H_3^+ \cdots HD$, $DH_2^+ \cdots H_2$, and $HHD^+ \cdots H_2$ (Notation: The central atom in Fig. 6.1 is the atom with the charge.) The branching ratios for various products were very different for these different initial configurations and it was noted there that a quantum distribution of the initial state very likely is quite different from these classical ones and we investigate that here.

One simple way to explore the three distinct possible arrangements for the atoms at the minimum is to perform a standard normal mode analysis at the C_{2v} minimum. This was done [63] and the results indicated that the $DH_2^+ \cdots HH$ is the most stable configuration, i.e., it is the one with the lowest harmonic ZPE and that the other two

are nearly degenerate. DMC calculations were done starting walkers from the three arrangements of the atoms and a single ZPE of $6826 \pm 15 \text{cm}^{-1}$ was reported; however, no exploration of the properties of the ground state wave function was done.

Table 6.1: ZPE (in cm^{-1}) of H_5^+ and its isotopomers obtained from DMC calculations, with and without importance sampling.

Species	D position	Importance sampling	No importance sampling	Comments
H_5^+		7208 ± 4	7213 ± 9	
H_4D^+	D: 4	6816 ± 2	6816 ± 7	e(D,1) [a]
	D: 5	6860 ± 1	6868 ± 11	c(D) [b]
$H_3D_2^+$	D: 1,2	6374 ± 1	6372 ± 5	e(D,1)
	D: 1,4	6420 ± 3	6422 ± 8	e(D,1)
	D: 4,5	6457 ± 1	6455 ± 5	c(d), e(D,1)
$H_2D_3^+$	D: 1,3,4	5980 ± 1	5979 ± 6	e(D,2) [c]
	D: 3,4,5	6000 ± 4	5998 ± 8	c(D), e(D,1)
	D: 1,4,5	6055 ± 1	6055 ± 7	c(D), e(D,2)
HD_4^+	D: 1,2,3,4	5533 ± 2	5535 ± 7	e(D,2)
	D: 1,2,3,5	5603 ± 7	5602 ± 8	c(D), e(D,2)
D_5^+		5151 ± 1	5154 ± 7	c(D), e(D,2)

[a] D atom(s) is (are) on one edge.
[b] One D atom is in the center position
[c] D atoms are on two edges.

We revisit these simulations using the importance sampling DMC and perform a careful analysis of the previous DMC results. In the same fashion, as was done previously, one can distinguish between the three distinct locations of the D, i.e., "in the middle" or "outside," in this case belonging to either the diatom or the triatom. In the importance sampling DMC a trial wave function of D_{2d} symmetry was used with D substituting for H in one of the H_2 sites or as the central atom. The lowest energy conformer has the deuterium in one of the H_2 sites and with the central H slightly closer to the DH molecule (see Tables 6.1 and 6.2, and Fig. 6.5). The ZPE for this conformation is $6816 \pm 2 \text{cm}^{-1}$, indicating that the conformer $DH_2^+ \cdots H_2$ is preferred

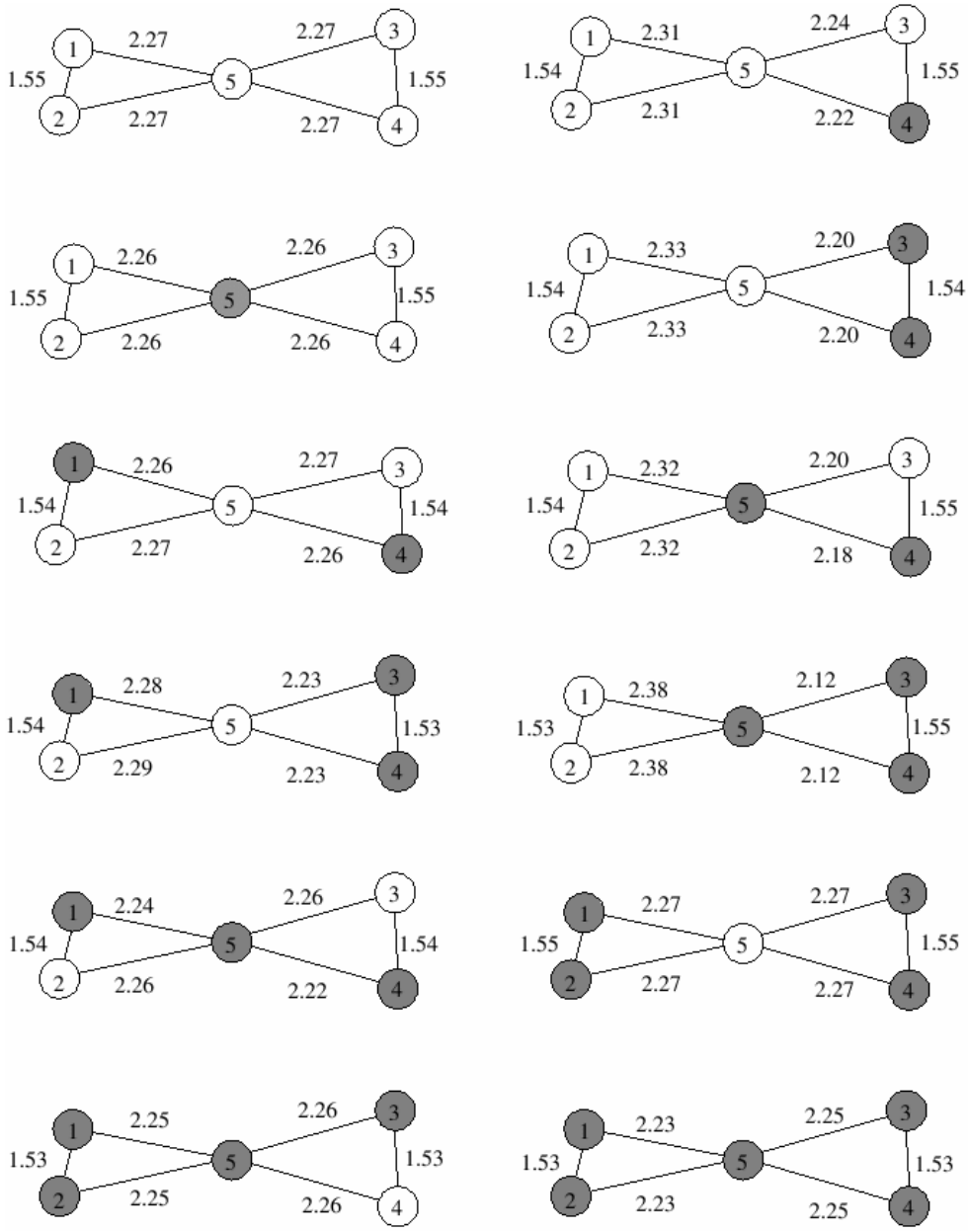

Figure 6.5: Geometry of the ground state of H_5^+ and its isotopomers. Also displayed are the geometries of other conformers of the same isotopomer. The open circles represent the H atoms and the gray circles represent the D.

over the $H_3^+ \cdots HD$ conformer. We confirmed this using a C_{2v} wave function that yields a ZPE of $6816 \pm 3\text{cm}^{-1}$ for $DH_2^+ \cdots H_2$ and $6819 \pm 4\text{cm}^{-1}$ for $H_3^+ \cdots HD$. For the $HHD^+ \cdots H_2$ complex the computed ZPE is $6860 \pm 1\text{cm}^{-1}$. This indicates that the conformer with D in the center is the least probable, based on the calculations of the ZPE.

These findings may have important consequences for the reaction mechanism and branching ratios of certain reactions where more than one product is possible. This is discussed next where results are presented for other isotopomers.

Higher Deuterated Isotopomers and Their Conformers In this subsection we present a summary of the results of our simulations for H_5^+ and its isotopomers, up to D_5^+. In Table 6.1 we present the ZPE obtained for a given conformer, where applicable, of the indicated isotopomer. From a quick inspection of the table one can determine that in all deuterated forms DH_4^+, $D_2H_3^+$, $D_3H_2^+$, and D_4H^+ the lowest energy form has the H^+ at the central position. Figure 6.5 presents the DMC computed expectation values of the bond distances of each of the isotopomers and its different conformers. The filled circles represent the D atoms. The isotopomers are ordered in increasing order of deuteration and each isotopomer is ordered by increasing energy. The geometries of all the isotopomers are slight distortions from the reference D_{2d} structure. The trend is that for the more symmetric arrangement of atoms the geometry is nearly an ideal D_{2d}, and for the less symmetric arrangements the preference is to have more deuterium in the triatom than in the diatom. The most stable conformer of D_4H^+ has H^+ in the middle, the other conformer with a deuterium in the central position can be viewed as D_3^+ bonded to DH instead of HD_2^+ bonded to D_2, although the difference in bond lengths is small. In summary, we have

found that for all mixed isotopomers the ground vibrational state has a preference for H^+ in the middle.

Table 6.2: ZPE of each of the possible fragmentation channels for unimolecular dissociation of H_5^+ and its isotopomers.

Fragments	ZPE (cm^{-1})
$H_3^+ + H_2$	9438 ± 1
$DH_2^+ + H_2$	9054 ± 1
$H_3^+ + DH$	9150 ± 1
$H_3^+ + D_2$	8808 ± 1
$DH_2^+ + DH$	8766 ± 2
$D_2H^+ + H_2$	8636 ± 2
$DH_2^+ + D_2$	8424 ± 1
$D_2H^+ + DH$	8349 ± 1
$D_3^+ + H_2$	8189 ± 2
$D_2H^+ + D_2$	8006 ± 2
$D_3^+ + DH$	7901 ± 1
$D_3^+ + D_2$	7557 ± 2

For completeness we have also computed the ZPE of each of the possible pairs of fragments in unimolecular dissociation. These energies are presented in Table 6.2. Table 6.3 contains the unimolecular dissociation energies of H_5^+ and all of the isotopomers displayed in Fig. 6.5. We consider only the dissociation into the lower energy pair of products.

We conclude this section with some speculations on the effect of the character of the vibrational ground state on the reaction mechanism and branching of products in the reactions between H_3^+ and its various isotopomers with H_2, HD, and D_2. Here, we want to shed some light on these reactions using only the information from the DMC computed energies and structures of the five atom complex and the separated diatom and triatom. We do not consider the symmetry and nuclear spin restrictions

Table 6.3: Dissociation energies for unimolecular dissociation of H_5^+ and its isotopomers.

Reaction channel	D_0 (kcal/mol)
$H_3^+ \cdots H_2 \rightarrow H_5^+ + H_2$	6.37 ± 0.01
$DH_2^+ \cdots H_2 \rightarrow DH_2^+ + H_2$	6.40 ± 0.01
$H_2D^+ \cdots H_2 \rightarrow H_2D^+ + H_2$	6.27 ± 0.01
$H_3^+ \cdots D_2 \rightarrow H_3^+ + D_2$	6.96 ± 0.01
$H_3^+ \cdots D_2 \rightarrow D_2H^+ + H_2$	6.47 ± 0.02
$HD_2^+ \cdots H_2 \rightarrow D_2H^+ + H_2$	6.73 ± 0.01
$H_2D^+ \cdots DH \rightarrow D_2H^+ + DH$	6.71 ± 0.01
$D_2H^+ \cdots DH \rightarrow D_2H^+ + DH$	6.77 ± 0.01
$D_3^+ \cdots H_2 \rightarrow D_3^+ + H_2$	6.94 ± 0.01
$HD_2^+ \cdots DH \rightarrow HD_2^+ + DH$	6.56 ± 0.01
$D_2H^+ \cdots D_2 \rightarrow D_2H^+ + D_2$	7.07 ± 0.01
$D_3^+ \cdots DH \rightarrow D_3^+ + DH$	6.57 ± 0.01
$D_3^+ \cdots D_2 \rightarrow D_3^+ + D_2$	6.20 ± 0.01

in this system and just focus on the properties of the ground state wave function of the relevant complex. First we have noted that the ground vibrational state of the complex prefers to have a D_{2d} or somewhat distorted D_{2d} geometry. This is a saddle point on the bare potential energy surface (PES) that corresponds to what is referred to in the literature as the "hopping" reaction mechanism [61, 62]. To be specific, consider the H_4D^+ complex that arises in the reaction $H_3^+ + HD$. In this case, based on the geometry of the zero-point state (cf. Fig. 6.5) the proton "hops" preferentially because it occupies the middle position and the preferred products would be H2+H2D+. This qualitative conclusion is in accord with experiment [62].

Conclusions for all isotopomers are summarized graphically in Fig. 6.6. As can be seen in Fig. 6.6, there are basically ten nontrivial combinations of H_3^+ (and its isotopomers) with H_2 (and its isotopomers). These combinations (we will call them separated molecules from now on) are at the top in each of the four panels in Fig. 6.6.

The difference in zero-point energies of the various triatom cation plus neutral diatom combinations are of importance in discussions of the possible thermal equilibrium of these species in the interstellar medium [62]. Here, we provide their energies based on the DMC calculations on our global potential energy surface. Below each separated pair of molecules are the various intermediate complexes for the scattering reactions. The importance of these intermediates is that they connect all the separated molecules and provide the possible pathways for the reactions transforming one pair of molecules to another. In this discussion we assume that the two separated molecules (one triatom plus a diatom) will join to form one of the complexes displayed in Fig. 6.4 and only the atom in the middle can be exchanged between the outer diatoms.

There is a wealth of information in Fig. 6.6 and a discussion of all possible reactions will be repetitive. So, we will restrict our discussion to reactions where more than one product can be formed and for very low collision energies (appropriate for the interstellar medium), where it is reasonable to assume that collision complex is formed dominantly in the ground vibrational state. Consider first the reaction $H_3^+ + D_2$. From Fig. 6.6 the preferred reaction channel is the proton "hopping" one, i.e., $HD_2^+ + H_2$. Moreover, of course for the reverse reaction $HD_2^+ + H_2$ the $H_3^+ + D_2$ products are preferred over the $H_2D^+ + HD$ ones. Next, consider the $D_3^+ + H_2$ reaction. This is an interesting case because the lowest energy configuration $D_2H^+ \cdots HD$ would require a high barrier rearrangement of the atoms and so is "forbidden." Instead, from Fig. 6.6 the $D_3^+ \cdots H_2$ configuration is the likely one and the likely products are $H_2D^+ + D_2$. (Note this again is the "hopping" mechanism.) The reactions $HD_2^+ + HD$ and $H_2D^+ + D_2$ are also quite interesting because either D^+ or H^+ could hop to make the corresponding set of products. Figure 6.6 indicates that H^+ is more likely to

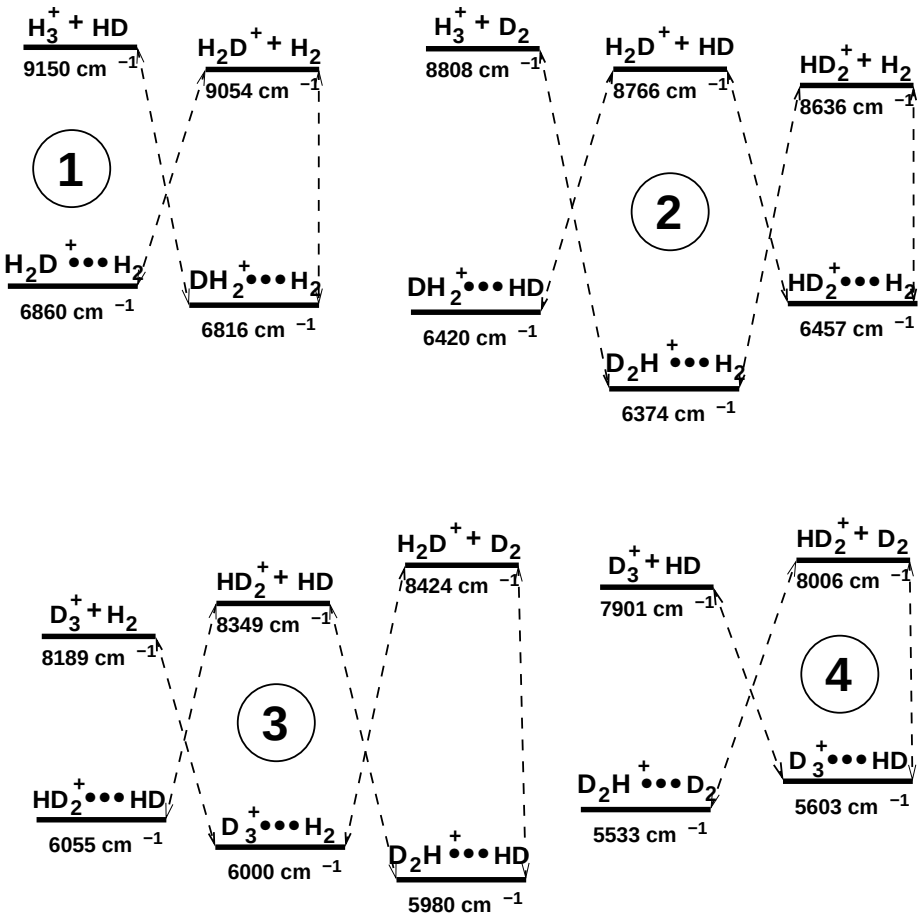

Figure 6.6: Energy landscape of the reactants, intermediate complexes, and products for scattering reactions of H_3^+ and H_2 and isotopomers.

hop since it is in the middle of the lowest energy conformer $D_2H^+ \cdots HD$ and gives rise to the products $D_2 + H_2D^+$ and $HD + HD_2^+$, respectively. In both reactions the preferred direction is the one that adds a deuterium to the triatom. Analysis of the reactions $H_3^+ + HD \leftrightarrow H_2D^+ + H_2$ and $D_3^+ + HD \leftrightarrow HD_2^+ + D_2$ leads to similar conclusions, that is, the products $H_2D^+ + H_2$ are favored over $H_3^+ + HD$ and $D_3^+ + HD$ are favored over $HD_2^+ + D_2$.

From a purely thermodynamic point of view, that is, considering only the energy differences between the reactants and the products and disregarding the role of the intermediate, the conclusions are even stronger, e.g., $H_2D^+ + H_2$ is favored over $H_3^+ + HD$. For the reactions involving two deuterium atoms the most likely products are $HD_2^+ + H_2$, then $H_2D^+ + HD$, and finally $H_3^+ + D_2$. The same conclusions will be drawn for the reactions involving 3 and 4 deuterium.

6.1.4 Summary and Conclusions

We have presented an extensive analysis of the ground state properties of H_3^+ and its isotopomers using two implementations of DMC, with and without importance sampling. The energies and structural properties predicted in both approaches are in excellent agreement with each other. The ground state of H_5^+ is predicted to have an ideal D_{2d} symmetry, whereas the isotopomers are found to be only slightly distorted from the H_5^+ reference geometry. As expected, the ZPE decreases as the number of deuterium in the isotopomer increases. Both approaches predict that the H prefers to be in the middle and there is a tendency of maximizing the number of deuterium in the triatomic ion. Implications of the ground state conformations on low energy reactive scattering were discussed. In particular, our simulations support

the experimental results of large DH_2^+ to H_3^+ ratio in interstellar space. We have also concluded that the ratio D_2H^+ to DH_2^+ should also be large, while the ratio of D_3^+ to D_2H^+ should also be large. These conclusions are in agreement with the conclusions from chemical model calculations which predict that $n(H_3^+) \leq n(DH_2^+) \leq n(D_2H^+) \leq n(D_3^+)$ [61, 85].

Acknowledgments We thank the National Science Foundation CHE-0431998, CHE-0443375, and CHE-0446527 for financial support. Support for computational resources from ONR/DURIP is acknowledged. P. A. thanks the hospitality of the Emerson Center for Scientific Computation and Department of Chemistry at Emory University during his visit to Atlanta.

6.2 Additional Information

There are mainly two lowest energy configurations as shown in Fig. 6.7 for H_5^+ on the potential energy surface (PES). The lowest one geometry in C_{2v} symmetry and the second lowest geometry is in D_{2d} symmetry. The main difference between these two configuration is the position of the middle proton, and the energy difference is about 60 cm^{-1}. The problem is what the real symmetry of the H_5^+ is in its ground state and its various isotopomers. Diffusion Monte Carlo (DMC) method was used to explore the ground state of H_5^+.

The Zero-Point Energies (ZPE) for various H_5^+ isotopomers are listed in Table 6.4. It is clear from the table that

- The more D atoms, the lower the ZPE
- The configurations for D in the center have higher ZPE than those D atoms on

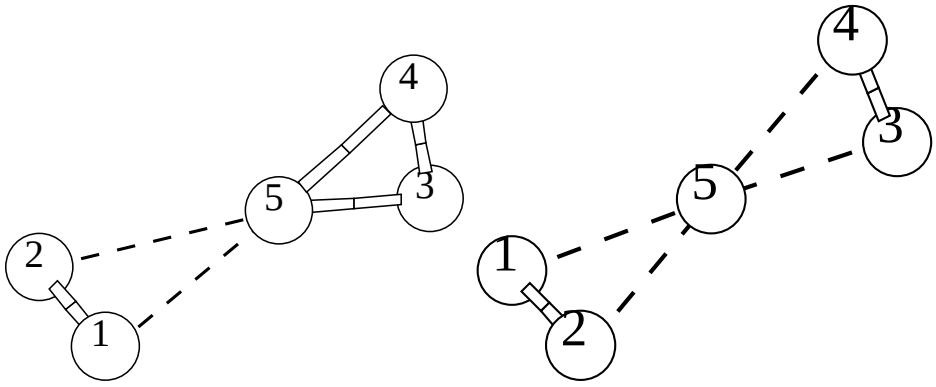

(a) 1-C_{2v} (b) 2-D_{2d}

Figure 6.7: Two lowest energy configurations of H_5^+. (a) is the global minimum configuration and (b) is the second lowest structure.

the edge.

- The more edges D atoms occupy, the high the ZPE.
- D atom center effect is great than edge effect.
- There is no significant difference if the central atom is close to one edge or the other. (The geometry H5+ may be in D_{2d} symmetry)

To have a clear picture of the central atom position, part of the bond lengths distribution in H_5^+ and its various isotopomers are plotted in the following figures (Fig. 6.8, Fig. 6.9, Fig. 6.10, Fig. 6.11, Fig. 6.12), and the expectation value of the all the interested bond length are shown in Table 6.2.

Table 6.4: Zero-Point energy of various H_5^+ isotopomers

Isotope	D Position	ZPE (cm^{-1})	Comments
H_5^+		7213 ± 9	
D_5^+		5154 ± 7	c(D)[1], e(D,2)[2]
HD_4^+	D: 1, 2; 3, 4	5535 ± 7	e(D,2)
HD_4^+	D: 2; 3, 4; 5	5599 ± 7	c(D), e(D,2)
HD_4^+	D: 1; 3, 4; 5	5604 ± 9	c(D), e(D,2)
HD_4^+	D: 1, 2; 4; 5	5602 ± 6	c(D), e(D,2)
HD_4^+	D: 1, 2; 3; 5	5604 ± 11	c(D), e(D,2)
H_4D^+	D: 1	6817 ± 5	e(D,1)
H_4D^+	D: 2	6818 ± 7	e(D,1)
H_4D^+	D: 3	6815 ± 9	e(D,1)
H_4D^+	D: 4	6813 ± 5	e(D,1)
H_4D^+	D: 5	6868 ± 11	c(D)
$H_2D_3^+$	D: 1, 2; 3	5976 ± 6	e(D,2)
$H_2D_3^+$	D: 1; 3, 4	5981 ± 6	e(D,2)
$H_2D_3^+$	D: 3, 4; 5	5995 ± 6	c(D), e(D,1)
$H_2D_3^+$	D: 1, 2; 5	6000 ± 6	c(D), e(D,1)
$H_2D_3^+$	D: 1; 3; 5	6055 ± 7	c(D), e(D,2)
$H_3D_2^+$	D: 3, 4	6372 ± 5	e(D,1)
$H_3D_2^+$	D: 2; 4	6422 ± 8	e(D,2)
$H_3D_2^+$	D: 4; 5	6454 ± 7	c(D),e(D,1)
$H_3D_2^+$	D: 2; 5	6456 ± 4	c(D),e(D,1)

[1] one D atom is in the center position

[2] there are two edges that have D atom

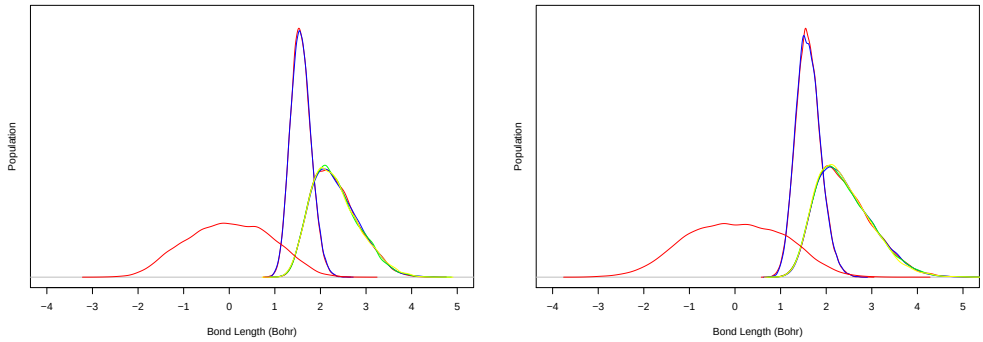

(a) D_5^+ (b) H_5^+

Figure 6.8: H_5^+ and D_5^+ bond length distributions. The broad red curve is the *rd* as in Table 6.2 distribution, the red curve in the middle is the bond r_{12} length distribution, the blue curve in the middle is the bond r_{34} length distribution, the red curve on the right side is the bond r_{15} length distribution, the right blue curve is the bond r_{25} length distribution, the green curve is the bond r_{35} length distribution, and the yellow curve is the bond r_{45} length distribution.

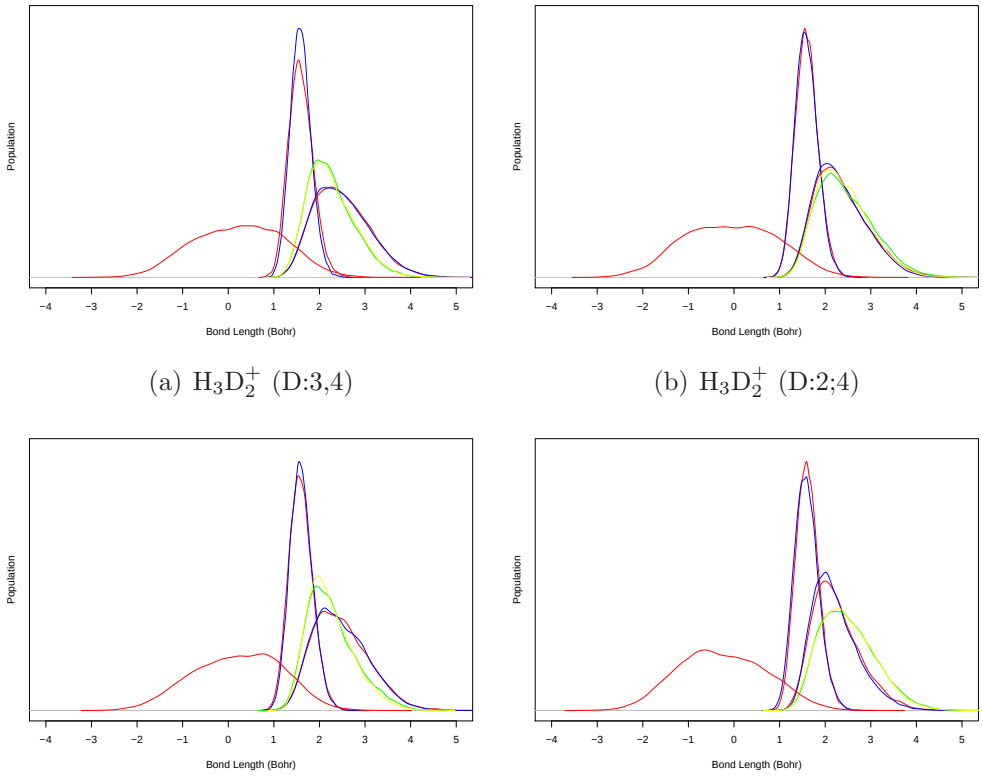

(a) $H_3D_2^+$ (D:3,4)

(b) $H_3D_2^+$ (D:2;4)

(c) $H_3D_2^+$ (D:4;5)

(d) $H_3D_2^+$ (D:2;5)

Figure 6.9: Various bond length distributions in $H_3D_2^+$, the D atom positions are indicated in the sub-figure labels and the labels for the curves are the same as in Fig. 6.8.

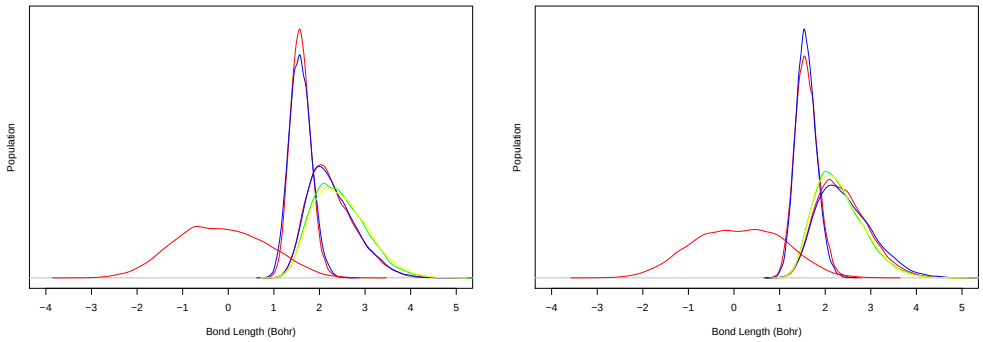

(a) $H_2D_3^+$ (D:1,2;3)

(b) $H_2D_3^+$ (D:1;3,4)

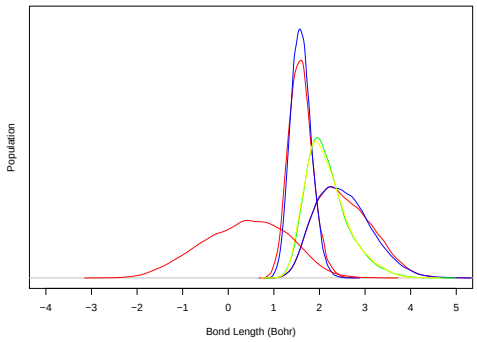

(c) $H_2D_3^+$ (D:3,4;5)

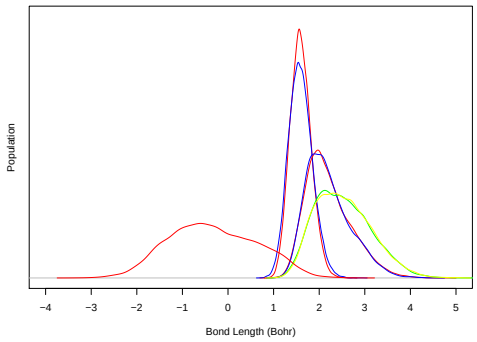

(d) $H_2D_3^+$ (D:1,2;5)

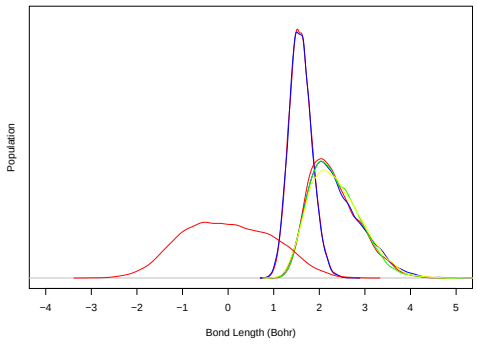

(e) $H_2D_3^+$ (D:1;3;5)

Figure 6.10: Various bond length distribution in $H_2D_3^+$, the D atom positions are indicated in the sub-figure label and the labels for the curves are the same as in Fig. 6.8.

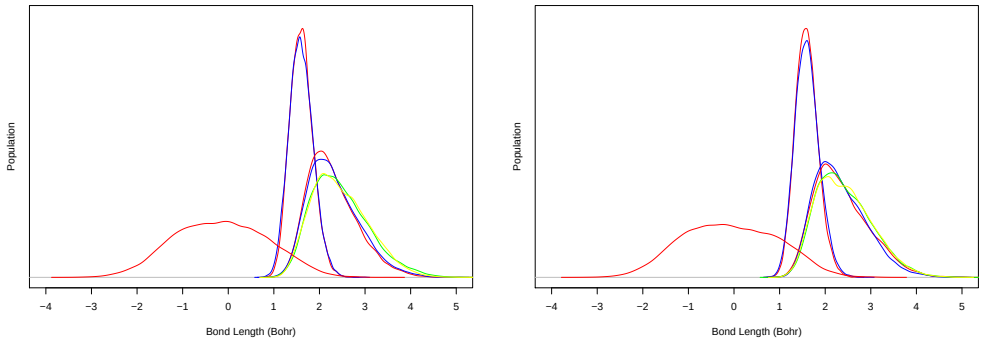

(a) H_4D^+ (D:1)

(b) H_4D^+ (D:2)

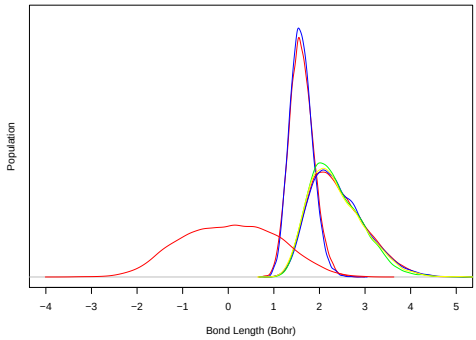

(c) H_4D^+ (D:3)

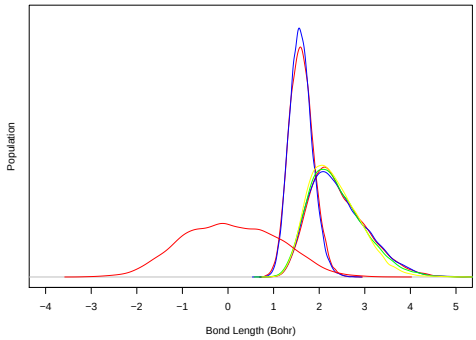

(d) H_4D^+ (D:4)

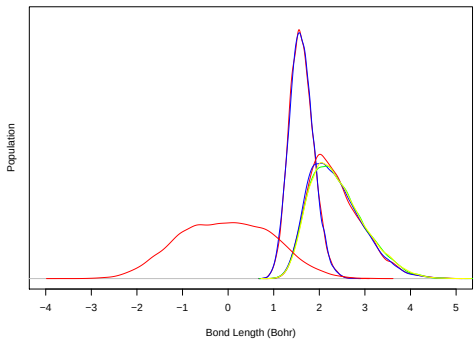

(e) H_4D^+ (D:5)

Figure 6.11: Various bond length distributions in H_4D^+, the D atom positions are indicated in the sub-figure labels and the labels for the curves are the same as in Fig. 6.8.

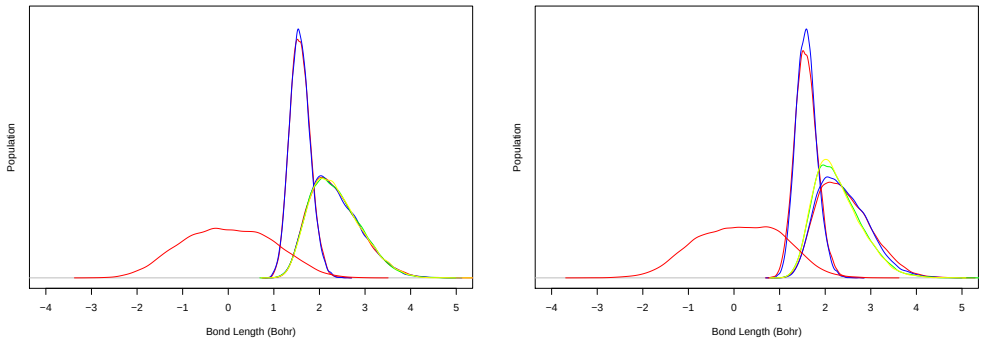

(a) HD_4^+ (D:1,2;3,4)

(b) HD_4^+ (D:2;3,4;5)

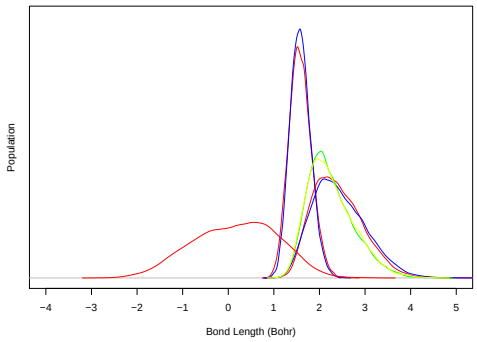

(c) HD_4^+ (D:1;3,4;5)

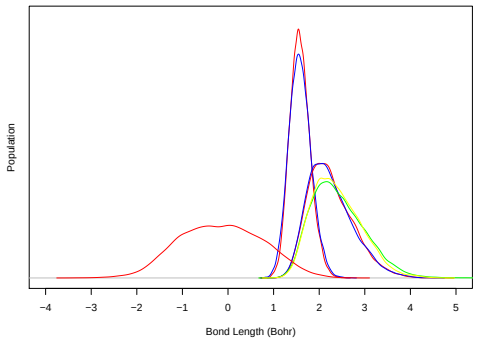

(d) HD_4^+ (D:1,2;4;5)

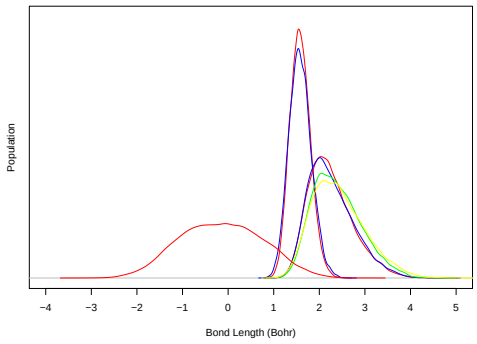

(e) HD_4^+ (D:1,2;3;5)

Figure 6.12: Various bond length distributions in HD_4^+, the D atom positions are indicated in the sub-figure labels and the labels for the curves are the same as in Fig. 6.8.

Table 6.5: Statistical bond lengths (Bohr) of H_5^+ and its isotopomers from DMC simulation.

	D Position	r_{12}	r_{34}	r_{15}	r_{25}	r_{35}	r_{45}	r_{13}	r_{14}	r_{23}	r_{24}	rd[1]
D_5^+		1.5740	1.5744	2.3336	2.3333	2.3188	2.3191	4.4030	4.4057	4.4035	4.3967	0.0146
HD_4^+	D: 1, 2; 3, 4	1.5763	1.5747	2.3435	2.3458	2.3509	2.3484	4.4083	4.4076	4.4112	4.4079	-0.0050
HD_4^+	D: 2; 3, 4; 5	1.5834	1.5855	2.4478	2.4089	2.2632	2.2612	4.4545	4.4456	4.4182	4.4183	0.1662
HD_4^+	D: 1; 3, 4; 5	1.5803	1.5863	2.4179	2.4452	2.2474	2.2517	4.4155	4.4160	4.4340	4.4382	0.1820
HD_4^+	D: 1, 2; 4; 5	1.5835	1.5830	2.2652	2.2655	2.4327	2.4010	4.4391	4.4158	4.4367	4.4153	-0.1515
HD_4^+	D: 1, 2; 3; 5	1.5853	1.5811	2.2564	2.2553	2.4085	2.4412	4.4138	4.4397	4.4117	4.4398	-0.1690
$H_2D_3^+$	D: 1, 2; 3	1.5817	1.5867	2.3041	2.3027	2.3993	2.4320	4.4141	4.4421	4.4153	4.4416	-0.1123
$H_2D_3^+$	D: 1; 3, 4	1.5885	1.5819	2.3960	2.4304	2.3136	2.3128	4.4187	4.4213	4.4476	4.4489	0.1000
$H_2D_3^+$	D: 3, 4; 5	1.5871	1.5965	2.5284	2.5261	2.1865	2.1835	4.4592	4.4456	4.4470	4.4545	0.3423
$H_2D_3^+$	D: 1, 2; 5	1.5957	1.5870	2.1897	2.1916	2.5259	2.5306	4.4569	4.4588	4.4554	4.4592	-0.3376
$H_2D_3^+$	D: 1; 3; 5	1.5924	1.5942	2.3379	2.3714	2.3331	2.3653	4.4229	4.4418	4.4432	4.4659	0.0055
$H_3D_2^+$	D: 3, 4	1.5956	1.5903	2.4976	2.4994	2.2578	2.2576	4.4592	4.4621	4.4586	4.4605	0.2407
$H_3D_2^+$	D: 2; 4	1.5936	1.5934	2.3866	2.3578	2.3906	2.3615	4.4797	4.4491	4.4480	4.4309	-0.0038
$H_3D_2^+$	D: 4; 5	1.5961	1.6056	2.4714	2.4707	2.2807	2.2449	4.4799	4.4582	4.4816	4.4533	0.2083
$H_3D_2^+$	D: 2; 5	1.6077	1.5952	2.2743	2.2432	2.4739	2.4717	4.4761	4.4753	4.4599	4.4539	-0.2140
H_4D^+	D: 1	1.6034	1.6002	2.2950	2.3283	2.4643	2.4625	4.4624	4.4558	4.4833	4.4901	-0.1517
H_4D^+	D: 2	1.6002	1.6016	2.3409	2.3135	2.4513	2.4497	4.4887	4.4842	4.4639	4.4677	-0.1233
H_4D^+	D: 3	1.6025	1.6019	2.4472	2.4478	2.3130	2.3432	4.4637	4.4822	4.4599	4.4869	0.1194
H_4D^+	D: 4	1.6028	1.6016	2.4482	2.4492	2.3431	2.3122	4.4833	4.4617	4.4876	4.4601	0.1211
H_4D^+	D: 5	1.6097	1.6092	2.3706	2.3730	2.3773	2.3805	4.4753	4.4797	4.4814	4.4810	-0.0071
H_5^+		1.6103	1.6096	2.3907	2.3934	2.4095	2.4078	4.4928	4.4886	4.4908	4.4931	-0.0166

[1] $\mathrm{rd} = (r_{15} + r_{25} - r_{35} - r_{45})/2$

6 VIBRATIONAL GROUND STATE PROPERTIES OF H_5^+ AND ITS ISOTOPOMERS FROM DIFFUSION MONTE CARLO CALCULATIONS

From all these bond length distribution for H_5^+ different isotopomers, it is clear that for the ground H_5^+ and D_5^+, the central H or D atom tends to be in the middle of two H_2 (D_2) fragments. From the bond length distribution, we can also see that the D atoms tend to aggregate together and also the H atoms tends join the fragment with more D atoms.

7 Quasiclassical Trajectory Study of the Reaction $H + CH_4(\nu_3 = 0, 1) \rightarrow CH_3 + H_2$ Using a New *ab initio* Potential Energy Surface

Abstract

Detailed quasiclassical trajectory calculations of the reaction H + $CH_4(\nu_3 = 0, 1) \rightarrow CH_3 + H_2$ using a slightly updated version of a recent *ab initio*-based CH_5 potential energy surface [X. Zhang, B. Braams and J.M. Bowman, J. Chem. Phys. **124**, 021104 (2006)] are reported. The reaction cross sections are calculated at initial relative translational energies of 1.52 eV, 1.85 eV and 2.20 eV in order to make direct comparison with experiment. The relative reaction cross section enhancement ratio due to the excitation of the C-H asymmetric stretch varies from 2.2 to 3.0 over this energy range, in good agreement with the experimental result of 3.0 ± 1.5 [J.P. Camden, H.A. Bechtel, D.J. Akeny Brown and R.N. Zare, J. Chem. Phys. **123**, 134301 (2005)]. The lab-frame speed and center-of-mass angular distributions of CH_3 are calculated as are the vibrational and rotational distributions of H_2 and CH_3. We confirm that this reaction occurs with a combination of stripping and rebound mechanisms by presenting the impact parameter dependence of these distributions and also by direct examination of trajectories.

7 QUASICLASSICAL TRAJECTORY STUDY OF THE REACTION H + $CH_4(\nu_3 = 0, 1) \rightarrow CH_3 + H_2$ USING A NEW *AB INITIO* POTENTIAL ENERGY SURFACE

7.1 Introduction

The reaction of hydrogen with methane plays a central role in experimental and theoretical reaction kinetics and dynamics. Much of the background literature related to this reaction has recently appeared in an important series of papers reporting experimental and theoretical investigations of this reaction (actually $H+CD_4$) at hyper-thermal collision energies (1.5 - 2.0 eV) [86–88]. In this work direct-dynamics quasiclassical trajectory (QCT) calculations, based on the DFT B3LYP/6-31G** energies and gradients, were able to capture the features seen experimentally. This level of theory predicts a barrier for the abstraction that is roughly 5 kcal/mol below the accurate result; however, at the high energies considered this level of error is evidently not serious.

One conclusion of these studies was the inadequacy of two existing global, analytical potential energy surfaces (PES) to describe the experimental findings, which included angular and laboratory speed distributions of the products. These PESs are due to Jordan and Gilbert (JG) [89] and Espinosa-García (EG) [90]. Both utilize an analytical form based on "LEPS" expressions with parameters determined to approximately reproduce *ab initio* properties of the abstraction saddle point and known properties of the reactants and products. Of the two PESs the EG one is more realistic since it was based on more recent, accurate *ab initio* saddle point calculations and it also corrected a symmetry-deficiency of the JG PES.

Although the EG PES is a significant improvement over the JG one, the EG PES barrier height of 12.9 kcal/mol is low compared to the most accurate *ab initio* value of 14.93 kcal/mol reported recently by Wu *et al.* [91, 92]. Those authors obtained a PES limited to the region of the abstraction saddle point based on CCSD(T)/cc-

pVTZ/cc-pVQZ calculations and estimated the error due to the basis set as less than 0.1 kcal/mol. They used this limited PES in accurate quantum calculations of the thermal rate constant. Prior to that calculation of the rate constant, the most extensive high-level study of the potential and rate constant was reported by Pu and Truhlar [93]. Those authors presented a number of so-called "implicit" PESs with fitted "reaction parameters" and calculated the thermal rate constant over a wide temperature range using multi-dimensional tunneling in the small curvature tunneling approximation. They concluded that the barrier height is 14.8 kcal/mol, in good agreement with the calculations of Wu *et al.* mentioned above.

Recently, we reported a global PES based on accurate fitting of roughly $20,000$ electronic energies obtained with CCSD(T)/aug-cc-pVTZ calculations [94]. We also reported a small set of QCT calculations for the H + CD_4 reaction using this PES and found agreement (at least semi-quantitative) with the DFT direct-dynamics results.

We have refined this potential, which we refer to as ZBB1, by adding more *ab initio* data and will report two new PESs here, which we denote as ZBB2 and ZBB3. ZBB2, which contains more data in the regions of the two van der Waals minima, is used in the QCT calculations. ZBB3 contains these data as well as additional energies to more accurately describe the exchange saddle point. While this property of the PES is not of direct interest here, for completeness we briefly present the properties of this PES. ZBB3 was completed after the QCT calculations using ZBB2 were done. We have re-done some QCT calculations at one energy using ZBB3 and the results agree very well with those done with ZBB2. (We will present that comparison in detail below.)

The major focus of this paper is the hyper-thermal collisions of H with CH_4 in

the ground vibration/rotation state and also in the first excited asymmetric C-H stretch state, *i.e.*, CH_4 ($\nu_3 = 1$), also in the ground rotational state. Our interest is to make direct comparisons with recent experiments of Zare and co-workers [95, 96]. This group determined several distributions of the products and were also able to determine the relative enhancement of the reaction cross section due to excitation of the asymmetric C-H stretch. We also examine the details of the reaction mechanism of H + CH_4; however, this work basically confirms the QCT results already presented by Schatz and co-workers [86–88], albeit for the H + CD_4 reaction in the ground vibrational state.

The paper is organized as follows. In the next section we discuss the new PESs and examine and compare properties of the abstraction saddle points and reactants and products with previous high-level calculations and experiment (for reactants and products). Following that we give some details of the quasiclassical trajectory calculations and also the procedure and tests to prepare CH_4 in the excited asymmetric stretch state. In section 7.3 we present our results and comparison with experiment. The discussion in that section focuses on the dependence of the scattering dynamics on the impact parameter. We give a summary and conclusions in the final section.

7.2 Calculations

7.2.1 Potential Energy Surface

As noted already the PES used in the QCT calculations here is a slight refinement of the PES reported by Zhang, Braams and Bowman [94]. The new PES contains additional *ab initio* energies, calculated with the same method and basis (RCCSD(T)/aug-cc-pVTZ) as before, at more configurations. The details of constructing the PES were

given elsewhere [43, 63, 94] and here we just show some of the main features of this new PES, which as noted above is denoted ZBB2. Another important property of all the ZBB PESs is the invariance with respect to any permutation of the five H atoms. The advantage of this property is that the reaction can occur with any H atom of CH_4. The details of PES permutation invariance are described elsewhere [43, 63].

The relevant properties of ZBB2 are given in Tables 7.2.1 and 7.2.1 where they are compared with recent high-level *ab initio* calculations of Wu *et al.* [91] and other sources, as indicated. In Table 7.2.1 H' refers to the abstracted H-atom and H" to the reacting H-atom. As seen the energetics and structures of the reactants, abstraction saddle point and products are precisely fitted by the PES. There are slight differences with our previous PES, [94] ZBB1, mainly in some of the normal mode frequencies. Also ZBB2 provides a better description of the van der Waals minima than ZBB1. The reactant vdW minima is -0.12 kcal/mol relative to the reactants H + CH_4 and 2.68 kcal/mol for the product vdW minima. These energies compare well with those reported by Wu *et al.* [91] using an aug-cc-pVTZ basis, i.e., -0.10 and 2.58 kcal/mol, respectively.

As is well known the abstraction saddle point has a collinear CH'H" configuration. The collinear, rebound reaction mechanism is shown in Fig. 7.1. This figure also illustrates the stripping mechanism which is now known to play an important role at hyper-thermal collision energies. These two mechanisms have been found in the direct-dynamics DFT calculations reported by Camden *et al.* to explain features observed for the hyper-thermal reactive scattering of H + CD_4 [86–88]. We confirm these mechanisms in the QCT calculations we report below.

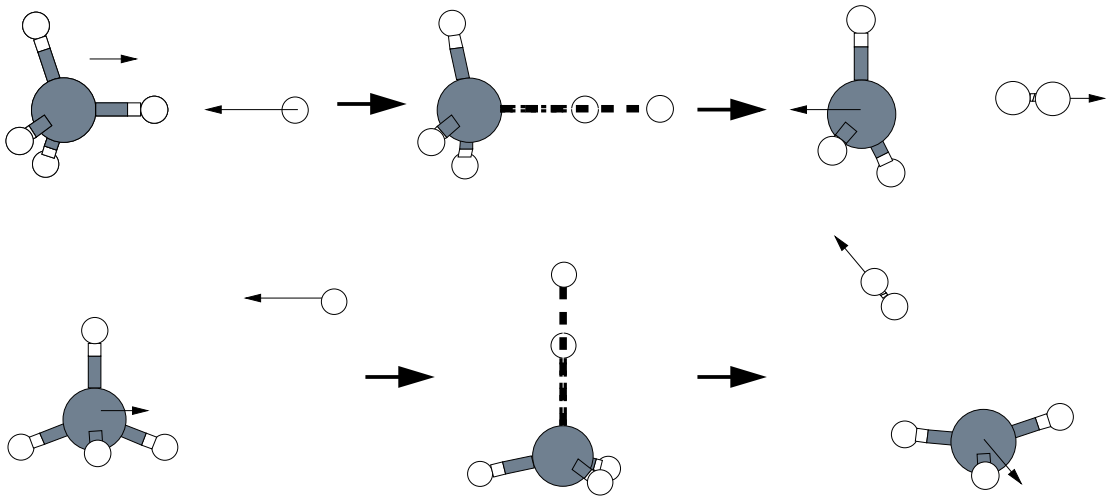

Figure 7.1: Illustration of the rebound and stripping mechanisms of reaction H + CH_4. The upper part shows the rebound and the lower part shows the stripping mechanism.

Table 7.1: CH_5 abstraction saddle point geometry and energy on the ZBB2 potential energy surface (PES) and other sources, as indicated.

	PES	Ref. 94[1]	Ref. 91[2]
Energy[3](kcal/mol)	14.8	14.8	14.93
R_{CH} (Å)	1.0843	1.0854	1.085
$R_{CH'}$ (Å)	1.4086	1.3991	1.401
$R_{H'H''}$ (Å)	0.9016	0.8970	0.895
∠H-C-H' (Degree)	102.8	103.12	103.1
∠C-H'-H" (Degree)	180.0	180.0	

[1] RCCSD(T)/aug-cc-pVTZ, Zhang, Braams and Bowman (2006)
[2] CCSD(T)/scaled cc-pVTZ, Wu, Werner and Manthe (2006)
[3] relative to the energy of H + CH_4

Table 7.2: Normal mode frequencies (cm^{-1}) of indicated geometries on the ZBB2 potential energy surface (PES) and other sources, as indicated.

CH_5(TS)			CH_4+H				CH_3+H_2			
PES	Ref. 94[1]	Ref. 91[2]	PES	Ref. 94[1]	Ref. 91[2]	EXPT[4]	PES	Ref. 94[1]	Ref. 93[3]	EXPT[5]
1320i	1437i	1414i								
440	531	534								
440	531	534								
1062	1082	1074	1320	1350	1341	1367				
1078	1126	1125	1320	1350	1341	1367				
1078	1126	1125	1320	1350	1341	1367	406	496	539	606
1434	1445	1442	1588	1575	1569	1583	1426	1419	1406	1403
1434	1445	1442	1588	1575	1569	1583	1426	1419	1406	1403
1726	1779	1795	3040	3028	3031	3026	3070	3115	3117	3004
3104	3073	3076	3174	3147	3151	3157	3293	3295	3299	3171
3289	3220	3223	3174	3147	3151	3157	3293	3295	3299	3171
3289	3220	3223	3174	3147	3151	3157	4420	4401	4400	4401

[1] RCCSD(T)/aug-cc-pVTZ, Zhang, Braams and Bowman (2006)
[2] CCSD(T)/scaled cc-pVTZ, Wu, Werner and Manthe (2006)
[3] MCG3-SRP, Pu and Truhlar (2002)
[4] Gray and Robiette (1979), Ref. 97
[5] latest NIST WebBook, Ref. 98

7 QUASICLASSICAL TRAJECTORY STUDY OF THE REACTION H + $CH_4(\nu_3 = 0, 1) \rightarrow CH_3 + H_2$ USING A NEW *AB INITIO* POTENTIAL ENERGY SURFACE

Properties of the ZBB3 PES are given in Table 7.2.1 along with those of ZBB2 for reference. Recall that ZBB3 PES is a fit to additional *ab initio* energies in the vicinity of the exchange saddle point. As seen ZBB3 faithfully reproduces the abstraction saddle point properties but gives a much better representation of the higher energy exchange saddle point than ZBB2. However, the abstraction saddle point is better represented that the exchange one. The present quasiclassical trajectory calculations, which are described next, focus strictly on the abstraction reaction and the effect of excitation of the asymmetric stretch were done using the ZBB2 PES. The result is checked and reproduced nearly perfectly at one energy using the ZBB3 PES as will be reported below.

Table 7.3: CH_5 abstraction (ABSP) and exchange (EXSP) saddle point geometries, energies, and harmonic frequencies (cm^{-1}) on the ZBB3, ZBB2 potential energy surfaces and those directly from *ab initio* calculations

	CH_5 ABSP[1]			CH_5 EXSP[2]		
	ab initio[3]	ZBB3	ZBB2	*ab initio*[3]	ZBB3	ZBB2
Energy (kcal/mol)	14.67	14.86	14.78	37.50	36.37	30.84
Mode 01	1437i	1375i	1320i	1537i	1687i	1385i
Mode 02	531	510	440	836	948	1008
Mode 03	531	510	440	836	948	1008
Mode 04	1082	1013	1062	1302	1373	1196
Mode 05	1126	1057	1078	1348	1373	1196
Mode 06	1126	1057	1078	1348	1393	1491
Mode 07	1445	1442	1434	1377	1440	1491
Mode 08	1445	1442	1434	1377	1440	1530
Mode 09	1779	1768	1726	1540	1607	1637
Mode 10	3073	3059	3104	3016	2966	2924
Mode 11	3220	3245	3289	3199	3350	3432
Mode 12	3220	3245	3289	3199	3350	3432
R_{CH} (Å)	1.0854	1.0853	1.0843	1.0863	1.0822	1.0629
$R_{CH'}$ (Å)	1.3991	1.4015	1.4086	1.3612	1.3645	1.4495
$R_{H'H''}$ (Å)	0.8970	0.9027	0.9016			
∠H-C-H' (Degree)	103.12	102.84	102.82			

[1] CH_5 abstraction saddle point
[2] CH_5 exchange saddle point
[3] RCCSD(T)/aug-cc-pVTZ, Zhang, Braams and Bowman (2006)

7.2.2 Trajectory Calculations

The initial conditions for the quasiclassical trajectories are essentially the usual ones [66]. For the reaction with the ground ro-vibrational state of CH_4 harmonic zero-point energy was added to CH_4 initially and random sampling of initial normal-mode coordinates and momenta was done. Standard adjustments were made to enforce zero angular momentum. In order to simulate the reaction with CH_4 with the ν_3 fundamental excited we proceeded carefully because of the possibility of rapid classical energy relaxation of the excited harmonic mode. This is made particularly likely because this mode is triply degenerate and so the expectation was that exciting one component of this mode would result in rapid sharing of the energy with the two other degenerate components of ν_3, which would be followed by relaxation to other vibrational modes of CH_4. One important mitigating factor that lessens this concern is the short interaction time of the hyper-thermal collisions we consider here. We determined this time by starting the trajectories with the incoming H atom 9 bohrs from the center of mass of CH_4 and initial relative kinetic energy of 1.52 eV. Trajectories with this initial condition reach the strong interaction region, *i.e.*, the near vicinity of the saddle point, in roughly 10 femtoseconds. So, the practical concern about relaxation of vibrationally excited CH_4 is limited to this relatively short time-scale. With this time-scale in mind we examined the vibrational relaxation as a function of time. At $t = 0$ vibrational energy equal to the harmonic fundamental was added to one component of ν_3 and zero-point energy was given to the remaining harmonic modes. Then the energy content of all normal modes was determined as a function of time. Since the isolated CH_4 potential of the full PES is not harmonic (in fact it is quite realistic relative to highly accurate CH_4 molecular potentials) there is

relaxation just due to anharmonicity of the ν_3 mode. In Fig. 7.2 we show the energy content of the initially excited component of ν_3 averaged over 41 trajectories. As seen there is energy relaxation; however, on the time scale of 10 fs more than 80 percent of the initial energy remains in the component of ν_3 initially excited and only after 25 fs does this energy drop below 80 percent. Thus, we conclude that the simple approach to excite the harmonic normal mode ν_3 is realistic for the collisions of interest here.

To conclude this discussion of initial conditions we note that all trajectories were initiated with the H atom 9 bohrs from the center of mass of CH_4 and the impact parameter b was scanned from 0.0 to $b_{\max}$ with a step size of 0.3 bohr ($b_{\max}$ was first determined precisely). Initial collision energies of 1.52, 1.85 and 2.20 eV were chosen in order to compare directly with experiment [96]. For every set of initial conditions $(E_{\rm col}, \nu_3, b)$, 6 independent batches of 5000 trajectories were run. Error estimators were determined form the results of these 6 batches. All trajectories were initiated with CH_4 initially non-rotating, but with random initial orientation.

Final state analysis of the products focused on the differential cross section of CH_3, the rotational and vibrational distributions of H_2 and CH_3 and lab-speed distribution of CH_3. All these distributions were obtained using the following approach. At each impact parameter, b, the scattering angle, rotation angular momenta, etc. of CH_3 and H_2 were calculated. The associated probability densities, denoted generically as $p(b)$, were then determined using a well-established Gaussian-window smoothing technique [99,100] and the final densities were obtained by the usual impact-parameter weighted integration of $bp(b)$. The CH_3 lab-speed distribution was obtained using the center-of-mass scattering angle and center-of-mass velocity in the standard way, as given elsewhere [96]. (Note, there is a missing factor of 2 in Eq. 9 of Ref. 96)

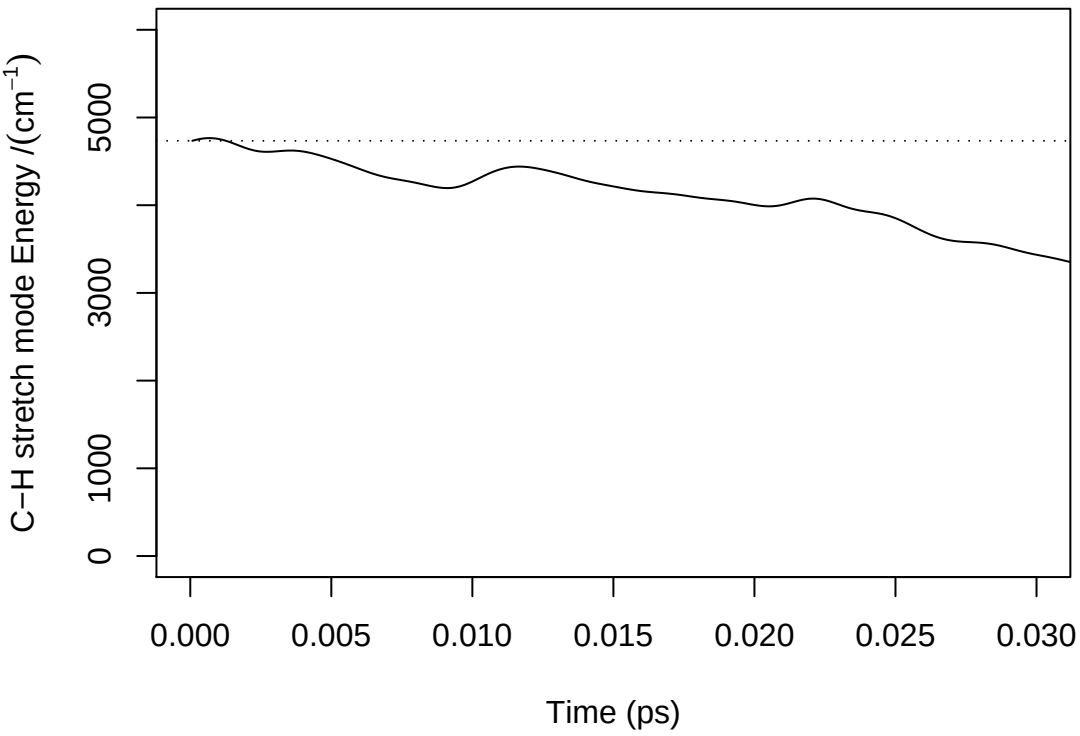

Figure 7.2: Time-Dependence of the energy in the excited ν_3 mode of CH_4. The mode energy is averaged over 41 trajectories.

Finally, the vibrational energy of each product was obtained as the difference of the total internal energy and the rotational energy of H_2 or CH_3. The rotational energy was calculated approximately as $\frac{1}{2}I\omega^2$, where I is the inertia tensor in the principal-axis frame and ω is the corresponding angular velocity. The rotational energy was determined at a fixed end-time of each trajectory instead of averaging over time. Since we ran many thousands of trajectories the averaging over trajectories effectively averages over the vibration/rotation interaction. In any case, this separation of vibration and rotation is not exact; however, since the rotational excitation of H_2 or CH_3 is not large (see below) this treatment should be quite reasonable.

The reaction cross sections were obtained in the usual way and the enhancement ratio r due to the CH_4 asymmetric stretch excitation was calculated as

$$r = \frac{\sigma[H + CH_4(\nu_3 = 1)]}{\sigma[H + CH_4(\nu_3 = 0)]}. \tag{7.1}$$

7.3 Results and Discussion

7.3.1 CH_3 Angular Distribution

The differential cross sections of the CH_3 product (normed arbitrarily so that they integrate to one) are shown in Fig. 7.3 for the three initial relative kinetic energies indicated and for CH_4 $\nu_3 = 0$ and 1. As seen the distributions show both forward and backward scattering, with the peak at sideways scattering. Note the similarities for CH_4 $\nu_3 = 0$ and 1, with somewhat more forward scattering seen for CH_4 $\nu_3 = 1$. For both initial states there is a noticeable shift in the peak to more backward scattering of CH_3 as the energy increases. This backward scattering of CH_3 is a clear indication of a stripping mechanism, as discussed elsewhere [95] and in more detail below. Thus

this mechanism is increasingly important as the collision energy increases.

Experimental and direct-dynamics DFT angular distributions for the isotopolog version of this reaction, H + CD_4 have been reported in Ref. 86 Fig. 1 at a collision energy of 1.20 eV. The present results agree qualitatively with these in showing forward and backward scattering and with a peak at sideways scattering.

To gain some insight into these angular distributions we plot the b-dependent CH_3 partial differential cross sections for selected impact parameters in Fig. 7.4. These cross sections are b-weighted so that integrating them and multiplying by 2π would give the absolute differential cross section. Note we examined these plots at the three collision energies, 1.52, 1.85 and 2.20 eV, and the changes with energy are not large. Thus, only the distributions at 1.85 eV are shown in the figure. As seen the CH_3 angular distributions show a strong b dependence. Examination of trajectories indicates that the reaction proceeds by the stripping mechanism at large impact parameters and a rebound mechanism at small impact parameters. Also as seen there is a slight shift in the CH_3 angular distribution between CH_4 $\nu_3 = 0$ and 1.

At this point, the collision mechanism of H + CH_4 is quite clear. At small impact parameter b, the rebound mechanism is favored and the stripping mechanism is favored for large impact parameters. Also, as the collision energy increases, the contribution of the stripping mechanism increases. Excitation of CH_4 ν_3 mode slightly favors the rebound process. (These mechanisms are clearly seen in representative trajectories, which can be viewed at the url

`http://www.chemistry.emory.edu/faculty/bowman/H+CH4.htm`.)

Next,we consider the consequences of these two mechanisms on the rotational distributions of the products.

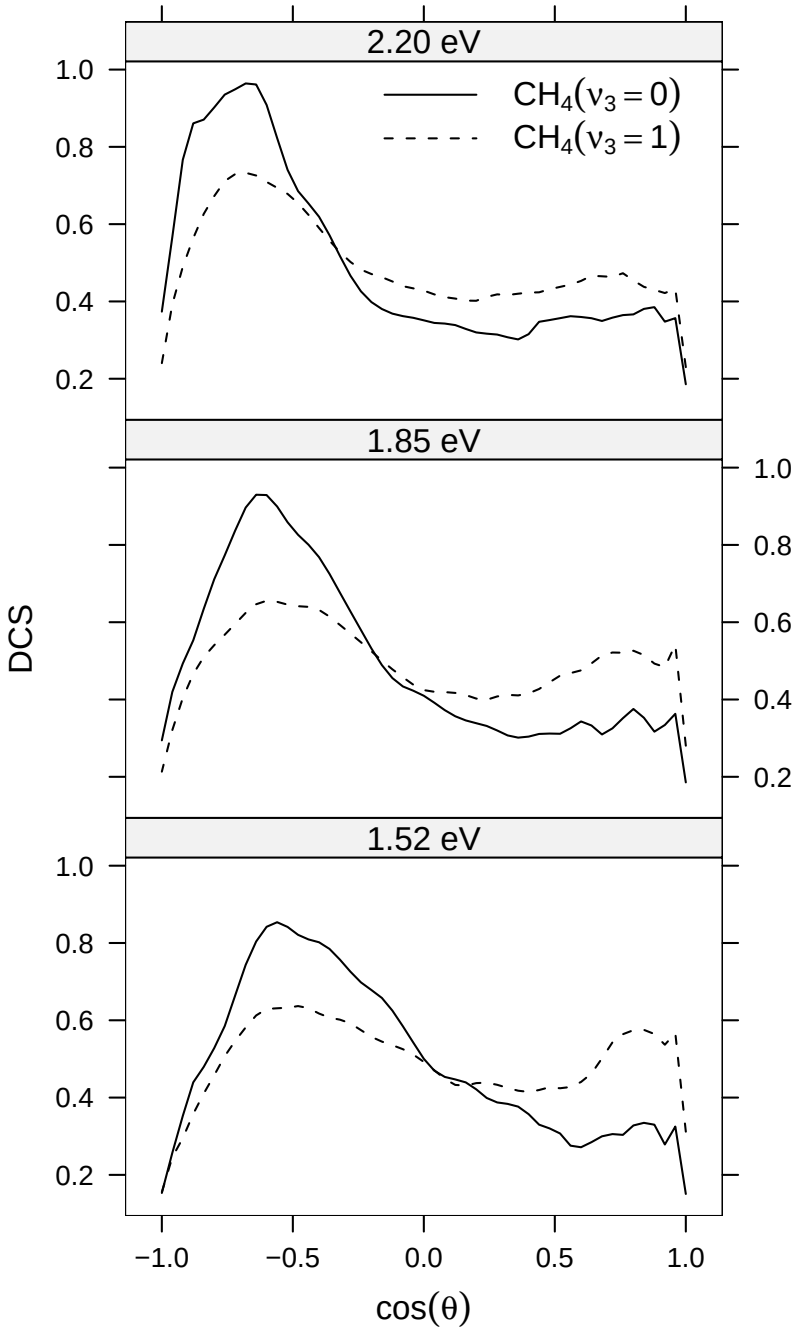

Figure 7.3: CH_3 differential cross sections at the indicated energies and for vibrational state of CH_4 indicated.

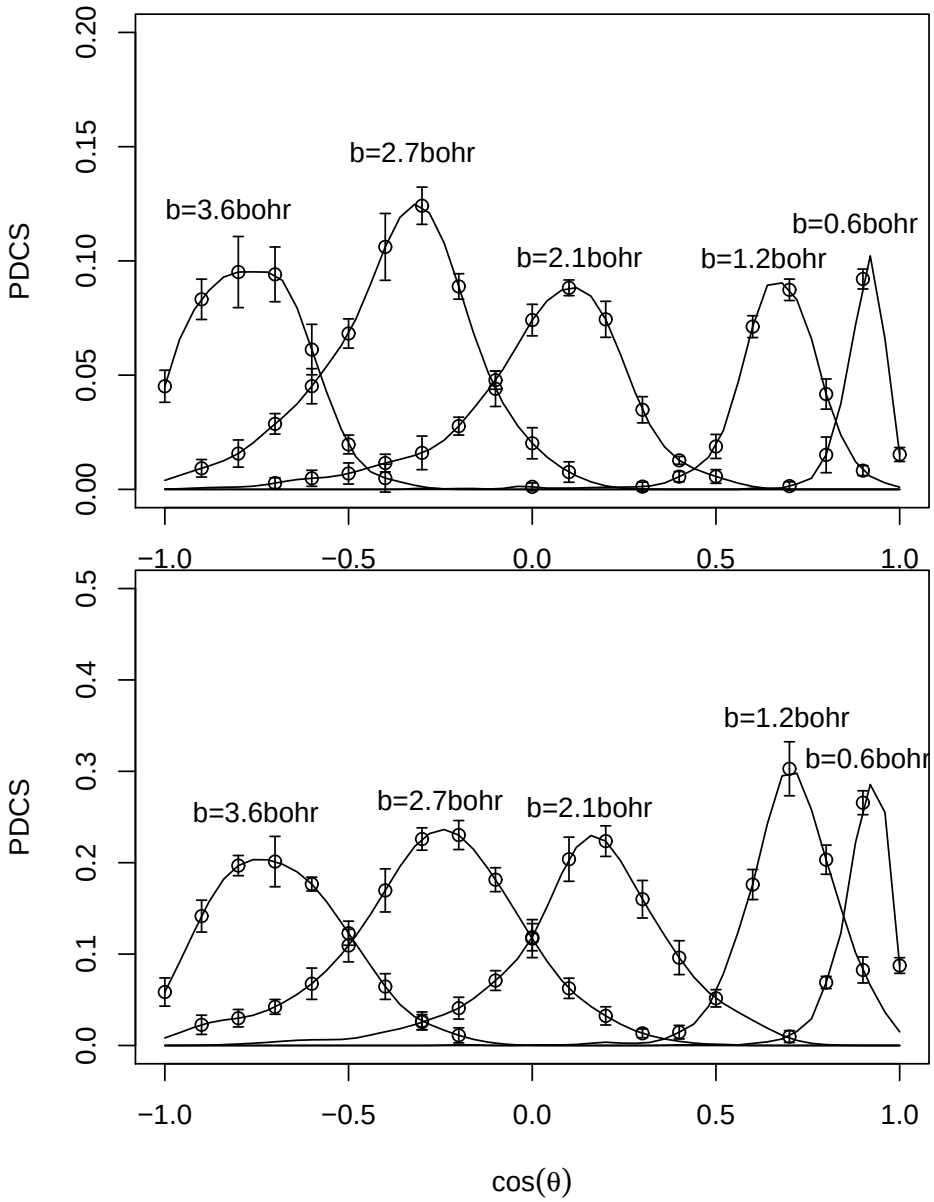

Figure 7.4: CH_3 partial differential cross sections (see text for definition) and initial collision energy of 1.85 eV. The upper figure is for the CH_4 ground state and the lower figure is for the CH_4 ν_3 excited state.

7.3.2 H_2 and CH_3 Rotational Distributions

From the schematic figure of the rebound and stripping mechanisms given in Fig. 7.1, it seems reasonable that the rotational distributions of the products will reflect these two mechanisms. To investigate this we calculated the rotational distributions of H_2 and CH_3 and the results are shown in Fig. 7.5. As seen the H_2 and CH_3 distributions are quite similar with the peak in the former one increasing with collision energy from 6 to 8, whereas the peak in the CH_3 distribution is constant at 5. Note also the vibrational excitation of CH_4 has very little effect on these rotational distributions. The b dependent H_2 rotational distribution is shown in Fig. 7.6 for vibrationally excited CH_4. From this figure it is clear that the large impact parameter collisions lead to higher rotational excitation. Smaller b tends to have colder H_2 rotational motion and this is attributed to the rebound mechanism at small b's and the stripping collisions at large b leads to rotationally hotter H_2. The results for CH_3 are much less dramatic with b with only a slight shift to lower rotational excitation as b increases.

7.3.3 Cross Section Enhancement Ratio

In a very recent experiment Zare and co-workers determined the enhancement of the reaction cross section due to vibrational excitation of CH_4 ν_3 mode [96]. They reported an enhancement of 3.0 ± 1.5 and found that this enhancement remained constant within their uncertainty for the three energies, 1.52, 1.85 and 2.20 eV. We calculated the reaction cross sections for CH_4 ν_3 excited and unexcited and the enhancement ratio. First, however, consider the impact parameter dependence of the corresponding reaction probabilities; these are shown in Fig. 7.7. As seen there is an enhancement of the reaction probability of about a factor of 3 and also that this factor

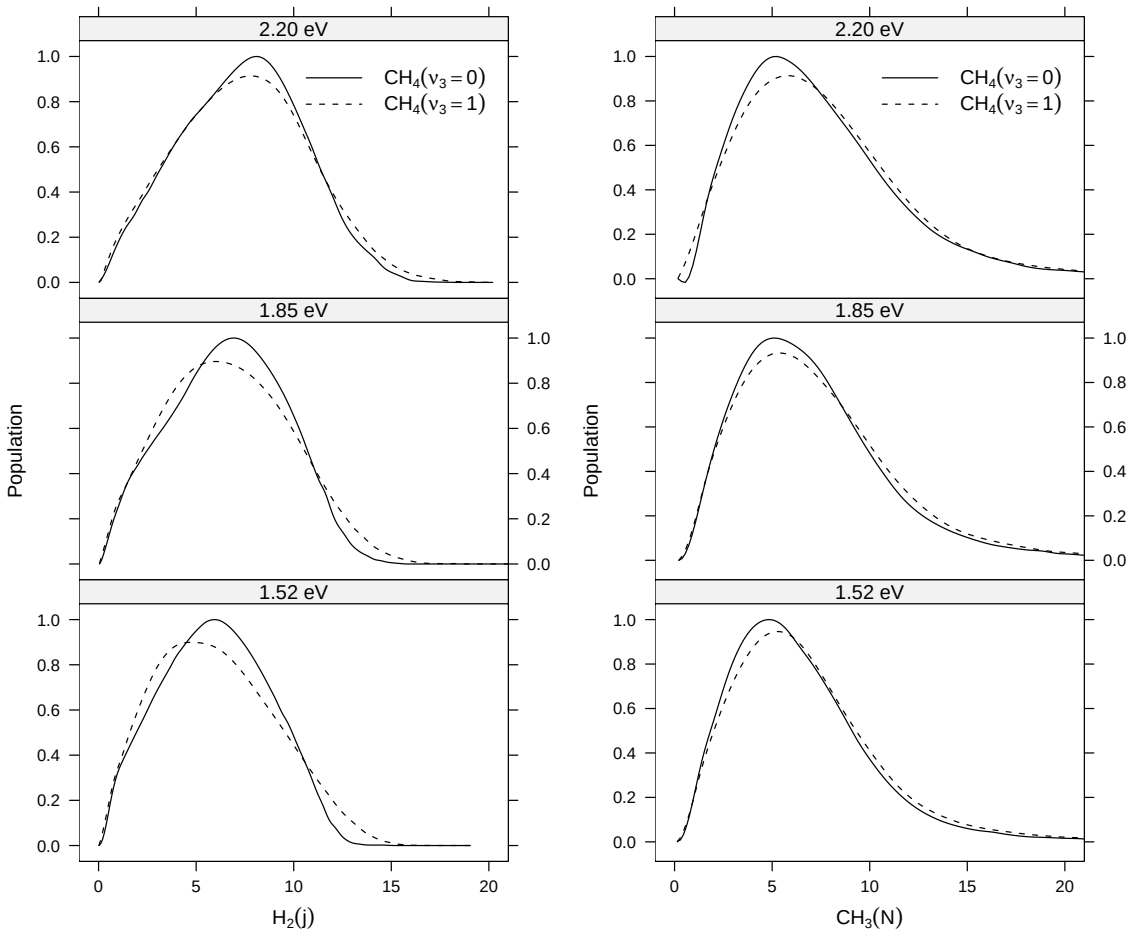

Figure 7.5: H_2 (the left three panels) and CH_3 (the right three panels) rotational distributions (normalized by the maximum to be 1) at collision energies as indicated.

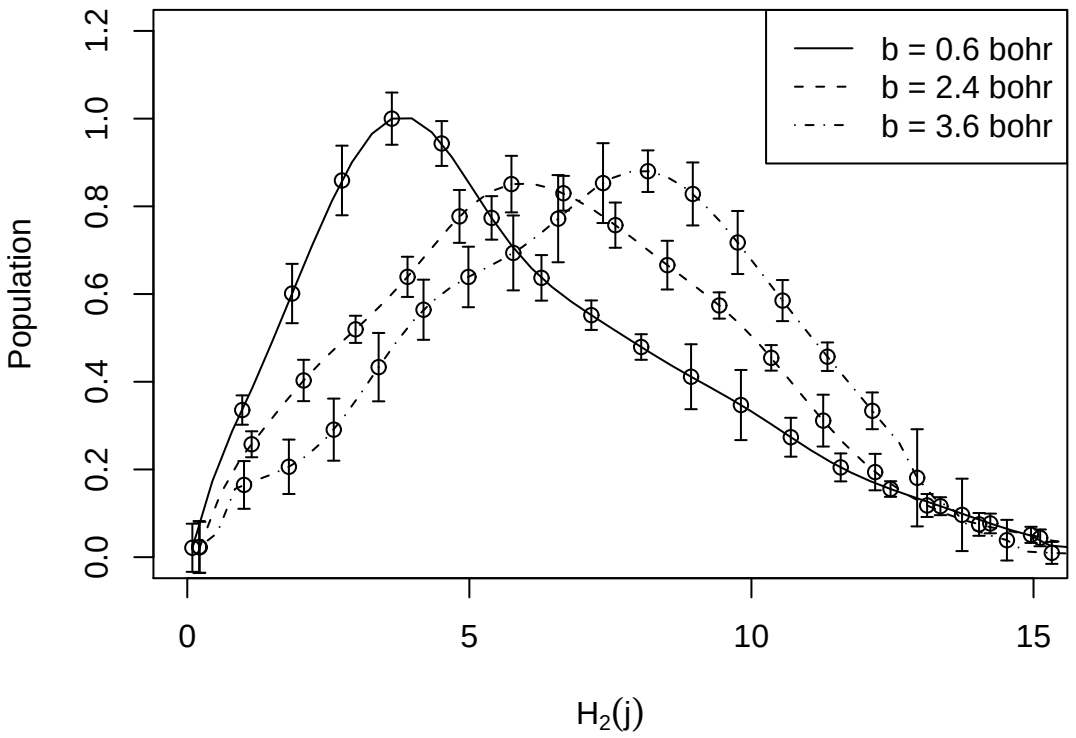

Figure 7.6: H_2 impact parameter dependent rotational distributions (normalized by the maximum to be 1) at collision energy of 1.85 eV and for CH_4 $\nu_3 = 1$

is largely independent of the impact parameter. The resulting reaction cross sections and ratios are plotted in Fig. 7.8. As seen the ratio varies in the range 2.2 - 3.0 over the collision energy range of the experiment and thus the agreement with experiment is excellent. However, we note that the calculated cross sections are summed over final "states" of the products whereas the experimental ratio is for the ground vibrational state of CH_3; it was noted that enhancement was found for all states populated by the ground state reaction [96]. The mild enhancement of the cross section together with the "spectator" characterization of this vibrational mode is consistent with the following simple vibrationally adiabatic (VA) argument. The VA barrier for this reaction is defined as the energy difference between the saddle point energy plus the vibrational energy in the CH_5 saddle point normal modes minus the corresponding vibrational energy of CH_4. The relevant quantity for the enhancement issue is the difference between the vibrationally adiabatic barriers for the vibrationally excited and ground state reactions. Assuming that one quantum of excitation in the triply degenerate ν_3 mode of CH_4 correlates with the single CH-mode of the saddle point (see Table 7.2.1) this energy difference is -100 cm^{-1}. Thus the VA barrier is lowered for the excited state reaction relative to the unexcited one by 100 cm^{-1}. This, at least naively, would be expected to result in a modest increase in the reaction cross section, consistent with the calculations and experiment. The VA approximation, which was also invoked by Camden *et al.* [96], has its limitations and it may only apply for the reaction up to the saddle point and then break down, at least partially, in the region of the products. This appears to be occurring in the case of the umbrella mode of CH_3 which is excited even for the reaction with CH_4 in the ground vibrational state, as pointed out by Camden *et al.* [96] and as seen in the QCT calculation.

We calculated this enhancement ratio using the ZBB3 PES at 1.52 eV and find a value of 2.3 in very good agreement with the result of 2.2 shown obtained with the ZBB2 PES (see Fig. 7.8).

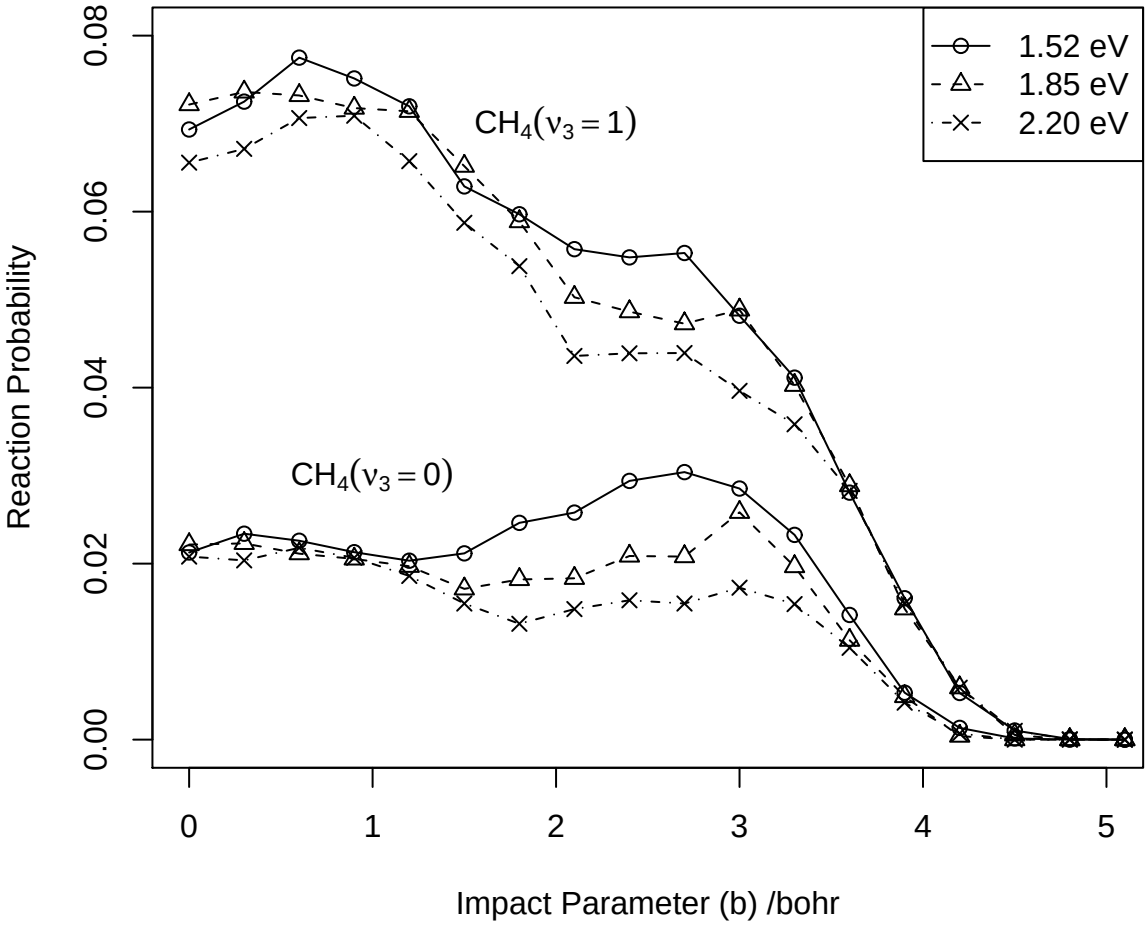

Figure 7.7: The impact parameter dependent reaction probabilities at the indicated initial collision energies for CH_4 $\nu_3 = 0, 1$.

7.3.4 CH_3 Vibrational Energy Distribution

The vibrational energy distributions of the CH_3 product were obtained at the three collision energies, as described above, and the results are shown in Fig. 7.9 for

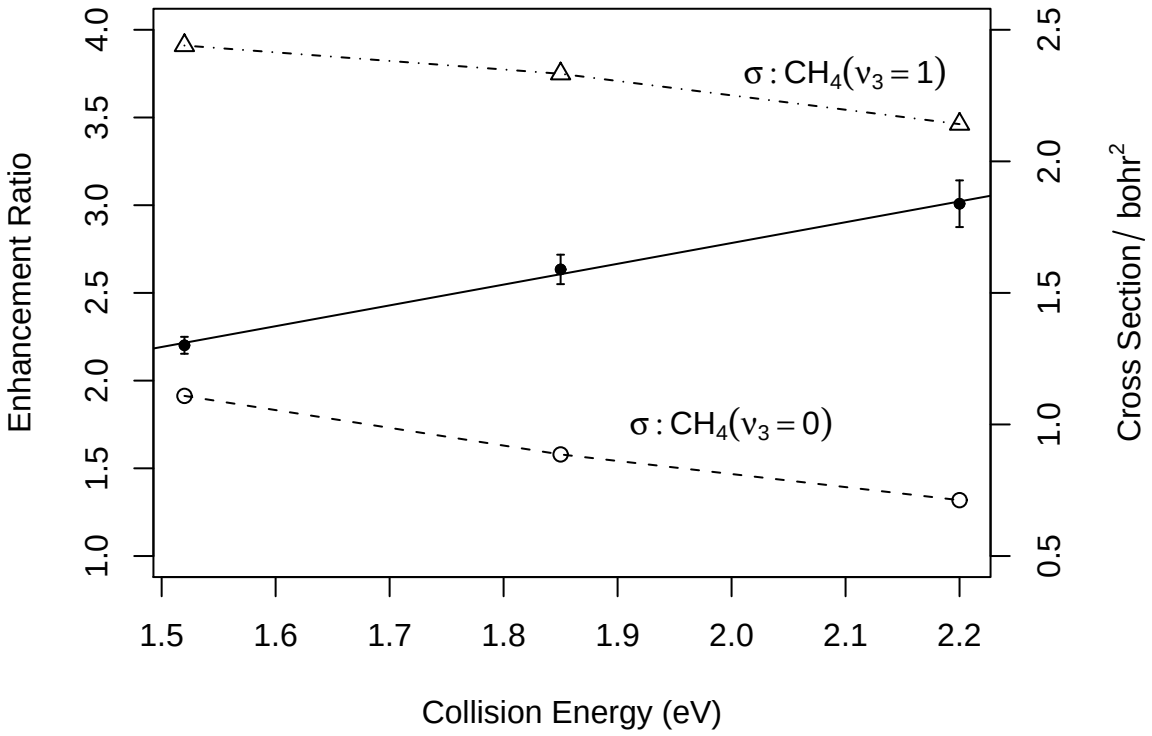

Figure 7.8: Reaction cross sections for H + CH_4 ($\nu_3 = 0, 1$) and their ratio versus the initial collision energy.

CH_4 ($\nu_3 = 0, 1$). As seen there is a large shift upwards in the vibrational energy distributions for the reaction with $CH_4(\nu_3 = 1)$. The peak of the distribution shifts by roughly 2500 cm^{-1}. We have not attempted an analysis of the specific modes of CH_3 that are excited in a systematic way; however, by examination of trajectories we conclude that the umbrella bend and CH-stretch modes are excited. (We also examined the impact parameter b dependence of these vibrational energy distributions and the result shows that there is no strong b dependence.) These results are in qualitative agreement with experiment, which showed that CH_3 is excited in the umbrella and symmetric stretch modes in the reaction with $CH_4(\nu_3 = 1)$.

7.3.5 Lab Speed Distribution

Finally we show a comparison between the calculated and experimental lab frame CH_3 speed distribution in Fig. 7.10 for the collision energy of 1.52 eV. The comparison is not totally consistent because the QCT calculations are summed over the internal "states" of the products whereas the experiment is specific to the indicated state of symmetric stretch of CH_3. With this caveat in mind, there is overall good agreement with experiment. Both the calculated and experimental speed distributions show virtually no dependence on the initial vibrational state of CH_4. Also note that the direct-dynamics DFT calculations of the lab-speed distribution agree well with the experimental one for the H+CD_4 reaction [88].

The peaks in the QCT distributions are about 200 m/s lower than the experimental ones. One possible source of the shift is easy to understand for the case $CH_3(\nu_1 = 0)$. In this case because the QCT distribution includes trajectories that correspond to vibrational excitation, the corresponding relative speeds would be lower

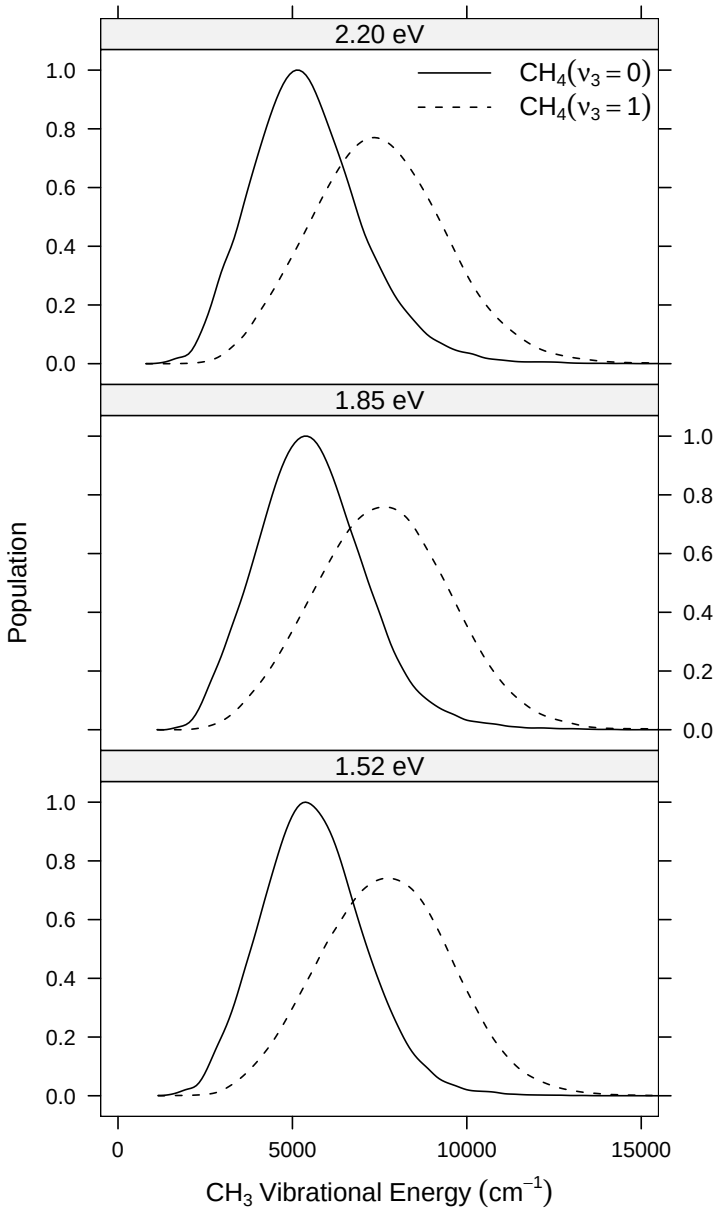

Figure 7.9: CH_3 vibrational energy distribution at initial collision energies as indicated for CH_4 $\nu_3 = 0, 1$.

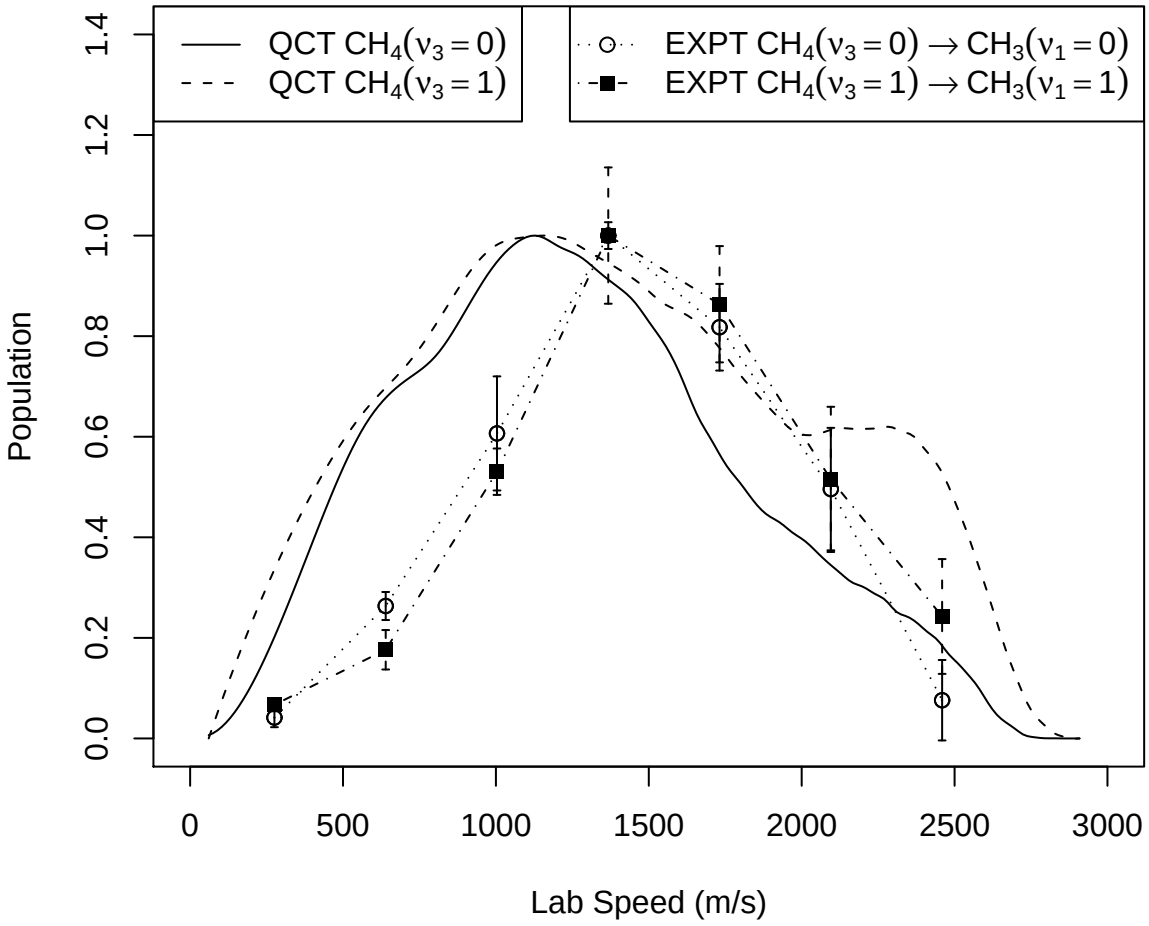

Figure 7.10: Calculated and experimental (reference 96) CH_3 lab speed distribution at the initial collision energy of 1.52 eV and for CH_4 ($\nu_3 = 0, 1$).

than experimental one. Another possible source of the shift is the approximation of the QCT method.

7.4 Summary and Conclusions

We reported a quasiclassical trajectory study of the H + $CH_4(\nu_3 = 0, 1)$ reaction at collision energies of 1.52, 1.85 and 2.20 eV, using an accurate, *ab initio*-based, full-dimensional CH_5 potential energy surface. The CH_3 center-of-mass angular distribution and lab-speed distribution were calculated and compared directly to experimental ones. The angular distribution was shown to be consistent with a rebound process at small impact parameter and stripping process at large impact parameter. Rotational distributions of H_2 and CH_3 were also calculated and the former one also showed clear signatures of the rebound and stripping reaction mechanisms. These distributions were shown to be largely the same for both vibrational states of CH_4, suggesting that the ν_3 mode is largely a spectator mode, in agreement with the conclusions of experiment. However, the experimental enhancement of the cross section due to fundamental excitation of this mode of 3.0 ± 1.5 is reproduced by the QCT calculations where the reaction cross section enhancement ratio was found to range from $2.2 - 3.0$ over the energy range 1.52 to 2.20 eV.

Acknowledgments We thank Jon P. Camden for providing the CH_3 lab speed distribution data and valuable discussions on it. JMB thanks the Department of Energy (DOE-DE-FG02-97ER14782) for financial support. Support for computational resources from ONR/DURIP is acknowledged.

8 Quasiclassical Trajectory Study of the Reaction of Fast H Atoms with C-H Stretch Excited CHD_3

Abstract

Quasiclassical trajectory calculations are reported of the reactions H + CHD_3 ($\nu_{\text{C-H stretch}} = 0, 1$) to give H_2 + CD_3 and HD + CHD_2 using a recent *ab initio*-based CH_5 potential energy surface. The cross sections, angular, and internal energy distributions are calculated at the initial relative kinetic energy of 1.53 eV in order to make comparisons with corresponding recent experiments, [J.P. Camden, H.A. Bechtel, D.J. Akeny Brown and R.N. Zare, J. Chem. Phys. 124 (2006) 034311].

8 QUASICLASSICAL TRAJECTORY STUDY OF THE REACTION OF FAST H ATOMS WITH C-H STRETCH EXCITED CHD_3

8.1 Introduction

The reaction H + CH_4 is one of most extensively studied atom-polyatomic reactions. It is a challenging reaction for rigorous dynamical studies and also requires high level *ab initio* electronic structure calculations to obtain an accurate reaction barrier.

Zare and co-workers recently reported a series of experimental papers [86–88,95,96, 101] describing the reaction of CD_4, CH_4 and most recently CD_3H with translationally hot H atoms [101], produced by photo-dissociation of HBr. Complementary calculations for the H + CD_4 reaction have been done by Schatz and co-workers [86–88] using direct-dynamics quasiclassical trajectory calculations (QCT) based on Density Functional Theory.

We recently reported a global potential energy surface (PES) based on fitting roughly 20000 *ab initio* energies obtained with the coupled cluster method, CCSD(T), with an aug-cc-pVTZ basis and preliminary QCT calculations of the H + CD_4 reaction using this PES [94]. This surface was used subsequently by us in a study of the effect of excitation of the antisymmetric C-H stretch in the H + CH_4 reaction [67] using a slightly refined version of the original PES. We obtained an enhancement factor and other results in very good agreement with experiment [67].

In this paper we extend our QCT studies to the H + CHD_3 reaction and examine the effect of vibrationally exciting the C-H stretch. The goal here, as before, is a direct comparison with experiments of Zare and co-workers [101]. In those experiments HBr was photolyzed to produce fast H atoms (resulting in a relative collision energy of 1.53 eV) and the C-H stretch was excited to the fundamental and first overtone. Experiments were also done with Cl as the reacting atom, through photolysis of Cl_2, which resulted in a much lower collision energy of 0.18 eV. We do not consider the

reaction with Cl here but only the reaction with the fast H atom. For that reaction both sets of products, i.e., HD + CHD_2 and H_2 + CD_3, were observed. For the reaction with CHD_3 in the ground vibrational the authors wrote that "...the ground state reaction shows no clear preference for the H- or D-abstraction products" [101]. However they did note that their detection sensitivity for CHD_2 was less than for CD_3. (Naively one might expect abstraction of D to be roughly three times more likely than abstraction of H given the 3 to 1 ratio of D to H in CHD_3.) These authors also reported that the reaction with the C-H stretch excited enhances the production of CHD_2, which is an indication that the C-H stretch excitation is maintained in the reaction and in that sense is a spectator. The reaction to abstract the H atom leading to CD_3 does produce some umbrella excitation but no C-D stretch excitation.

The paper is organized as follows. In the next section we present a brief review of the PES and give some relevant details of the quasiclassical trajectory calculations. Following that we present results and discussion. Finally we give a summary in section 8.4.

8.2 Potential Energy Surface and Calculation Details

The PES used here is the the updated one, denoted ZBB3 in our recent paper describing QCT calculations of the H + CH_4 reaction [67]. The PES is based on accurate fitting of roughly 20000 CCSD(T)/aug-cc-pVTZ electronic energies; details of this construction of this PES are given elsewhere [67, 94].

The harmonic normal-mode frequencies of the reactant and products are given in Table 8.1. The C-H stretch harmonic frequency is 3136 cm^{-1} and, as is well known, this is basically a local mode. The results compare well with earlier *ab initio* and DFT

ones, compiled from several sources in Table III of Camden *et al.* [101]. We also give the harmonic frequencies at the abstraction saddle point for the two cases where either D or H is the abstracted atom. As seen, there are differences in these frequencies, as expected. Note especially that the zero-point energy of the H-abstraction saddle point is 400 cm^{-1} less than the one for D-abstraction. (This is easy to understand as the high frequency C-H stretch in the case of D-abstraction is the imaginary frequency mode in the case of H-abstraction.)

Table 8.1: Present PES normal mode frequencies (cm^{-1}) for reactants and products and for the H-atom and D-atom abstraction saddle point configurations, denoted as H-ABSP and D-ABSP, respectively. The last row is the harmonic zero-point energy and the values denoted as "REF" are from a compilation of results in Ref. 101.

H-ABSP	D-ABSP	CHD_3		CHD_2 + HD		CD_3 + H_2	
PES	PES	PES	REF	PES	REF	PES	REF
1361i	1034i	1018	1003	456	431	413	458
421	421	1046	1036	1043	1006	1037	1026
421	461	1046	1036	1292	1248	1037	1026
792	783	1306	1291	2269	2187	2192	2158
994	791	1306	1291	2453	2358	2453	2381
994	883	2187	2142	3236	3114	2453	2381
1071	1089	2343	2263	3821		4411	
1071	1300	2343	2263				
1746	1737	3136	2993				
2173	2243						
2409	2409						
2409	3192						
7252	7655	7865	7659	7285	5172	6998	4715

The initial conditions for the QCT calculations (done with our own code) are essentially the standard ones [66]. For the reaction with the ground ro-vibrational state of CHD_3 harmonic zero-point energy (Table 8.1) was added to CHD_3 initially and random sampling of initial normal-mode coordinates and momenta was done.

Standard adjustments were made to enforce zero angular momentum.

In order to simulate the reaction with the C-H stretch fundamental excited the energy of that normal mode was given as 3/2 the normal-mode harmonic energy. The approach was taken by us previously for the H + CH_4 reaction [67], where it was shown that the C-H stretch energy remained 80 percent localized up to 25 fs. This time scale for localization is also seen for CHD_3 and is satisfactory since the collision time is of the order of 10 fs at the high translational kinetic energy of 1.5 eV, with the H atom initially 9 Bohrs from the center-of-mass of CD_3H. Thus, we conclude that the simple approach to excite the C-H stretch is realistic for the collisions of interest here. Although this paper is centered on the reaction with CHD_3, to aid in the analysis we also calculated the reaction cross sections for the reactions with CD_4 and CH_4, unexcited and also with the antisymmetric C-H(D) stretch excited.

Final state analysis of the products includes the differential cross sections and vibrational distributions of CD_3 and CHD_2 and the rotational distributions of H_2 and HD. The details of obtaining these distributions are given elsewhere [67].

8.3 Results and Discussion

The six reactions we consider are:

$$H + CH_4(\nu_3 = 0) \rightarrow H_2 + CH_3 \tag{8.1}$$

$$H + CH_4(\nu_3 = 1) \rightarrow H_2 + CH_3 \tag{8.2}$$

$$H + CHD_3(\nu_1 = 0) \rightarrow H_2 + CD_3 \tag{8.3}$$

$$H + CHD_3(\nu_1 = 1) \rightarrow H_2 + CD_3 \tag{8.4}$$

$$H + CHD_3(\nu_1 = 0) \rightarrow HD + CHD_2 \tag{8.5}$$

$$H + CHD_3(\nu_1 = 1) \rightarrow HD + CHD_2 \tag{8.6}$$

We denote the six reactions using a shorthand notation (CH_4,G,H_2), (CH_4,E,H_2), (CHD_3,G,H_2) or (CHD_3,G,CD_3), (CHD_3,E,H_2) or (CHD_3,E,CD_3), (CHD_3,G,HD) or (CHD_3,G,CHD_2), and (CHD_3,E,HD) or (CHD_3,E,CHD_2). The first element in a triple indicates the reactant (CH_4 or CHD_3). The second element in the triple indicates the C-H stretch vibrational state, where "G" stands for ground state and "E" stands for the first excited state. The last element in a triple identifies the product. In addition, we use "[ ]" to enclose all the possible value for any element in a triple to represent a series of reactions. For example, (CH_4,[GE],H_2) represents reactions of (CH_4,G,H_2) and (CH_4,E,H_2).

8.3.1 Reaction Probabilities and Cross Sections

The impact-parameter dependence of the reaction probabilities for the reactions (CHD_3,[GE],[CD_3 and CHD_2] is shown in Fig. 8.1, and the corresponding reaction cross sections are given in Table 8.2, along with cross sections for (CH_4,[GE],H_2) and (CD_4,[GE],H_2). As seen the reaction (CHD_3,E,H_2) has a much larger reaction probability than that of any other reactions and at all impact parameters. Clearly exciting the C-H stretch promotes the H-atom abstraction; this result is in qualitative agreement with experiment. The cross section ratio of (CHD_3,G,H_2)/(CHD_3,G,HD) is about 0.5 which also agrees qualitatively with the experimental finding of "no clear preference" for H or D abstraction. As noted in the Introduction, from a simple statistical viewpoint, the ratio of cross section to abstract D vs H would be 3:1, but

Table 8.2: Reaction cross sections for reactions indicated at the initial relative kinetic energy of 1.53 eV.

Notation	Reactant	Product	Cross Section ($Bohr^2$)
(CH_4,G,H_2)	H + CH_4 (G)	H_2 + CH_3	1.08
(CH_4,E,H_2)	H + CH_4 (E)	H_2 + CH_3	2.51
(CD_4,G,HD)	H + CD_4 (G)	HD + CHD_3	0.31 ± 0.03
(CD_4,E,HD)	H + CD_4 (E)	HD + CHD_3	1.17 ± 0.02
(CHD_3,G,H_2)	H + CHD_3 (G)	H_2 + CD_3	0.13 ± 0.01
(CHD_3,G,HD)	H + CHD_3 (G)	HD + CHD_2	0.28 ± 0.01
(CHD_3,E,H_2)	H + CHD_3 (E)	H_2 + CD_3	1.75 ± 0.03
(CHD_3,E,HD)	H + CHD_3 (E)	HD + CHD_2	0.34 ± 0.02

from Table 8.2 this ratio is closer to 2:1. This indicates that the incident H atom is more likely to abstract the H atom than the D atom. One way to rationalize this difference in reactivity is by recalling that the vibrationally ground state adiabatic barrier is 400 cm^{-1} higher for the D-atom abstraction than the H-atom abstraction.

The higher reactivity of the H atom in methane is also seen in the differences in reaction cross sections for (CH_4,G,H_2) and (CD_4,G,HD), which are also given in Table 8.2. As seen the cross section for (CH_4,G,H_2) is roughly 3.6 times the one for (CD_4,G,HD).

Also note that the ratio of cross sections for (CHD_3,E,H_2) and (CHD_3,G,H_2) is about 14, which is much greater that the reaction cross section enhancement ratio due to the C-H stretch excitation in CH_4 as we reported in Ref. [67] and also indicated in Table 8.2. Also as seen in the table, there is virtually no effect on the cross section to abstract the D atom due to excitation of the C-H stretch. Both of these results are in agreement with experiment which determined qualitative but not quantitative effects due to C-H stretch excitation.

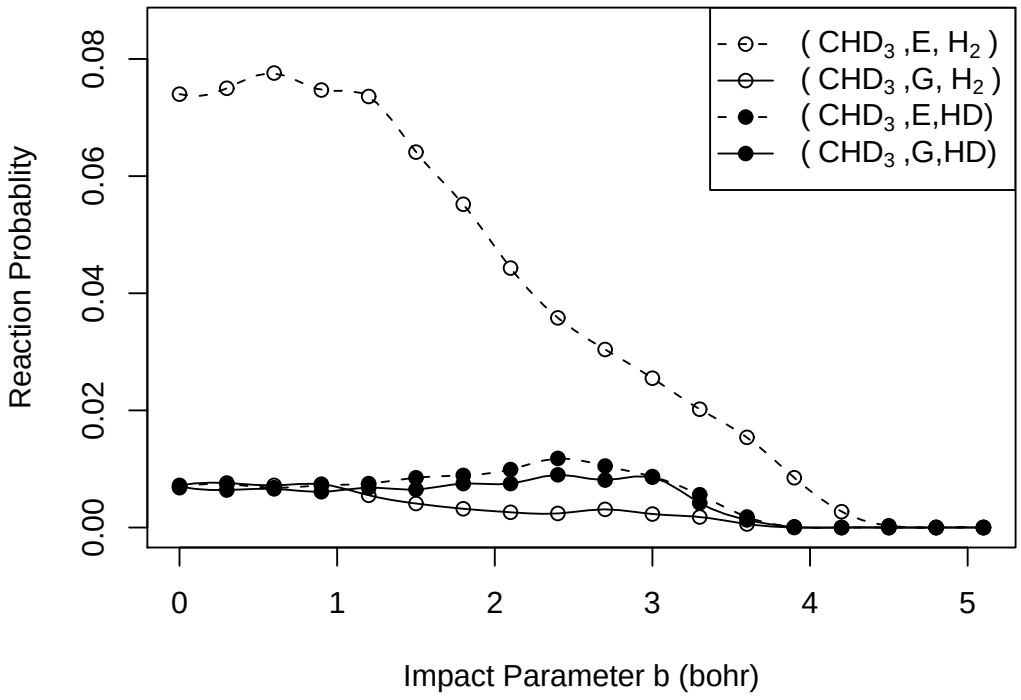

Figure 8.1: $H + CHD_3$ reaction probability to produce products $H_2 + CD_3$ and $HD + CHD_2$.

8.3.2 CD_3 and CHD_2 Angular Distributions

Consider now the differential cross sections for CD_3 and CHD_2 for ground and vibrationally excited CHD_3. These are shown in Fig. 8.2, and as seen there are some differences among them. The CHD_2 product is generally more sideways and backward scattered than CD_3, which is more forward scattered. These results follow from the impact-parameter dependence of the corresponding reaction probabilities shown in Fig. 8.1. ¿From previous analysis done by us [67] and Schatz and co-workers [86–88] for H + CD_4 and H + CH_4 it is known that reaction at smaller b corresponds to a rebound mechanism leading to forward scattering of the methyl product, i.e., $\cos\theta = 1$, whereas reaction at larger b corresponds to the stripping mechanism leading to backward scattering of the methyl product. For those reactions both mechanisms contributed about equally resulting in both sideways, backward and forward scattering. Evidently the rebound mechanism is dominant for the CD_3 + H_2 products in the present reaction.

8.3.3 H_2 and HD Rotational Distributions

Now consider the H_2 and HD rotational distributions; these also reflect the reaction mechanism as we have shown previously [67]. Specifically the stripping mechanism leads to greater rotational excitation of H_2 and HD than does the rebound mechanism. This is clearly seen in Fig. 8.3 which shows these distributions for the reactions (CHD_3,[GE],[HD/H_2]). As seen, H_2 from (CHD_3,E,H_2) is the rotationally coldest and that is attributed to the dominance of the rebound mechanism for this product. H_2 from (CHD_3,G,H_2) is a little colder than HD from (CHD_3,[GE],HD). The rotational distributions for the HD products are hotter than for H_2 (beyond what might be

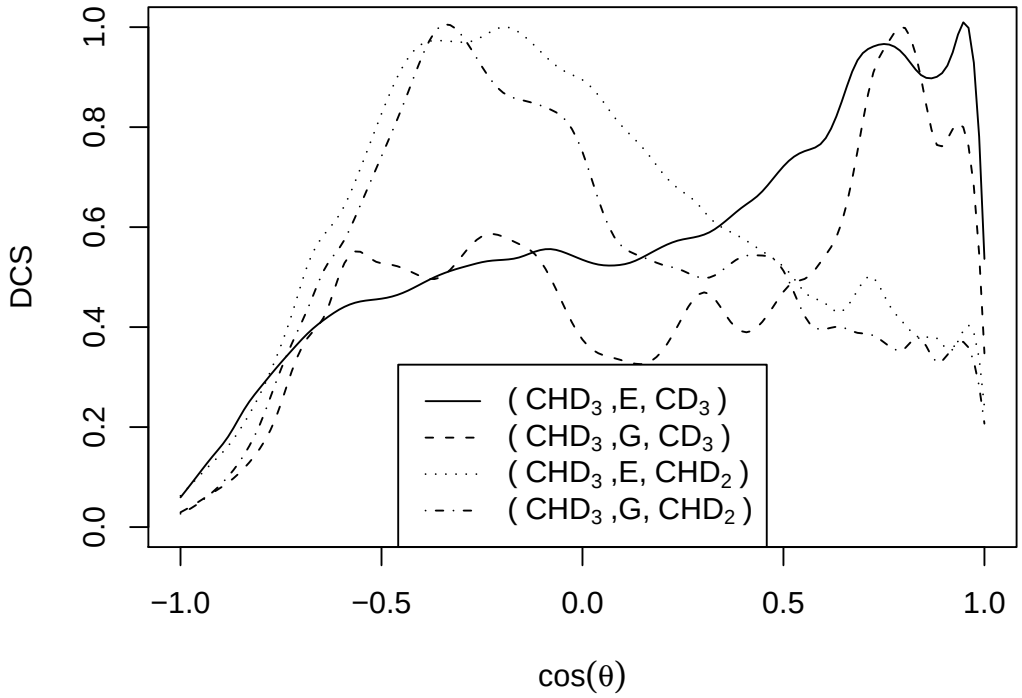

Figure 8.2: CD_3 and CHD_2 differential cross sections.

expected just based on a difference in rotation constant) and this reflects the relative dominance of the stripping mechanism for the HD product. These rotational distributions and their attribution to the rebound or stripping mechanism are completely consistent with the angular distributions shown for the corresponding CD_3 and CHD_3 products.

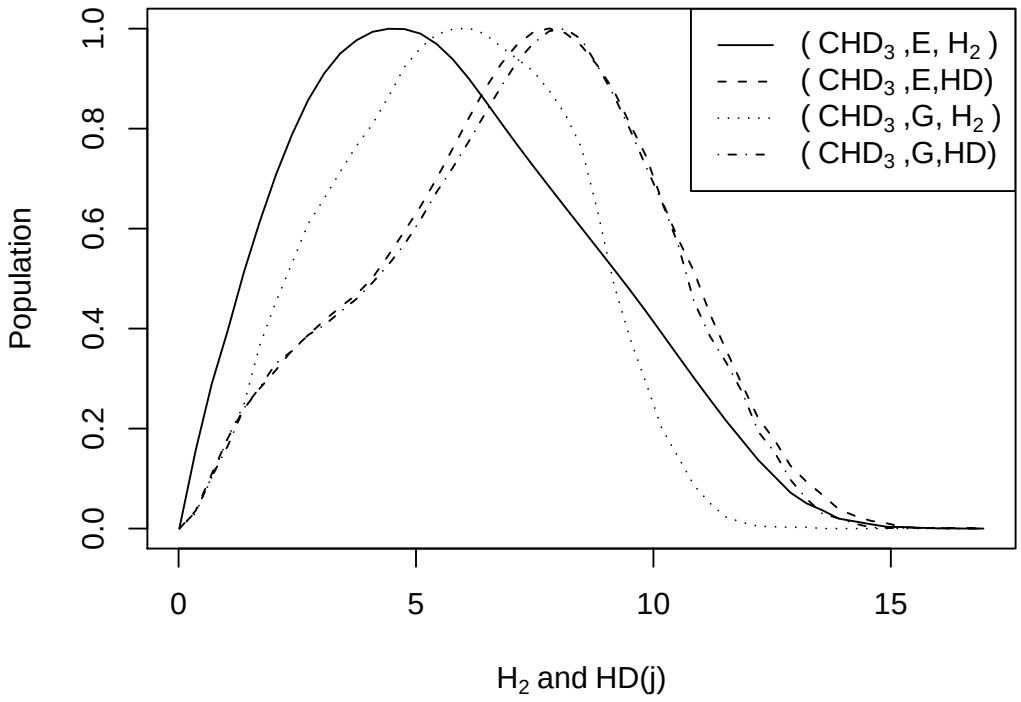

Figure 8.3: H_2 and HD rotational distributions.

8.3.4 CD_3 and CHD_2 Vibrational Energy Distributions

Fig. 8.4 shows the vibrational energy distributions of CD_3 and CHD_2 for the reactions indicated. They are all quite symmetric and unimodal. If we assign the most probable

vibrational energy to a quantum state we would assign the products of the reaction with $CHD_3(\nu_1 = 0)$ to the zero-point state. For the reaction with $CHD_3(\nu_1 = 1)$ we would assign the product CD_3 to the zero-point state with excitation in some other mode(s). Examination of trajectories indicates some excitation in the CD_3 umbrella mode, ν_2. For the CHD_2 product, which has the largest amount of vibrational energy, the peak position equals 84 percent of the sum of the harmonic ZPE plus one quanta of C-H stretch. Inspection of trajectories does confirm that the C-H stretch is excited in the CHD_2 product, confirming this assignment. This indicates again that excitation of the C-H stretch in CHD_3 is well-preserved in the reaction at least at the high energy considered here. This finding is completely consistent with the conclusions of Zare and co-workers [101].

8.4 Summary and Conclusions

We reported quasiclassical trajectory calculations of the reaction of H with CHD_3 at an initial relative kinetic energy of 1.53 eV and with the C-H stretch excited and unexcited, using an *ab initio*-based potential energy surface. Reaction cross sections for the two sets of products were presented as were the angular and vibrational distributions of the CD_3 and CHD_2 products and the rotational distributions of the H_2 and HD products. For the ground state reaction the cross sections are small, i.e., 0.13 and 0.28 $Bohr^2$ respectively for H-and D-abstraction. For the vibrationally excited reaction the cross section for H-abstraction is enhanced by a factor of 14 whereas the cross section for D-abstraction is virtually unchanged. This clearly indicates the the C-H stretch is highly localized and remains so during the reaction. These results were compared to recent experiments of Zare and co-workers. Agreement with experiment

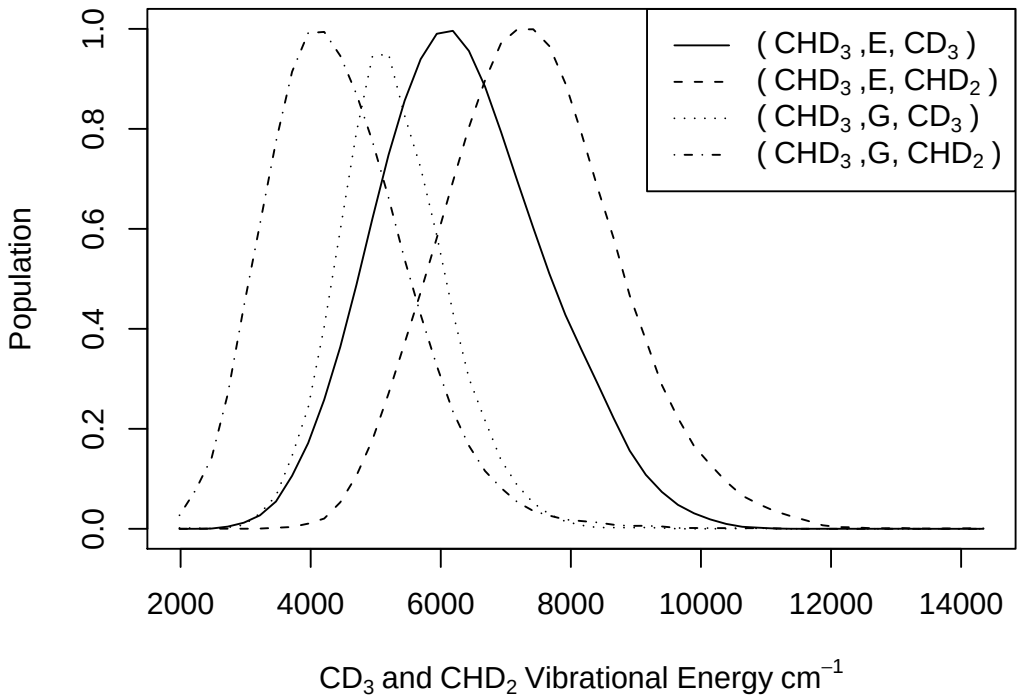

Figure 8.4: CD_3 and CHD_2 vibrational energy distributions. The positions of peaks from left to right are 4160, 5120, 6080 and 7280 cm^{-1}.

is good and conclusions drawn in that work are confirmed in the calculations. Finally, evidence was presented that indicates that the reaction to abstract H is dominated by the rebound mechanism whereas abstraction of D is dominated by the stripping mechanism.

Acknowledgments JMB thanks the Department of Energy (DOE-DE-FG02-97ER14782) for financial support. Support for computational resources from ONR/DURIP is also acknowledged.

9 CH_5^+/CH_5

Abstract

Dissociative charge exchange of CH_5^+ with Cs, coupled with quasiclassical trajectory calculations on an ab initio PES for CH_5, has been used to probe the structure of the CH_5^+ cation. Product kinetic energy release distributions and branching ratios for $CH_5 \rightarrow CH_4 + H$ and $CH_5 \rightarrow CH_3 + H_2$ have been compared. The agreement of the product branching ratios provides evidence for the fluxional nature of CH_5^+.

9.1 Probing the Structure of CH_5^+ by Dissociative Charge Exchange

The simplest nonclassical carbonium ion is CH_5^+ [102]. It is an important ion in the interstellar medium, where it is formed via radiative association of $CH_3{}^+$ and H_2 [103]. The ion was first observed in a mass spectrum in the 1950s and later shown to dissociate upon neutralization by charge exchange [104]. However, it has only been within the past 10 years that Oka and co-workers were able to measure its high resolution infrared spectrum [105]. The highly fluxional character of the CH_5^+ zero-point wave function and the "quantum deconstruction" of the IR spectrum using a global potential energy surface (PES) was recently reported [106]. The H atoms freely exchange by passage over low energy isomerization barriers of C_s and C_{2V} symmetry. The neutralization of CH_5^+ by dissociative recombination with free electrons is of importance in astrophysics, and there has been some controversy about the product branching ratios from ion storage ring and flowing afterglow measurements [107,108]. From a fundamental perspective the attachment process serves as a probe of the nascent phase space of CH_5^+.

In the current work, the product branching ratios in the dissociative charge exchange (DCE) of CH_5^+ with Cs are examined and compared to predictions using quasiclassical trajectory calculations on accurate *ab initio* potential energy surfaces. In these experiments, fragment channels 9.1 and 9.2 are detected in coincidence, yielding product kinetic energy release (KER) distributions and the branching ratios.

$$CH_5 \rightarrow CH_4 + H \tag{9.1}$$

$$CH_5 \rightarrow CH_3 + H_2 \tag{9.2}$$

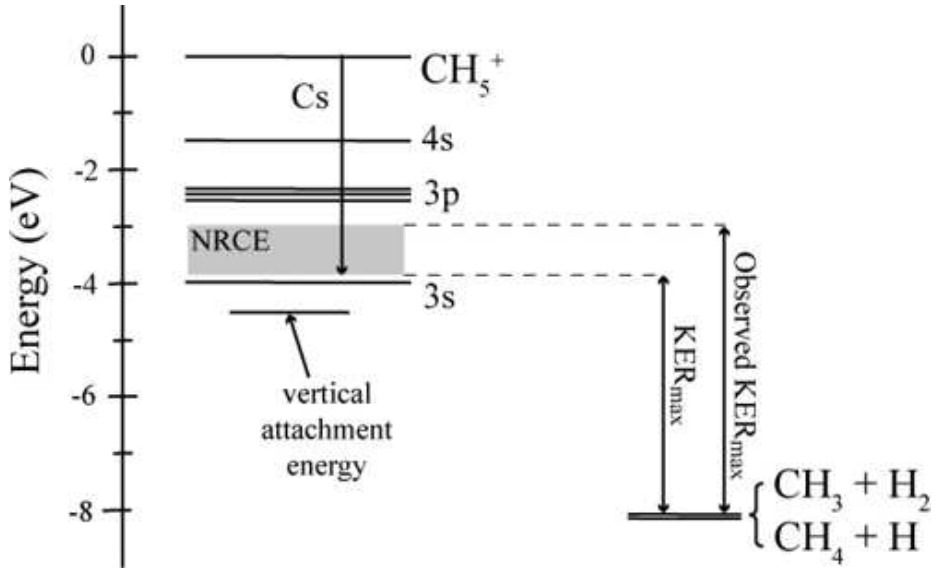

Figure 9.1: Energy level diagram showing the two energetically accessible dissociation limits of CH_5 and where on the neutral surface the CH_5 is formed via DCE with Cs. The three-body dissociation limit is nearly resonant with the 3S state and was not observed

The comparison with theory provides experimental evidence for the fluxional nature of CH_5^+. The experimental apparatus has been described elsewhere and will only be discussed briefly [109]. CH_5^+ was formed with a pulsed discharge in a supersonic expansion (1 kHz) with a 1:9:60 $CH_4/Ar/H_2$ mixture. This source is expected to produce CH_5^+ with a rotational temperature of 20-60 K and a vibrational temperature less than 1660 K as discussed further in the Supporting Information (SI). The cations were skimmed, accelerated to 16 keV, and massselected by time-of-flight. Before reaching the Cs cell all ions with the exception of CH_5^+ are deflected. The transient CH_5 is formed when it is passed through an $\sim$ 1mm^3 interaction region

containing $\sim 1 \times 10^{-5}$ Torr of Cs. Remaining CH_5^+ is deflected into an ion detector. The neutral fragments fly ~ 110 cm to a multiparticle time and position-sensitive detector. Using this information along with the parent mass and ion beam velocity, the fragment masses and center-of-mass KER of each dissociation channel can be calculated, yielding experimental N(KER) distributions. These experimental distributions are corrected to yield P(KER) probability distributions by accounting for any loss of products owing to the kinematics as discussed in the Supporting Information (SI). Integration of the P(KER)s over KER yields product branching ratios from a single data set.

To simulate the experiment, quasiclassical trajectory (QCT) calculations were performed in the classical Franck-Condon approximation, i.e., by making vertical transitions from the CH_5^+ phase space to CH_5 using an *ab initio* PES for CH_5 [67]. The CH_5^+ phase space was obtained from trajectories with the quantum zero-point energy of roughly 11000 cm^{-1} on an *ab initio* CH_5^+ PES [110]. In addition to these vertical trajectories, two other batches were run with initial kinetic energy to be consistent with the experiment for the "resonant" and "nonresonant" cases, as described below and in detail in the SI. Product branching ratios, internal energy distributions, and the KER distributions were obtained from roughly 25000 trajectories with zero total angular momentum for each of these cases. For diagnostic purposes, trajectories were also performed at the CH_5^+ equilibrium geometry with standard normal mode sampling of initial conditions appropriate for a semirigid molecule [66] for both the vertical transition and the nonresonant case.

Experimentally, the neutral CH_5 is formed slightly (~ 0.1eV) above the predicted energy of the 3S Rydberg state [111], rather than directly on the ground neutral

surface, as assumed in the calculations. The transition to the neutral surface is assumed to be vertical. The two lowest dissociation channels are nearly isoenergetic as shown in Figure 9.1 . Although H_2 loss is kinematically more favorable to detect, H atom loss is found to be the dominant dissociation channel.

The difference in energy between the ground vibrational state of $CH_5^+ + e^-$ and the dissociation limit of CH_4 + H from the present PESs is 8.0 eV, in agreement with the experimental estimate of 8.0 ± 0.5 eV [112]. (This is further discussed in the SI.) For the case of resonant charge exchange with Cs, the neutral is formed 3.9 eV below the cation, yielding a maximum KER (KER_{max}) of 4.1 eV, approximately the same for both product channels.

However, the experimentally observed KER_{max} is $\sim$ 5eV. This may be a result of some vibrational excitation in CH_5^+ as well as nonresonant charge exchange [113] leading to the production of neutral states above the resonant level. Experimentally, the branching ratio is $11 \pm 2 : 1$, for H loss to H_2 loss. The results from the three batches of trajectories described above using the correct "fluxional" phases pace sampling of CH_5^+ are 14:1 (vertical), 11:1 (resonant), and 9:1 (nonresonant) in very good accord with the experiment. The results from standard mode sampling are 34:1 (vertical) and 18:1 (nonresonant) which are not in agreement with experiment. This result provides a strong consistency argument for the fluxional nature of the parent CH_5^+ cation determining the experimental branching ratio.

The P(KER) for the dominant channel, CH_4 + H, is shown in Figure 9.2(a), along with the theoretical prediction. Both exhibit a peak with a shoulder at lower energy. It is clear that most of the energy goes into internal excitation (vibrational and rotational) of the CH_4, as shown by the small probability for products at KER_{max}.

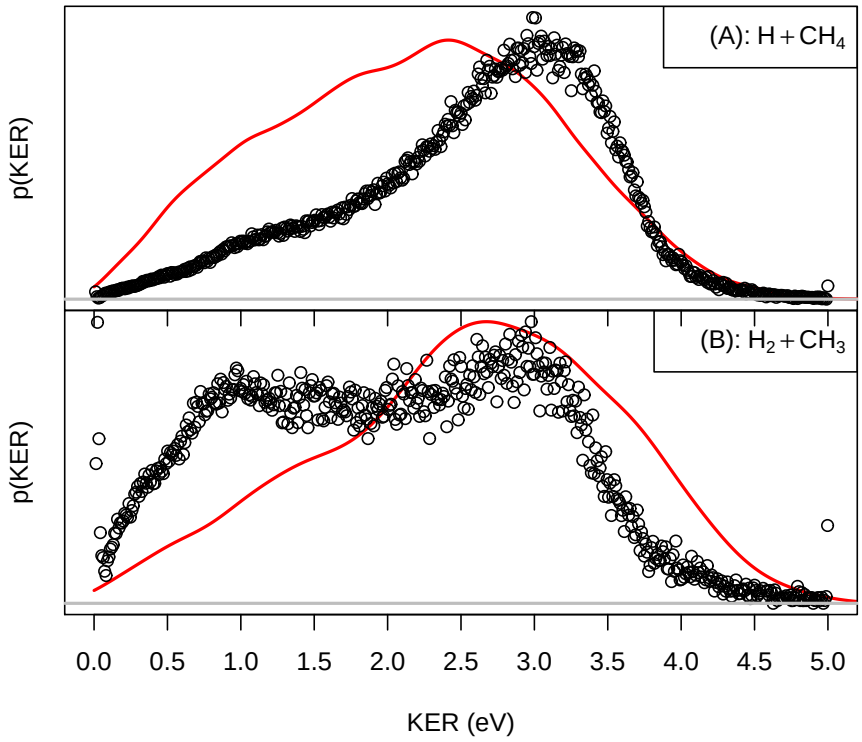

Figure 9.2: (a) P(KER) distribution for $CH_5 \rightarrow CH_4 + H$ and (b) $CH_5 \rightarrow CH_3 + H_2$. The open circles represent the experimental KER, while the solid line is the theoretical KER

The P(KER) for the molecular hydrogen loss channel is shown in Figure 9.2(b). This channel exhibits a bimodal distribution, with peaks at 1.0 and 2.9 eV. The theoretical KER peaks at approximately 2.8 eV but does not reveal the bimodal distribution seen experimentally; however, a shoulder at around 1.3 eV is observed.

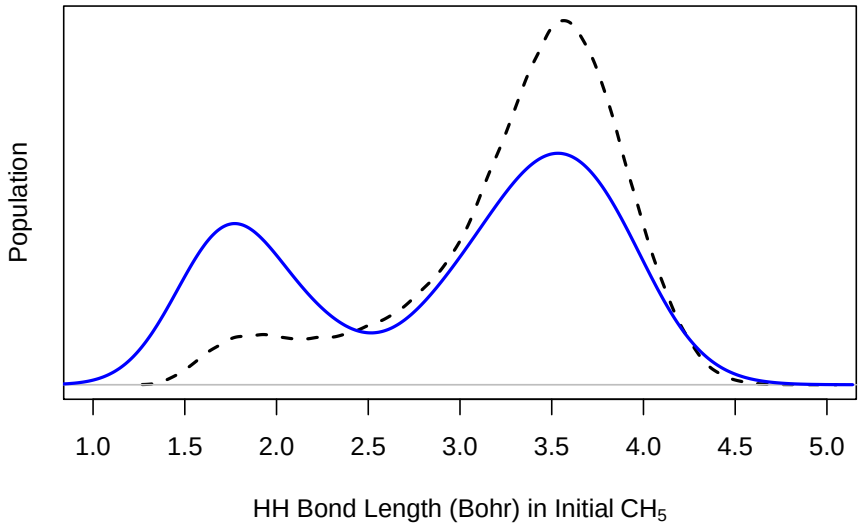

Figure 9.3: Classical HH bond length distribution of CH_5^+ with zero-point energy (dashed curve) and magnified part of that distribution that correlates with the CH_3 + H_2 products. The shoulder near 2.0 Bohr corresponds to the H2 moiety, whereas the peak at 3.5 Bohr corresponds to the HH distances with H atoms in the CH_3 group.

The explanation for this shoulder comes from consideration of the HH bond length distribution in the parent CH_5^+ and more significantly the portion of that distribution that correlates with CH_3 + H_2 products; both are shown in Figure 9.3. The full classical distribution, which agrees well with quantum diffusion Monte Carlo calculations [41], is bimodal with a short bond length corresponding to the H_2 moiety in CH_5^+ and a long bond length arising from the other HH distances. The distribution correlating with CH_3 + H_2 shows a larger contribution from the short HH distance than

the long one. Examination of the trajectories leading to highly vibrationally excited H_2 indicates a greater contribution from the large HH bond length in the correlated distribution than from the short HH bond length. It is important to note that the corresponding correlated distribution from the normal mode sampling is unimodal for both the vertical and nonresonant cases with a peak at the HH moiety equilibrium distance. Also the corresponding $CH_3 + H_2$ P(KER) for the nonresonant case shows less probability at low KER than that seen for the theoretical P(KER) with fluxional phase space sampling shown in Figure 9.3. The vibrational distributions of CH_3 and H_2 are shown in the SI.

QCT calculations are not exact dynamics, and there are also uncertainties in the CH_5 PES. However, both represent the current, feasible state-of-the-art calculations for a problem this complex. With these caveats in mind, the agreement between the experimental and theoretical branching ratios provides evidence that the quantum mechanically predicted fluxional nature of CH_5^+ [41] is responsible for the experimental branching ratio. However, the lack of quantitative agreement between the calculations and experiment for the more dynamically detailed KERs, in particular, the bimodal distribution in the $CH_3 + H_2$ channel, may indeed result from these caveats. Neglect of the coupling of the 3S Rydberg state to the ground electronic state in the present calculations may also play a role in the discrepancy.

DCE experiments on selected isotopologues of CH_5^+, namely $CD_3H_2^+$, CD_4H^+, and CD_5^+, have also been performed. Comparison of those results with QCT simulations will be reported and discussed in a later publication.

Acknowledgment J.E.M., J.D.S., and R.E.C. thank the AFOSR (Grant FA9550-04-1-0035). Z.X. thanks the NSF (Grant CHE0446527), and B.J.B. and J.M.B. thank

the ONR (Grant N0001405-0460).

Supporting Information Available: Branching ratio calculations; detection efficiency; ion temperature; details of QCT calculations and energetics. This material is available free of charge via the Internet at http://pubs.acs.org.

9.2 Supporting Information

In the supporting information, several issues will be clarified from both an experimental and theoretical perspective. Experimentally, the temperature of the CH_5^+ formed in the pulsed discharge supersonic expansion ion source will be discussed, followed by the procedure used to extract the product branching ratios. Theoretically, further details concerning the energetics and the quasiclassical trajectory (QCT) calculations and results are presented.

9.2.1 Experimental

CH_5^+ Temperature Accurate knowledge of the vibrational and rotational distributions in the cation beam is necessary to determine the total available energy for the dissociation and assign the features observed in the kinetic energy release (KER) spectra. In the case of the dissociation of CH_5, there are no peaks in the KER that can be assigned to vibrational or rotational excitation in the cation, so the temperature of CH_5^+ cannot be determined directly. However, the dissociative charge exchange (DCE) of O_2^+ with Cs and the DCE of H_3^+ with Cs can be used to determine the vibrational temperatures for different vibrational frequencies of ions produced in the pulsed discharge supersonic expansion. In addition, spectroscopic studies of H_3^+

formed in a similar ion source can provide an estimate of the rotational temperature.

The DCE of O_2^+ with Cs is used to calibrate the detector [114] in these experiments. The dissociation dynamics of the DCE of O_2^+ with Cs have been studied previously [115, 116] and have shown that the vibrational distribution of the cation can be correlated to peaks in the KER of the neutral dissociation. A thorough study of the vibrational distribution of the O_2^+ beam was carried out by Petrignani and coworkers in 2005 [117]. In that experiment the ions were generated in different vibrational populations, neutralized by Cs and their KER measured. The P(KER) for the DCE of a 16 keV beam of O_2^+ with Cs, which was collected as a calibration file for the data presented in this work, is shown in Figure 9.4 . The KER at 16 keV shows the most vibrational excitation observed in the O_2^+/Cs spectra collected on this apparatus, and its temperature is taken as an upper limit for the 1904.7 cm^{-1} harmonic frequency of O_2^+. It should be noted that the KER shown in Figure 9.4 actually has less vibrational excitation than the coldest spectrum collected by Petrignani et al [117]. The main feature of the O_2 KER are the peaks at 1.06 and 1.15 eV, corresponding to the dissociation of the low-lying Rydberg states of O2 shown in reactions 9.3 and 9.4 below:

$$O_2^+(X^2\Pi_g, \nu = 0) \xrightarrow{Cs} O_2^*(3s\sigma^3\Pi_g, \nu = 0) \rightarrow O(^3P) + O(^1D) + KER \qquad (9.3)$$

$$O_2^+(X^2\Pi_g, \nu = 0) \xrightarrow{Cs} O_2^*(3s\sigma^1\Pi_g, \nu = 0) \rightarrow O(^3P) + O(^1D) + KER \qquad (9.4)$$

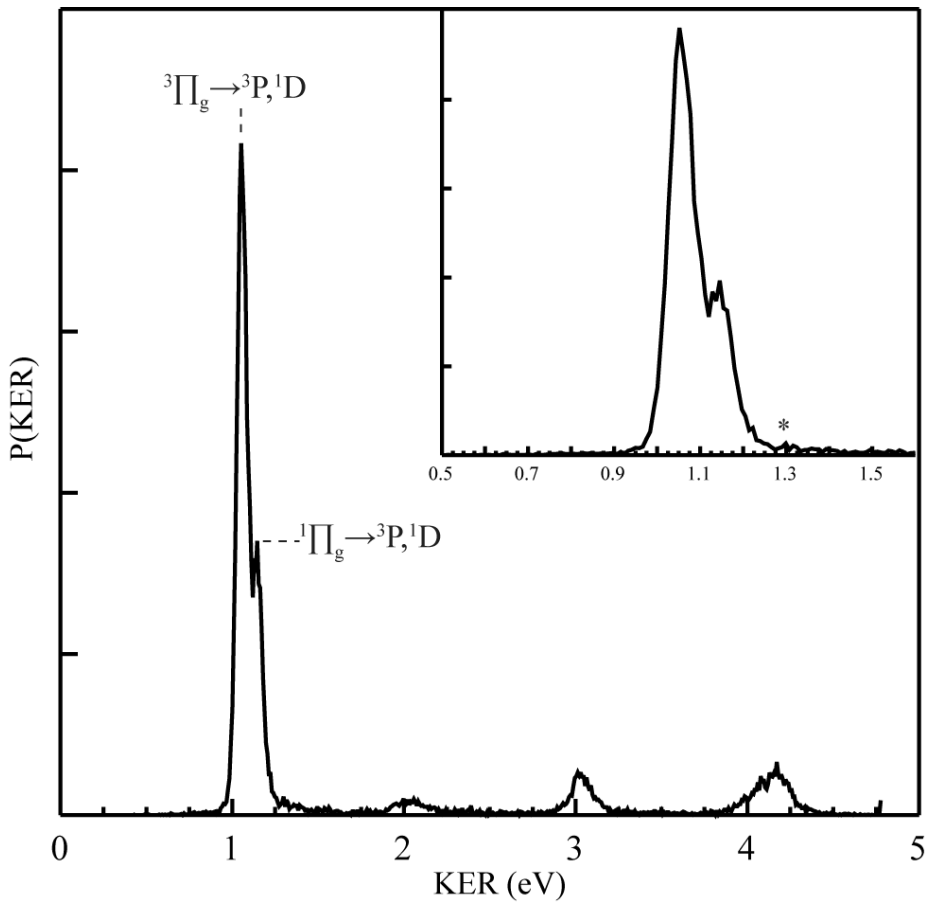

Figure 9.4: The P(KER) of DCE of O_2 with Cs. The * marks the location of the dissociation resulting in $\nu = 1$ excitation in O_2^+

In order to determine an approximate temperature for the O_2^+ beam, the spectrum between 0.5 and 1.5 eV was fit to four Gaussian distributions, one each for the peaks at 1.06 eV, 1.15 eV, one for the dissociation of the $O_2^*(3s\sigma^3\Pi_g, \nu = 1)$ peaked at $\sim$ 1.3 eV, and one for the background. The fits of the first and third Gaussian were integrated and a beam temperature of 710 K was obtained by using a Boltzmann distribution. The fit assumed that the only two vibrational states of the cation to contribute to the spectrum were the $\nu = 0$ and $\nu = 1$ states. At the calculated beam temperature, 98% of the O_2^+ is in the $\nu = 0$ state, while 2% is in the $\nu = 1$ state.

9 CH_5^+/CH_5

The 3-body dynamics of the dissociation from DCE of H_3^+ with Cs has also been studied on this apparatus and the results presented in a previous publication [113], so the KER will not be shown here. The KER of this dissociation shows a peak at 1.5 eV corresponding to overlapping contributions of vibrational excitation in the ν_1 (3178 cm^{-1}) [118] and ν_2 (2521 cm^{-1}) [119] modes of H_3^+. A similar treatment to that followed for O_2^+ was applied to recent data for 16 keV H_3^+/Cs, with the further assumption that only the higher energy vibration $\nu_1 = 1$ contributes. This provides an upper limit to the vibrational temperature for this mode of 1660 K. It should also be noted that McCall and co-workers [120] have used an ion source almost identical to the one used in this experiment in order to produce rotationally cold (20-60 K) H_3^+. The dependence of the rotational temperature on source conditions was studied by changing several parameters and was insignificant.

The O_2^+/Cs and H_3^+/Cs experiments provide evidence for vibrational temperatures of 710 K (1872 cm^{-1}), 1660 K (3178 cm^{-1}) and a rotational temperature of $\sim$ 40 K. CH_5^+ has twelve normal modes of vibration, 200, 839, 1297, 1303, 1478, 1500, 1587, 2418, 2708, 3001, 3133, and 3224 cm^{-1} [110]. The average thermal excitation energy in CH_5^+ can be calculated using the sum of the average energy of each normal mode in the separable harmonic approximation. As noted in the manuscript, excess energy of 0.9 eV was added to the QCT calculations to match the experimental KER. If all of this excess energy derived from vibrational excitation in the cation as opposed to near-resonant charge exchange, it would imply a vibrational temperature of 1840 K, which is likely in excess of the true cation temperature. Lower frequency vibrations are expected to relax more efficiently in a supersonic expansion and a reasonable model for the vibrational excitation would use the 40 K rotational tempera-

ture as a lower limit on the vibrational temperature, with the temperatures scaling quadratically with vibrational frequency using the experimental points at 1872 cm^{-1} and 3178 cm^{-1} discussed above. This fit yields a CH_5^+ internal energy an order of magnitude lower $\sim$ 0.09 eV. This treatment ignores possible chemical variations in vibrational relaxation in the source. However, coupled with the relative insensitivity of the QCT branching ratios to this CH_5^+ internal energy, these considerations lead us to conclude that ambiguity concerning the initial state of the cation in the experiment is not a significant issue.

Product Branching Ratios Both channels are collected simultaneously and the same data set is used to determine the branching ratio. Descriptions of the calculations for the fragment masses, center-of-mass velocity, and kinetic energy release have been described elsewhere [114]. The parent and fragment masses are set for a specific channel. The centroid for each dissociation event is calculated in terms of the position-of-arrival of the center-of-mass at the detector in each dimension, x, y, and z, where x and y are on the face of the detector and z is in the direction of the beam. The centroid is based on the conservation of momentum between the two particles, for example in the z coordinate:

$$z_{\text{centroid}} = \sum_{i=1}^{j} m_i \cdot \nu_{z,i} \tag{9.5}$$

Here, j is the number of fragments, m_i is the assigned mass, and $\nu_{z,i}$ is the center-of-mass velocity in the z direction. In order to separate the two channels, assuming that the dissociation is prompt, the events that are associated with the assigned fragment masses will have centroid values between $\pm$1 mm, while dissociation events associated

with the other fragmentation channel and false coincidences will be outside this range. The fragment mass distribution is calculated using the three-dimensional recoil radius at the detector and the parent mass by the following equations

$$m_{\text{calc},2} = M \cdot \frac{d_1}{d_1 + d_2} \tag{9.6}$$

where d_i is given by the equation:

$$d_i = \sqrt{x_i^2 + y_i^2 + z_i^2}. \tag{9.7}$$

The mass of the other particle, $m_{\text{calc},1}$, is determined in a similar manner with an error of $m/\Delta m = 32$ at 16 amu. In the case of CH_5, a plot of the calculated fragment mass for all particles shows peaks at 1, 2, 15, and 16 amu, consistent with the two fragmentation channels observed. Calculated masses between the FWHM of the assigned fragment mass are assigned to belong with the appropriate channel. The experimental KER distribution, given by, $N_n^E(\text{KER})$, where n is the dissociation channel, over the range of 0-5 eV for data falling within the centroid and mass ranges previously stated is obtained. As discussed in the paper, the kinematics of the dissociation causes some fragments to miss the detector [121]. A corrected $P_n(\text{KER})$ distribution, taking this into account, is determined using a Monte Carlo simulation of the experiment for a constant KER distribution over the same range as the experiment. From the simulation the $N_n^{\text{MC}}(\text{KER})$ distribution is obtained. The detector-acceptance function (DAF) corrected $P_n(\text{KER})$ is calculated by the following equation:

$$P_n(KER) = \frac{N_n^E(KER)}{N_n^{\text{MC}}(KER)} \cdot \eta. \tag{9.8}$$

In this equation, η is a normalization factor, taken as the maximum intensity of the N_n^{MC}(KER). This assumes that 100% of the particles will be detected at the maximum intensity of the N_n^{MC}(KER) distribution. Once a P_n(KER) is obtained for each channel, the branching ratio (BR) is calculated using the following equation:

$$BR = \frac{\int_0^{5eV} P_1(KER)dKdKER}{\int_0^{5eV} P_2(KER)dKER} \tag{9.9}$$

The P_n(KER) of each channel are integrated and the ratio of the integration between the two channels is the branching ratio.

The other significant question experimentally involves the detection efficiency for the neutral products with the microchannel-plate-based time- and position-sensitive detector. At a beam energy of 16 keV, the laboratory energies of the CH_4, CH_3, H_2 and H products are 15060, 14120, 1880, and 940 eV, respectively. The difference between the energies of H_2 and H laboratories energies is the largest, and the detection efficiencies of these would be the most likely source of error. However, examination of the work of Peko and Stephen [122] indicates that at lab energies approaching 1000 eV the detection of both H and H_2^+ converge to approximately equal detection efficiencies. H_2 was not specifically measured in this study, however, H^-, H and H^+ were and all of the detection efficiencies for these species also saturated $\sim$ 1000 eV. Thus, the detection efficiency of this experiment for H and H_2 should be nearly the same and will not significantly effect the branching ratio calculation.

9.2.2 Theoretical

Energetics Energetics from the potential energy surface (refs. 67 and 110) that lead to the adiabatic electron attachment energy are given in Figure 9.5.

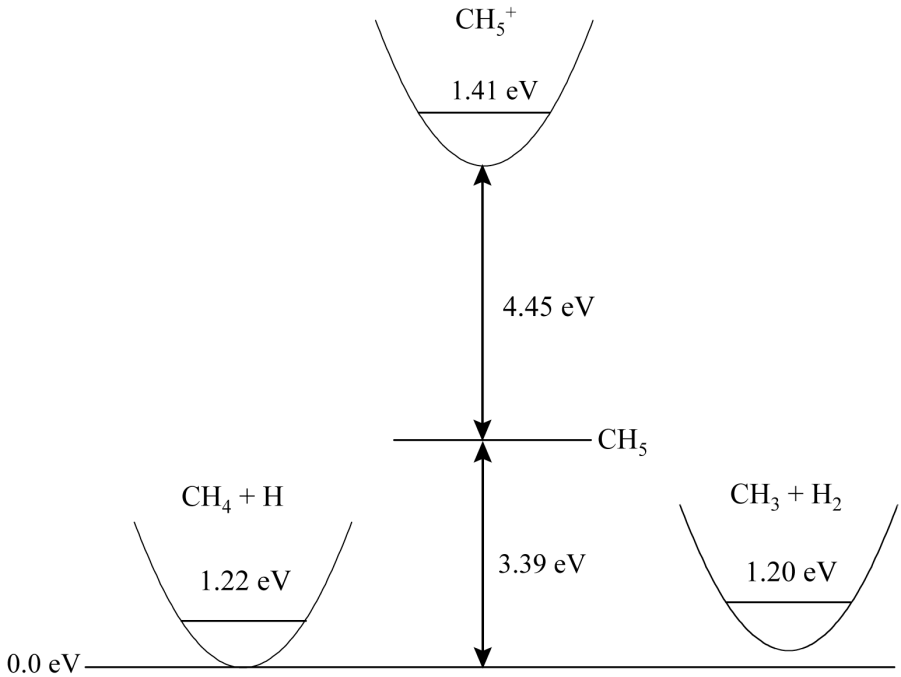

Figure 9.5: Schematic of the potential and zero point energies (in eV) of CH_5^+, CH_5 and products CH_4 + H, CH_3^+ + H_2 from the potential energy surfaces. The CH_5^+ zero point energy (ZPE) is relative to the CH_5^+ global minimum, and the neutral products harmonic ZPEs are relative to CH_4(eq) + H. The vertical attachment energy from the minimum of the CH_5^+ PES to the neutral PES is 4.45 eV and the energy at that geometry on the neutral PES is 3.39 eV relative to CH_4(eq) + H. Thus the adiabatic attachment energy from the PESs $\approx$ 8.0 eV for either product

The initial conditions for the three sets of quasiclassical trajectory calculations were obtained as follows. First trajectories were run for CH_5^+ with zero total angular momentum and with the approximate quantum zero point energy of 11000 cm^{-1} to establish the associated phase space in Cartesian coordinates and momenta, denoted $\rho(\mathbf{p}, \mathbf{q})$. (The trajectories were "equilibrated", i.e., run long enough to sample the minima of the highly fluxional CH_5^+ and the distribution of HH bond lengths, shown in Figure 9.3, was obtained from the CH_5^+ phase space distribution.) CH_5 trajectories for the "vertical" case were initiated with coordinates and momenta sampled from $\rho(\mathbf{p}, \mathbf{q})$. For example, from Figure 9.5 the value of the potential is 3.39 eV (corresponding to the geometry of the CH_5^+ global minimum) and the value of the initial kinetic energy would be the CH_5^+ zero-point energy, 1.41 eV for a total energy of 4.8 eV. For the resonant case we need to account for the energy released in the charge exchange with Cs. This energy is the difference between the "energy gap" (EG), defined as the difference between the CH_5^+ and CH_5 electronic energies from the respective PESs at $\mathbf{q}$ and the ionization potential of Cs, 3.9 eV. In the example in Figure 9.5 this would result in an additional kinetic energy of 0.55 eV for a total energy of 5.35 eV. Then, subtracting the ZPE of the CH_4 + H products results in a maximally observed "available energy" in relative kinetic energy of 4.1 eV. Finally, for the non-resonant case, which gives a maximum available energy of $\sim$ 5 eV due to non-resonant effects as discussed in the text a final adjustment to the initial kinetic energy was to add 0.9 eV to it. This was done by a simple scaling of the initial momenta. Thus the total initial energy of the CH_5 trajectories was 6.25 eV not 5.35 eV. Note that because EG varies somewhat with $\mathbf{q}$ the total energies of the 25000 trajectories run for the fluxional CH_5^+ phase space are distributed narrowly about the value of 6.25 eV with

a FWHM of roughly 0.25 eV.

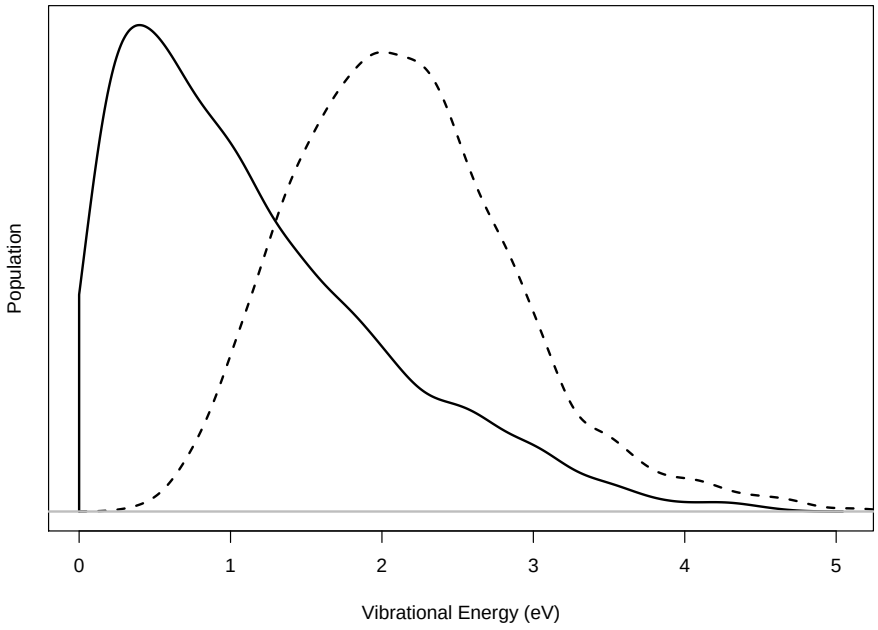

Figure 9.6: Vibrational distribution of H_2 (solid curve) and CH_3 (dashed curve) for the minor channel $CH_3 + H_2$. The energies are measured relative to the minimum of the respectively separated molecular potentials

Classical vibrational distributions were obtained for the products of the minor channel $CH_3 + H_2$ and these are given in Figure 9.6. (Note the zero point energies of H_2 and CH_3 are approximately 0.3 eV and for 0.9 eV, respectively.) The tail of the H_2 distribution at high energies is due mainly to initial HH distances that are larger than 2.5 Bohrs.

9.3 Additional Information

Here are some details for the QCT calculations of the dissociative charge exchange of CH_5^+.

To simulate the experiments, quasiclassical trajectory (QCT) calculations were performed in the spirit of Frank-Condon approximation, using the *ab initio* PESs for CH_5^+ and CH_5. Initial conditions were determined from the CH_5^+ phase space, obtained from trajectories with the quantum zero-point energy of roughly 11000 cm^{-1}. Since the experiments conditions are a little complicated and the experimentalists claimed that CH_5^+ charge exchange may occurred in both resonant and near resonant cases, for testing purpose, we simulate the whole process with some difference in charge exchange process. These processes include semi-rigid sampling, direct jumping, resonant and near-resonant models as discussed in the following sections.

9.3.1 Semi-Rigid Sampling

For semi-rigid sampling model, all the initial CH_5^+ geometries are put at the global minimum (C_s(I)) structure, then a standard normal mode sampling scheme is applied to all these geometries on the cation surface. After this is done (the **p** and **q** are determined), the potential energy surface is switched to the neutral surface (CH_5), and the trajectories propagate there.

Tab. 9.1 shows some main parameters and results for this simulation.

Table 9.1: Key parameters for semi-rigid sampling simulation

TNT[1]	NT(CH_4 + H)[2]	NT (CH_3 + H_2)[3]	Branching Ratio
1000	977	23	42.5

[1] Total number of trajectories
[2] Trajectories giving CH_4 + H
[3] Trajectories CH_3 + H_2

As can be seen from Tab. 9.1, the dissociation of nascent CH_5 are mainly CH_4 + H.

9.3.2 Direct Jumping

The semi-rigid Sampling model is not very close to the real experimental conditions, though it reveals that CH_4 + H channel is more favored to the CH_3 + H_2 channel. The second case we tested is so called direct jumping model. In this model, initially, all the CH_5^+ are sampled as that in "semi-rigid" case. Instead of jumping to the neutral surface directly, the trajectories are first propagated on the cation surface for 2000 steps to represent the correct CH_5^+ ground state phase space. Then, all the trajectories jump to the neutral surface. The geometry and momentum for each jumping CH_5^+ are kept on the neutral surface. Then those trajectories propagate until dissociation.

Tab. 9.2 shows some key parameters and the branching ratio for the reaction.

Table 9.2: Key parameters for direct jumping simulation

TNT[1]	NIS[2]	NITES[3]	NT(CH_4 + H)[4]	NT(CH_3 + H_2)[5]	Branching Ratio
50,000	50	1,000	46,725	3,275	14.3

[1] Total Number of Trajectories
[2] Number of independent simulations
[3] Number of independent trajectories in each simulation
[4] Number of trajectories giving CH_4 + H
[5] Number of trajectories giving CH_3 + H_2

One direct comparison between the experiment results and theoretical simulation is the kinetic energy release (KER) distribution which is the sum of the relative translational energy of the two fragments in the products.

The KER distributions capture some features of the experimental ones, but the may be not quite similar to the experiments considering the energy conservation in the experiments. In the experiments, the free electron is supposed to come from the

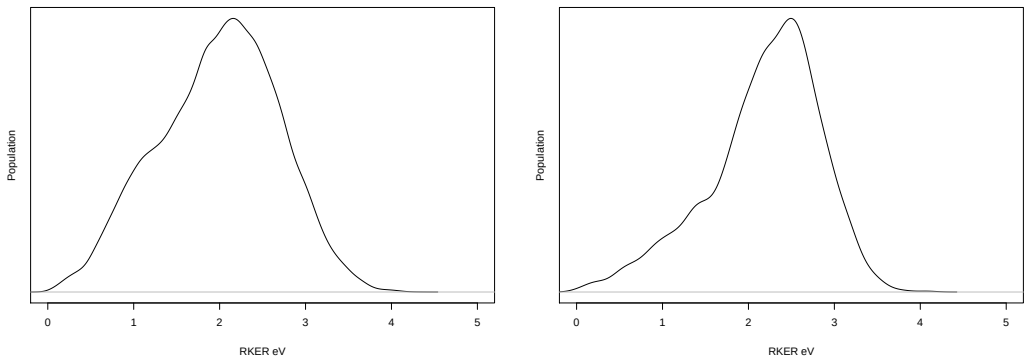

(a) H + CH_4 (b) H_2+CH_3

Figure 9.7: Kinetic energy release (KER) distribution for the two channels.

Cs atoms, considering the ionization energy of Cs atom which is roughly 3.9 eV, this energy should somehow come from the energy gap between the two potential energy surface at the jumping position. To get some idea on this energy gap, we define the potential energy gap between the cation (CH_5^+) and neutral (CH_5) at the jumping position as EG, then, we can get the EG distribution for the two channels and they are shown in Fig. 9.8. These two EG distribution should be the same and they reveals the energy difference between the two potential energy surfaces.

It's clear from the distributions that the energy gap is almost always great than the Cs ionization energy.

Associated with the energy gap and kinetic energy release, it is useful to obtain some other energy distributions for the products to understand more on the CH_5 dissociation.

Fig. 9.9 is the translational energy (TE), vibrational energy (VE) and rotational energy (RE) distributions for the CH_3 and H_2 fragments in the products. From these distributions, we can see that the both CH_3 and H_2 are vibrational excited, and H_2

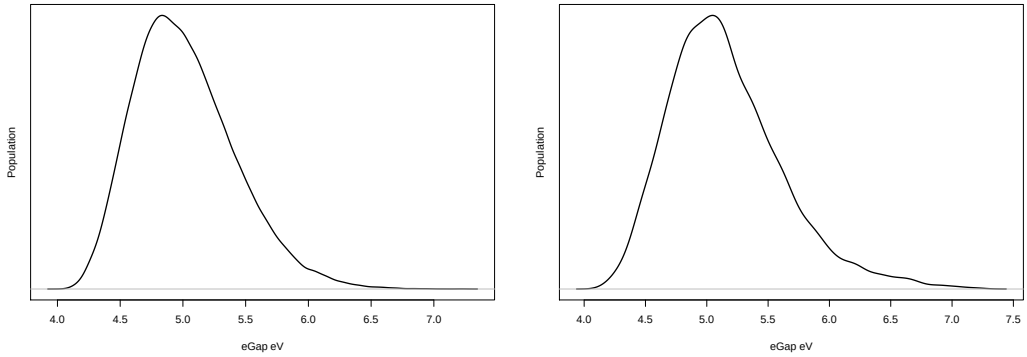

(a) H + CH_4 (b) H_2+CH_3

Figure 9.8: Energy gap (EG) distribution for the two channels. (a) is the EG distribution for H + CH_4 channel and (b) is for H_2 + CH_3 channel.

is rotationally hot.

Fig. 9.10 is the various energy distributions for both CH_4 and H in the CH_4 + H channel. Similarly, the CH_4 is vibrationally excited.

One of the goals of the experiments on this project is to explore the fluxional nature of CH_5^+, and also for the simulation. There are some DMC work done by McCoy on CH_5^+, and here we want also get the various bond length distributions in CH_5^+ as shown in Fig. 9.11. It clearly shows that the five H atoms are scrambled in CH_5^+ from Fig. 9.11 (a), but these H atoms are classified into two main groups as seen from Fig. 9.11 (b). One group H atoms are closed to each other and the H atoms in the other groups are loosely gathered.

Since there are mainly two groups on H atoms in CH_5^+, one consequent interesting issue is which group does the H_2 in CH_3 + H_2 channel comes from. If we label all the five H atoms in CH_5^+ and trace back the two H atoms in the final products H_2 to the nascent CH_5, and then get the bond length distribution of the two H atoms in the nascent CH_5 and draw the plot as shown in Fig. 9.11 (c), we can see that almost all

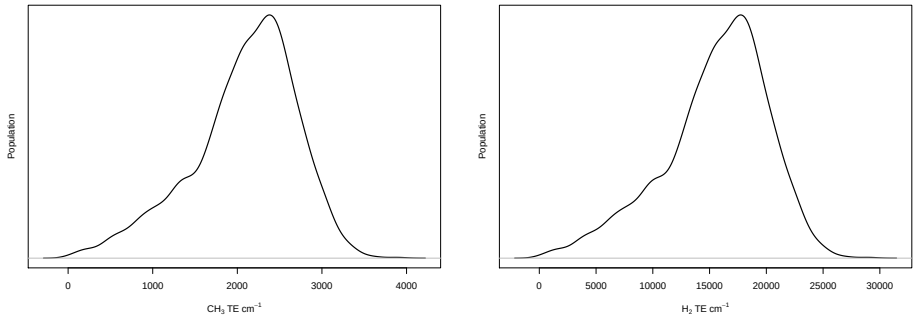

(a) CH_3 TED

(b) H_2 TED

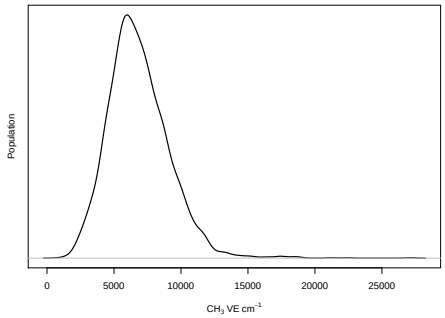

(c) CH_3 VED

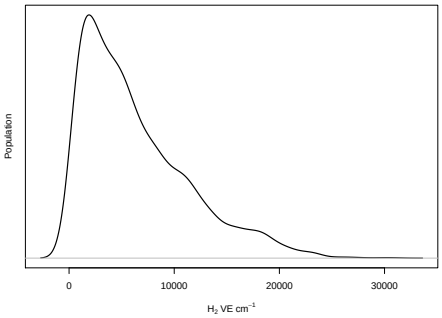

(d) H_2 VED

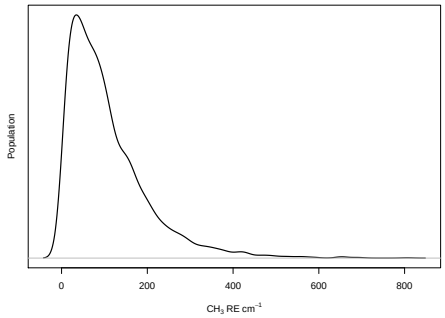

(e) CH_3 RED

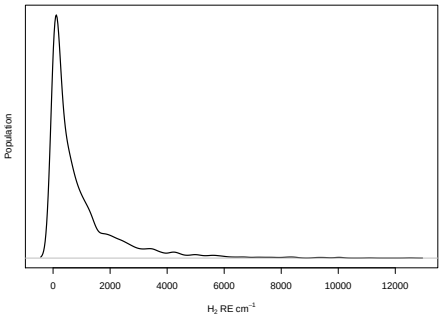

(f) H_2 RED

Figure 9.9: CH_3 and H_2 translational energy (TE), vibrational energy (VE) and rotational energy (RE) distributions from channel $CH_3 + H_2$ in the direct jumping model.

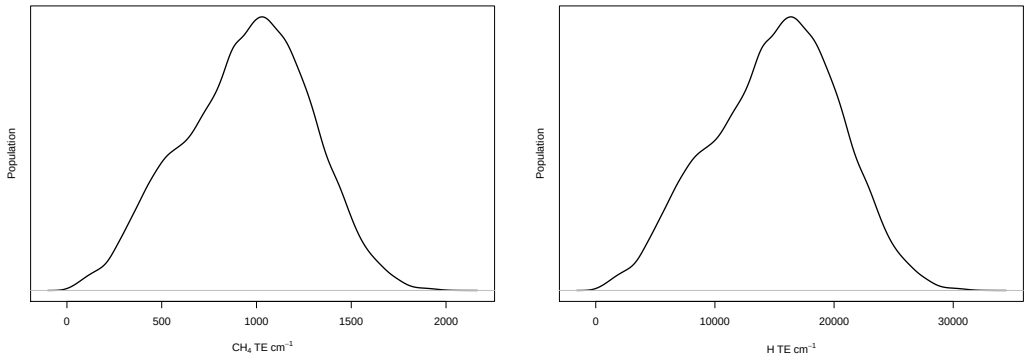

(a) CH_4 TED (b) H TED

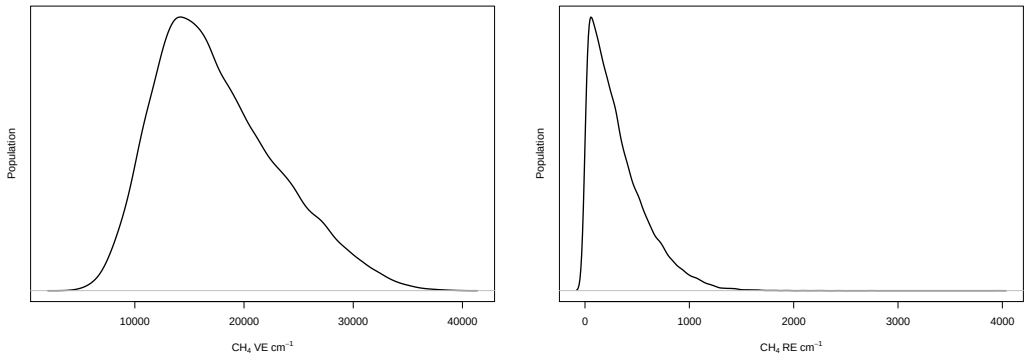

(c) CH_4 VED (d) CH_4 RED

Figure 9.10: CH_4 translational energy (TE), vibrational energy (VE) and rotational energy (RE) distributions and H translational energy distribution from channel CH_4 + H in the direct jumping model.

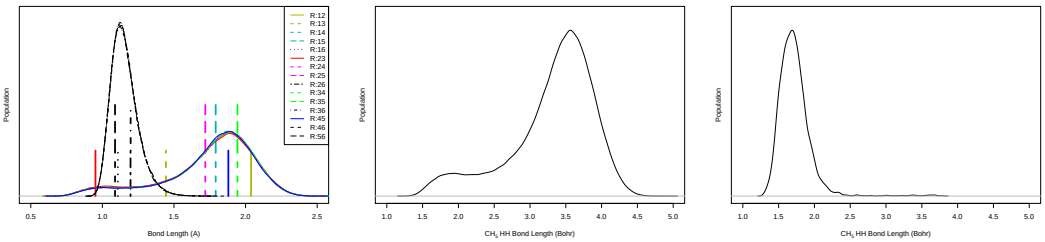

(a) (b) (c)

Figure 9.11: Bond length distribution for the CH_5^+ at the jumping position. (a) is the bond length distribution for all the bonds in CH_5^+, (b) is the bond length distribution for all the HH bonds and (c) is the bond length distribution for those HH pairs which finally appear in the products of the channel CH_3+H_2.

the H_2 are from the short HH distance group in CH_5^+. Here we should note that, the short HH distance group in CH_5^+ may not be the original diatomic part HH in CH_5^+. This reveals the fluxional nature of CH_5^+ and also that the five H atoms in CH_5^+ are not identical.

9.3.3 Resonant Case

In the CH_5^+ charge exchange dissociation experiment, both resonant and near-resonant cases are possible. For resonant case, we suppose that potential energy gap all goes into the nascent CH_5 except for the energy to ionize Cs atom which is about 3.9 eV. Consequently, the sampling of the CH_5^+ phase space is the same as in the direct jumping case. The only difference in the algorithm is the energy difference between energy gap and Cs ionization energy is treated as some extra kinetic energy for the nascent CH_5^+.

Tab. 9.3 shows some key parameters for this simulation and the main difference between this case and direct jumping model is the branching ratio decreasing.

Table 9.3: Key parameters for resonant case simulation

TNT[1]	NIS[2]	NITES[3]	NT(CH_4 + H)[4]	NT(CH_3 + H_2)[5]	Branching Ratio
50,000	50	1,000	45,847	4,124	11.1

[1] Total Number of Trajectories
[2] Number of independent simulations
[3] Number of independent trajectories in each simulation
[4] Number of trajectories giving CH_4 + H
[5] Number of trajectories giving CH_3 + H_2

Fig. 9.12, 9.13, 9.14, 9.15, 9.16 show the similar distributions to those in the direct jumping model.

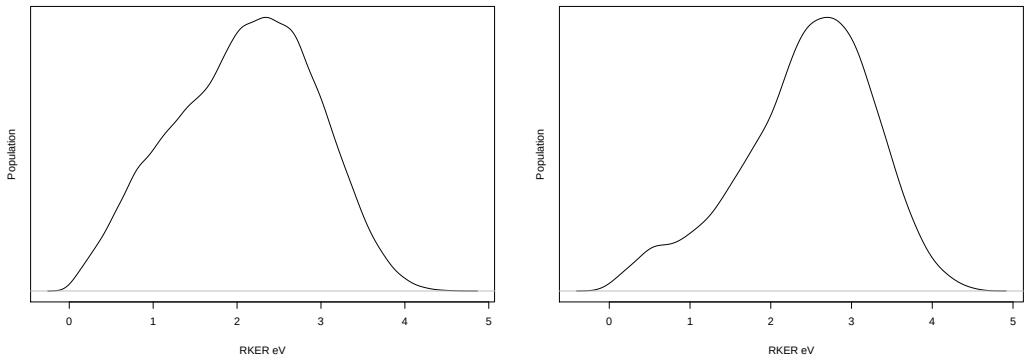

(a) H + CH_4 (b) H_2+CH_3

Figure 9.12: Kinetic energy release (KER) distribution for the two channels.

9.3.4 Non-Resonant Case

Experiments always have intrinsic complexity. Except for the pure resonant case, the near-resonant case is also possible. Different from resonant case, in the near-resonant case, the nascent CH_5 is not in its ground state, but in the so called 3S Rydberg state which is energetically slightly higher than the ground state Ch_5. To simulate this case, an extra energy about 0.9 eV is added to the trajectories as kinetic energy

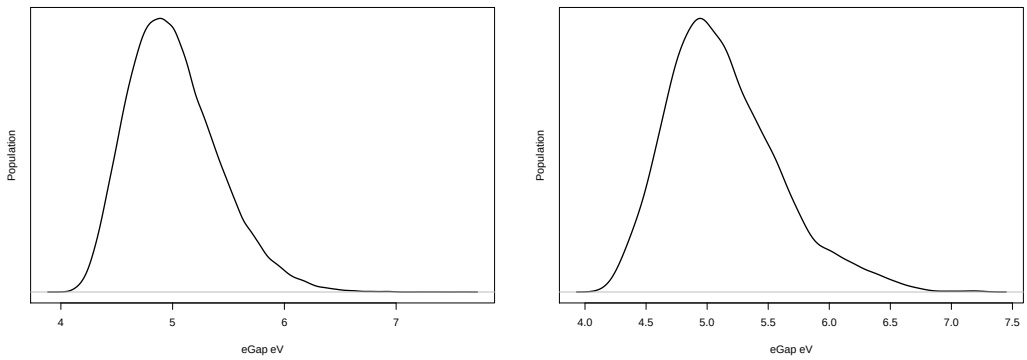

(a) H + CH_4 (b) H_2+CH_3

Figure 9.13: Energy gap (EG) distribution for the two channels. (a) is the EG distribution for H + CH_4 channel and (b) is for the H_2+CH_3 channel.

comparing to the "resonant" case, and all the other steps are essentially the same as the "resonant" model.

Tab. 9.4 shows some key parameters for this simulation and the main difference between this case and resonant model is the branching ratio decreasing.

Table 9.4: Key parameters for Near-Resonant Case simulation

TNT[1]	NIS[2]	NITES[3]	NT(CH_4 + H)[4]	NT(CH_3 + H_2)[5]	Branching Ratio
25,000	50	500	22,303	2,510	8.9

[1] Total Number of Trajectories
[2] Number of independent simulations
[3] Number of independent trajectories in each simulation
[4] Number of trajectories giving CH_4 + H
[5] Number of trajectories giving CH_3 + H_2

Fig. 9.17, 9.18, 9.19, 9.20, 9.21 show the similar distributions to those in the resonant model.

For the three models (direct jumping, resonant and near-resonant), the nascent CH_5 got more and more kinetic energy, and as shown in the Tab. 9.2, 9.3 and 9.4, the

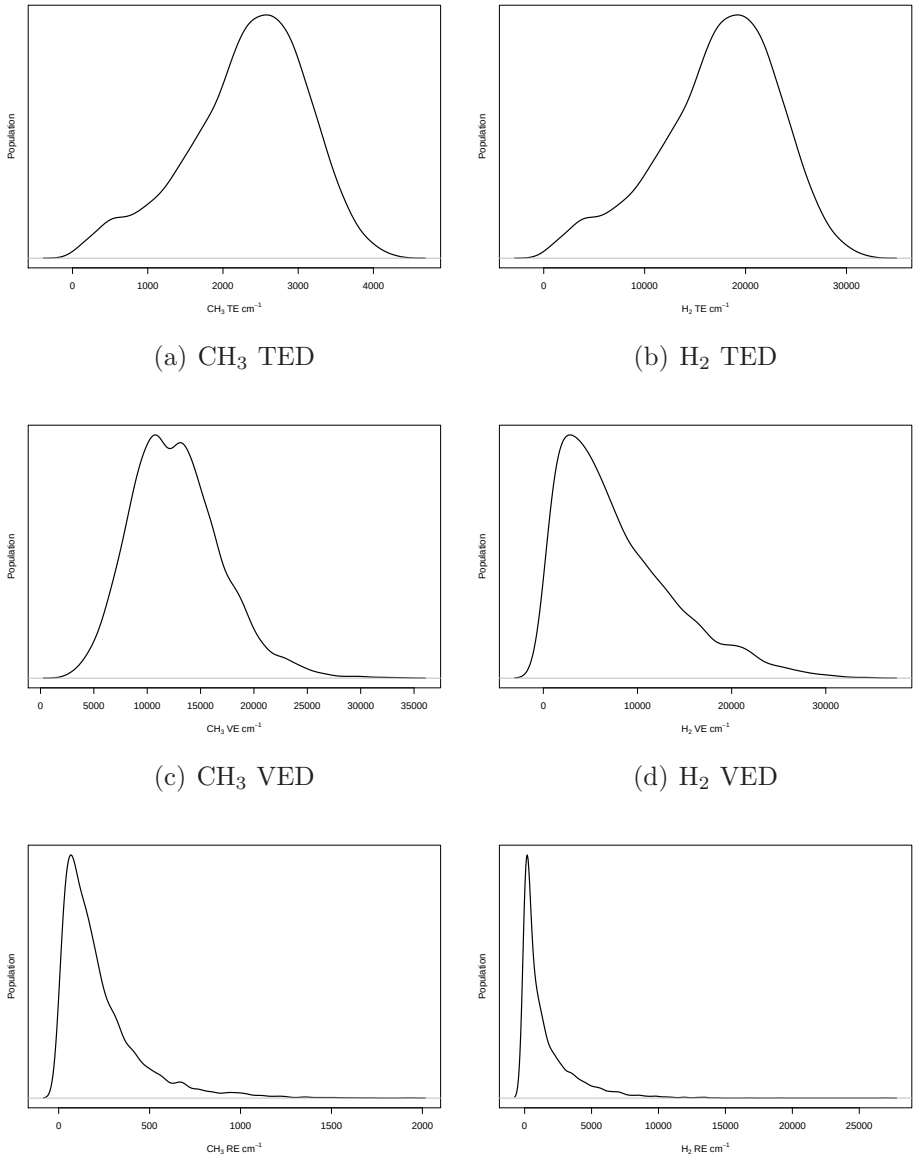

(a) CH_3 TED (b) H_2 TED

(c) CH_3 VED (d) H_2 VED

(e) CH_3 RED (f) H_2 RED

Figure 9.14: CH_3 and H_2 translational energy (TE), vibrational energy (VE) and rotational energy (RE) distributions from channel CH_3 + H_2 in the direct resonant model.

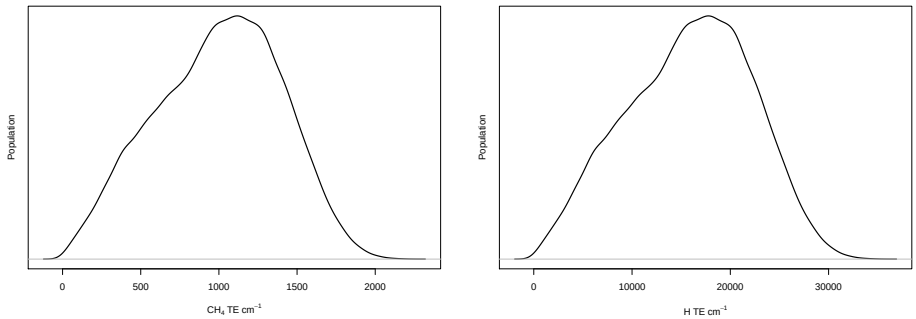

(a) CH_4 TED (b) H TED

(c) CH_4 VED (d) CH_4 RED

Figure 9.15: CH_4 translational energy (TE), vibrational energy (VE) and rotational energy (RE) distributions and H translational energy distribution from channel CH_4 + H in the resonant model.

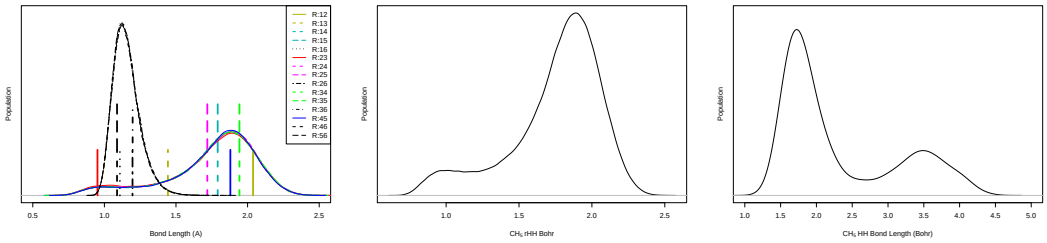

(a) (b) (c)

Figure 9.16: Bond length distribution for the CH_5^+ at the jumping position. (a) is the bond length distribution for all the bonds in CH_5^+, (b) is the bond length distribution for all the HH bonds and (c) is the bond length distribution for those HH pairs which finally appear in the products of the channel CH_3+H_2.

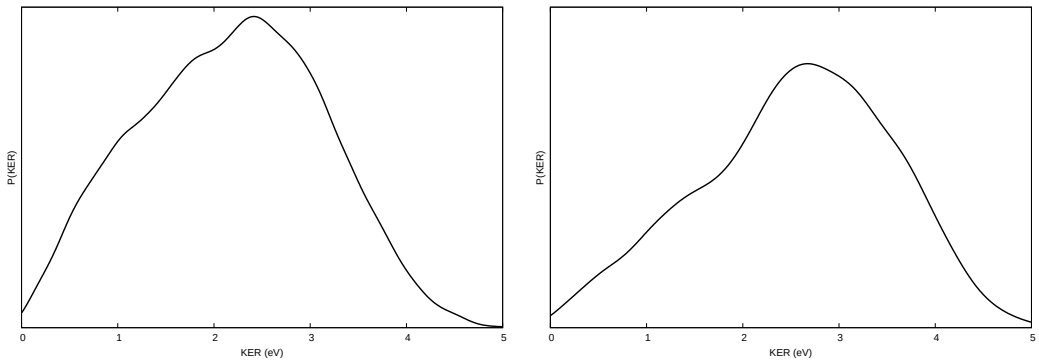

(a) H + CH_4 (b) H_2+CH_3

Figure 9.17: Kinetic energy release (KER) distribution for the two channels.

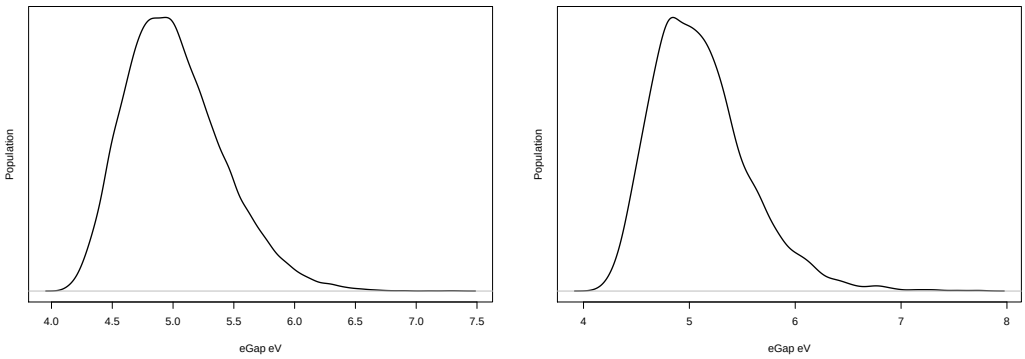

(a) H + CH_4 (b) H_2+CH_3

Figure 9.18: Energy gap (EG) distribution for the two channels. (a) is the EG distribution for H + CH_4 channel and (b) is for the H_2+CH_3 channel.

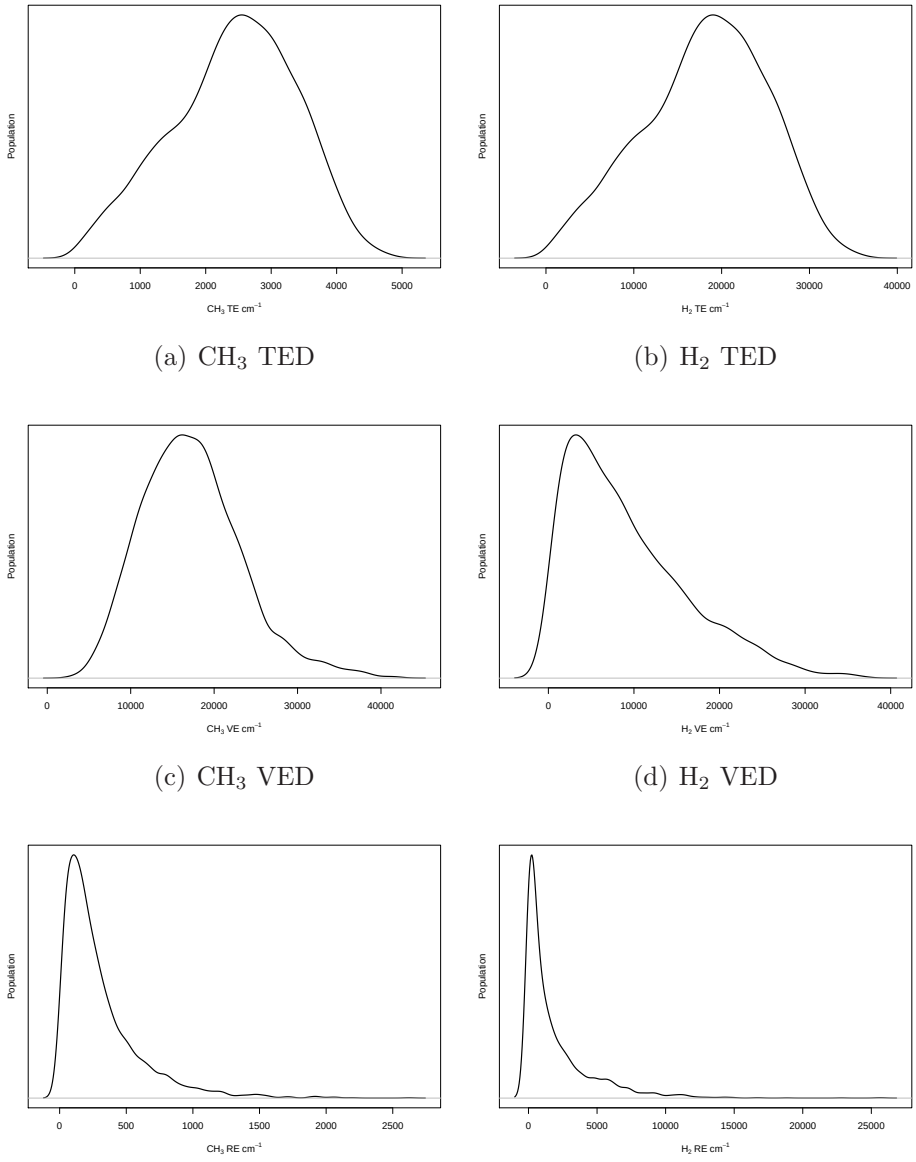

(a) CH_3 TED (b) H_2 TED

(c) CH_3 VED (d) H_2 VED

(e) CH_3 RED (f) H_2 RED

Figure 9.19: CH_3 and H_2 translational energy (TE), vibrational energy (VE) and rotational energy (RE) distributions from channel $CH_3 + H_2$ in the near-resonant model.

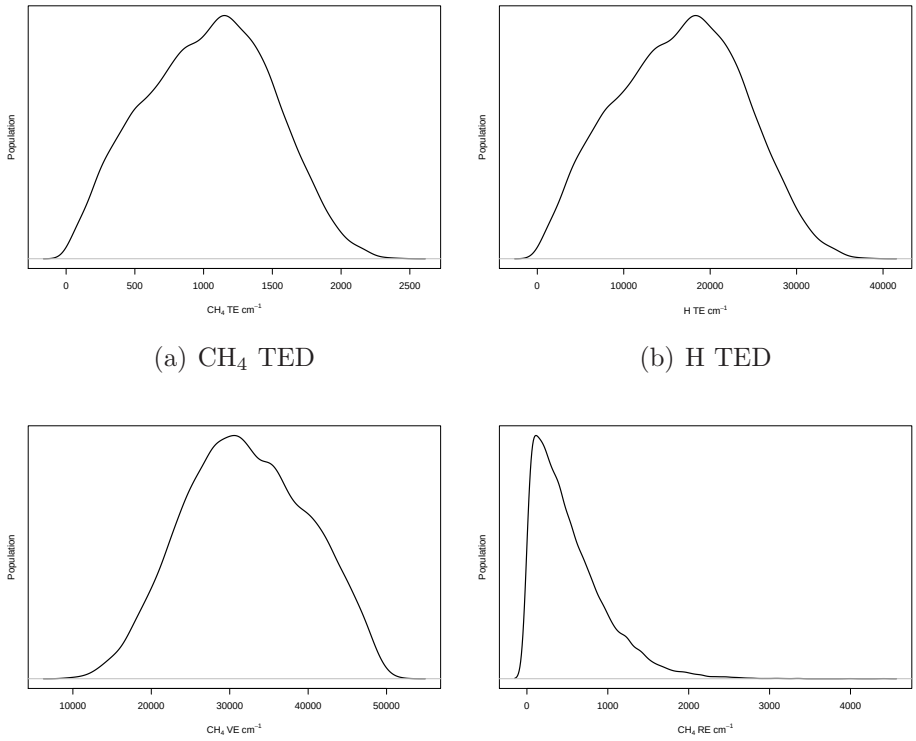

(a) CH_4 TED

(b) H TED

(c) CH_4 VED

(d) CH_4 RED

Figure 9.20: CH_4 translational energy (TE), vibrational energy (VE) and rotational energy (RE) distributions and H translational energy distribution from channel CH_4 + H in the near-resonant model.

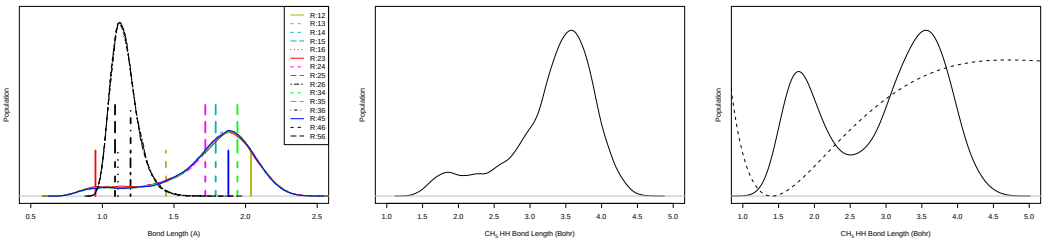

(a) (b) (c)

Figure 9.21: Bond length distribution for the CH_5^+ at the jumping position. (a) is the bond length distribution for all the bonds in CH_5^+, (b) is the bond length distribution for all the HH bonds and (c) is the bond length distribution for those HH pairs which finally appear in the products of the channel CH_3+H_2. The dashed line in (c) is the potential energy curve for H_2.

branching ratio is decreasing as the initial kinetic energy increases. In addition, the KER distribution as shown in Fig. 9.7, 9.12 and 9.17 is moving slightly right, and the shoulder on the lower KER site is increasing. This may caused by the more and more excitation of the vibrational state of H_2 and CH_4/CH_3.

Interestingly, for the source of H_2 of channel $CH_3 + H_2$, as the kinetic energy increases, the portion of H from the large HH distance H group in CH_5^+ is increasing.

9.4 DMC Calculation on CH_5^+ and its Isotopomers

There some several low lying structure of CH_5^+ according to the newly developed global potential energy surface [110], Fig. 9.22 shows the global minimum structure of CH_5^+ which is often denoted as C_s(I) geometry.

As labeled in Fig. 9.22, the five H atoms are not identical in the global minimum structure of CH_5^+. The bond length between H(2) and H(3) is the shortest distance among all the bond lengths in CH_5^+ as shown in Tab. 9.5, and we call H(2)-H(3) as the diatomic part in CH_5^+ and the other three H atoms as tripod part.

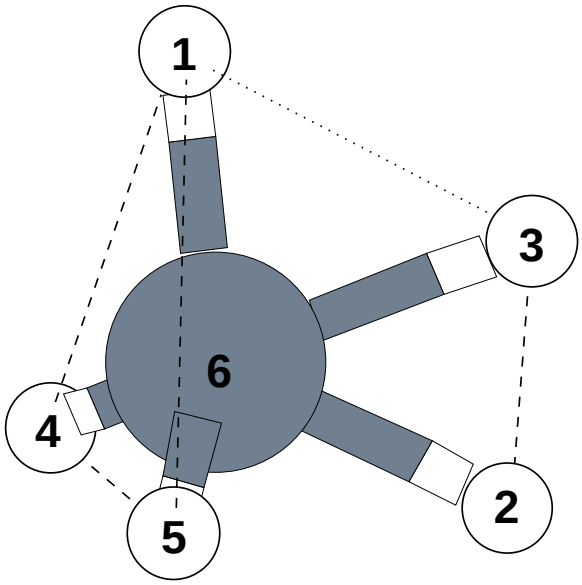

Figure 9.22: CH_5^+ global minimum C_s(I) geometry

Table 9.5: Bond distances in CH_5^+

Bond	Distance (Å)
R_{12}	2.0382
R_{13}	1.4437
R_{14}	1.7912
R_{15}	1.7912
R_{16}	1.1084
R_{23}	0.9517
R_{24}	1.7187
R_{25}	1.7187
R_{26}	1.1965
R_{34}	1.9432
R_{35}	1.9432
R_{36}	1.1973
R_{45}	1.8797
R_{46}	1.0884
R_{56}	1.0884

To study the geometries of CH_5^+ and its various isotopomers, standard diffusion Monte Carlo method is performed. Tab. 9.6 lists zero-point energies of various CH_5^+ isotopomers. In addition, the D position effect is also studied and shown in Tab. 9.6. In most of the DMC simulations, we initiated 10 independent trajectories, and there are about 20000 walkers in each trajectory and propagated in the imaginary time for 5000 steps.

Table 9.6: Zero-Point energy (cm^{-1}) of CH_5^+, CHD_4^+ and $CD_3H_2^+$ from the DMC simulation

isotope	H Position	ZPE (cm^{-1})
CH_5^+		10914 ± 12
CD_5^+		8049 ± 8
CD_4H^+	H: 2	8570 ± 9
CD_4H^+	H: 3	8568 ± 11
CD_4H^+	H: 1	8608 ± 5
CD_4H^+	H: 4	8662 ± 6
CD_4H^+	H: 5	8666 ± 11
$CD_3H_2^+$	H: 2, 3	9089 ± 7
$CD_3H_2^+$	H: 1, 3	9105 ± 12
$CD_3H_2^+$	H: 2, 4	9163 ± 11
$CD_3H_2^+$	H: 2, 5	9157 ± 14
$CD_3H_2^+$	H: 1, 2	9181 ± 9
$CD_3H_2^+$	H: 3, 4	9195 ± 6
$CD_3H_2^+$	H: 3, 5	9184 ± 9
$CD_3H_2^+$	H: 1, 4	9195 ± 18
$CD_3H_2^+$	H: 1, 5	9216 ± 15
$CD_3H_2^+$	H: 4, 5	9297 ± 14

From Tab. 9.6, it is clear that the more the D atoms, the lower the zero-point energy, and there are some preference for the H atom positions. In the case of CD_4H^+, the energy when H is in the position 2,3,1 has relative lower energy then those configurations where H is in the 4 and 5 position. Similarly, when the two H

atoms are in the position 2,3 seems has the lowest ZPE comparing to all the other $CD_3H_2^+$ configurations.

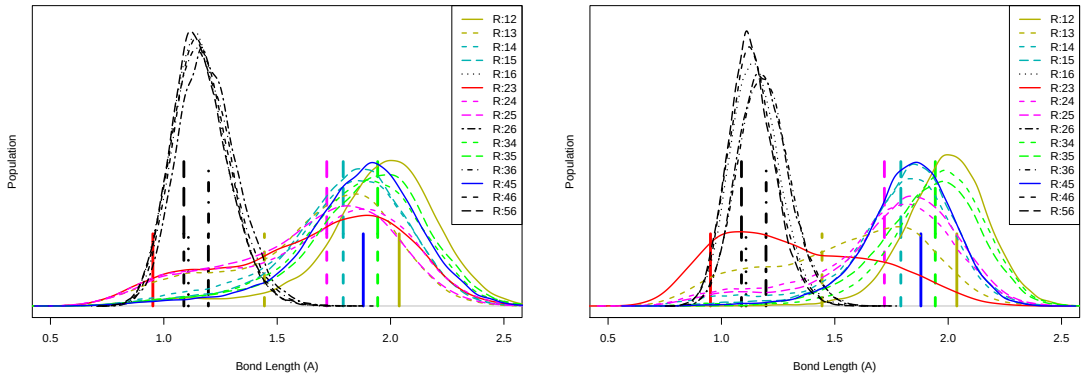

(a) CH_5^+ (b) CD_5^+

Figure 9.23: CH_5^+ and CD_5^+ bond length distributions from the DMC simulation

All the internal bond length distribution of CH_5^+ and CD_5^+ are shown in Fig. 9.23. Comparison between Fig. 9.23(a) and Fig. 9.23(b) may reveal that the D atoms in CD_5^+ are more localized than the H atoms in CH_5^+.

The bond length distribution of four deuterated CH_5^+ (CD_4H^+) is shown in Fig. 9.24. Comparing to the initial bond length of CD_4H^+, we may conclude that the H atom tends to gather together with an D atoms and forms the diatomic part in CD_4H^+, and this is verified from the long time DMC trajectories (30000 steps for each trajectory) as shown in Fig. 9.25.

For the triple deuterated CH_5^+ ($CD_3H_2^+$), all the bond length distributions from the DMC simulation are shown in Fig. 9.26 and Fig. 9.27. One of the conclusion can be drew from these distribution is that the two H atoms tend to gather together to form the diatomic part and the three D atoms prefer to constitute the tripod part in $CD_3H_2^+$.

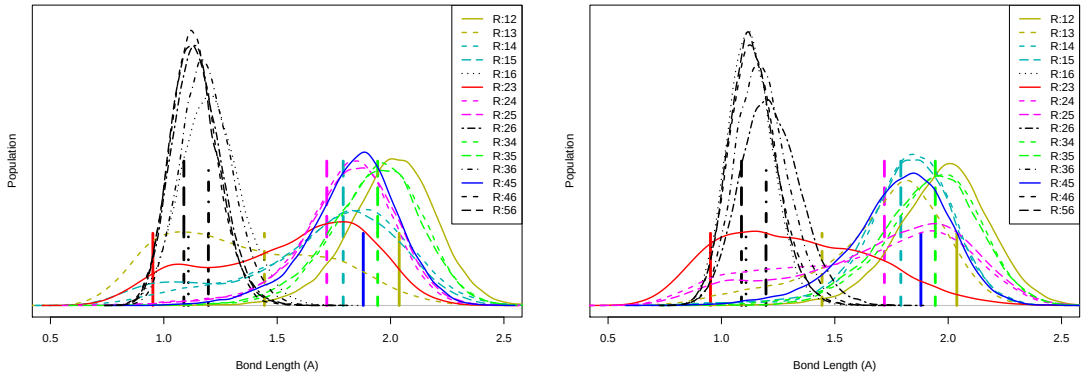

(a) CD_4H^+,H:1

(b) CD_4H^+,H:2

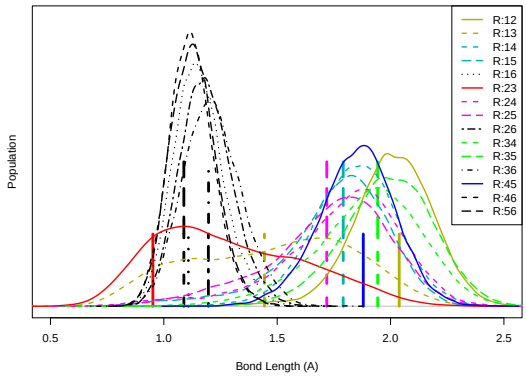

(c) CD_4H^+,H:3

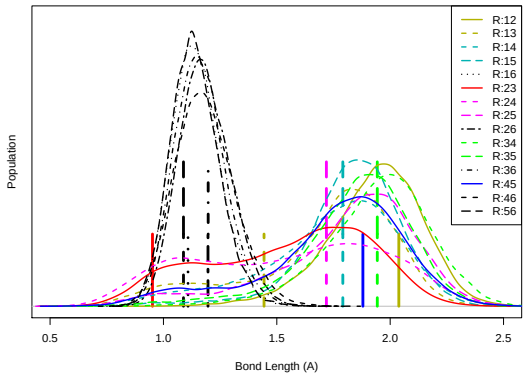

(d) CD_4H^+,H:4

Figure 9.24: CD_4H^+ bond length distributions from the DMC simulation

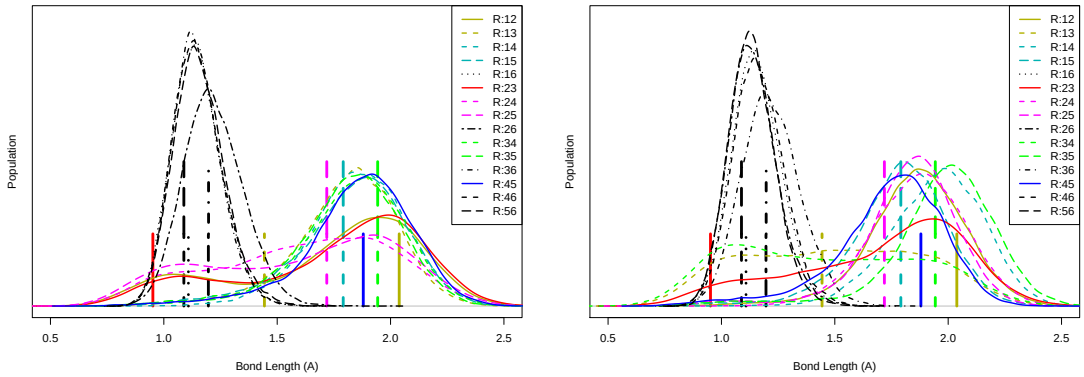

(a) CD_4H^+,H:2 (b) CD_4H^+,H:3

Figure 9.25: CD_4H^+ bond length distributions from the long DMC simulation

The long time DMC trajectories (30000 steps in each trajectory) results shown in Fig. 9.28 confirm this result.

9.5 PIMC Study of the Geometry of $CD_3H_2^+$

DMC provides an good method to get the grand state property of the molecule, with the assumption that the temperature is in 0 K. In addition to DMC, path integral Monet cargo (PIMC) provides an alternate method to add the temperature effect. Here we just study the $CD_3H_2^+$ in two temperature (30 K and 300 K) using PIMC method and the bond length distributions are shown in Fig. 9.29. Note that in these simulations, the initial positions of the two H atoms are at site 2,3 and 4,5 which means that the initial H atoms can be in both diatomic part and tripod part. There two choice of initial configurations may reveal the migration or scrambling of H and D atoms in $CD_3H_2^+$.

As can be seen in Fig. 9.29(a) and 9.29(b) which is the case in 300 K, all the HH/HD/DD bond length distributions are quite similar. This may indicate that at

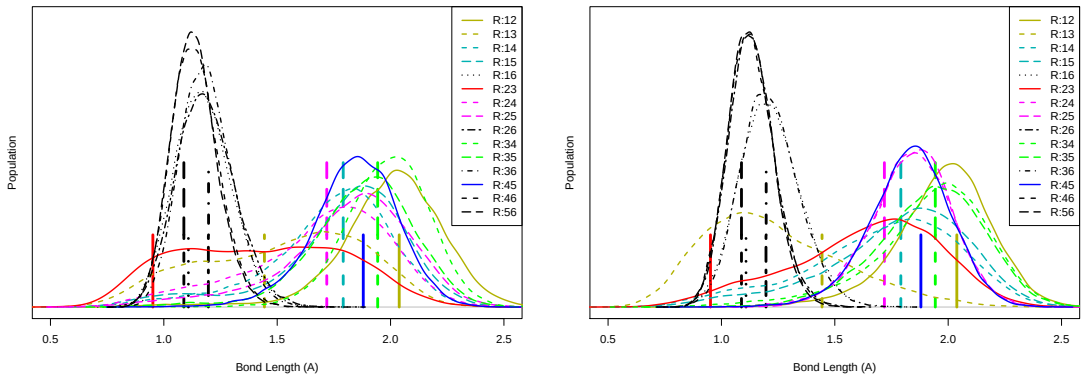

(a) $CD_3H_2^+$,H:12

(b) $CD_3H_2^+$,H:13

(c) $CD_3H_2^+$,H:14

(d) $CD_3H_2^+$,H:23

Figure 9.26: $CD_3H_2^+$ (H:12,H:13,H:14,H:23) bond length distribution from the DMC simulation

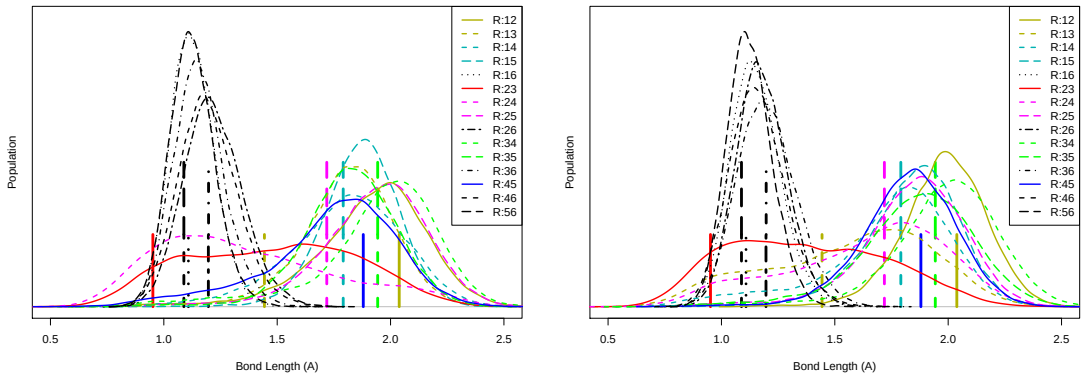

(a) $CD_3H_2^+$,H:24

(b) $CD_3H_2^+$,H:34

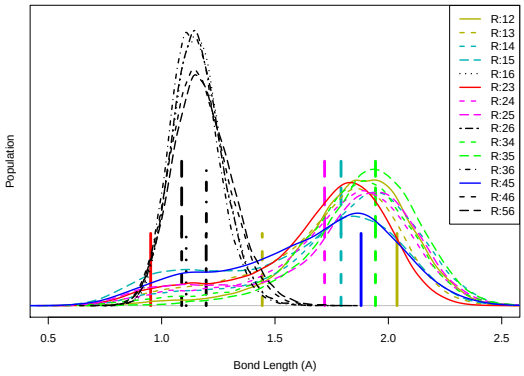

(c) $CD_3H_2^+$,H:45

Figure 9.27: $CD_3H_2^+$ (H:24,H:34,H:45) bond length distributions from the DMC simulation

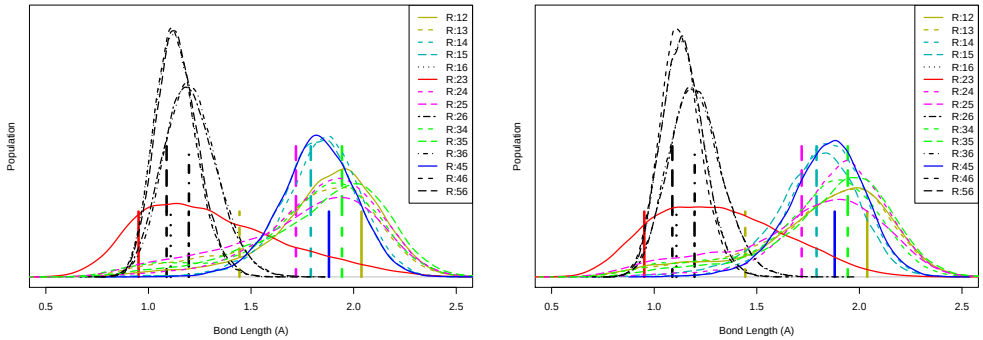

(a) $CD_3H_2^+$,H:23 (b) $CD_3H_2^+$ (C_s(II)),H:23

Figure 9.28: $CD_3H_2^+$ bond length distributions from long time DMC trajectories. The initial configuration for (a) is from the global minimum structure and the initial configuration for (b) is from the C_s(II) geometry.

300 K, all the atoms are scrambled. However, when the temperature drops to 30 K, the bond length distribution changes to Fig. 9.29(c) and 9.29(d). By analyzing the bond length distribution, it is not difficult to see that the structure looks like that HH diatomic part is rotating around an axis which pass through the plane of the three D atoms and the carbon atom. This information may suggest that if the nascent CD_3H_2 was produced by the charge exchange of $CD_3H_2^+$ at low temperature such as 30 K, the probability for the dissociation into CD_3 + H_2 may enhanced.

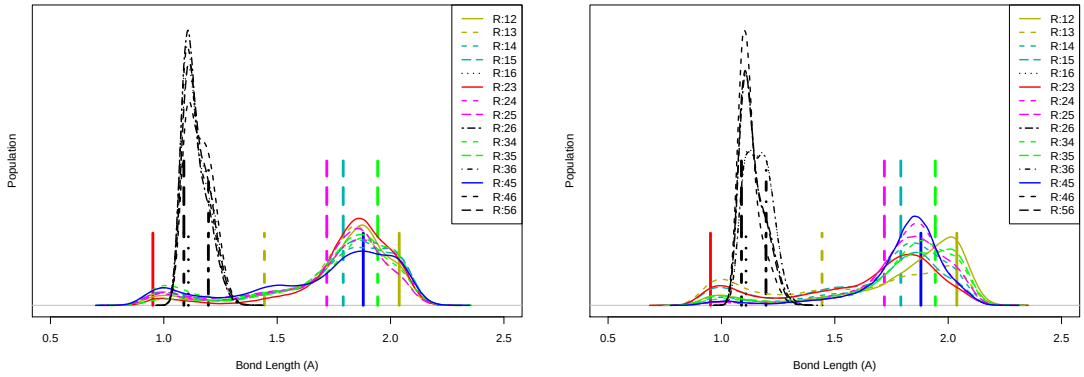

(a) $CD_3H_2^+$,H:23,300K

(b) $CD_3H_2^+$,H:45,300K

(c) $CD_3H_2^+$,H:23,30K

(d) $CD_3H_2^+$,H:45,30K

Figure 9.29: $CD_3H_2^+$ Bond length distribution from the PIMC simulations (300, 30K)

10 H_3O^+/H_3O

H_3O^+, or Hydronium is the simplest type of oxonium ion. Together with water (H_2O), they are of greatest interest in interstellar space, hence the charge exchange reaction of H_3O^+ to become H_3O and further dissociation into H_2O is of particular interest and importance.

10.1 Experimental Work

Similar to the charge exchange reactions of CH_5^+ as performed at UCSD, another charge exchange reaction as following

$$H_3O^+ + e \rightarrow H_3O \rightarrow H_2O + H \tag{10.1}$$

was performed. The electron e in the reaction 10.1 was from the ionization of C_s atom as

$$C_s \rightarrow C_s^+ + e. \tag{10.2}$$

Theoretically, there are at least two possible dissociation channels for H_3O. One is shown in Eq. 10.1, and the other is

$$H_3O^+ + e \rightarrow H_3O \rightarrow H_2 + OH. \tag{10.3}$$

It can be seen from the reaction energetics shown in Fig. 10.1 that both channels for H_3O dissociation are energetically accessible.

To understand the dissociation of the nascent H_3O molecules, the kinetic energy release of the products was measured and shown in Fig. 10.2.

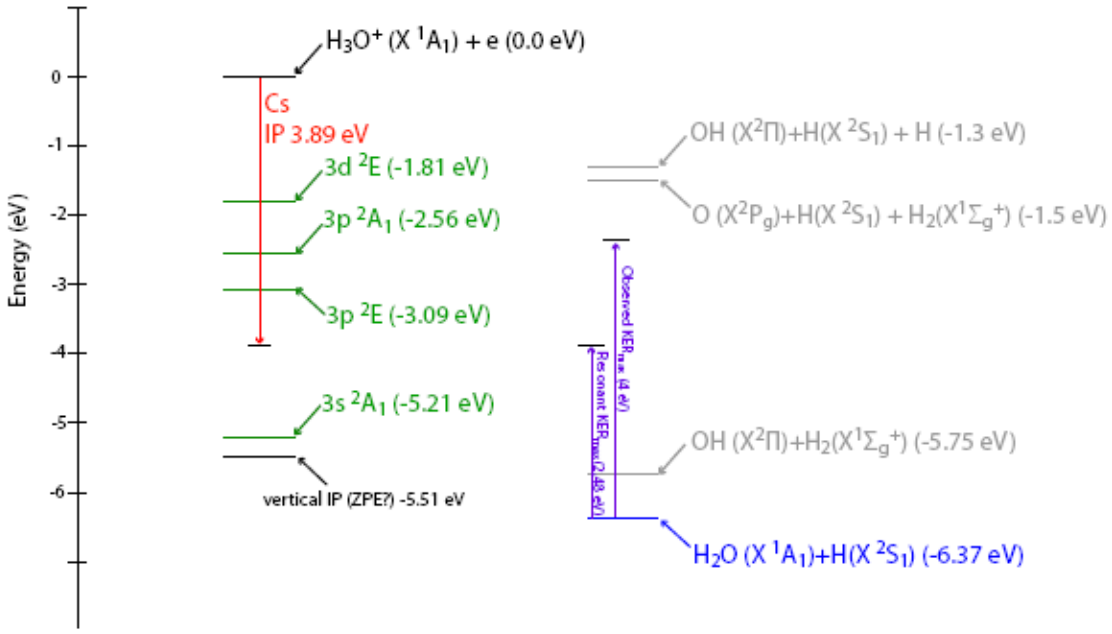

Figure 10.1: Experimental H_3O^+/H_3O energy levels

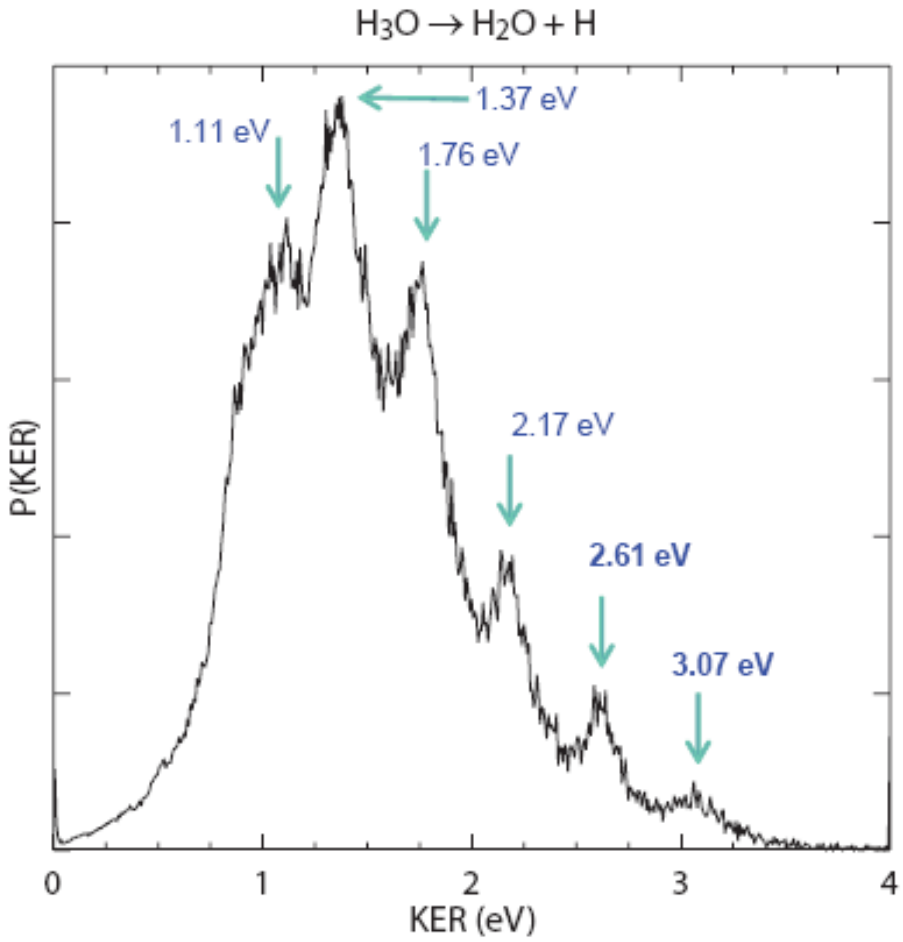

Figure 10.2: H_3O experimental kinetic energy release spectrum at 16 keV

As is known, the total energy of the nascent H_3O is distributed as the internal energy of the products and also as the translational energy of the products or the kinetic energy release. Under the assumption that the total initial energy of H_3O is constant, once the kinetic energy release (KER) is measured, the internal energy of the products can be known.

From the experiments, it can be seen that most of the products of the dissociation of H_3O are H + H_2O. Considering the single atom nature of H atoms, all the internal energy is in the H_2O molecule. Consequently, the KER spectra should be the mirror image of the H_2O internal energy distribution.

From the KER spectra of $H_3O \rightarrow H + H_2O$, one may notice that the peaks are almost separated by 0.4 eV, which is roughly the sum of the symmetric and asymmetric stretch energies of H_2O molecule. The highest peak in the KER spectrum should be corresponding to the ground rovibrational state of H_2O. Complementary to the experiments, quasiclassical trajectory simulations were also performed to shine more light on the dissociation of the nascent H_3O.

To simulate the dissociation of H_3O, we need both of the potential energy surfaces for H_3O^+ and H_3O that are discussed in the following subsections.

10.2 H_3O^+ Potential Energy Surface

14230 geometries of H_3O^+ were sampled by using the low level (HF/VDZ) direct dynamics. After obtaining these configurations, *ab initio* energy for them were calculated at the CCSD(T)/aug-cc-pVTZ level. Thus, the date set is prepared and followed by the invariant polynomial least squares fitting.

The RMS for the current fit is 3.3445 cm^{-1} for 14230 *ab initio* CCSD(T)/aug-cc-

pVTZ energies. As usual, the transformed bond lengths $r' = 2.0(1.0 - \exp(-0.4r))^2$ are used as variables in fitting.

There is a known global minimum structure of H_3O^+ in C_{3v} symmetry and also a D_{3h} saddle point for the inversion of H_3O^+ that are shown in Fig. 10.3.

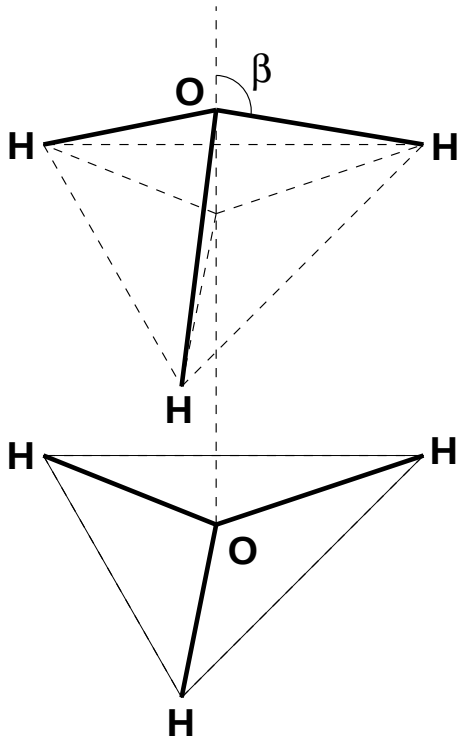

Figure 10.3: The C_{3v} global minimum and the D_{3h} saddle point structure of the H_3O^+ molecule

The energy difference between the inversion saddle point and the C_{3v} minimum is about 800 cm^{-1}, which is a small barrier under a deep well. The energy comparison between the *ab initio* calculation and PES fitting values is listed in Table 10.1.

Table 10.1: H_3O^+ energy and geometry

Method	C_{3v} MIN			D_{3h} ISP		Barrier (cm^{-1})
	r_{OH} (Å)	β (Degree)	Energy (Hartree)	r_{OH} (Å)	Energy (Hartree)	
AVQZ	0.9765	107.11	-76.63701932	0.9692	-76.63380081	706.38
AVTZ	0.9792	107.44	-76.61565495	0.9713	-76.61199574	803.10
PFIT	0.9796	107.43	-76.61591732	0.9717	-76.61229810	794.33
HCB-1	0.9789	107.60		0.9708		783.00
HCB-2	0.9782	107.40		0.9686		693.00
HCB-3	0.9761	107.20		0.9687		690.00

The harmonic frequencies for the two stationary geometries are characterized on the PES as shown in Table 10.2.

Table 10.2: Normal mode frequencies (cm^{-1}) of H_3O^+ C_{3v} and D_{3h} structure

Method	Mode 1	Mode 2	Mode 3	Mode 4	Mode 5	Mode 6
			H_3O^+ (C_{3v})			
AVQZ	895.03	1698.57	1698.85	3600.28	3698.98	3699.17
AVTZ	918.35	1700.06	1700.19	3585.27	3682.65	3682.66
PFIT	918.92	1702.03	1702.03	3575.33	3677.05	3677.05
HCB-1	916.00	1693.00	1693.00	3578.00	3691.00	3691.00
HCB-2	881.00	1693.00	1693.00	3582.00	3695.00	3695.00
HCB-3	891.00	1696.00	1696.00	3597.00	3707.00	3707.00
			H_3O^+ (D_{3h})			
AVQZ	680.34i	1633.23	1633.23	3655.37	3806.53	3806.61
AVTZ	723.73i	1627.30	1627.34	3642.52	3793.30	3793.35
PFIT	713.92i	1628.96	1628.97	3631.67	3786.87	3786.87
HCB-1	695.00i	1628.00	1628.00	3651.00	3808.00	3808.00
HCB-2	662.00i	1633.00	1633.00	3664.00	3819.00	3819.00
HCB-3	670.00i	1632.00	1632.00	3662.00	3816.00	3816.00

Both Table 10.1 and 10.2 indicate that the H_3O^+ PES is very accurate.

10.3 H_3O Potential Energy Surface

Different from H_3O^+, the PES for H_3O is floppy and difficult for the usual global fitting strategy. One approach called *integrated local PES fitting* is under developing and will be addressed in future publications. To overcome the shortage of H_3O PES, direct *ab initio* dynamics was performed instead.

10.4 Direct Dynamics Simulation

Initial Conditions The direct dynamics simulation was performed at the Frank-Condon principle. Assume a H_3O^+ molecule at some configuration fetched an electron from Cs, then it becomes a H_3O neutral molecule with the same configuration, and also the same momentum. In the picture of potential energy surfaces, a H_3O^+ configuration is a point on the cation surface. When it absorbs an electron, it jumps to the neutral surface directly from the same position.

To start the simulation, a sample of H_3O^+ was generated on the H_3O^+ PES. The sample of H_3O^+ was basically from 1000 H_3O^+ trajectories.

Fig. 10.4 shows the various energy distributions of H_3O^+. The right most red curve in Fig. 10.4 is the initial total energy of H_3O^+. In the beginning, all the H_3O^+ molecules are supposed to be in their ground vibrational states. As a result, they all have the zero point energy. Due to the anharmonicity of the real PES and the approximation of the normal mode sampling, there is a small variation of the total H_3O^+ initial energy.

To sample the phase space of the H_3O^+, 10,000 H_3O^+ with random normal coordinates displacement (from the normal mode sampling) were sampled as the starting configurations of 10,000 trajectories. Every trajectory was run for 3000 steps. Then, every final configuration of the H_3O^+ jumped to the H_3O PES, and the energy gap between the cation PES and the neutral surface was named as the energy gap. For example, suppose one H_3O^+ was in configuration $\mathbf{x}$ after 3000 steps on the cation PES, and the cation PES function is denoted as PP. Similarly, the neutral PES function is denoted as PN. As a result, the potential of the H_3O^+ on the cation surface is $PP(\mathbf{x})$ and its potential energy on the neutral surface is $PN(\mathbf{x})$. The difference be-

tween $PP(\mathbf{x})$ and $PN(\mathbf{x})$ is defined as the energy gap as $E_{\text{gap}}(\mathbf{x}) = PP(\mathbf{x}) - PN(\mathbf{x})$. Since the potential energy surfaces of H_3O^+ and H_3O are not supposed to be parallel around it C_{3v} minimum geometry, the energy distribution is not supposed to be a delta function. The real distribution is shown as the grey curve in Fig. 10.4. During the jumping process of H_3O^+ to the neutral surface, the gap energy is supposed to be released. As a result, the total energy of the nascent H_3O is the difference between the cation initial total energy and the energy gap, or $PP(\mathbf{x}) - E_{\text{gap}}(\mathbf{x})$, which is shown as the blue curve in Fig. 10.4.

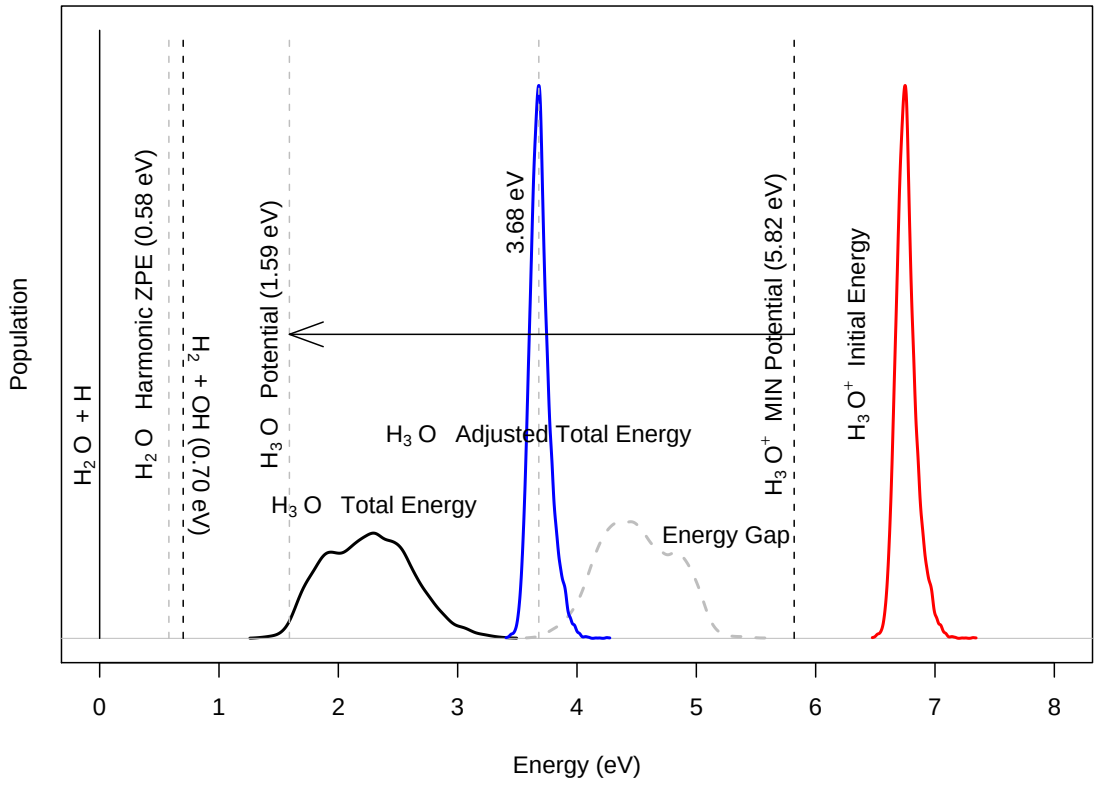

Figure 10.4: H_3O various energy distributions for the trajectory simulation.

Final Conditions Fig. 10.5 is the final energy distribution for $H_3O \rightarrow H + H_2O$. As for final energy, there is a total energy for the whole system (H and H_2O), which we denote as E(total), and the distribution of this energy is plotted as the dotted lines in Fig. 10.5. Note that the dotted line is the total energy for H and H_2O, and it is exactly the same as the initial total energy distribution of H_3O during the simulation which is shown as the blue curve in Fig. 10.4. There is also some rotational energy (classically, the rotational energy can be computed as Eq. 3.17) for H_2O, which can be denoted as E(rotation). The distribution of E(rotation) is plotted as the dashed line in Fig. 10.5. The difference between E(total) and E(rotation) should be the translational energies of both H and H_2O, along with the vibrational energy of H_2O. The sum of translational and vibrational energy of H + H_2O is plotted as the solid curve in Fig. 10.5, and this energy distribution is peaked at 3.59 eV as shown in the Figure.

For each dissociation trajectory of H_3O, it is easy to calculate the sum of the kinetic energy of H and H_2O, also known as the kinetic energy release, which is plotted in Fig. 10.6. The gray sticks on the bottom of the figure is corresponding to the vibrational states of H_2O (the right most stick is for the ground state of H_2O, and the sticks on the left are for those high energy vibrational states).

Similarly, the H_2O vibrational energy can be calculated and is plotted in Fig. 10.7. The bottom sticks in fig. 10.7 show the vibrational states of the H_2O.

Since the sum of the H_2O vibrational energy (VE) and the total H + H_2O translation energy is the energy distribution shown in Fig. 10.5, which is sharply distributed around 3.59 eV, the kinetic energy release distribution and vibrational energy distribution are almost mirror images of each other.

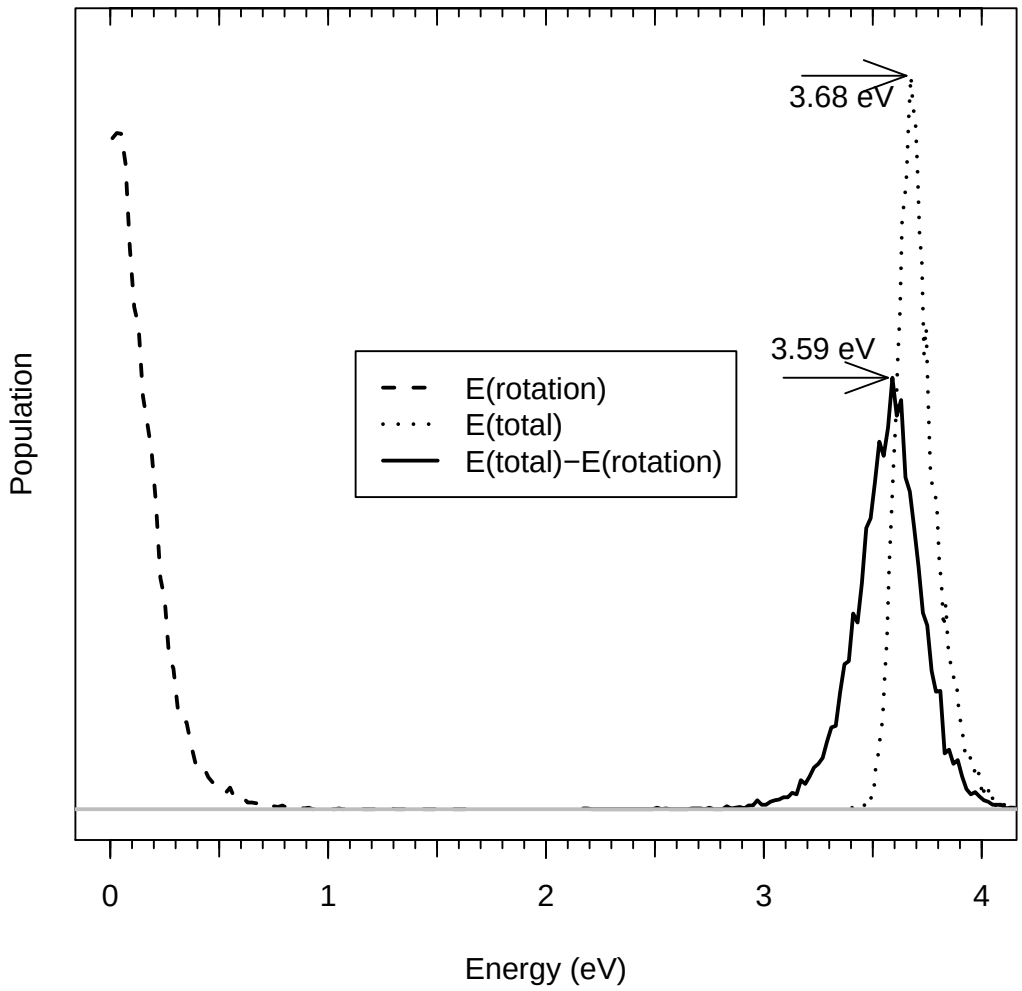

Figure 10.5: The final energy distribution for $H_3O \rightarrow H + H_2O$.

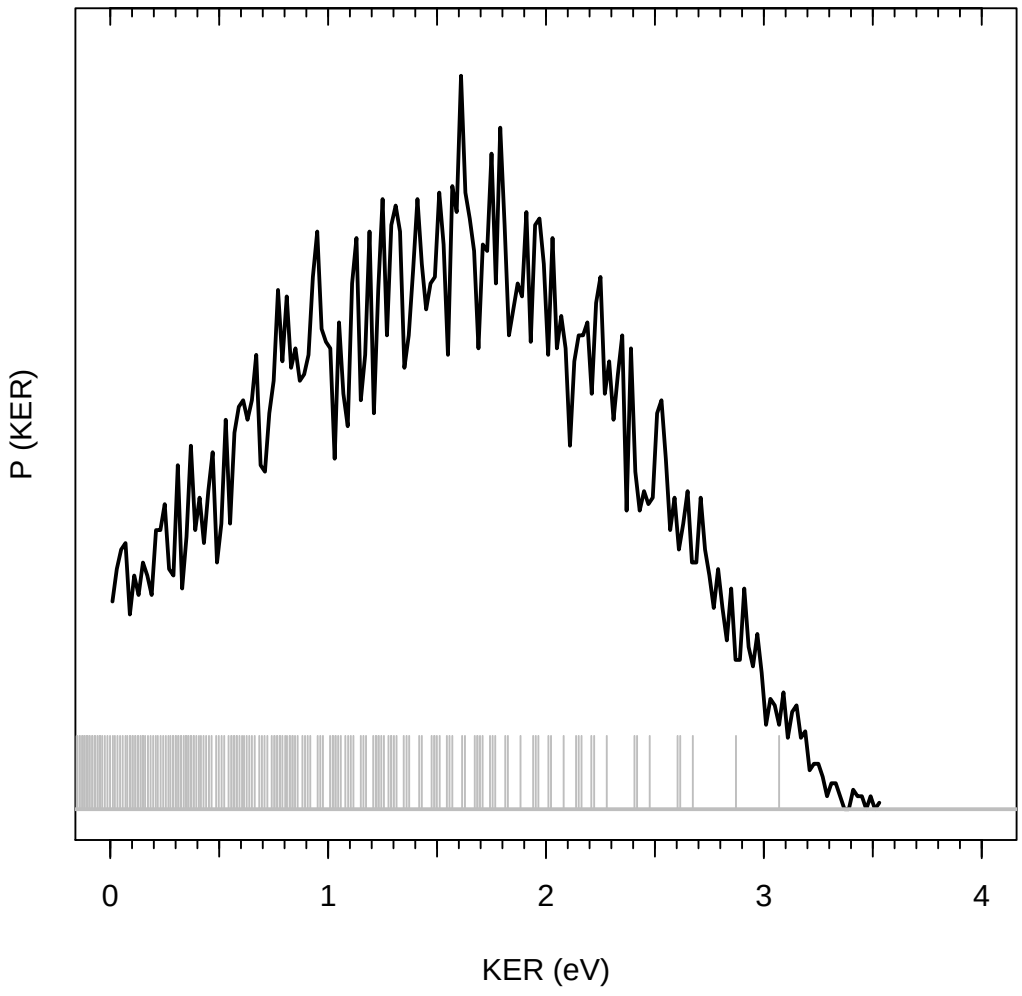

Figure 10.6: The classical $H_3O \rightarrow H + H_2O$ kinetic energy release distributions.

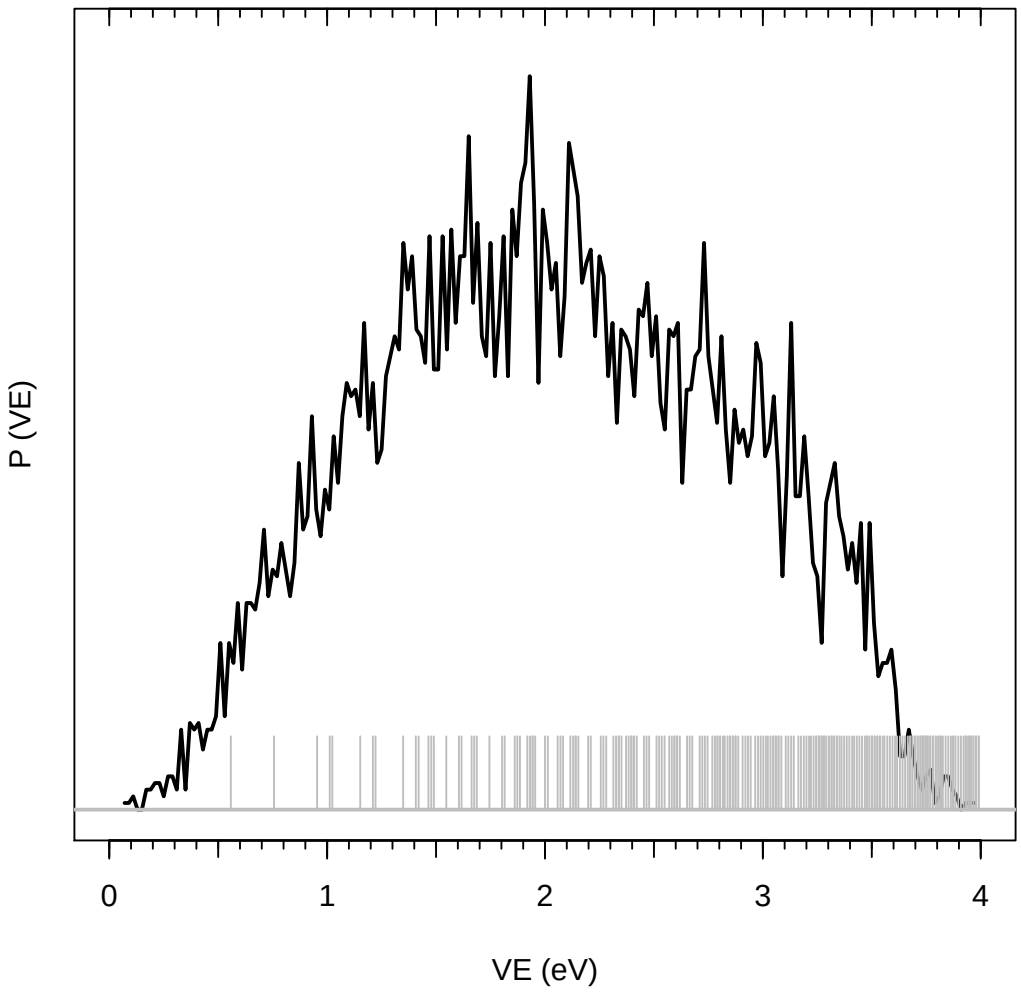

Figure 10.7: The classical H_2O vibrational energy distributions from $H_3O \rightarrow H + H_2O$.

It is well known that the classical trajectories are not aware of the vibrational states of the H_2O, hence both the KER and VE distributions are supposed to be continuous, and some quantization techniques should be employed to approximate the experimental results.

Suppose the vibrational energy from the simulation trajectory is E, and all the energies for all the vibrational states of H_2O are $E_1, E_2, \cdots, E_n$. We suppose that the trajectory vibrational energy is the combination of all the vibrational states of H_2O, i.e.,

$$E = \sum_{i=1}^{n} p_i E_i, \tag{10.4}$$

where p_i is the probability for the energy E associated with the vibrational state i whose energy is E_i. Naively, p_i should be related to the energy difference $E - E_i$, and here we assume $p_i \propto \frac{1}{(E-E_i)^{\frac{2}{m-1}}}$ where $m > 1$ is an adjustable parameter.

Considering the normalization condition as

$$\sum_{i=1}^{n} p_i = 1, \tag{10.5}$$

we can compute p_i as

$$p_i = \frac{1}{\sum_{k=1}^{n} \left(\frac{E-E_i}{E-E_k}\right)^{\frac{2}{m-1}}} \tag{10.6}$$

Based on the probability, we can assign an intensity to each H_2O vibrational states i as I_i. For each trajectory vibrational energy E, every H_2O vibrational state i's intensity I_i get populated by p_i, and finally the energy state has a total intensity. For each state with energy E_i and total intensity I_i, we can represent the state as a scaled Gaussian distribution as $I_i N(E_i, \sigma) = \frac{I_i}{\sigma\sqrt{2\pi}} \exp\left(-\frac{(x-E_i)^2}{2\sigma^2}\right)$, where σ is an

adjustable parameter representing the resolution (in this work, $\sigma = 0.08$).

Based on the above quantization approach, the classical VE distribution is quantized as Fig. 10.8. In addition to the overall spectra of quantized VE distribution,

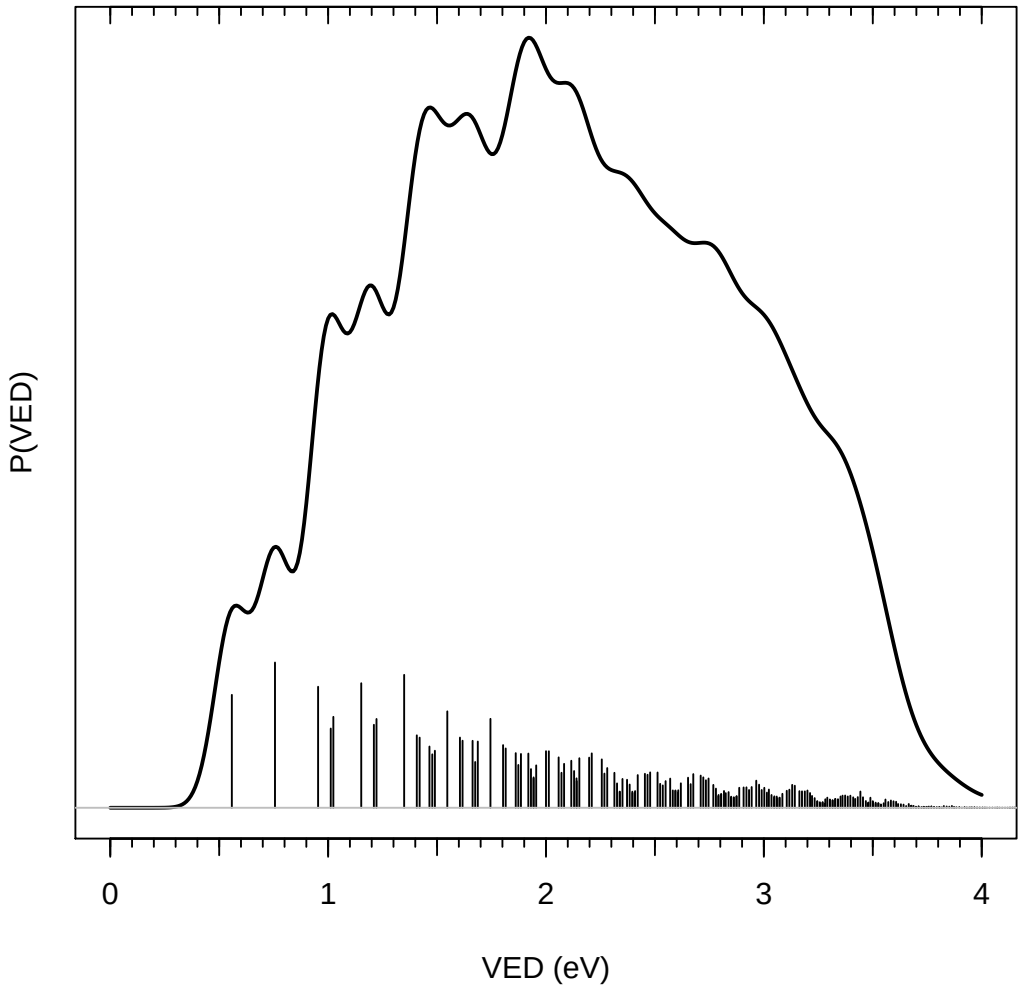

Figure 10.8: The quantized H_2O vibrational energy distribution from $H_3O \rightarrow H + H_2O$.

the intensities for each H_2O vibrational states are also shown as sticks on the bottom of Fig. 10.8.

Since the sum of the rotational energy of H_2O and the total kinetic energy release is peaked at 3.59 eV and the spread of this distribution is not wide, we can approximate KER as 3.59 - VE, which is shown in Fig. 10.9.

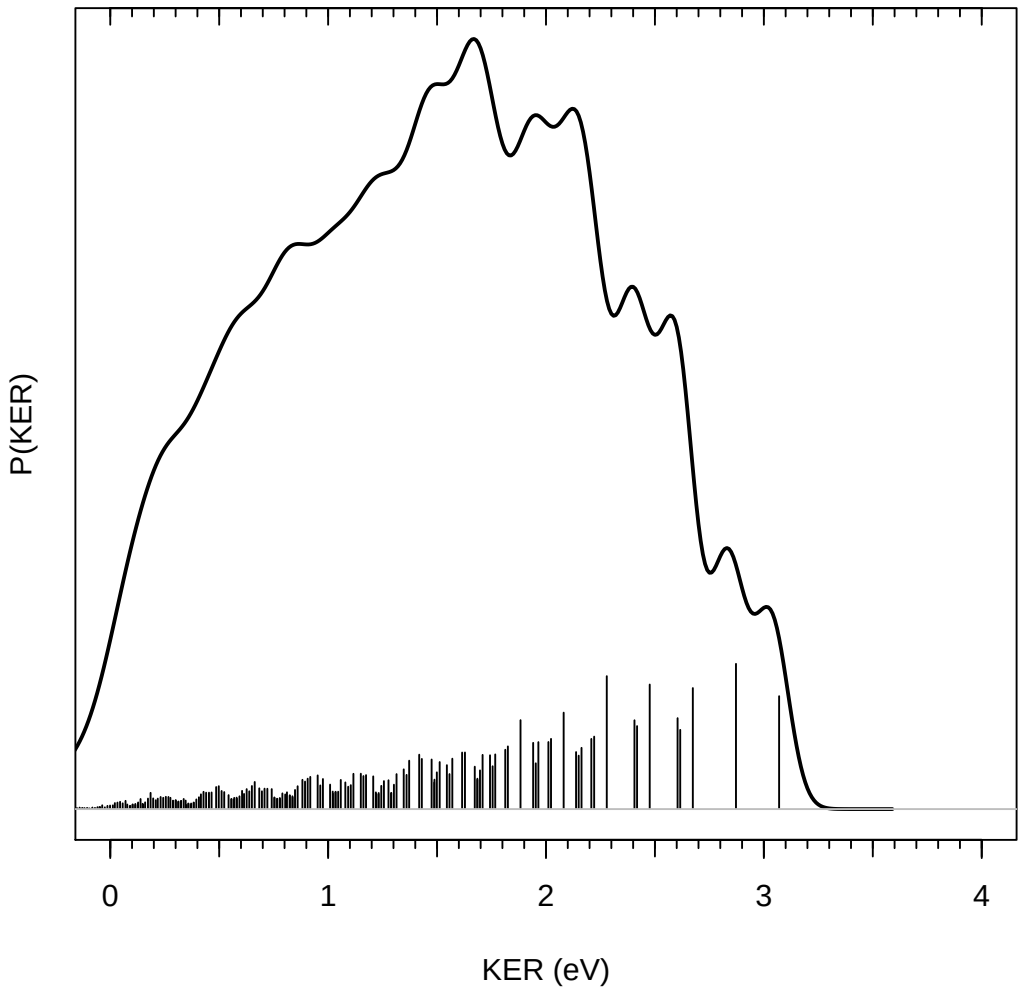

Figure 10.9: The $H_3O \rightarrow H + H_2O$ kinetic energy release distributions from the quantization of the classical vibrational energy distribution as shown in Fig. 10.7.

In the experimental KER distribution (Fig. 10.2), the right most peak is corresponding to the ground vibrational state of H_2O. Given the classically simulated KER

distribution and the vibrational energy states of H_2O, we can line them up and the anchor points are the H_2O ground vibrational state energy and the right most peak position in the experimental KER distribution. This approach is shown in Fig. 10.10. As expected, the distributions calculated by using different approximations should be

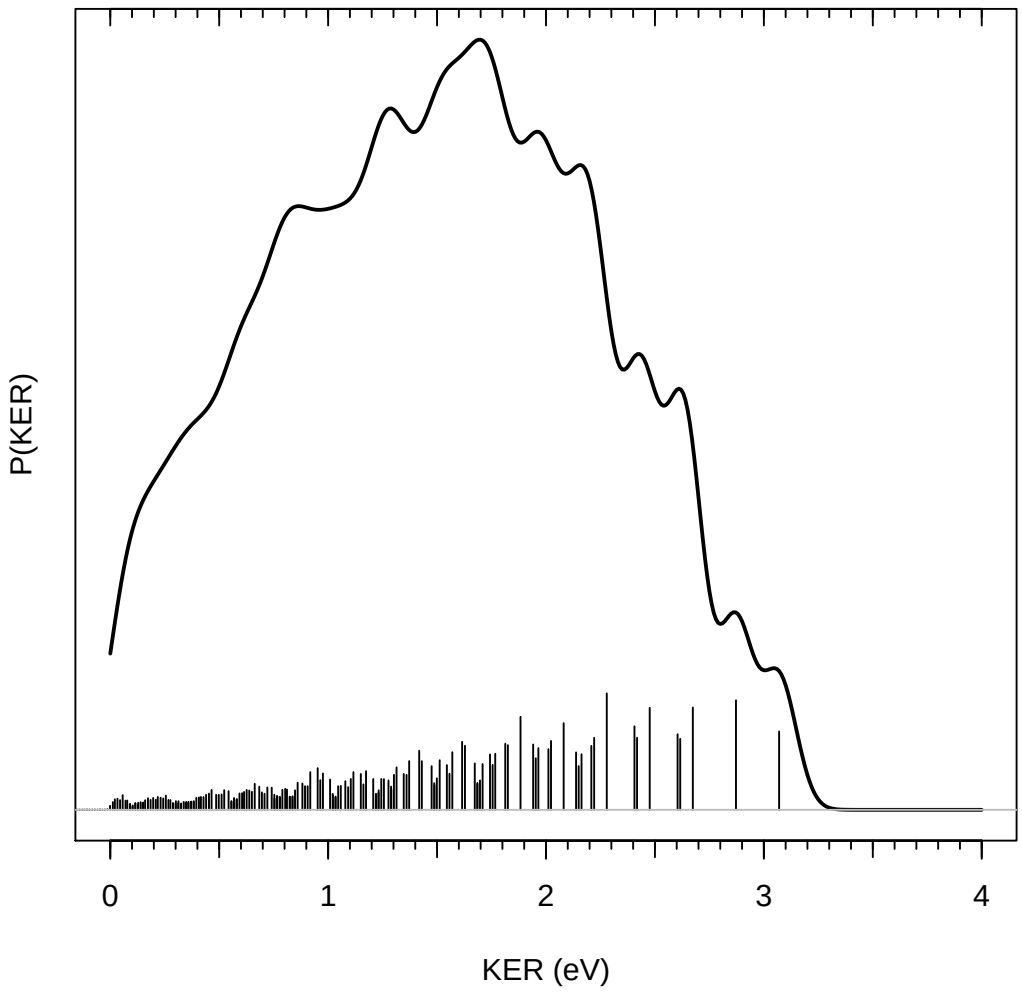

Figure 10.10: The $H_3O \rightarrow H + H_2O$ kinetic energy release distributions from the direct quantization of the classical KER distribution as shown in Fig. 10.6.

similar to each other, which can be seen in Fig. 10.9 and Fig. 10.10.

Comparing the experimental KER distribution (Fig. 10.2) and the simulated KER (Fig. 10.9, 10.10), we may notice that the peak positions are approximately matched. This shows that the peaks in the experimental KER distributions are due to the excitation of the vibrational states of H_2O, and most of the H_2O molecules from the dissociation of H_3O are highly vibrational excited.

The bending angle distribution of H_2O is also plotted in Fig. 10.11 to throw some light on the bending state of H_2O. The $\angle$H-O-H in the equilibrium H_2O configuration is about 100 degree and as can be seen in Fig. 10.11, the H_2O bending angle distribution is peaked around 100 degree and spreads mostly between 80 and 120 degree.

Based on the $\angle$H-O-H distribution, all the high overtone states ($n_1 > 3$) of H_2O bending are removed to quantize the H_2O vibrational energy distribution as shown in Fig. 10.12.

Similarly, the KER distribution is generated and shown in Fig. 10.13.

Distinct from the KER distributions in Fig. 10.9 and 10.10, the peaks in Fig. 10.13 are more isolated. This is due to the clustering of the vibrational states of H_2O as shown in Fig. 10.12. As can be seen in Fig. 10.7 and Fig. 10.8, the energy gap between H_2O vibrational states becomes smaller and smaller as the vibrational energy increases, and almost continuous above 3 eV. If all the $n_1 > 3$ states are removed, the vibrational states of H_2O become isolated clusters below 4 eV, which causes the peaks in Fig. 10.13 to be more isolated than those in Fig. 10.9 and 10.10.

Comparing the experimental KER distribution (Fig. 10.2) and the simulated KER distributions as shown in Fig. 10.9, Fig. 10.10 and Fig. 10.13, we can see that the experimental result is somewhat between the simulated ones. Considering the ap-

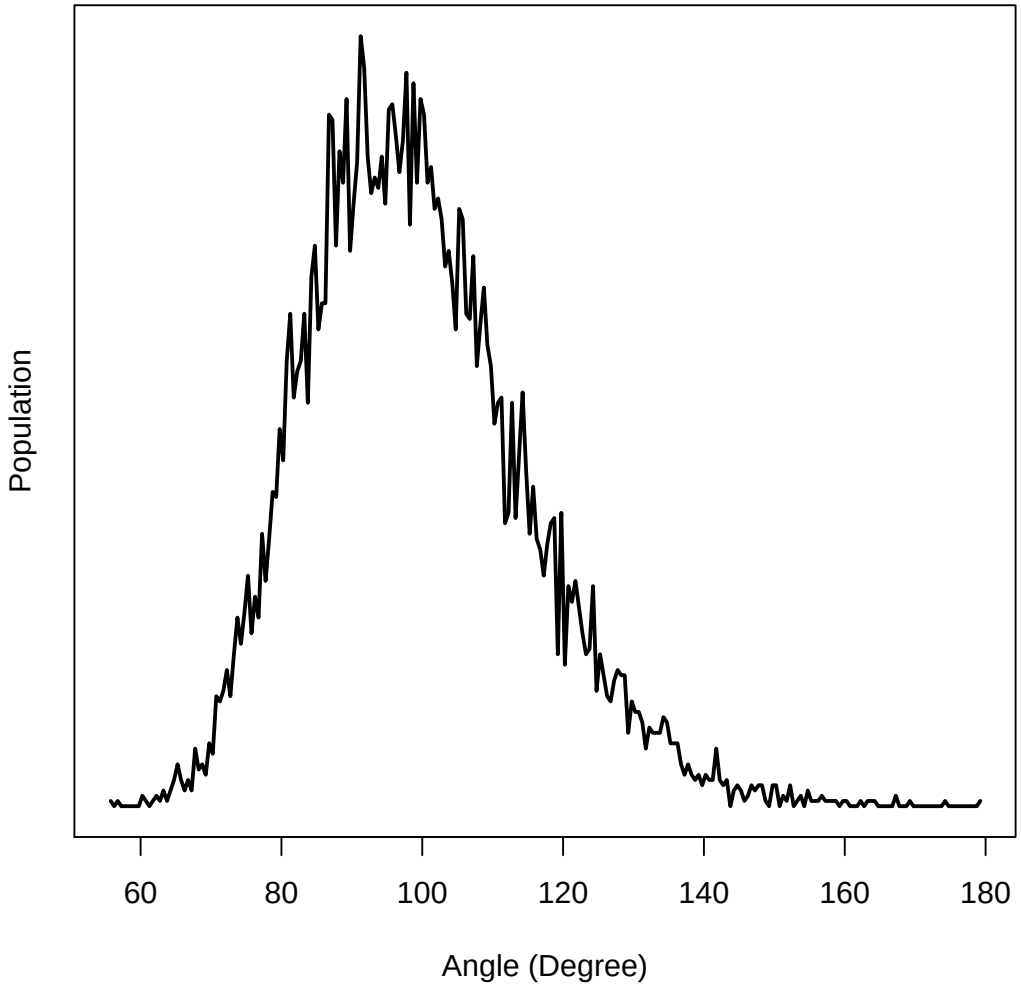

Figure 10.11: The ∠H-O-H distribution for H_2O from $H_3O \rightarrow H + H_2O$.

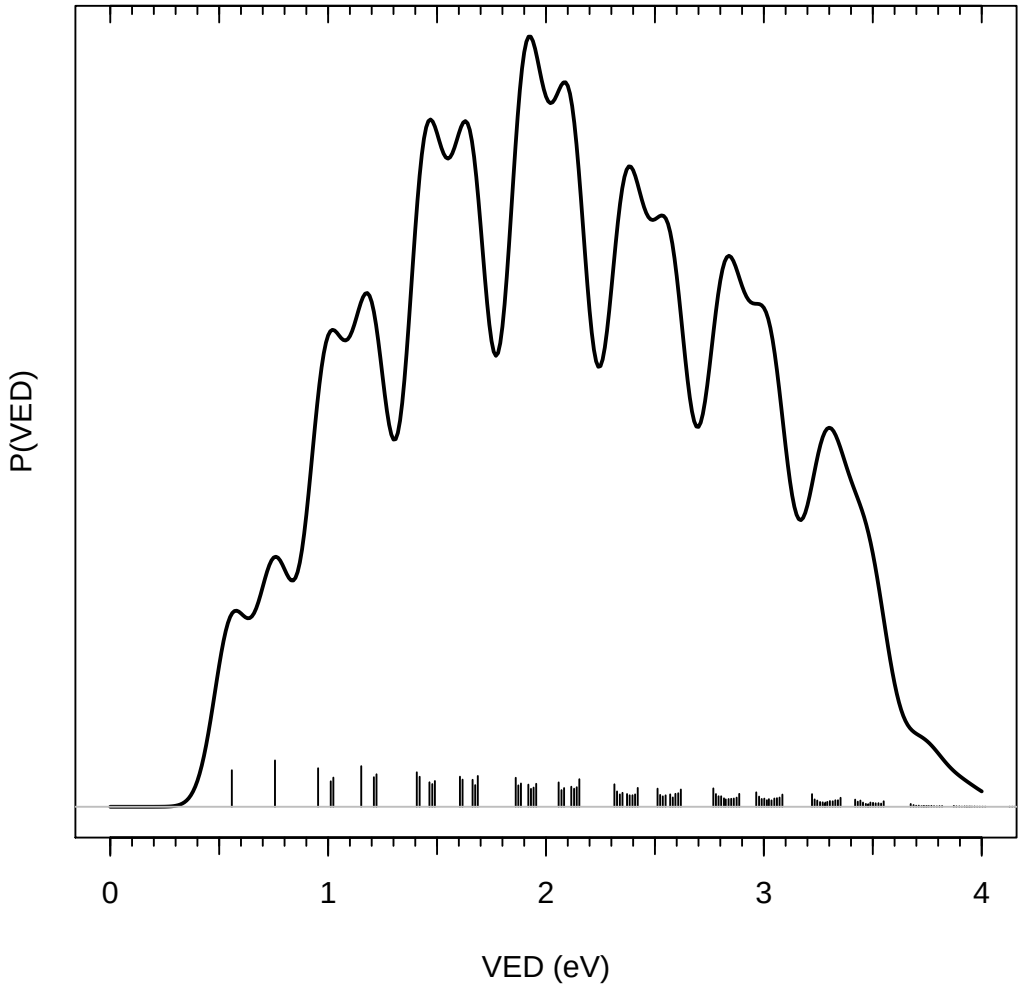

Figure 10.12: The quantized H_2O vibrational energy distribution from $H_3O \rightarrow H + H_2O$. Note that during the quantization, all the H_2O vibrational states with $n_1 > 3$ are removed.

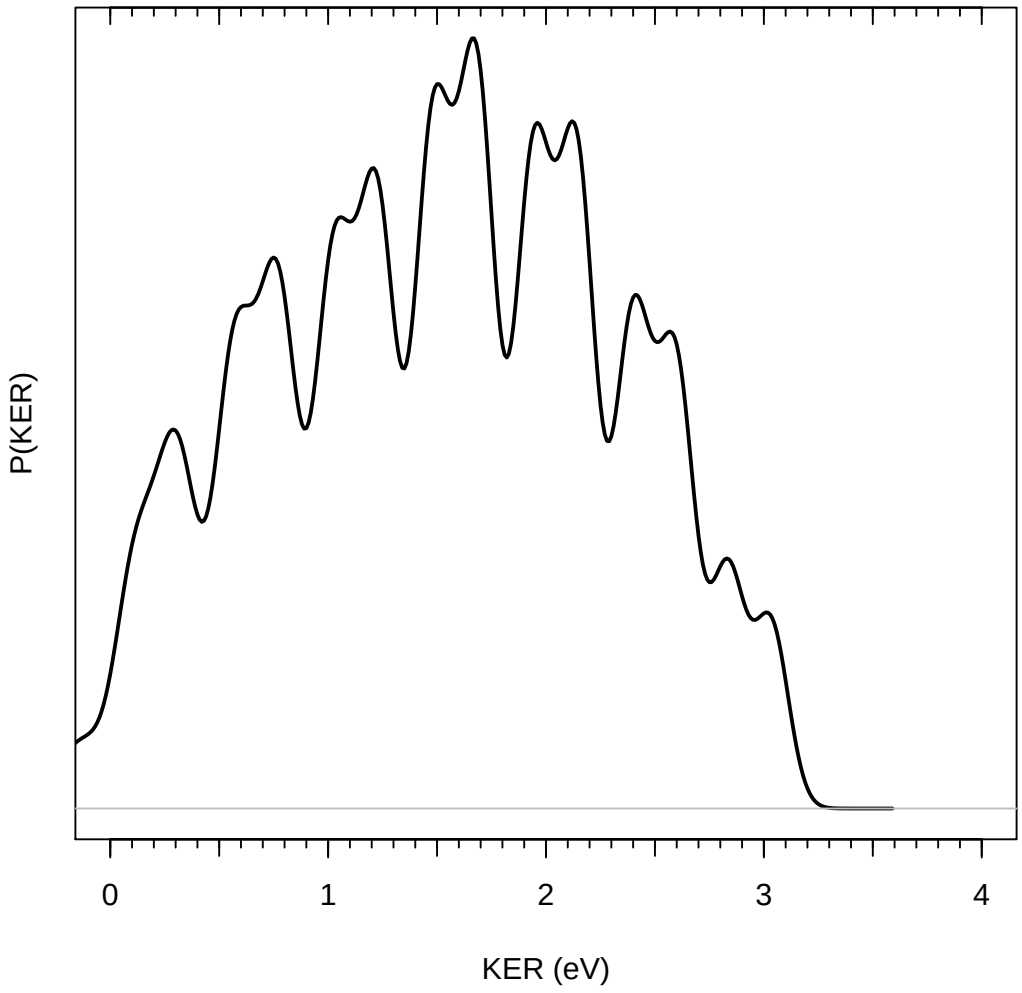

Figure 10.13: The $H_3O \rightarrow H + H_2O$ kinetic energy release distributions from the quantization of the classical vibrational energy distribution as shown in Fig. 10.7. Note that during the quantization, all the H_2O vibrational states with $n_1 > 3$ are removed.

proximation inherited in the classical trajectory simulation, the experimental and theoretical results match quite well, and the conclusion we can draw from this study is that during the charge exchange dissociation of H_3O^+, H_2O and H are the dominate products, and the H_2O molecules from the dissociation of H_3O are highly vibrational excited. Among the vibrational modes of H_2O, the bending one is relatively cooler than the symmetric and asymmetric stretch mode of H_2O.

For the charge exchange dissociation of H_3O^+, only one H atom is leaving, but the experiments can not tell which H atom actually leaves the H_3O. It will be very interesting to see if the initial H_3O^+ is deuterated, and that has been done for in the experiments and is still in the progress for the simulation.

11 Summary

In summary, the adoption of the invariant polynomials (primary and secondary invariants) in the PES construction process not only satisfies the permutation symmetry of molecules but also enhances the potential energy function fitting and evaluating processes. Some quasiclassical and *ab initio* direct trajectory simulations were performed to study the microscopic reaction mechanism of the reactions H_2 + H_3^+, H + CH_4, CH_5^+ and H_3O charge exchange dissociation dynamics, plus their various isotopomers. The theoretical simulation results agree quite well with most of the known experimental results, and there are also limitations showed for the classical trajectory simulations. One of them is the notorious zero-point energy (ZPE) issue, which is due to the inherit limitation of the classical mechanism. Overall, quasiclassical trajectory method remains a robust, intuitive and simple tool to investigate the chemical reaction dynamics. If quantum effects, such as ZPE etc, can be incorporated into the classical picture, this method will be extremely useful to understand the reaction dynamics. As for the potential energy surface fitting, the current approach is still limited to small molecules. This limitation comes from the lack of efficient representation of molecules, the complexity in computing the primary and secondary invariants, and the cost in obtaining the high quality *ab initio* energies. Considering the fast development of the computer techniques, it is still very promising to construct highly accurate potential energy surfaces for large molecule systems.

References

[1] H. Eyring and M. Polanyi, Z. Phys. Chem. (Leipzig) Abt. B **12**, 279 (1931).

[2] J. O. Hirschfelder, H. Eyring, and B. Topley, J. Chem. Phys. **4**, 170 (1936).

[3] B. Topley and H. Eyring, J. Chem. Phys. **4**, 178 (1936).

[4] M. Karplus, R. N. Porter, and R. D. Sharma, J. Chem. Phys. **43**, 3259 (1965).

[5] M. Baer, editor, *Theory of Chemical Reaction Dynamcs*, CRC Press, Boca Raton, FL, 1985.

[6] J. N. L. Connor, Comput. Phys. Commun. **17**, 117 (1979).

[7] J. N. L. Connor, J. Chem. Soc., Faraday Trans. **86**, 1627 (1990).

[8] C. Lawson and R. Hanson, *Solving Least Squares Problems*, Prentice-Hall, 1974.

[9] H. Derksen and G. Kemper, *Computational Invariant Theory*, Springer, 2002.

[10] W. Bosma, J. Cannon, and C. Playoust, J. Symbolic Comput. **24**, 235 (1997).

[11] E. Mortensen, J. Chem. Phys. **49**, 3526 (1968).

[12] S. Wu and R. Marcus, J. Chem. Phys. **53**, 4026 (1970).

[13] J. Bowman and A. Kuppermann, J. Chem. Phys. **59**, 6524 (1973).

[14] J. Maruhn and W. Greiner, Phys. Lett. B **B 44**, 9 (1973).

[15] K. Lee, J. Bowman, A. Wagner, and G. Schatz, J. Chem. Phys. **76**, 3563 (1982).

[16] G. Schatz, J. Chem. Phys. **79**, 5386 (1983).

[17] L. Gibson, G. Schatz, M. Ratner, and M. Davis, J. Chem. Phys. **86**, 3263 (1987).

[18] D. Lu and W. Hase, J. Chem. Phys. **89**, 6723 (1988).

[19] W. Miller, W. Hase, and C. Darling, J. Chem. Phys. **91**, 2863 (1989).

[20] T. Sewell, D. Thompson, J. Gezelter, and W. Miller, Chem. Phys. Lett. **193**, 512 (1992).

[21] A. Varandas and J. Marques, J. Chem. Phys. **100**, 1908 (1994).

[22] D. Shen, W. Chan, and H. Pritchard, J. Chem. Soc.-Faraday Trans. **91**, 3747 (1995).

[23] Y. Guo, D. Thompson, and T. Sewell, J. Chem. Phys. **104**, 576 (1996).

[24] D. McCormack and K. Lim, J. Chem. Phys. **106**, 572 (1997).

[25] J. Bowman, B. Gazdy, and Q. Sun, J. Chem. Phys. **91**, 2859 (1989).

[26] J. Bowman, S. Carter, and X. Huang, Int. Rev. Phys. Chem. **22**, 533 (2003).

[27] J. M. Bowman, B. Gazdy, P. Schafer, and M. C. Heaven, J. Phys. Chem. **94**, 2226 (1990).

[28] Wolfram Research, Inc., Mathematica version 5.1, 2004.

[29] M. P. Allen and D. J. Tildesley, *Computer simulation of liquids*, Oxford, 1987.

[30] J. M. Haile, *Molecular dynamics simulation*, Wiley, 1992.

[31] L. Verlet, Phys. Rev. **159**, 98 (1967).

[32] L. Verlet, Phys. Rev. **165**, 201 (1967).

[33] R. P. Feynman, R. B. Leighton, and M. Sands, *The Feynman Lectures on Physics*, volume 1, chapter 9, Addison-Wesley, 1963.

[34] D. Gerlich, E. Herbst, and E. Roueff, Planet Space Sci. **50**, 1275 (2002).

[35] Y. Yamaguchi, J. F. Gaw, R. B. Remington, and H. F. Schaefer III, J. Chem. Phys. **86**, 5072 (1987).

[36] R. Prosmiti, A. A. Buchachenko, P. Villarreal, and G. Delgado-Barrio, Theor. Chem. Acc **106**, 426 (2001).

[37] G. Moyano and M. Collins, J. Chem. Phys. **119**, 5510 (2003).

[38] R. Prosmiti, P. Villarreal, and G. Delgado-barrio, J. Phy. Chem. A **107**, 4768 (2003).

[39] H. Müller and W. Kutzelnigg, Phys. Chem. Chem. Phys. **2**, 2061 (2000).

[40] A. Brown, B. Braams, K. Christoffel, Z. Jin, and J. Bowman, J. Chem. Phys. **119**, 8790 (2003).

[41] A. Mccoy et al., J. Phys. Chem. A **108**, 4991 (2004).

[42] X. Huang, B. Braams, S. Carter, and J. Bowman, J. Am. Chem. Soc. **126**, 5042 (2004).

[43] X. Huang, B. J. Braams, and J. M. Bowman, J. Chem. Phys. **122**, 044308 (2005).

[44] H.-J. Werner et al., Molpro, version 2002.6, a package of ab initio programs, 2003, see http://www.molpro.net.

[45] J. Murrell, S. Carter, S. Farantos, P. Huxley, and A. Varandas, *Molecular Potential Energy Functions*, John Wikey & Sons, 1984.

[46] S. Foster et al., J. Chem. Phys. **84**, 91 (1986).

[47] R. Rohse, W. Kutzelnigg, R. Jaquet, and W. Klopper, J. Chem. Phys. **101**, 2231 (1994).

[48] W. Kolos and Wolniewicz, J. Chem. Phys. **49**, 404 (1968).

[49] K. Huber and G. Herzberg, *Constants of Diatomic Molecules*, Van Nostrand Reinhold, New York, 1979.

[50] Y. Yamaguchi, J. Gaw, and H. Schaefer, J. Chem. Phys. **78**, 4074 (1983).

[51] I. Stich, D. Marx, M. Parrinello, and K. Terakura, J. Chem. Phys. **107**, 9482 (1997).

[52] E. Ignacio and S. Yamabe, Chem. Phys. Lett. **287**, 563 (1998).

[53] M. Barbatti, G. Jalbert, and M. Nascimento, J. Chem. Phys. **113**, 4230 (2000).

[54] M. Elford, J. Chem. Phys. **79**, 5951 (1983).

[55] R. Beuhler, S. Ehrenson, and L. Friedman, J. Chem. Phys. **79**, 5982 (1983).

[56] K. Hiraoka, J. Chem. Phys. **87**, 4048 (1987).

[57] K. Hiraoka and T. Mori, J. Chem. Phys. **91**, 4821 (1989).

[58] T. Pang, Chem. Phys. Lett. **228**, 555 (1994).

[59] W. Kolos and L. Wolniewicz, J. Chem. Phys. **46**, 1426 (1967).

[60] L. Wolniewicz, I. Simbotin, and A. Dalgarno, Astrophys. J. Suppl. Ser. **115**, 293 (1998).

[61] T. Oka, Philos. Trans. R. Soc. A-Math. Phys. Eng. Sci. **364**, 2847 (2006).

[62] D. Gerlich, F. Windisch, P. Hlavenka, R. Plasil, and J. Glosik, Philos. Trans. R. Soc. A-Math. Phys. Eng. Sci. **364**, 3007 (2006).

[63] Z. Xie, B. Braams, and J. Bowman, J. Chem. Phys. **122**, 224307 (2005).

[64] T. Millar, A. Bennett, and E. Herbst, Astrophys. J. **340**, 902 (1989).

[65] T. Millar, Planet Space Sci. **50**, 1189 (2002).

[66] W. H. Hase, *Encyclopedia of Computational Chemistry*, pages 399–407, Wiley, New York, 1998.

[67] Z. Xie, J. Bowman, and X. Zhang, J. Chem. Phys. **125**, 133120 (2006).

[68] Z. Xie and J. Bowman, Chem. Phys. Lett. **429**, 355 (2006).

[69] M. Cordonnier et al., J. Chem. Phys. **113**, 3181 (2000).

[70] K. Giles, N. Adams, and D. Smith, J. Phys. Chem. **96**, 7645 (1992).

[71] T. Geballe and T. Oka, Nature **384**, 334 (1996).

[72] S. Petrie and D. Bohme, Mass Spectrom. Rev. **26**, 258 (2007).

[73] T. Geballe, Philos. Trans. R. Soc. A-Math. Phys. Eng. Sci. **364**, 3035 (2006).

[74] T. Geballe and T. Oka, Science **312**, 1610 (2006).

[75] P. Dawson and A. Tickner, J. Chem. Phys. **37**, 672 (1962).

[76] M. Okumura, L. Yeh, and Y. Lee, J. Chem. Phys. **88**, 79 (1988).

[77] Y. K. Bae, Chem. Phys. Lett. **180**, 179 (1991).

[78] J. B. Anderson, J. Chem. Phys. **63**, 1499 (1975).

[79] P. Reynolds, D. Ceperley, B. Alder, and W. Lester, J. Chem. Phys. **77**, 5593 (1982).

[80] P. Whitlock, D. Ceperley, G. Chester, and M. Kalos, Phys. Rev. B **19**, 5598 (1979).

[81] B. Bernu, D. Ceperley, and W. Lester, J. Chem. Phys. **93**, 552 (1990).

[82] F. Prudente, L. Costa, and P. Acioli, J. Phys. B-At. Mol. Opt. Phys. **33**, R285 (2000).

[83] A. Sarsa, K. Schmidt, and W. Magro, J. Chem. Phys. **113**, 1366 (2000).

[84] S. Baroni and S. Moroni, Phys. Rev. Lett. **82**, 4745 (1999).

[85] H. Roberts and T. Millar, Philos. Trans. R. Soc. A-Math. Phys. Eng. Sci. **364**, 3063 (2006).

[86] J. P. Camden et al., J. Am. Chem. Soc. **127**, 11898 (2005).

[87] J. P. Camden et al., J. Phys. Chem. A **110**, 677 (2006).

[88] W. Hu et al., J. Phys. Chem. A **110**, 3017 (2006).

[89] M. J. T. Jordan and R. G. Gilbert, J. Chem. Phys. **102**, 5669 (1995).

[90] J. Espinosa-García, J. Chem. Phys. **116**, 10664 (2002).

[91] T. Wu, H.-J. Werner, and U. Manthe, J. Chem. Phys. **124**, 164307 (2006).

[92] T. Wu, H.-J. Werner, and U. Manthe, Science **306**, 2227 (2004).

[93] J. Z. Pu and D. G. Truhlar, J. Chem. Phys. **116**, 1468 (2002).

[94] X. Zhang, B. J. Braams, and J. M. Bowman, J. Chem. Phys. **124**, 021104 (2006).

[95] J. P. Camden, H. A. Bechtel, and R. N. Zare, Angew. Chem.-Int. Edit. **42**, 5227 (2003).

[96] J. P. Camden, H. A. Bechtel, D. J. A. Brown, and R. N. Zare, J. Chem. Phys. **123**, 134301 (2005).

[97] D. L. Gray and A. G. Robiette, Mol. Phys. **37**, 1901 (1979).

[98] Nist chemistry webbook, http://webbook.nist.gov/chemistry.

[99] B. W. Silverman, *Density Estimation*, Chapman and Hall, London, 1986.

[100] D. W. Scott, *Multivariate Density Estimation. Theory, Practice and Visualization*, Wiley, New York, 1992.

[101] J. Camden, H. Bechtel, D. Brown, and R. Zare, J. Chem. Phys. **124**, 034311 (2006).

[102] G. Olah, G. Klopman, and Schlosbe.rh, J. Am. Chem. Soc. **91**, 3261 (1969).

[103] E. Herbst and D. Bates, Astrophys. J. **329**, 410 (1988).

[104] J. Bordasnagy, J. Holmes, and C. Hop, Int. J. Mass Spectrom. Ion Process. **85**, 241 (1988).

[105] E. White, J. Tang, and T. Oka, Science **284**, 135 (1999).

[106] X. Huang et al., Science **311**, 60 (2006).

[107] N. Adams et al., J. Chem. Phys. **94**, 4852 (1991).

[108] J. Semaniak et al., Astrophys. J. **498**, 886 (1998).

[109] K. Hanold, A. Luong, T. Clements, and R. Continetti, Rev. Sci. Instrum. **70**, 2268 (1999).

[110] Z. Jin, B. Braams, and J. Bowman, J. Phys. Chem. A **110**, 1569 (2006).

[111] S. Raynor and D. Herschbach, J. Phys. Chem. **86**, 3592 (1982).

[112] W. Griffiths, F. Harris, A. Brenton, and J. Beynon, Int. J. Mass Spectrom. Ion Process. **74**, 317 (1986).

[113] C. Laperle, J. Mann, T. Clements, and R. Continetti, Phys. Rev. Lett. **93**, 153202 (2004).

[114] C. M. Laperle, PhD thesis, University of California, San Diego, La Jolla, CA, 2004.

[115] W. J. Van Der Zandea, W. Koota, J. R. Petersonb, and J. Losa, Chem. Phys. Lett. **140**, 175 (1987).

[116] W. J. van der Zande, W. Koot, and J. Los, J. Chem. Phys. **91**, 4597 (1989).

[117] A. Petrignani, P. C. van der Zande, W. J.and Cosby, F. Hellberg, R. D. Thomas, and M. Larsson, J. Chem. Phys. **122**, 014302 (2005).

[118] W. A. Majewski, M. D. Marshall, A. R. W. Mckellar, J. W. C. Johns, and J. K. G. Watson, J. Mol. Spectrosc. **122**, 341 (1987).

[119] T. Oka, Phys. Rev. Lett. **45**, 531 (1980).

[120] B. J. McCall et al., Phys. Rev. A **70**, 052716 (2004).

[121] C. R. Sherwood and R. E. Continetti, Chem. Phys. Lett. **258**, 171 (1996).

[122] T. M. Stephen and B. L. Peko, Rev. Sci. Instrum. **71**, 1355 (2000).